Numerical Investigations of Macroscopic Particle Dynamics in Microflows

Lomholt, Sune

Publication date:
2001

Document Version
Publisher's PDF, also known as Version of record

Risø–R–1215(EN)

Numerical Investigations of Macroscopic Particle Dynamics in Microflows

Sune Lomholt

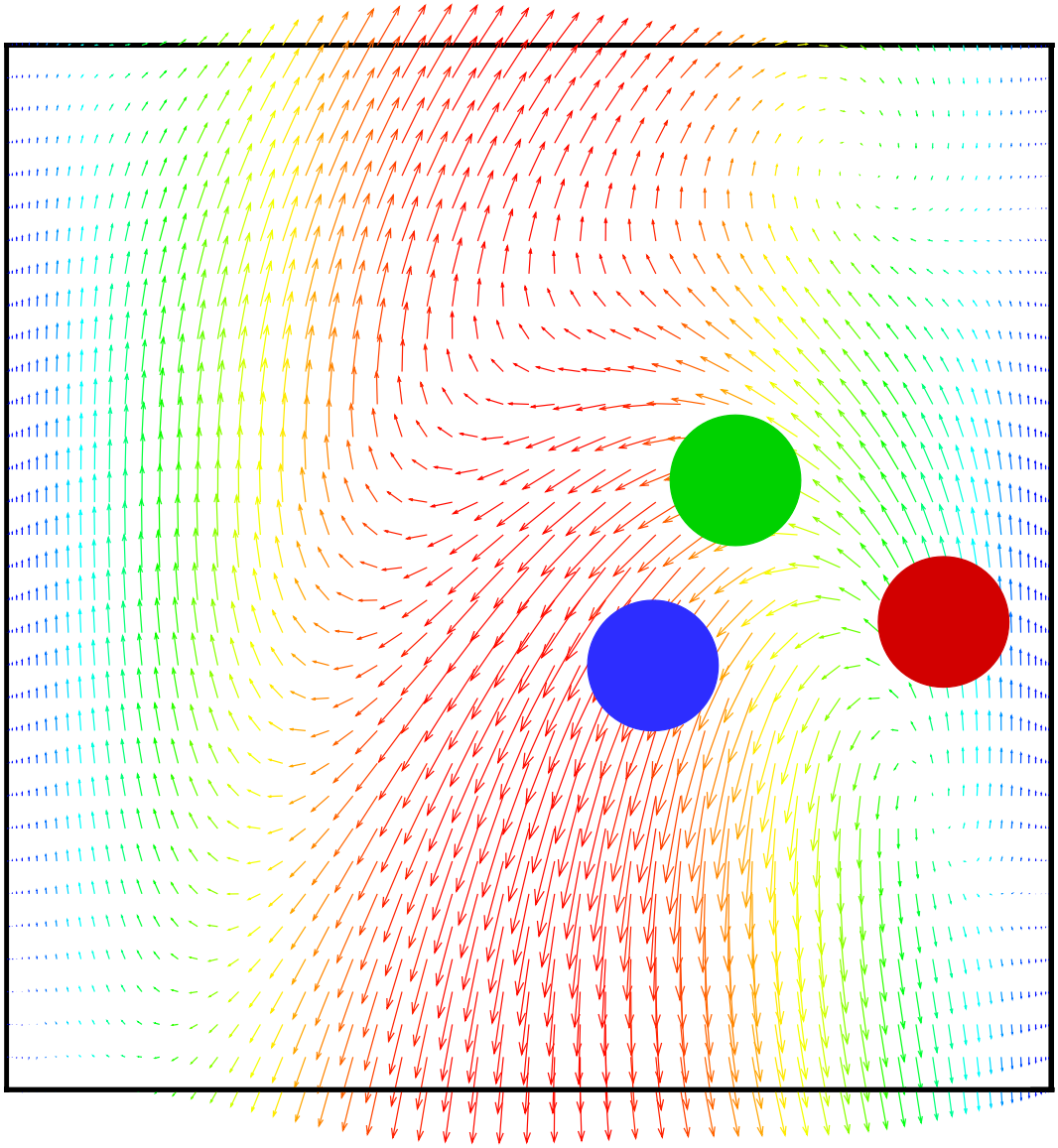

Risø National Laboratory, Roskilde, Denmark
October 2001

Abstract During the last decade microflows has become an important scientific field with applications in the area of chemical, biological, and biomedical analyses. The increasing interest in using microflows for sorting and analysing cells or particles has resulted in the need of methods for computing the transport dynamics of these objects.

In particulate microflows two main problems arise. Firstly, the size of the particles are only one or two orders of magnitude smaller than the smallest length scale of the carrying flow. Secondly, in many microsystems a considerably amount of particles are present (leading to a high volume fraction). So far no equation of motion for a particle in a fluid flow has been able to overcome these two problems. Consequently, another approach is needed for computing the particle dynamics in fluidic microsystems.

A method called force coupling is introduced and developed. The method is not limited to small particles or to few particles (low volume fraction). It uses knowledge about the forces from the particles on the fluid flow to solve the equations of motion for the fluid. The motion of each of the particles are determined from the fluid velocity field as a volume average of the fluid velocity in the neighbourhood of each of the particles.

The results from the force coupling method are verified by comparing with experimental data for a single sphere, two spheres, and three spheres rising in an inclined or vertical channel. Comparision of the trajectories and particle velocities show good agreement. Special attention is also given to the pressure driven Poiseuille flow, since microflows a typically of this kind. The force coupling method allows one to examine the disturbance flow created by the moving particles, and this can be used in the process of designing microfluidic structures for sorting, separating, or analysing particles or cells.

Front Page The figure on the front page shows the disturbance flow created by three neutrally buoyant spheres in an upwards Poiseuille flow in a channel. The diameter of the spheres is 1/8 of the channel width. The direction of flow is upward and the walls of the channel are placed at the rigth and left boundary of the figure. The color on the vectors shows the contour plot of the vorticity due to the undisturbed Poiseuille flow.

This thesis was submitted in partial fulfillment of the requirements for the degree of Doctor of Philosophy at the Technical University of Denmark, Microelectronic Center. It was submitted on September 4, 2000.

ISBN 87-550-2584-6 (Internet)
ISSN 0106-2840

List of Symbols

Latin Symbols

a	particle radius.
A	function related to analytic solution to the motion of a single particle.
A_i	non-dimensional vector related to the particle trajectory.
B	function related to analytic solution to the motion of a single particle.
C_D	drag coefficient.
C_i	various constants ($i = 1, 2, \cdots$).
d_i	separation between particles in direction i.
D_p	particle diameter.
e	internal energy.
e_i^n	surface normal vector.
e_i^Y	unit vector in direction of particle trajectory.
E_{ij}	rate of strain tensor.
f_H	Reynolds number depend function for the integration kernel K.
f_u	function of the force coupling terms in the velocity equations.
f_ω	function of the force coupling terms in the vorticity equations.
F_i	force or force monopole strengths.
F_{ij}	force dipole strengths.
F_{ijk}	force quadrupole strengths.
g	is used for various functions.
g_i	body force per unit mass or gravitational acceleration.
G	is used for various functions.
G_i	function of the force coupling terms.
h	length scale for balence between convection and diffusion.
h_u	function of the nonlinear terms in the velocity equations.
h_ω	function of the nonlinear terms in the vorticity equations.
H_i	function of the nonlinear terms.
J	various integrals.
k_i	Fourier modes.
K	integration kernel function in the Basset-history force.
Kn	Knudsen number.
ℓ	mean free path between collision of molecules.
l	distance between particles.
L	characteristic length scale.
L_s	slip length of boundary condition.
L_s^0	asymptotic slip length of boundary condition.
m	mass of a given volumen.
N	number of particles.
$O(...)$	order of magnitude.
O_{ij}	Oseen tensor.
p	pressure at point x_i and time t.
q_i	heat flux at point x_i and time t.
Q	volume flow rate.
r	radial distance ($r^2 = x_i x_i$).
Re	Reynolds number.
s	dummy variable for integration.
S_i	source term for the Navier-Stokes equations.
S_p	surface of particle.

Sl	Strouhal number.
t	time.
T	characteristic time scale of undisturbed fluid flow or temperature.
T_i	torque.
T_{ij}	tensor due to external torque (force dipole strength from external torque).
u_i	fluid velocity at point x_i and time t.
U_i	fluid free stream velocity at point x_i and time t.
U	characteristic velocity scale.
V	volume.
V_i	particle velocity at time t.
W_i	Stokes settling velocity.
x_i	point in space.
$\mathbf{x}$	equal to x_i, only used as function argument.
Y_i	position of particle (center of mass) at time t.
$\mathbf{Y}$	equal to Y_i, only used as function argument.

Greek Symbols

α	volumen fraction.
β	inter-particle spacing.
γ	shear rate.
γ_c	critical shear rate.
δ	Dirac delta function.
δt	small time step.
δ_{ij}	Kronecker delta (second order unit tensor).
Δ	Gaussian envelope function.
ε	ratio between $\sqrt{Re_\gamma}$ and Re_p.
ε_{ijk}	alternating tensor (vector product or create a second order tensor from a first order).
θ	angle.
λ	correction factor to Stokes drag or torque.
μ	dynamic viscosity (first coefficient).
μ_2	dynamic viscosity (second coefficient).
ν	kinematic viscosity.
ρ	density.
σ	length scale for the Gaussian Δ related to particle radius.
σ_{ij}	stress tensor at point x_i and time t.
τ	characteristic time of variation.
τ_S	relaxation time of Stokes drag.
ϕ	used for various functions or angles.
ω_i	vorticity at point x_i and time t.
Ω_i	particle angular velocity at time t.
Ω_{ij}	tensor from prescribed angular velocity at time t.

Subscripts

γ	denote quantities related to shear rate.
con	denote convection.
dif	denote diffusion.
D	denote quantities related to the force dipole.
f	denotes variable related to fluid.

i, j, k	used as tensor indices.
l	denotes leading sphere.
L	denotes lift force.
m	mean velocity or migration velocity.
M	denote quantities related to the force monopole.
Mc	denotes variables related to McLaughlin.
p	denotes variables related to particle.
u	denotes variables related to velocity.
t	denotes trailing sphere.
T	denotes variables related to torque.
ω	denotes variables related to vorticity.
Ω	denotes variables related to particle angular velocity.
VC	denotes variables related to Vasseur and Cox.

Superscripts

AM	denotes added mass force.
Mc	denotes variables related to McLaughlin.
n	summation index.
$Oseen$	denotes Oseen related quantities.
p	denotes variables related to particle.
q	iteration parameter.
RK	denotes variables related to Rubinow and Keller.
Sa	denotes variables related to Saffman.
$Steady$	denotes quantaties related to steady flow.
$Stokes$	denotes Stokes related quantities.
VC	denotes variables related to Vasseur and Cox.

Accents and Other

$\breve{a}$	denotes Fourier coefficient.
$\hat{a}$	denotes non-dimensional variables.
$\tilde{a}$	denotes integral averaged quantities.
∇	is the gradient $\frac{\partial}{\partial x_i}$.
∇^2	is the Laplacian $\frac{\partial^2}{\partial x_i \partial x_i}$.

Contents

Preface

This thesis describes the main results from the work in which I have participated during the last three and a half year. The work has been carried out at the Optics and Fluid Dynamics department (OFD) at Risø National Laboratory, Denmark in collaboration with the Microelectronic Center (MIC) at the Technical University of Denmark (DTU). Within this period I was on parental leave for five months, and on an extended stay at the Department of Applied Mathematics, Brown University, Providence, Rhode Island, for six months. I have had three advisers; Prof. L.Lading from Sensor Technology Center A/S & MIC, Dr. J.P. Lynov from OFD, Risø and Dr. P.Telleman from MIC, DTU.

The time as a Ph.D. student has been an experience which I would not have been without, my benefit from the time has been tremendous. However, none of the work presented here would have been possible, if it had not been for the support and help I have received from everyone. During the work I have had a considerable amount of support from my three advisers, Prof. L. Lading, Dr. J.P. Lynov, and Dr. P. Telleman. In particular, Dr. J.P. Lynov has been ever encouraging and motivating. Without his guidance this work would probably never have been completed.

During and after my stay at Brown University I had the pleasure of working with Prof. M.R. Maxey. Without doubt this collaboration has been a corner stone in the development of my scientific knowledge concerning particulate flows. His patience and willingness to answer my sometimes obscure questions has definitely been a great source of inspiration.

Dr. B. Stenum at OFD have also been a source of inspiration and his everlasting "scepticism" about my ideas has certainly kept me going. Without his experimental evidence I would never have been certain whether my results were succesful or not.

Furthermore, I will thank Robert Handler at the Naval Research Laboratory in Washington DC for providing me with the channel code, which has been used as the Navier-Stokes solver in the main parts of the thesis.

I would also like to thank the staff and students at both OFD and MIC for providing an informal and friendly atmosphere. They have certainly contributed to the enjoyment of these last three and a half years.

A huge graditude is also given to my beloved family. Without their support and help throughout the study, it would never have been completed.

Finally, I would like to thank Risø National Laboratory and UNI • C the Danish Computing Centre for Research and Education for their financial support.

Dansk resumé

Kemiske, biokemiske og biomedicinske analyser spiller en vigtig rolle inden for medicinal diagnostik, miljøovervågning og kvalitetskontrol af fødevareproduktion. Behovet for hurtige resultater uden store laboratorieomkostninger har ført til udviklingen af micro Total Analysis System (μTAS). μTAS er et automatiseret og miniaturiseret analysesystem, hvor små prøver nemt kan analyseres og resultaterne følges på computer.

En vigtig bestanddel af μTAS er mikrostrømninger. Inden for f.eks. biomedicin benyttes kanaler med dimensioner vinkelret på strømningen i størrelsesordenen 100μm til at transportere, sortere og analysere biologiske celler med dimensioner en eller to størrelsesordener mindre end kanalbredden. Den smalle kanalbredde er begrundet i ønsket om at kunne håndtere og analysere celler af størrelsesordenen $1 - 50\mu$m. Mens strømningen af bærevæsken er rimelig simpel at analysere, da Reynolds tallet for strømningerne typisk er meget lav ($Re < 100$), så er partikeldynamikken i strømningen ikke triviel, da man ikke kan betragte partiklerne som ideelle, dvs. masseløse og punktformige. Partiklernes bevægelse i bærestrømningen kan endvidere betyde, at den ellers simple strømning forstyrres, hvorved analysen af bærestrømningen kompliceres.

I nærværende arbejde gives en kort beskrivelse af mikrostrømninger og i særdeleshed af tre forskellige typer af mikrostrømninger med partikler. Disse tre typer danner udgangspunkt for en gennemgang og diskussion af mulighederne for at anvende en af de eksisterende ligninger for partiklers bevægelse i væsker. I denne gennemgang beskrives de forskellige bidrag til den hydrodynamiske kraft, som en partikel i en væskestrømning er udsat for. Bidragene afhænger af især tre parametre; Reynolds tallet, Strouhal tallet, samt hvor stor en del af det samlede volumen partiklerne udgør (volumen fraktionen). Baseret på Reynolds tallet og Strouhal tallet kan løsningerne til strømningen omkring en partikel deles op i fire forskellige regioner. Hver af disse regioner bliver beskrevet, og hvis der findes en løsning (bevægelsesligning) bliver denne forklaret. Konklusionen af gennemgangen er, at de eksisterende løsninger (bevægelsesligninger) kun kan anvendes til de tre typer af partikelholdige mikrostrømninger i et meget begrænset omfang. Derfor bliver en anden mulighed beskrevet og udviklet.

Den alternative løsning hedder "Force Coupling Method". Den er baseret på, at partiklen påvirker væsken med en kraft svarende til partikelinertien og de eksterne kræfter på partiklen (tyngdekraft, magnetiske kræfter, etc.). Effekten af disse kræfter indføres via et led i Navier-Stokes ligninger. Dermed opfattes hele beregningsvolumet som væske, og strømningsproblemet kan løses med eksisterende standardmetoder til løsning af Navier-Stokes ligninger. Partiklernes bevægelse i væsken bestemmes ud fra partiklernes hastighed. Partiklernes hastigheder beregnes som et vægtet volumengennemsnit af hastighedsfeltet i nærheden af den enkelte partikel. Efterfølgende findes partiklernes baner gennem væsken ved integration af deres hastighed.

Metoden verificeres ved at sammenligne de numeriske resultater med eksperimentelle resultater opnået på Risø. Sammenligningerne er for en enkelt partikel, der stiger opad i en skråt stillet kanal. Samt for to eller tre partikler, som ligeledes stiger opad i en lodret kanal. Resultaterne fra simuleringerne er i god overensstemmelse med resultaterne fra eksperimenterne. Da simuleringerne giver adgang til hele hastighedsfeltet, er det muligt at studere forstyrrelsesstrømningen, som følge af partiklernes bevægelse. Dette giver et særdeles godt indblik i, hvorfor de enkelte partikler bevæger sig som de gør. Derfor er dette et meget vigtig element, når en metode skal benyttes til design af mikrostrukturer beregnet til strømninger med partikler.

Mikrostrømninger med partikler er typisk kanalstrømninger, hvor bevægelse af væsken sker med en trykgradient. Derfor er metoden også blevet verificeret for denne type af strømninger. Simuleringerne af en partikel i en Poiseuille strømning viser, at metoden er i stand til at fange effekterne af bærestrømningen på partiklen. Det kan derfor konkluderes, at metoden er meget velegnet til simuleringer af partikelholdige mikrostrømninger, hvor en viden om både partiklernes bevægelse og om partiklernes indvirken på bærestrømningen er ønskelig. Således vil metoden være velegnet indenfor design af mikrosystemer til sortering og analyse af celler eller partikler, hvor simuleringer af partiklernes bevægelse vil kunne reducere udviklingstiden af et mikrosystem.

1 Introduction

In the last decade, it has become possible by means of microtechnology to manufacture microelectromechanical systems (MEMS) combining electrical and mechanical components on small silicon or polymer chips. The length scales involved in MEMS range from 1 μm to 1 mm. MEMS have attracted a lot of interest in areas as chemical, biochemical and biomedical analyses, where quick and good results with limited laboratory costs and small amounts of chemicals are highly desirable. The important role of chemical and biological analyses in medical diagnostic, environmental monitoring and quality process control has led to the development of a new concept, namely the micro Total Analysis System (μTAS). μTAS is an automated and miniaturized system for chemical and biological investigation based on MEMS technology, where very small samples are quickly and easily analyzed with the results simultaneously monitored on a computer.

In many biological and chemical analyses, particles or cells are to be analyzed or removed. Therefore particulate flows are an inherent part of the analysis. Some example applications of μTAS, where particulate flows are important are

- Cell transport, sorting and analysis in biomedicine and foodcontrol.
- Particle transport, sorting and analysis in environmental monitoring and control.
- Localized medical treatment through magnetic trapping of particles (medicine etc.) in blood veins.

A few examples of micro devices for the first two types of applications are given in section 2.3. The third application is not related to μTAS, but may be considered as a particulate microflow.

Due to the applications, microflows are an inherent part of μTAS. Microflows are needed for transport, mixing or sorting of samples, chemicals, particles, and biological cells. The tiny dimensions of the devices and the channels employed in μTAS lead to a fluid flow at low Reynolds number so the flow is generally laminar. On the other hand, the dimensions of the cells or the particles to be transported or sorted are often smaller than the dimensions of the channels by only one or two orders of magnitude. Therefore the movement of the particles in the carrying fluid will lead to a disturbance of this otherwise simple flow, resulting in the need of a more complicated analysis of the involved dynamics. This coupling between the carrying flow and the particles has implications for the dynamics of both the fluid flow and the particle trajectories.

Goal of the Thesis

The complex dynamics arising in the situations described above is the subject of this thesis. The focus of these studies is on both single particle dynamics and the dynamics of several interacting particles. The aim is to develop numerical tools for investigation not only of the particle dynamics, but also of the influence of the moving particles on the carrying fluid flow. This goal is reached with the development of a force coupling method that is able to reproduce the nonlinear dynamics of both the particles and the fluid flow. The results from the numerical model are compared with experimental results in a macroscopic channel operating at Reynolds numbers $Re < 10$, so that these are in the range of the Reynolds numbers in the microchannels.

Assumptions used in the Thesis

Based on the descriptions of microflows and particulate flows in chapters 2 and 3 several assumptions are given in order to simplify the problem and limit the scope of the thesis. These assumptions are summarized here:

1. Variations in the temperature are negligible, thus the energy equation is decoupled from the momentum and continuity equations and thus not considered.
2. The flow is incompressible and the density and viscosity are constant.
3. The boundary conditions on the channel walls are no-slip, thus at the solid boundaries $u_{fluid} = u_{wall}$.
4. The particles or cells are modelled by solid spheres.
5. On the particle or cell surface no-slip boundary conditions are assumed.
6. Particle inertia is neglected.

The physical interpretations of these assumptions are given in chapters 2 and 3. The limitations of the results, due to some of these assumptions will be discussed in chapter 6.

Outline of Thesis

Chapter 2 contains a short introduction to the physics and modelling of microflows with focus on the validity of the Navier-Stokes equations and associated boundary conditions. The chapter contains some examples of micro devices with particulate flows, and a short discussion of the implications for particulate microflows. The aim of the chapter is to give the reader a short introduction to the various aspects of fluid flows in micro devices. The chapter is concluded with a summary and a discussion.

Chapter 3 contains a description of particulate flows aiming at illuminating the problems and possibilities of computing particulate flows. The chapter gives a description of the hydrodynamic force acting on a particle dispersed in a fluid flow under various conditions with respect to length, time and velocity scales. The first three sections of the chapter describe various equations of motion depending on two characterstic properties of the flow, namely the Reynolds number and the Strouhal number. Then follows a section on lift forces and wall effects not included in the equations of motion. The effect of the particle motion on the fluid flow and interaction between particles are shortly described in the fifth section. Finally, the chapter contains a summary and discussion of the possibilities of computing particulate flows using an equation of motion.

In chapter 4 a force coupling method for computing particulate flows with large particles is presented. The method is described under Stokes flow conditions and examples of the method for Stokes flow are given. Since the method is based on the multipole representation of particulate Stokes flow, the chapter contains a brief introduction to the standard multipole representation in Stokes flow.

The force coupling method is extended to finite Reynolds numbers in chapter 5. The remaining parts of chapter 5 is devoted to verification of the model through examples of particle motion at finite Reynolds numbers in a channel. The first example concerns a single particle in order to investigate wall effects. The second and third examples, examine the capability of the force coupling method for computing interaction between two and three particles. The final examples are particulate Poiseuille flows, where cases with both a single particle and several interacting particles will be presented.

In the final chapter of the thesis concluding remarks and future perspectives are discussed. The chapter also considers the effect of the assumptions on the limitation of the results and the force coupling method.

Notation

A notice on the notation used in the thesis. In general, tensor notation with indices are used, i.e. a vector is written as v_i and a tensor as T_{ij}. One exception to this rule is a vector used as a function argument. In this case the vector is written with bold symbols as $\mathbf{v}$. Einsteins summation rule is applied, i.e. $v_i u_i = \sum_i v_i u_i$. In some cases the subscript on a variable consist of the indices separated from an additional subscript by a comma. This notation is used for distinguishing between various definitions of the variable. It is not used for derivatives. Derivatives are written out, i.e. as

$$\frac{\partial v_i}{\partial x_i} = 0 \qquad \text{or} \qquad \frac{\partial v_i}{\partial x_j} = 0$$

One special tensor used in the thesis is the alternating sign tensor,

$$\varepsilon_{ijk} = \begin{cases} 1 & \text{for } ijk = 123,\ 231,\ 312 \\ -1 & \text{for } ijk = 132,\ 321,\ 213\ . \\ 0 & \text{for } else \end{cases}$$

It can be used for creation of a tensor from a vector, $T_{ij} = \varepsilon_{ijk} T_k$, or to specify the product between two vectors, $v_i = \varepsilon_{ijk} a_j b_k$. A definition of this and a describtion of tensors may be found in Betten (1987).

2 Aspects of Microflows

As already mentioned in the introduction, microflows are a necessary part of MEMS and μTAS devices designed for chemical and biological analyses. Therefore it is important to consider the fluid mechanical aspects of microdevices. A complete review and description of the many micromachined components available for fluid handling is outside the scope of this thesis. The main purpose of this chapter is to discuss various aspects of fluid flows in microchannels, because of the importance it has for the description and modelling of particulate microflows. Descriptions of microdevices such as pumps, valves, nozzles, turbines and flow sensors are given in the extensive reviews by Gravesen et al. (1993), Spiering et al. (1997) and Ho & Tai (1998). In addition, these reviews contain a large amount of information on the many different applications of microdevices within the area of fluid handling.

Fluid flows in microchannels differ from those in macroscopic ducts. In macroscopic channels the continuum description of fluid flow given by the Navier-Stokes equations with no-slip boundary conditions at the solid walls, has been and is being used succesfully to predict the dynamics of the fluid flow. However, due to the small length scales of the channels in microdevices the validity of the Navier-Stokes equations or the no-slip boundary conditions for describing microflows may fail. As an example Pfahler et al. (1991) investigated the flow rate of liquid in channels with characteristic length scales ranging from 0.5μm to 40.0μm, and found a higher flow rate than predicted by the classical theory. This may be due to a violation of the no-slip boundary condition. The continuum assumption implied by the Navier-Stokes equations fails, if the mean free path between the molecules becomes comparable with the dimensions of the small channel. This is a severe constraint on gas flows, where the mean free path is much larger[1] than for liquids.

2.1 Microfluidic Gas Flows

For gas flows the Knudsen number can be used as a parameter characterizing the flow conditions. The Knudsen number is defined as

$$Kn = \frac{\ell}{L} \ ,$$

where ℓ is the mean free path between collision of molecules and L is a characteristic length scale of the fluid flow. Based on this, gas flows can be divided into four regimes:

1. $Kn \leq 10^{-3}$*:* Continuum hypothesis apply and Navier-Stokes equations with no-slip boundary conditions are valid. For example for air at atmospheric conditions this apply for channels with characteristic length scales larger than 100μm.

2. $10^{-3} \leq Kn \leq 10^{-1}$*:* Continuum boundary conditions fail and Navier-Stokes equations with slip boundary conditions applies. Slip boundary conditions are defined such that there is a jump in the velocity, but not necessarily free slip.

3. $10^{-1} \leq Kn \leq 10$*:* Moderately rarefied transition regime, continuum hypothesis fail and molecular models are needed.

4. $10 \leq Kn$*:* Highly rarefied regime, continuum hypothesis fail and molecular models are needed.

[1] For air at atmospheric conditions the mean free path is about 0.1 μm

A comprehensive review of the continuum model, the boundary conditions and molecular models in relation to microflows is given by Gad-el-Hak (1999). In the context of transport of large particles only the two first regimes are of importance, since particle transport in a rarefied gas is a seldom case. For these two first regimes the fluid flow is governed by the Navier-Stokes equations

$$\begin{aligned} \frac{\partial \rho_f}{\partial t} + \frac{\partial (\rho_f u_i)}{\partial x_i} &= 0 \\ \frac{\partial u_i}{\partial t} + u_j \frac{\partial u_i}{\partial x_j} &= \frac{1}{\rho_f} \frac{\partial \sigma_{ij}}{\partial x_j} + g_i \\ \frac{\partial e}{\partial t} + u_j \frac{\partial e}{\partial x_j} &= -\frac{1}{\rho_f} \frac{\partial q_j}{\partial x_j} + \frac{1}{\rho_f} \sigma_{ij} \frac{\partial u_i}{\partial x_j} \ , \end{aligned} \tag{1}$$

where ρ_f is the fluid density, u_i is the fluid velocity, σ_{ij} is the stress tensor, g_i is the body force per unit mass, e is the internal energy, and q_i is the heat flux. The stress tensor is related to the rate of strain. For a Newtonian fluid the relation is linear and given by

$$\sigma_{ij} = -p\delta_{ij} + \mu \left(\frac{\partial u_i}{\partial x_j} + \frac{\partial u_j}{\partial x_i} \right) + \mu_2 \frac{\partial u_k}{\partial x_k} \delta_{ij} \ , \tag{2}$$

where p is the pressure, δ_{ij} is the Kronecker delta, while μ and μ_2 are the first and second coefficients of viscosity. The two viscosity coefficients are often assumed to be related by (White (1991))

$$\mu_2 = -\frac{2}{3}\mu \ .$$

Derivation of (1) can be found in standard textbooks on fluid dynamics, e.g. White (1991). In this thesis we will assume that variations in the temperature are negligible. Therefore the energy equation (the last equation in (1)) is decoupled from the other four equations, and it will not be considered further. For a Newtonian fluid the governing equations then become

$$\begin{aligned} \frac{\partial \rho_f}{\partial t} + \frac{\partial (\rho_f u_i)}{\partial x_i} &= 0 \\ \frac{\partial u_i}{\partial t} + u_j \frac{\partial u_i}{\partial x_j} &= g_i - \frac{1}{\rho_f} \frac{\partial p}{\partial x_i} \\ &+ \frac{1}{\rho_f} \frac{\partial}{\partial x_j} \left(\mu \left(\frac{\partial u_i}{\partial x_j} + \frac{\partial u_j}{\partial x_i} \right) - \frac{2\mu}{3} \delta_{ij} \frac{\partial u_k}{\partial x_k} \right) \end{aligned} \tag{3}$$

The momentum equations in (3) need both initial and boundary conditions to be solved. The boundary conditions at solid walls in the continuum limit are

$$u_f - u_w = L_s \frac{\partial u}{\partial x_2}|_{wall} \ , \tag{4}$$

where L_s is the slip length, u_f and u_w are the fluid and wall velocity, and $\frac{\partial u}{\partial x_2}|_{wall}$ is the strain rate computed at the wall.

In gas flows the molecules will strike and reflect from the solid wall. The slip velocity is a result of the reflection of the molecules. If the mean free path is very small the molecules are closely packed. Therefore reflection from the wall is almost zero and the fluid will stick to the wall. When the mean free path becomes larger, the molecules will be reflected from the wall. If the wall is perfectly smooth, the molecules are reflected without any loss of momentum and there is perfect slip at the wall. However, it is more likely that the molecules will experience the wall as rough. This causes a loss of momentum for the molecules and this loss is transmitted to the wall as shear (White (1991)). Equilibrium across a plane adjacent to the wall requires that the momentum loss is balanced by a finite slip velocity. This balance leads to the expression (4) (White (1991)). For gases the mean free path is often used as the slip length, i.e. $L_s = \ell$ (White (1991)).

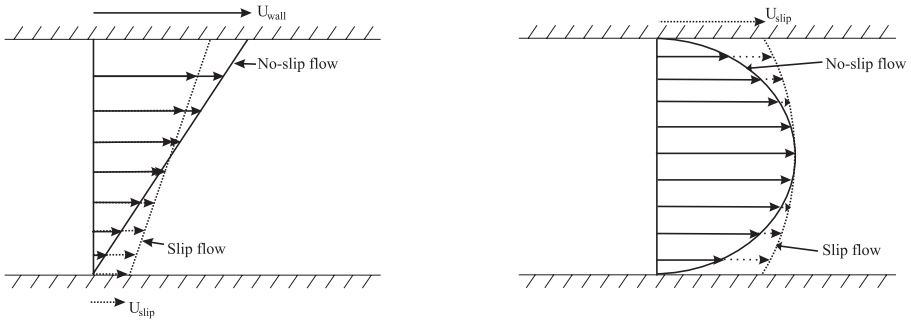

(a) Couette slip flow.

(b) Poiseuille slip flow.

Figure 1. Schematic drawings of the effect of slip boundary condition for bounded shear flows.

2.2 Microfluidic Liquid Flows

In liquids the molecules are closely packed, and the mean free path concept defined for gases does not apply (Gad-el-Hak (1999)). This results in the lack of a Knudsen number to obtain a division into regimes similar to that given above for gaseous fluids. The conditions under which the no-slip boundary condition fails are therefore not known. Additionally the linear relation (2) between the stress tensor and the strain rates may break down, when a very large stress is applied to the fluid; parameters specifying this is still lacking. Therefore the characterization relies on experiments and molecular dynamics simulations (Gad-el-Hak (1999)). Rheological studies of non-Newtonian flows yield some insight into the effect of shear stresses on fluids. If the shear stress becomes large enough, the Newtonian behaviour given by (2) of ordinary liquids like water will fail, and the relation between the stress and the strain rates is no longer linear. Although this critical stress is extremely large for water, other liquids may have properties where the breakdown is reached within reasonable values of the stress (Gad-el-Hak (1999)). The study of non-Newtonian fluid dynamics is a huge field in itself and the main topic is modelling of the stress tensor, i.e. determining an expression for the relation between the stress tensor and the rate of strain. Non-Newtonian effects will not be considered in this thesis and the reader is referred to the comprehensive textbook by Bird et al. (1987).

The slip boundary condition has been investigated by Thompson & Troian (1997) using a molecular dynamics simulation of a Couette flow as shown in figure 1(a). In a Couette flow the motion of the fluid is created by moving one or both of the walls in figure 1(a). Thompson & Troian (1997) found a general boundary condition as given by (4) with the slip length given as

$$L_s = L_s^0 \left(1 - \frac{\gamma}{\gamma_c}\right)^{-1/2} , \tag{5}$$

where L_s^0 is the asymptotic slip length, γ is the shear rate and γ_c is the critical shear rate. The critical shear rate is defined as the value of γ, where the slip length diverge and the boundary conditions are perfect slip. This must be determined by molecular dynamics simulations or from experiments. For liquids like water very large shear rates are needed in order to see any effect of the above boundary condition. Such shear rates are only found in very small channels with very high flow

velocities (Gad-el-Hak (1999)). Nevertheless, the slip boundary condition applies for Newtonian liquids at very high shear rates, because γ_c is obtained for stresses much smaller than the critical stress at which the Newtonian behaviour of the liquid fails. For the Couette flow situation, the slip flow may result in a reduced flow rate, since the slip reduces the momentum transfer from the moving boundary to the liquid. On the other hand, the momentum transfer in Poiseuille flow is obtained by applying a pressure gradient over the channel, and therefore the slip boundary condition may cause an increased flow rate as observed by Pfahler et al. (1991), see figure 1(b).

The above considerations about the validity of the continuum approximation inherent in the Navier-Stokes equations, has been the starting point of a number of investigations concerning the applicability of Computational Fluid Dynamics (CFD) to model the fluid dynamics of microflows. As already mentioned, the experiments by Pfahler et al. (1991) showed that for channels in the range 0.5 to 40 μm the experimental values of the flowrates deviated from those predicted using Navier-Stokes equations. On the other hand, Harper et al. (1995) performed a numerical and experimental investigation of liquid flow through channels with characteristic length scales above 25 μm. They compared mass flow rates computed using a commercial CFD program with experimental values in both straight channels and channels with curved or squared (90^0) bends. They found the computed values to be less than the experimental values with the error being smaller than 5%. This is a moderate error, probably due to the numerical approximations and the experimental uncertainties. Flockhart & Dhariwal (1998) made a similar study for straight channels with characteristic length scales in the range 50 μm to 120 μm. They also conclude that the errors in the numerical results are within the acceptable limit, and that the continuum description given by the Navier-Stokes equations is appropriate for their range of channel dimensions. In a numerical and experimental study of mass transfer in channels ranging from 10 μm to 100 μm Shaw et al. (1996) showed that CFD may be used for accurately predicting the mass transfer between two adjacent liquids. Harper et al. (1995) also examined flow fields in a micromanifold, and found qualitative agreement between the computed flow field and the experimental flow field. This further supports the validity of the continuum assumption for channels with characteristic length scales larger than 10 μm.

2.3 Particulate Microflows

Microdevices with particulate flows may be divided into three different kinds with respect to their use.

1. *Sorting:* Separation of a specific cell type or particle from a mixture.
2. *Analysing:* Analysing an individual cell or particle.
3. *Removal:* Removing particles or cells from a sample.

Obviously, the three types defined above are not totally distinct. Firstly, in all three kinds of devices, transport of the cells or particles is an inherent part. Secondly, the first and third type both include a change in direction of the particle trajectory in order to guide some or all the particles away from the sample.

Examples of the first type are microdevices based on micro fluorescent activated cell sorting (μFACS) and micro magnetic activated cell sorting (μMACS) described by Telleman et al. (1998). In both these systems the sorting device consists of three inlets and two outlets[2] as shown in figure 2. In μFACS, the targeted cells

[2]More inlets or outlets are possible, this depends on the actual application and design. Here only three inlets and two outlets are drawn.

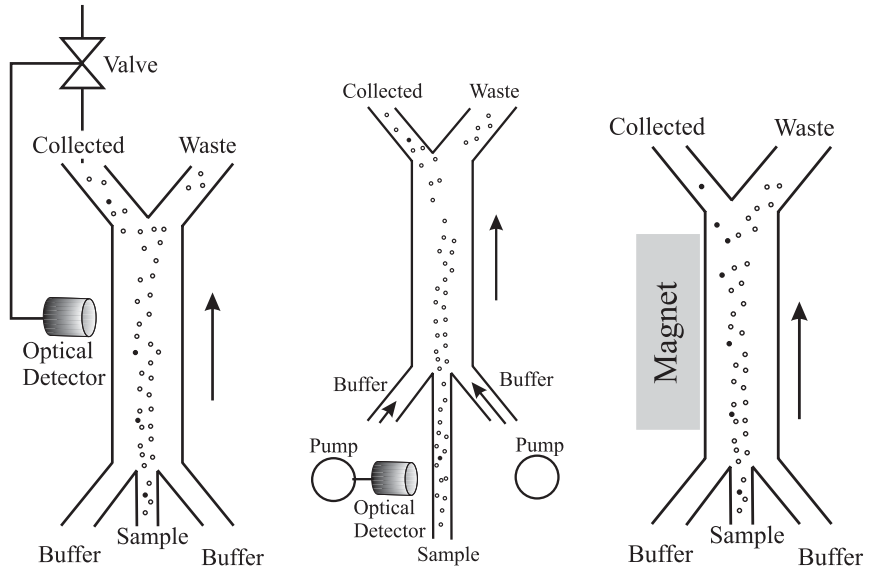

(a) Valve controlled μFACS.

(b) Flow rate controlled μFACS.

(c) Example of μMACS.

Figure 2. Schematic drawings of three kinds of particle separators (Telleman et al. (1998) and Blankenstein et al. (1996)). The arrows indicate the flow direction.

are labelled with fluorescent antibodies. When they pass an optical sensor, a valve is activated and the sample outlet is opened until the cell has been collected, see figure 2(a). Another method for collecting cells is based on flow rate switching. In this case the optical sensor is placed at the sample channel, see figure 2(b). When a positive cell is detected by the sensor, a pump is activated. This creates a larger flow rate in the right buffer channel in figure 2(b). Hence, the sample stream is forced into the collection outlet instead of the waste outlet (Blankenstein et al. (1996)). In both methods there will be an amount of unwanted cells following the desired cell. This is a disadvantage of the μFACS method, see figures 2(a) and 2(b). However, repeating the sorting process on the collected sample using several μFACS devices in series connection will increase the concentration of desired cells. In μMACS this may be avoided, since the collection outlet is only reached by the desired cells. This is obtained by labelling the cells with paramagnetic antibodies. The trajectory of the cell is deflected using a magnetic gradient in the sorting channel, and the desired cell is transported into the collecting outlet, see figure 2(c). An application of these sorting devices is rare event cell sorting, where a few cells are to be taken out of a mixture of several million cells (Wolff et al. (1998)). In these cases the typical characteristic length of the channel is about 100 μm and the cells are about 5-10 μm (Telleman et al. (1998), Wolff et al. (1998)). Since the sorting devices are intended for living cells, the carrying fluid and the buffers are neutral liquids. Furthermore, high shear rates should be avoided in order to ensure that the stresses on the cell surfaces is low enough for the cells to stay alive.

A device for analysing embryos has been described by Glasgow et al. (1998). They transported single mouse embryos of diameters 90-120 μm in channels with characteristic lengths of 200 μm. In contrast to the cell sorting devices above, the problem here is to accurately transport a single large living cell from one place to the next in order to analyse, fertilize or culture the cell, see figure 3. This requires accurate management of the pressure controls. As in the cell sorting devices, the carrying fluid is still a liquid and the shear rates must be low in order to avoid

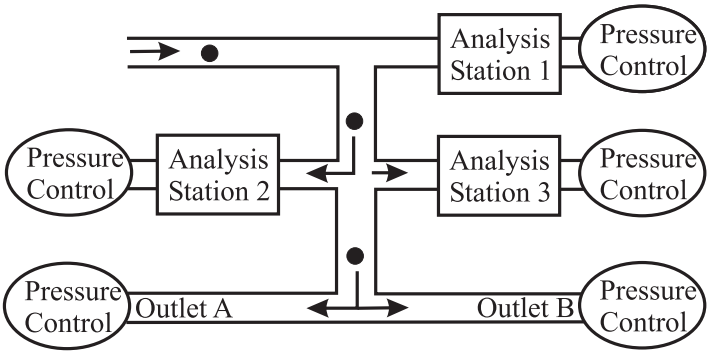

Figure 3. A device for embryo analysis (Glasgow et al. (1998)).

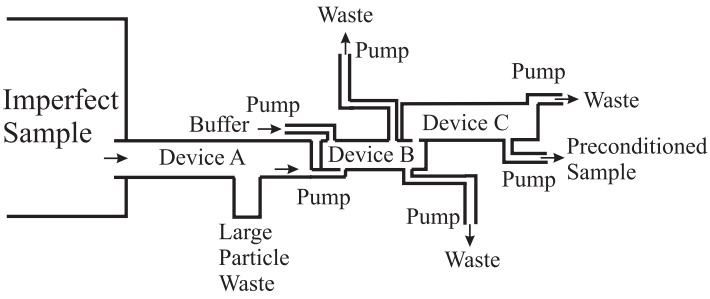

Figure 4. A device for sample preconditioning (Yager et al. (1998)).

stresses on the cell surface that may damage the cell.

Removal of particles or cells from a sample is important in continuous operation of a microdevice, since undesired particles or cells may clog small channels, damage coatings on channel walls or interfere with optical measurements (Yager et al. (1998)). A sample preconditioning device for environmental use is described by Yager et al. (1998) and shown in figure 4. The device was constructed to remove particles of sizes up to 10 μm from an airstream. The air stream moves through various stages in the microdevice, each of these designed to remove a given size and density of the particles, see figure 4. In this device the fluid is a gas and the particles are solids. Thus, the situation is quite different from the two previous examples. A wide range of particle sizes and types may be present and a high value of shear rate plays no role concerning the "survival" of the particle as it was in the case of cell transportation and sorting. Hence, the flow may be compressible with slip boundary conditions, contrary to the sorting and analysing examples where the flow is incompressible with no-slip boundary conditions. On the other hand, if the flow rate is low and the characteristic channel sizes are large, the device described by Yager et al. (1998) may also be modelled by an incompressible flow with no-slip boundary conditions.

2.4 Summary and Discussion of Microflows

Summarizing the considerations in sections 2.1 and 2.2, we are able to conclude the following. Gas flows in microchannels fall into four different regimes depending on the Knudsen number. For particle transport only the first two are relevant. In these two regimes the Navier-Stokes equations with no-slip or slip boundary conditions at the channel walls can be used for modelling the gas flow. Furthermore, it may be necessary to include the compressibility of the gas in the model. Liquid flows may

in general be considered as incompressible, and for channels with a characteristic length scale larger than approximately 50 μm the Navier-Stokes equations with no-slip boundary conditions are adequate. The exceptions are cases with very large shear rates, where the no-slip boundary condition may fail. For channels with characteristic sizes larger than 50 μm, this requires an extremely high fluid velocity and is therefore unrealistic. In channels smaller than 50 μm high shear rates may be possible, and this will then cause a change in the boundary condition from no-slip to slip conditions as described by Thompson & Troian (1997). Obviously, the value of the characteristic length, at which the no-slip boundary condition will fail, depend on the quantities (density, viscosity, etc.) of the fluid.

The examples of particulate microflows given above all considered channels with a characteristic length scale larger than 50 μm. In the first two examples liquid flow is considered and therefore Navier-Stokes equations are a suitable model. In the third example the fluid was a gas and the considerations regarding the Knudsen number determines whether the Navier-Stokes equations are suitable or not. However, the model of the particulate microflow studied in this thesis is an incompressible flow with no-slip boundary conditions. The particles or cells are modelled as solid spheres with a no-slip boundary. This model is obviously not fully correct for any of the three examples, but it provides a frame that can be used as an approximation to all of them. The assumptions for the particulate microflows considered in this thesis are summarized as:

1. Variations in the temperature are negligible, thus the energy equation is decoupled from the momentum and continuity equations and it is not considered.
2. The flow is incompressible, thus the density and viscosity are constant.
3. The boundary conditions on the channel walls are no-slip, thus at the solid boundaries $u_f = u_w$.
4. The particles or cells are modelled as solid spheres.
5. On the particle or cell surface no-slip boundary conditions are assumed.
6. Particle inertia is neglected.

Some of these assumptions may relatively easily be relaxed. For example, the no-slip boundary condition on the channel walls may be replaced by the more general boundary condition given by (4) and (5). It is also possible to allow temperature variations, although it requires considerations regarding the effect of the temperature on the particles or cells. Extending the work to non-spherical particles and/or including particle inertia will be discussed in chapter 6. Relaxing the condition of incompressibility is more subtle, and will not be discussed in this thesis.

3 Aspects of Particulate Flows

In this chapter we will discuss some general aspects of particles in fluid flows. The focus will be on liquid-solid flows, because applications in microfluidic systems will typically be of this type, e.g. sorting, counting or characterization of particles or cells, as explained in chapter 2. However, with small modifications many of the general statements will also apply to other types of particulate flows.

Characterization of particulate flows can be based on various properties (Sommerfeld (2000)). The volume fraction is a commonly used property. It measures whether the particulate flow is dilute or dense. The volume fraction is given by the volume occupied by the particles relative to the total volume, i.e.

$$\alpha = \frac{\sum_i N_i \mathrm{V}_{p,i}}{\mathrm{V}} \ ,$$

where N_i is the number of particles of volume $\mathrm{V}_{p,i}$ and V is the total volume. A property related to the volume fraction is the inter-particle spacing, β. The inter-particle spacing is important for characterizing the coupling between the fluid phase and the particulate phase, as well as for the particle-particle and particle-wall interaction (Sommerfeld (2000)). Analytical expressions for the inter-particle spacing is only available for regular configurations of particles. According to Sommerfeld (2000) the inter-particle spacing for a cubic arrangement of spheres is

$$\beta = \frac{l}{D_p} = \left(\frac{\pi}{6\alpha}\right)^{1/3} \ ,$$

where l is the distance between the spheres and D_p is the sphere diameter. Using the volume fraction and inter-particle spacing, Elghobashi (1994) classified particulate flows with respect to the importance of various interaction mechanisms. The classification is shown in figure 5, where three different regimes are displayed. When the volume fraction α is less than 10^{-3}, the particulate flow is considered as dilute. In a very dilute flow, $\alpha < 10^{-6}$, the influence of the particles on the fluid flow is negligible. This is called one-way coupling since the coupling is only from the fluid to the particles. For $10^{-6} < \alpha < 10^{-3}$, the influence of the particles on the fluid flow must be considered. This is known as two-way coupling since there is a coupling both from the fluid to the particle and from the particles to the fluid. In the dense regime, $\alpha > 10^{-3}$, fluid dynamic interaction and collisions between the particles become significant and must be accounted for. This regime is called four-way coupling since the two-way coupling is extended with two types of interaction between particles namely fluid dynamic interaction and collision.

Besides the characterization based on the volume fraction, the particle motion is also characterized by other non-dimensional parameters for the flow. This is best illustrated by considering the basic problem of a rigid particle moving in an unbounded fluid with free stream velocity U_i. The problem is given by the incompressible Navier-Stokes equations, i.e.

$$\frac{\partial u_i}{\partial x_i} = 0 \tag{6}$$

$$\rho_f \frac{\partial u_i}{\partial t} + \rho_f \ u_j \frac{\partial u_i}{\partial x_j} = -\frac{\partial p}{\partial x_i} + \mu \frac{\partial^2 u_i}{\partial x_j \partial x_j} \ . \tag{7}$$

Equations (6) and (7) are solved so that the boundary conditions on the particle and at infinity are satisfied. In the case of a rigid particle a no-slip condition is appropriate, thus the boundary condition at the particle surface, S_p, is

$$u_i(\mathbf{x}, t) = V_i(t) + \varepsilon_{ijk}\Omega_j(x_k - Y_k) \qquad \text{for } x_i \in S_p \ , \tag{8}$$

where V_i, Ω_i and Y_i are the velocity, angular velocity and position of the center of mass of the particle, while $\varepsilon_{ijk}\Omega_j\,(x_k - Y_k)$ is the vector product of Ω_j and $(x_k - Y_k)$. Far from the particle the boundary condition is

$$u_i = U_i \ .$$

The characteristic properties for the flow, are found by making equations (7) non-dimensional in order to see the importance of the various terms. Hence, if we make (7) non-dimensional by introducing the characteristic velocity scale U, the characteristic length scale L and the characteristic time scale of variation τ we obtain

$$\frac{\rho_f U}{\tau}\frac{\partial \hat{u}_i}{\partial \hat{t}} + \frac{\rho_f U^2}{L}\hat{u}_j\frac{\partial \hat{u}_i}{\partial \hat{x}_j} = -\frac{1}{L}\frac{\partial p}{\partial \hat{x}_i} + \mu\frac{U}{L^2}\frac{\partial^2 \hat{u}}{\partial \hat{x}_j \partial \hat{x}_j} \ ,$$

where $\hat{}$ denotes non-dimensional variables. This is rearranged into

$$Re\ Sl\ \frac{\partial \hat{u}_i}{\partial \hat{t}} + Re\ \hat{u}_j\frac{\partial \hat{u}_i}{\partial \hat{x}_j} = -\frac{\partial \hat{p}}{\partial \hat{x}_i} + \frac{\partial^2 \hat{u}}{\partial \hat{x}_j \partial \hat{x}_j} \ , \tag{9}$$

where $\hat{p} = p(L/\mu U)$ is the non-dimensional pressure. The Reynolds number and the Strouhal number are

$$\begin{aligned} Re &= \frac{\rho_f L U}{\mu} = \frac{LU}{\nu} \\ Sl &= \frac{L}{U\tau} \ , \end{aligned}$$

where ν is the kinematic viscosity of the fluid. The Reynolds number is a measure of the inertia forces relative to the viscous forces, while the Strouhal number gives a measure of the time scale of convection, L/U, relative to the time scale of variation, τ. With respect to these two dimensionless quantities four different regimes may be observed:

1. *No inertia:* In this region both Re and Sl are zero or at least very small, so that both inertia terms in (9) may be neglected and the result is a steady Stokes flow.

2. *Convective inertia:* In this region the Reynolds number is finite and $ReSl$ is very small or zero. Therefore only convective inertia in (9) is included. For $Re < 1$ the result is a steady Oseen flow.

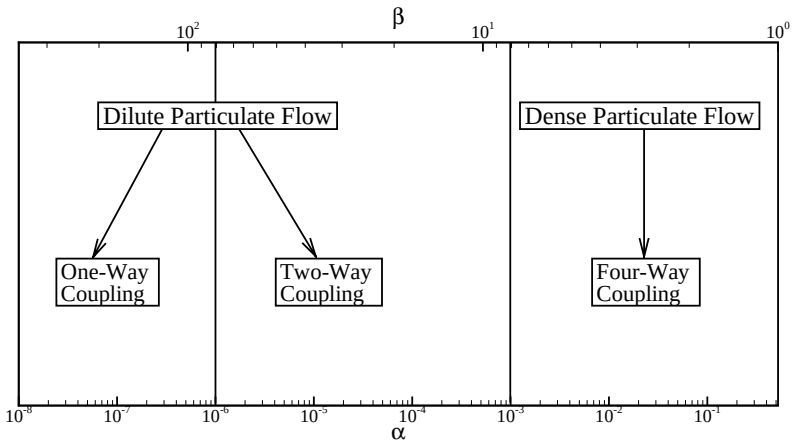

Figure 5. Classification of particulate flows into different regimes with regard to the importance of the interaction mechanisms (Elghobashi (1994)).

3. *Unsteady inertia:* In this region the Strouhal number large ($Sl \gg 1$), while the Reynolds number is small enough to neglect the the non-linear term. Thus only unsteady inertia in (9) is retained and the result is an unsteady Stokes flow.

4. *Both inertia terms:* In this region both Re and Sl are finite and may be large, thus all terms in the Navier-Stokes equations must be considered.

In the following sections we will discuss the differences between the regimes. Furthermore, there will be a section on other forces such as lift forces due to shear flow or particle rotation.

3.1 Steady Flow

The first solution to the problem of the hydrodynamic force on a sphere in a fluid flow is due to Stokes. Stokes considered the force on a sphere placed in a uniform stream with velocity, U_i, in the limit of zero Reynolds number. The solution was thus based on the steady Stokes equations

$$\frac{\partial p}{\partial x_i} = \mu \frac{\partial u_i}{\partial x_j \partial x_j} \ , \tag{10}$$

with the boundary conditions

$$u_i = \begin{cases} 0 & \text{for } x_i x_i = a^2 \\ U_i & \text{for } x_i \to \infty \ , \end{cases}$$

where a is the sphere radius and the sphere center is fixed at the origin. The solution to this problem may be found in standard textbooks on fluid dynamics, e.g. White (1991) or Langlois (1964). Figure 6 shows the streamlines and vorticity contours for the solution. The most notable property of the solution is the perfect fore-and-aft symmetry. From the solution for the flow field, Stokes found the hydrodynamic force on the sphere to be

$$F_i^{Stokes} = 6\pi\mu a U_i \ . \tag{11}$$

This is known as Stokes drag law.

Since the velocity goes to zero at the surface of the sphere, the assumption of low Reynolds number holds in the vicinity of the sphere. On the other hand, the velocity far from the sphere approaches the free stream, and here the largest convective term is of the order of

$$\rho_f u_j \frac{\partial u_i}{\partial x_j} \sim O\left(\frac{\rho_f U^2 a}{r^2}\right) \ ,$$

where r is the radial distance from the sphere center. The largest viscous term is of the order of

$$\mu \frac{\partial^2 u_i}{\partial x_j \partial x_j} \sim O\left(\frac{\mu U a}{r^3}\right) \ .$$

Therefore the ratio of convective inertia to viscous forces far from the sphere is

$$\frac{\text{convective inertia force}}{\text{viscous force}} = \mathrm{O}\left(\rho \frac{U^2 a}{r^2} \frac{r^3}{\mu U a}\right) = \mathrm{O}\left(\frac{r}{2a} Re_p\right) \ ,$$

where Re_p is the particle Reynolds number

$$Re_p = \frac{2a|V-u|}{\nu} = \frac{2aU}{\nu} \ ,$$

with $|V-u|$ being the absolute value of the slip velocity of the sphere at the sphere center of mass. This shows that the convective term is comparable with the viscous term for distances from the sphere of order $r = \mathrm{O}\left(\frac{2a}{Re_p}\right)$. Hence, the

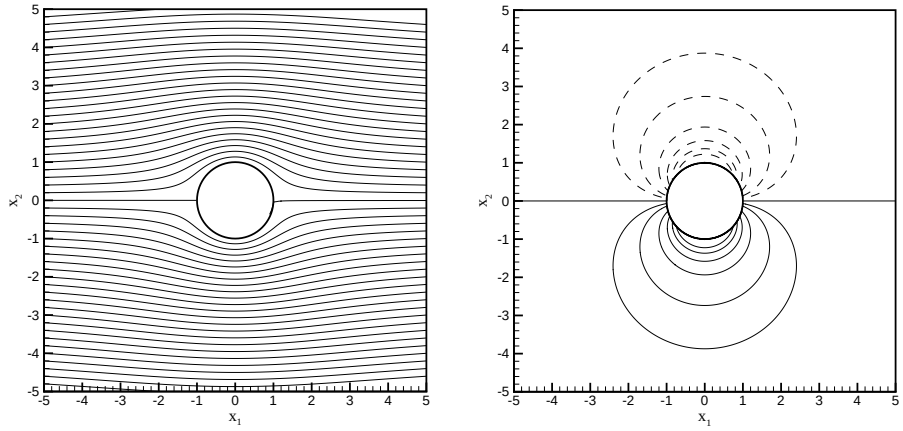

(a) Streamlines (b) Vorticity contours

Figure 6. Streamlines and vorticity contours for the steady Stokes flow past a sphere. The vorticity is made non-dimensional with U/a. The vorticity contours are ± 1 (innermost), ± 0.8, ± 0.6, ± 0.4, ± 0.2 and ± 0.1 (outermost). On the sphere top and bottom ($(x_1, x_2) = (0, \pm 1)$) the vorticity has its maximum of ± 1.5. Negative vorticity is denoted by dashed lines.

solution found by Stokes is not a uniformly valid approximation to the Navier-Stokes equations except for the special (and unphysical) case of $Re_p = 0$. This criticism of Stokes' solution was first given by Oseen (White (1991)), who also proposed a scheme to solve the problem. The scheme is based on the observation that far from the sphere the flow field is given by $u_i \approx U_i$, and the convective terms in the steady Navier-Stokes equations can be linearized as

$$\rho_f u_j \frac{\partial u_i}{\partial x_j} \approx \rho_f U_j \frac{\partial u_i}{\partial x_j} \ ,$$

Thus, the linearized Navier-Stokes equations or Oseen equations are

$$\rho_f U_j \frac{\partial u_i}{\partial x_j} = -\frac{\partial p}{\partial x_i} + \mu \frac{\partial^2 u_i}{\partial x_j \partial x_j} \ .$$

The solution to these can be found in Langlois (1964).

The difference between the Stokes and the Oseen solution lies in the disturbance flow due to the sphere. Therefore the free stream velocity should be subtracted before comparing the two solutions. Subtracting the free stream velocity is equivalent to consider a sphere translating with the free stream velocity, i.e. $V_i = U_i$. The streamline pattern for the Stokes and Oseen solution for a translating sphere is given in figure 7. Comparing 7(a) with 7(b) the fore-and-aft symmetry has disappeared in the Oseen solution, because a wake is created behind the sphere. As we will see in sections 3.2 and 3.3 this wake, which is due to convective effects, plays an important role in the unsteady-convective case. Close to the sphere ($r < \mathrm{O}\left(\frac{2a}{Re_p}\right)$) the streamlines are almost identical and therefore this region is called the Stokes region. The region $r > \mathrm{O}\left(\frac{2a}{Re_p}\right)$ is called the Oseen region, and the distance $r = \mathrm{O}\left(\frac{2a}{Re_p}\right)$ is the Oseen length. If the Oseen solution is used, the drag on the sphere becomes (Langlois (1964))

$$F_i^{Oseen} = \left(1 + \frac{3}{16} Re_p\right) F_i^{Stokes} \ . \tag{12}$$

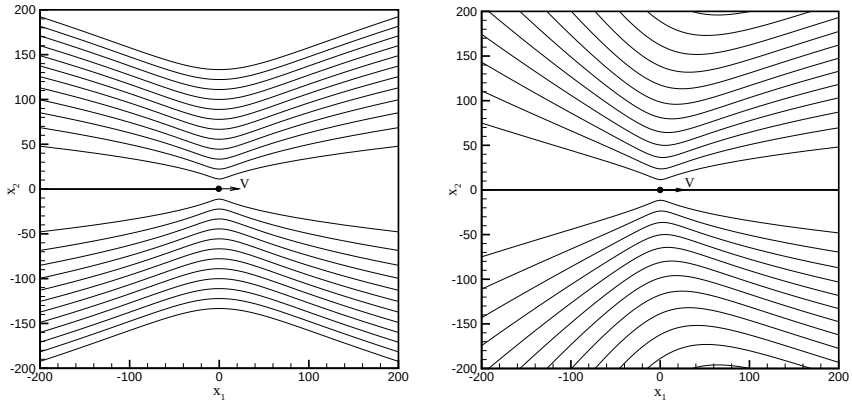

(a) Stokes streamlines

(b) Oseen streamlines

Figure 7. Stokes and Oseen streamlines for a sphere translating with constant velocity V.

The results (11) and (12) for the hydrodynamic force on a sphere are only valid at low Reynolds number. Comparisons with experiments show that they agree reasonably for $Re_p < 1$ (White (1991) and Clift et al. (1978)). For higher Reynolds numbers no analytical expressions are available and a semi-empirical expression must be used. In this context the steady drag on a sphere is given by

$$F_i^{Steady} = \frac{1}{2} C_D \pi \rho_f a^2 \left| V_i - u_i^\infty \right| \left(V_i - u_i^\infty \right) \ ,$$

where C_D is a non-dimensional drag coefficient and u_i^∞ is the undisturbed flow taken at the sphere center of mass. For Stokes flow C_D is

$$C_D^{Stokes} = \frac{24}{Re_p} \ ,$$

with Re_p given by (3.1). For higher Reynolds numbers

$$C_D = \phi(Re_p) C_D^{Stokes} \ ,$$

where $\phi(Re_p)$ is a semi-empirical correction. Expressions for various ranges of Reynolds numbers are given in Clift et al. (1978), e.g.

$$\phi(Re_p) = \begin{cases} 1 + \frac{3}{16}\ Re_p & \text{for } Re_p \leq 0.01 \\ 1 + 0.1315\ Re_p^{0.82 - 0.05 \log Re_p} & \text{for } 0.01 < Re_p \leq 20 \\ 1 + 0.1935\ Re_p^{0.6305} & \text{for } 20 < Re_p \leq 260 \ , \end{cases} \tag{13}$$

where the first correction corresponds to the Oseen solution. The reader is referred to Clift et al. (1978) or White (1991) for expressions of $\phi(Re_p)$ at higher Reynolds numbers. The description in this section covers the regions with no inertia (steady Stokes flow) and the region with convective inertia (steady flow).

3.2 Unsteady Stokes Flow

When the Reynolds number is small and the Strouhal number is large, the unsteady inertia term must be included. Therefore the problem of a single sphere dispersed in a fluid flow is described by the unsteady Stokes equations

$$\rho_f \frac{\partial u_i}{\partial t} = -\frac{\partial p}{\partial x_i} + \mu \frac{\partial^2 u_i}{\partial x_j \partial x_j} \ , \tag{14}$$

together with the continuity equation (6) and with the no-slip boundary condition (8) at the particle surface. Maxey & Riley (1983) solved this problem for a small sphere in a non-uniform flow. Their result is

$$\begin{aligned} m_p \frac{dV_i}{dt} = &\left(m_p - m_f\right) g_i + m_f \frac{Du_i^\infty}{Dt} - \frac{m_f}{2}\frac{d}{dt}\left(V_i - u_i^\infty - \frac{a^2}{10}\frac{\partial^2 u_i^\infty}{\partial x_j \partial x_j}\right) \\ &-6\pi\mu a\left(V_i - u_i^\infty - \frac{a^2}{6}\frac{\partial^2 u_i^\infty}{\partial x_j \partial x_j}\right) \\ &-6\pi\mu a^2 \int_0^t \frac{1}{\sqrt{\pi\nu\left(t-s\right)}}\frac{d}{ds}\left(V_i - u_i^\infty - \frac{a^2}{6}\frac{\partial^2 u_i^\infty}{\partial x_j \partial x_j}\right) ds \ , \end{aligned} \tag{15}$$

where m_p is the mass of the particle and m_f is the mass of the fluid displaced by the particle. The derivative $\frac{D}{Dt}$ is taken following the fluid, i.e.

$$\frac{Du_i}{Dt} = \frac{\partial u_i}{\partial t} + u_j \frac{\partial u_i}{\partial x_j} \ ,$$

and the derivative $\frac{d}{dt}$ is taken following the particle, i.e.

$$\frac{du_i}{dt} = \frac{\partial u_i}{\partial t} + V_j \frac{\partial u_i}{\partial x_j} \ .$$

The terms $\frac{\partial^2 u_i^\infty}{\partial x_j \partial x_j}$ are the Faxen corrections due to curvature in the fluid velocity (Maxey & Riley (1983)). The first term on the right hand side describes the forces due to gravity and buoyancy, while the second term is a pressure gradient force from the undisturbed flow field. The third term is the added-mass force arising because the acceleration of the particle leads to acceleration of the surrounding fluid. Thus, it represents the additional mass the particle appears to have due to the mass of the surrounding fluid. The fourth term is a time dependent Stokes drag. The fifth term is the Basset history force, which results from diffusion of vorticity generated at the sphere surface into the bulk fluid flow. The added-mass force and the Basset history force result from retaining the unsteady term in equation (14) for the disturbance flow.

Equation (15) is based on the following assumptions:

1. The particle Reynolds number is small, i.e. $Re_p \ll 1$.
2. The relaxation time Reynolds number is small, i.e. $Re_{\tau_s} = \frac{U}{L}\frac{a^2}{\nu} \ll 1$.
3. The particle is small, i.e. $\frac{a}{L} \ll 1$.
4. The sphere is far from any other boundary (wall or particle).
5. No Oseen corrections are included.
6. Forces due to shear or rotation are not included.

The first and third assumptions imply that the slip velocity is small. The second assumption implies that a characteristic relaxation time due to the action of Stokes drag, $\tau_S = \frac{a^2}{\nu}$, is much smaller than the characteristic time scale of the undisturbed flow, $T = \frac{L}{U}$. The fourth assumption excludes particle-particle and particle-wall interactions. The fifth assumption states that no Oseen type corrections are made, therefore no far field inertia effects are included. Finally, there is a restriction on the initial conditions. For the solution written in the form (15) the initial velocity of the sphere must be $V_i = u_i^\infty + \frac{\partial^2 u_i^\infty}{\partial x_j \partial x_j}$ (zero slip velocity). If there is an initial slip velocity, an additional term must be added to the right hand side of (15), which can be considered as an appendage to the Basset history term. This appendage is (Michaelides (1997)),

$$-6\pi a\mu\left(V_i - u_i^\infty - \frac{\partial^2 u_i^\infty}{\partial x_j \partial x_j}\right)\left(\frac{1}{\sqrt{\pi\nu t}}\right)$$

The above assumptions restrict the importance of some of the terms in the equation of motion (15). The condition of small particles implies that the Faxen terms may be neglected and that generally Stokes drag is the most important term. Nevertheless, for some specific problems the other forces may be important. If the particle is very heavy[3] ($\rho_f \ll \rho_p$) particle inertia and gravity becomes important. The Basset history term becomes important in two cases. Firstly, if the particle or the fluid is oscillating the oscillations will limit the diffusion of vorticity, because of the constant change in direction of the disturbance flow. Secondly, for a particle with initially very little relative motion the quasi-steady Stokes drag is small. Thus, the Basset history term is comparable with the Stokes drag and therefore of importance during the initial motion. Despite the constraints and their limits on applications, the equation of motion (15) has been widely used for studying particle dynamics in various types of fluid flows. Many of the investigations have concentrated on very small heavy particles such that the added-mass, the pressure gradient from the undisturbed flow, and the Basset history term all are negligible, and equation (15) reduces to a balance between particle inertia, gravity and Stokes drag, see e.g. Wang & Squires (1996) and Uijttewaal & Oiemans (1996). On the other hand, Maxey (1987) and Raju & Meiburg (1997) neglected only the Basset history term in their investigations of particle motion in vortical flows. A study with the Basset history term included is given in Lomholt et al. (1998).

The Basset history term has been the subject of many investigations, e.g. Liang & Michaelides (1992), Druzhinin & Ostrovsky (1994), and Vojir & Michaelides (1994). In general it is difficult and expensive to compute, and the main subject of these investigations has been to examine the importance of the force in various situations. The most recent investigations were initiated by Reeks & McKee (1984). They computed the dispersion of particles in a turbulent flow. When the Basset history force was retained in the equation of motion the initial slip velocity had a finite contribution to the dispersion coefficient of the particles. This shows that the particles retained the memory of their initial velocity. This is unphysical, because the viscosity of the fluid would result in dissipation of the initial velocity disturbance and eventually erase any memory of it.

Mei et al. (1991) and Mei & Adrian (1992) solved this paradox using a finite difference direct numerical simulation. As a model for the particles in the simulation of Reeks & McKee (1984), they investigated the hydrodynamical forces on a sphere in an oscillating flow field at a low Reynolds number. Mei et al. (1991) found that for long times the drag given by the solution (15) to the unsteady Stokes equation is incorrect. The source for this is an incorrect Basset history force and this causes the paradox found by Reeks & McKee (1984). The reason is, that on a short time scale the vorticity generated at the sphere surface has not diffused out of the Stokes region. Therefore the diffusion term is balanced by the unsteady inertia term and equation (15) is valid. On the other hand, the vorticity on long time scales has diffused into the Oseen region, where it is transported by the convective wake. Therefore convective inertia becomes important. The hydrodynamic force is no longer determined by the unsteady Stokes equations, and the equation of motion (15) is no longer valid. Mei & Adrian (1992) conclude that the Basset history term for a small amplitude oscillating flow decays as $(t-s)^{-\frac{1}{2}}$ (as given by equation (15)) for short times and as $(t-s)^{-2}$ for long times.

The above results show that the wake associated with convective inertia is important for the long time behaviour of the hydrodynamic force even at very low Reynolds number. Therefore equation (15) should be corrected in order to include convective effects.

[3] we will use the term heavy for particles with density higher than the fluid.

3.3 Finite Reynolds number corrections to the equation of motion

One of the main problems concerning equation (15) is the complete neglect of convective inertia leading to the constrains of very low Reynolds numbers and short time scales, as explained above. In order to overcome this, Lovalenti & Brady (1993a) considered the problem of a small particle dispersed in a non-uniform flow at small but finite Reynolds number. The rather complex equation of motion derived by Lovalenti & Brady (1993a) is valid to $O(Re_p)$ for an arbitrarily moving rigid particle with no assumption about the particle shape. For a sphere, Lovalenti & Brady (1993a) obtained the following equation of motion

$$\begin{aligned} m_p \frac{dV_i}{dt} = & (m_p - m_f)\, g_i + m_f \frac{Du_i^\infty}{Dt} - \frac{m_f}{2}\frac{d}{dt}\left(V_i - u_i^\infty\right) - 6\pi\mu a \left(V_i - u_i^\infty\right) \\ & -\frac{9}{2}\pi\mu a^2 \int_{-\infty}^{t} \left[\frac{2}{3}\left(u_i^{S\parallel}(s) + u_i^{S\perp}(s)\right)\right. \\ & \left. - G\left(A_i\right)\left(u_i^{S\parallel}(s) + \frac{1}{2}u_i^{S\perp}(s)\right)\right] \frac{ds}{(t-s)\sqrt{\pi\nu(t-s)}} \ , \end{aligned} \tag{16}$$

where $u_i^{S\parallel}$ and $u_i^{S\perp}$ are given as the slip velocities parallel and perpendicular to the non-dimensional vector $Y_i(t) - Y_i(s)$, i.e.

$$\begin{aligned} u_i^{S\parallel} &= \left(\left(V_j - u_j^\infty\right) e_j^Y\right) e_i^Y \\ u_i^{S\perp} &= \left(V_i - u_i^\infty\right) - \left(\left(V_j - u_j^\infty\right) e_j^Y\right) e_i^Y \ , \end{aligned} \tag{17}$$

with e_i^Y being a unit vector in the direction of $Y_i(t) - Y_i(s)$. The function $G(A_i)$ is

$$G(A_i) = \frac{1}{A_j A_j}\left(\frac{\pi^{1/2}}{2(A_j A_j)^{1/2}}\,\mathrm{erf}((A_j A_j)^{1/2}) - \exp(-A_j A_j)\right) \ ,$$

and the non-dimensional vector A_i is

$$A_i(t,s) = \frac{1}{2}\frac{Y_i(t) - Y_i(s)}{\sqrt{\nu(t-s)}} \ .$$

The reader is referred to Lovalenti & Brady (1993a) for the details in the derivation and the more general equation. Comparing equation (16) by Lovalenti & Brady (1993a) with equation (15) by Maxey & Riley (1983), the changes only concern the Basset history term, and thus only the long time behaviour of the total hydrodynamic force.

Using equation (16) Lovalenti & Brady (1993a+b) investigated the long time behaviour of the hydrodynamic force with regard to step changes in the sphere velocity and small-amplitude oscillations in the undisturbed flow. Lovalenti & Brady (1993a+b) found:

1. Sudden start, sphere velocity goes instantaneously from zero to V_i: the Basset history force decays as $(t-s)^{-2}$.
2. Sudden stop, sphere velocity goes instantaneously from V_i to zero: the Basset history force decays as $(t-s)^{-1}$.
3. Sudden increase, sphere velocity goes instantaneously from V_i^1 to V_i^2: the Basset history force decays exponentially.
4. Flow with small-amplitude oscillations: the Basset history force decays exponentially.

Mei (1994) and Lawrence & Mei (1995) performed a thorough investigation of the long time behaviour of the Basset history term, using the same direct numerical method as Mei et al. (1991). They examined the same cases as Lovalenti & Brady (1993a+b) for a range of Reynolds numbers up to $Re_p = 60$. Mei (1994) and Lawrence & Mei (1995) found the following:

1. Sudden start, sphere velocity goes instantaneously from zero to V_i: the Basset history force decays as $(t-s)^{-2}$.
2. Sudden stop or reverse of motion, sphere velocity goes instantaneously from V_i to zero or $-V_i$: the Basset history force decays as $(t-s)^{-1}$.
3. Sudden increase, sphere velocity goes instantaneously from V_i^1 to V_i^2: the Basset history force decays as $(t-s)^{-2}$.
4. Flow with small-amplitude oscillations: the Basset history force decays as $(t-s)^{-2}$.

In contrast to Lovalenti & Brady (1993a+b), the results of Mei (1994) and Lawrence & Mei (1995) showed no exponential decay in any of the cases. Lawrence & Mei (1995) explains this, with the fact that the equation of Lovalenti & Brady (1993a) only include the first-order contribution ($O(Re_p)$). This contribution decays exponentially, however there exists a second-order contribution ($O(Re_p^2)$) with a $(t-s)^{-2}$ decay. When the first-order contribution has decayed the second-order contribution will dominate the long-time behaviour. Therefore the exponential decay is only a stage towards the second-order decay. In a subsequent paper Lovalenti & Brady (1995) modified their equation to include the second-order contribution and with this modification, they found the same long time behaviour as Mei (1994) and Lawrence & Mei (1995).

The most interesting feature about these results is the fact that the form of the Basset history force changes with time. Initially it behaves as the classical $(t-s)^{-1/2}$ decay. Then as the vorticity has diffused out to the wake, convective transport mechanisms changes the behaviour to a faster decay ($(t-s)^{-1}$ or a $(t-s)^{-2}$). In some cases, the transition from the $(t-s)^{-1/2}$ decay to the $(t-s)^{-2}$ decay involves a period with exponential decay.

In a direct numerical simulation using a spectral method Chang & Maxey (1995) investigated the same cases as Lovalenti & Brady (1993a+b). In their investigation of the hydrodynamic force, they only observed the exponential decay except for the case of a sudden stop. Chang & Maxey (1995) used a zero vorticity boundary condition at a distance of 50 sphere radii from the sphere center. This could be the reason for the discrepancy with the results of Lawrence & Mei (1995) and Lovalenti & Brady (1995), because this boundary condition will absorb any far field vorticity in the convective wake (Maxey (2000a)). Another possibility is the first-order time integration used by Mei (1994) and Lawrence & Mei (1995). This may give considerable errors, when considering long-time behaviour. Nevertheless, all the investigations show a long-time behaviour of the Basset history force different from the classical one in equation (15).

Mei (1994) also examined the added-mass term and found that it always has the form given by Auton et al. (1988)

$$F_i^{AM} = -\frac{m_f}{2}\left(\frac{dV_i}{dt} - \frac{Du_i^\infty}{Dt}\right) .$$

Note that the added-mass given in equations (15) and (16) is

$$F_i^{AM} = -\frac{m_f}{2}\left(\frac{dV_i}{dt} - \frac{du_i^\infty}{dt}\right) ,$$

but at the low Reynolds number condition for equations (15) and (16)

$$\frac{du_i}{dt} \approx \frac{Du_i}{Dt} \ ,$$

and the two expressions agree (Maxey & Riley (1983)).

Based on the results from the direct numerical simulations, Mei (1994) suggested the following equation of motion for a small sphere,

$$\begin{aligned} m_p \frac{dV_i}{dt} = &\left(m_p - m_f\right) g_i + m_f \frac{Du_i^\infty}{Dt} - \frac{m_f}{2}\left(\frac{dV_i}{dt} - \frac{Du_i^\infty}{Dt}\right) \\ &-6\pi\mu a \left(V_i - u_i^\infty\right)\phi(t) - 6\pi\mu a \int_{-\infty}^{t} K\left(t-s\right) \frac{d\left(V_i - u_i^\infty\right)}{ds} ds \ , \end{aligned} \tag{18}$$

where the function $\phi(t)$ is a modification of the quasi-steady Stokes drag due to finite Reynolds number. Some expressions for $\phi(t)$ are given in equation (13) in section 3.1. The kernel in the history force is

$$K(t-s) = \left[\left(\frac{\pi\nu(t-s)}{a^2}\right)^{1/4} + \left(\frac{\pi}{2}\frac{|u_i^\infty(s) - V_i(s)|^3}{a\nu f_H^3(Re_s)}(t-s)^2\right)^{1/2}\right]^{-2} \ ,$$

where

$$f_H(Re_s) = 0.75 + 0.105 Re_s \ .$$

Equation (18) is valid at Reynolds numbers up to $O(Re_p) \sim 100$. The difference between (18) and (15) is the Reynolds number dependence of the correction to the Stokes drag and the kernel in the Basset history force. The form of the new kernel behaves as the classical $(t-s)^{-1/2}$ for short times and as $(t-s)^{-2}$ for long times.

Mei (1994) found that this "empirically" modified equation of motion gave qualitatively good results for the cases with step changes in the particle velocity and for the small-amplitude oscillating flow. A comparision of numerical results using (18) with experimental data were performed by Domgin et al. (1998). They examined two cases, a sphere falling in a quiescent fluid and a sphere dispersed in a turbulent flow. They found a general agreement between the numerical and the experimental results. This suggests that the equation of motion in the form (18) can be applied at higher Reynolds numbers.

A modified version of equation (18), with a new modified kernel in the history term, has been suggested by Kim et al. (1998) in order improve the quantitative prediction. The modification involves two new functions, six new constants and two new parameters and is thus more difficult to handle, see Kim et al. (1998) for the details. Comparing results from their version with results from (18) and results from a direct numerical simulation, Kim et al. (1998) show that their modification does improve the accuracy.

The above considerations show that convective inertia plays an important role for the long time behaviour of the hydrodynamic force. Therefore Oseen corrections to equation (15) are needed in order to include an approximation to these nonlinear effects.

3.4 Lift Forces and Wall Effects

A shortcoming of all the equations of motion given in (15), (16) and (18) is the lack of the lateral migration due to a transverse lift force. Lift forces have been observed experimentally for particles sedimenting near a wall by Vasseur & Cox (1977), Shinohara (1998) and Cherukat & McLaughlin (1990) and in shear flows by Segre & Silberberg (1961), Jeffrey & Pearson (1965), Repetti & Leonard (1966) and Cherukat et al. (1994).

Wall Induced Lift Forces

The experiments with particles sedimenting near a vertical wall show the existence of a lift force on the particle away from the wall. In the case of a particle in a vertical channel or in a tube, the particle moves to an equilibrium position at the symmetry axis. When a particle moves parallel to a wall, a geometric blocking of the disturbance flow appears between the particle and the wall. This blocking cause changes in the pressure distribution on the side of the particle facing the wall as indicated in figure 8(a). The increased pressure at the left front side of the sphere, is due to squeezing of fluid forced through the gap between the sphere and the wall. The decrease in pressure on the left back side of the sphere, is a result of the relief of this squeezing. Thus, the wall repulsion is somewhat similar to lubrication effects. In the case of a Stokes flow the pressure increase and the pressure decrease match each other, so that no resulting lateral force is present. However, it does result in an increased drag on the sphere in the direction of motion. Including the nonlinear terms results in a larger increase than decrease in the pressure, leading to a resultant force away from the wall. Further, it causes an increased drag on the sphere.

Wall-induced lift in the case of a low Reynolds number was investigated by Vasseur & Cox (1977). They found expressions for the migration velocity for two cases; a single sphere near a single plane wall and a single sphere between two plane walls. Their result for the migration velocity is

$$V_m = \frac{Re_p}{2} V J_{VC} \ , \tag{19}$$

where V_m is the velocity perpendicular to the settling velocity V and J_{VC} is an integral that needs numerical evaluation. The form of the integral J_{VC} depends on whether there are one or two walls. Equation (19) results in a lift force

$$F_L^{VC} = 6\pi\mu a V_m \ ,$$

in the normal direction away from the wall. Vasseur & Cox (1977) verified the results for the sphere between two plane walls by comparing (19) with experiments. The results for a single wall have been verified by Cherukat & McLaughlin (1990). Although (19) is valid for $Re_p < 3$ (Cherukat & McLaughlin (1990)), it is not widely used for modelling the wall induced lift force.

Shear Induced Lift Forces

The shear-induced transverse lift force, called the Saffman effect, is caused by shear in the surrounding fluid flow. Segre & Silberberg (1961) and Jeffrey & Pearson (1965) observed, that neutrally buoyant spheres dispersed in Poiseuille flow in a tube migrate away from the wall and from the center line to an equilibrium position about 0.6 of the tube radius. The precise value of the equilibrium position depends on the flow rate or magnitude of shear.

The two-dimensional simulations by Feng et al. (1994b) give a physical explanation for the migration. A neutrally buoyant sphere placed in a Poiseuille flow as shown in figure 8(b) will slightly lag the undisturbed flow taken at the center of the sphere. Consequently, the flow relative to the sphere will be stronger on the left-hand side than on the right-hand side of the sphere, see figure 8(b). As indicated in the figure, this causes a pressure increase/decrease similar to the case of a sphere settling near a wall. However, for the neutrally buoyant sphere in Poiseuille flow, the decrease is larger than the increase and the sphere is sucked to the left. This is the main mechanism that forces the sphere away from the centerline towards the equilibrium position. When the sphere is placed between the equilibrium position and the wall, the wall repulsion discussed above becomes

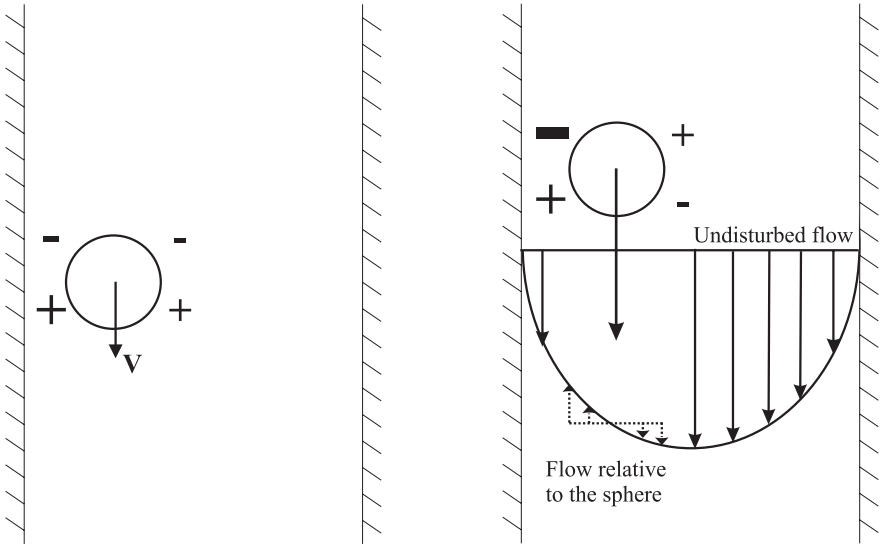

(a) Sphere settling near a wall.

(b) neutrally buoyant sphere in Poiseuille flow.

Figure 8. Schematic drawings of the pressure for a sphere settling near a wall and a neutrally buoyant sphere in Poiseuille flow.

larger than the shear induced force. Hence, the sphere is forced away from the wall toward the equilibrium position.

If the sphere is non-neutrally buoyant it will either increase the lag velocity or create a lead velocity of the sphere, relative to the undisturbed flow taken at the center of the sphere. This causes the flow relative to the sphere to change. A small increase in the lag velocity will result in a weaker relative flow on the left side of the sphere. This diminishes the pressure differences, leading to an equilibrium position closer to the centerline than for the neutrally buoyant sphere. A further increase in the lag velocity will cause the sphere to move even closer to the centerline. If the sphere is leading the undisturbed flow, the relative flow on the left side becomes stronger and the sphere is moved further towards the wall. For large lead velocities the sedimentation of the sphere becomes dominant. Therefore the wall repulsion dominates and the equilibrium position of the sphere moves back towards the centerline between the walls.

Migration of small spheres in Couette flow has been observed experimentally by Cherukat et al. (1994) and numerically by Feng et al. (1994b). The situation for a neutrally buoyant sphere in Couette flow generated by two moving walls is similar to the settling of a sphere near a wall. The imposed flow forces fluid through the gap between the wall and the sphere. This causes a pressure increase and decrease similar to that seen in figure 8(a), so the sphere is pushed towards the center line. Buoyant particles are subjected to the same mechanisms as discussed for Poiseuille flow. Therefore a leading sphere will move towards slower velocity (the center line) and a lagging sphere will move towards faster velocity (the walls) (Feng et al. (1994b)). In both Couette and Poiseuille flow the shear induced mechanisms described above may be limited, if the sphere is very light or very heavy. In both cases the settling of the sphere dominates the motion, and the wall repulsion will determine the lateral motion (Feng et al. (1994b)).

For a small sphere in a slow shear flow in an unbounded fluid, the lift force

perpendicular to the direction of motion was found by Saffman (1965) to be

$$F_L^{Sa} = 81.2\mu a^2(V-u)\sqrt{\frac{|\gamma|}{\nu}} \ , \tag{20}$$

where $V-u$ is the sphere slip velocity in the direction of the fluid flow and γ is the shear rate of the fluid flow. The constrains for (20) are

$$\begin{aligned} Re_\gamma &= \frac{4a^2|\gamma|}{\nu} \ll 1 \\ Re_p &= \frac{2a|V-u|}{\nu} \ll 1 \end{aligned} \tag{21}$$

$$\begin{aligned} Re_\Omega &= \frac{4a^2\Omega}{\nu} \ll 1 \\ Re_p &\ll \sqrt{Re_\gamma} \ . \end{aligned}$$

Despite the fact that equation (20) was derived without the full physical picture of the disturbance flow, Saffman (1965) used it to show that a sphere leading the flow will move towards the slower stream, while a sphere lagging the flow will go towards the faster stream, as already discussed above. The last condition in (21) limits the expression (20) to apply only for a slowly moving sphere in a strong shear. This limitation was later removed by McLaughlin (1991) and his result was

$$F_L^{Mc} = \frac{3.23}{2.255}\mu a(V-u)\sqrt{Re_\gamma}J_{Mc}(\epsilon) \ , \tag{22}$$

where $J_{Mc}(\epsilon)$ is a three-dimensional integral depending on $\epsilon = \sqrt{Re_\gamma}/Re_p$. This expression for the lift force was compared with experimental results by Cherukat et al. (1994) and numerical results by Kurose & Komori (1999). Their conclusion is, that (22) can be used to predict the lift force for conditions with $Re_p < 5$. McLaughlin (1993) has also extended the above result to include wall-bounded shear flows.

Due to the relative simplicity of (20) and (22) these expressions have been used for modelling the lift force by adding them to the right hand side of the equation of motion given by equation (15). The expressions (20) and (22) for the lift force are limited to $Re_p < 5$. Therefore they do not apply to equation (18) for higher Reynolds numbers. In fact, the numerical study by Kurose & Komori (1999) shows that, for $Re_p > 60$ the lift force changes sign, which is not included in the expressions (20) and (22). Many other researchers have been working with lift forces due to shear. The reader is referred to McLaughlin (1993) or Kurose & Komori (1999) for further details.

Rotation Induced Lift Forces

A particle settling either in a stagnant fluid near a wall or in a shear flow will rotate due to the asymmetry in the pressure forces and/or due to the shear of the fluid flow. This rotation results in a lift force. The lift force of a rotating sphere settling in a stagnant fluid a low Reynolds number found by Rubinow & Keller (1961) is

$$F_{L,i}^{RK} = \pi a^3 \rho_f \varepsilon_{ijk}\Omega_j V_k \ . \tag{23}$$

This force is perpendicular to the direction of the settling motion, and the trajectory of the spinning sphere will be a curve instead of a straight line. This force has sometimes been used in conjunction with (20) or (22) to model the total lift force for a sphere in a simple shear flow.

Ben Salem & Oesterle (1998) performed a direct numerical simulation of a shear flow around a rotating sphere. They found that for small Re_p adding (23) and (22) gives the correct lift force for the sphere. An investigation for shear flow around a spinning sphere at higher Reynolds numbers have been performed by Kurose & Komori (1999) and in contrast to the stationary sphere no sign change appears in the lift force for $Re_p > 60$. Although an expression for the lift force at high Re_p is difficult to find, Kurose & Komori (1999) provide expressions for both the drag and the lift forces dependind on Re_p, γ and Ω together with five constants that depend on Re_p.

Rotation of a particle may also result from particle-particle or particle-wall collisions. These effects are shortly discussed below in section 3.5.

3.5 Two- and Four-way Coupling

So far the discussion have only been of the motion of the particulate phase, and not of the influence of the particles on the fluid flow nor of interaction between particles. From figure 5 it is seen that two-way coupling becomes important at volume fractions as low as $\alpha = 10^{-6}$, thus two-way coupling is often present. One very common method to handle this is by adding a source term to the right hand side of the momentum equation (7). The source term corresponds to the momentum exchange between the particles and the fluid. It is therefore given by the total hydrodynamic force on the particle. If an equation of motion of the type (15) is used, the force is

$$\begin{aligned} F_i^n = \Bigg[& m_f \frac{Du_i^\infty(\mathbf{Y^n})}{Dt} - \frac{m_f}{2}\frac{d}{dt}\left(V_i(\mathbf{Y^n}) - u_i^\infty(\mathbf{Y^n})\right) \\ & - 6\pi\mu a\left(V_i(\mathbf{Y^n}) - u_i^\infty(\mathbf{Y^n})\right) \\ & - 6\pi\mu a^2 \int_0^t \frac{1}{\sqrt{\pi\nu(t-s)}}\frac{d}{ds}\left(V_i(\mathbf{Y^n}) - u_i^\infty(\mathbf{Y^n})\right) ds \Bigg] \ , \end{aligned} \tag{24}$$

where the Faxen terms have been neglected. Due to the third assumption for equation (15) the particle is considered to be much smaller than the characteristic length scale of the flow. Therefore the force given by (24) is applied in a single point. The source term is the sum of the forces from all the particles, i.e.

$$S_i^p = -\sum_{n=1}^{N} F_i^n \delta(\mathbf{x} - \mathbf{Y^n}) \ , \tag{25}$$

where $\delta(\mathbf{x} - \mathbf{Y^n})$ is the Dirac delta function. This specifies that the force is applied in a single point. This type of source term has been used by Squires & Eaton (1990) and Elghobashi & Truesdell (1993) to study the modification of turbulence by the presence of many particles, while Barton (1996) studied two-way coupling in a laminar flow over a backward-facing step. Using a source term of the type (25) two-way coupling can be included in any particulate computation, once the total hydrodynamic force is determined. The disadvantages are the limitations of the equation of motion (15) and the numerical treatment of the Dirac delta function, see chapter 4.

Hydrodynamic interactions among particles and particle-particle collisions become important for volume fractions $\alpha > 10^{-3}$. Hydrodynamic interactions between particles are caused by the disturbance flow created by the particles. When two particles are close enough, the disturbance flow of one particle has an effect on the forces of the second particle and vice versa. Examples of the hydrodynamic interaction among two spheres are given in the experiments by Fortes et al. (1987). Fortes et al. (1987) observed a process, they named drafting, kissing and tumbling (DKT). The two spheres, with an initial vertical and horizontal separation, were

settling in an essentially two-dimensional channel[4]. During the experiment the trailing sphere is drafted into the wake of the leading sphere, where it experiences a smaller drag than the leading sphere. Thus, the trailing sphere falls with a higher velocity and at some point it reaches the leading sphere. They collide (kiss) and the trailing sphere overtakes the leading sphere by tumbling around it. If the Reynolds number is high enough this process may continue for a long time with the spheres shifting place.

Computation of such nonlinear hydrodynamic interactions requires that the disturbance flow of the particles is resolved. This puts a serious demand on the form of the source terms and the equation of motion. Using the source (25) with F_i^n given by (24) it is assumed that the particles are far from any other particles and nonlinear effects are neglected. Therefore hydrodynamic interactions between particles are not included in computations using source terms of the form (25) with F_i^n given by (24).

Particle-particle collisions are impossible to compute directly and some kind of modelling must be considered. Sommerfeld (2000) gives a description of the collision of two hard spheres with both sliding and non-sliding conditions. Including collisions requires solution of a set of equations. Since many particles are present, finding collision pairs and solving the equations may be very time consuming. Therefore collisions are neglected in many investigations. If the spheres are able to deform the collision process is much more difficult to handle, leading to even more complicated models.

Particle-wall collisions are similar to particle-particle collisions and a collision model is given in Sommerfeld (2000). In contrast to particle-particle collisions, the wall roughness may play an important role in particle-wall collisions. The importance depends on the ratio of the particle radius to the wall roughness height. If the particle radius is much larger than the wall roughness height the particle will "feel" the rough wall as an approximately smooth wall, and the roughness has no effect. On the other hand, if the particle radius is comparable to or smaller than the wall roughness height, the roughness will effect the rebound. A model for this is given by Sommerfeld & Huber (1999).

3.6 Summary and Discussion of Particulate Flows

The aim of this chapter was to review the physics involved in the dynamics of a particle dispersed in a fluid flow. It was shown that the dynamics depend on three parameters; the volume fraction, the Reynolds number and the Strouhal number.

The volume fraction specifies the coupling of the particle motion to the fluid motion. When the volume fraction is lower than 10^{-6} the influence of the particles on the fluid can be neglected. For volume fractions between 10^{-6} and 10^{-3} the motion of the particles has an influence on the fluid motion. This is often modelled by the source term given in (25). Hydrodynamic interactions and collision between particles are important for dense particulate flows with volume fractions higher than 10^{-3}.

The Reynolds number and the Strouhal number specify the importance of the inertia terms. The effect of convective inertia is to create a wake behind the particle as shown in section 3.1. This wake has an important effect on the history of the hydrodynamic force. The vorticity created on the surface of the sphere must be transported away be diffusion and convection. In an unsteady flow this transport leads to an additional contribution to the hydrodynamic force, namely the Basset history force. In the discussion of this force it became apparent that convective inertia increases the decay of the force. The reason is that near the particle

[4] a rectangular channel with very large aspect ratio.

convective inertia is small and the main transport mechanism for the vorticity is diffusion. When the vorticity has diffused out to the Oseen distance convective inertia become important. At this distance the vorticity is taken up by the convective wake, and the additional transport results in the faster decay of the Basset history force.

Effects not included in the various equations of motion were lift forces induced by the presence of a wall, or of shear in the undisturbed fluid flow, or of rotation of the particle. These effects have all been investigated at small Reynolds numbers. The expressions for the lift forces found in these investigations, may be added to the equation of motion in order to model the effect of a wall, or of shear in the undisturbed flow, or of rotation of the particle.

Although some of the equations of motion were valid at Reynolds numbers above one, all the equations have the assumption of a small particle compared with the characteristic length scale of the flow. For the particulate microflows described in section 2.3 this is very restrictive assumption. Therefore an equation of motion, as those given in the section above, can only be used for dilute microflows with very small particles. This will probably only be the case for some parts of the microdevice given in figure 4. In the other two examples in figure 2 and figure 3, the particles may be large. Therefore the equations of motion for a small sphere cannot be used for computing these types of microflows. Another reason for discarding the equations of motion described in this chapter, is that they do not include hydrodynamic interactions between particles. For the microdevices in figure 2 and 4 it is likely that the particulate flow will be dense (volume fraction $\alpha > 10^{-3}$). Thus, hydrodynamic interactions between particles will have a strong effect on the motion of both the particles and the fluid. Therefore the method for computing both the particle dynamics as well as the fluid flow in these microdevices, must be able to handle large particles and include the nonlinear effects of hydrodynamic interaction between particles. The force coupling method developed in the following chapters is able to handle large particles, and it includes hydrodynamic interaction between particles. Further, the method includes other nonlinear effect such as the lift forces described in section 3.4.

4 The Force Coupling Method

In the previous chapter various methods for determining the hydrodynamic force on a particle in a fluid flow were discussed. We saw that for steady or unsteady Stokes flow in the vicinity of a small particle it was possible to obtain approximate analytical solutions for the particle motion. On the other hand, the problem is much more difficult and no analytical solutions exist, when the convective inertia terms become important or the size of the particle becomes comparable with the characteristic length scale of the flow. The source for this complexity is the nonlinearity of the convective inertia, which results in an asymmetric flow around the particle. For sufficiently large particle Reynolds number[5] flow separation occurs. Although flow separation probably never exists in microflows, the nonlinear convective inertia will still be of importance.

So how is it possible to compute the particle motion in a flow with important convective inertia and/or large particles, when the hydrodynamic forces are unknown? The straightforward method is to do a direct numerical simulation, where the flow around the particles is fully resolved. The forces are found from the pressure and shear stress distribution on each of the particles, and the particles are moved in correspondence with these forces using Newton's second law of mechanics. This requires generation of a new mesh at each timestep, and if a particle is close to a wall or another particle a very fine mesh is needed in order to resolve the flow within this region. Therefore direct simulations are computationally extremely expensive and the number of particles will be limited. Nevertheless, they have been performed in both 2D and 3D, e.g. Feng et al. (1994a+b) (2D) and Johnson & Tezduyar (1996) (3D). These direct simulations provide usefull information about the hydrodynamic forces and the flow around the particles, as we have already seen in the previous chapter on the discussion of lift forces, see section 3.4.

An alternative approach is the force coupling method. The force coupling method has several advantages over the direct numerical simulations. Firstly, the same mesh is used through out the simulation. Therefore no time is used on remeshing, resulting in a much faster computation. Secondly, the method is relatively easy to implement in already existing codes for the solution of the Navier-Stokes equations. Finally, the method can be used with spectral schemes in contrast to the direct simulations, where the constant remeshing makes it very difficult to use a spectral method for solving the particulate flow. The disadvantage of the force coupling method is, that the hydrodynamic forces on the particles are not known to the same degree of accuracy as in the direct numerical simulations.

In this chapter the force coupling method will be described. The first section explains the basic idea. Section 4.2 reviews the multipole method for Stokes flow. This review is included, because the force coupling method is based on the ideas developed for the multipole method. The core part of the chapter is section 4.3, where the force coupling method for Stokes flows is described. The section is based on work done by Maxey & Patel (2001), while some parts are developed by the author in collaboration with Prof. Maxey. The chapter is concluded with some Stokes flow examples of the force coupling method computed by the author.

4.1 The Basic Idea

As shown in chapter 3 on page 25, the motion of rigid particles in a fluid flow is determined by solving the Navier-Stokes equations (7) subject to the boundary

[5] $Re_p > 20$ for a sphere.

conditions of the bounding geometry and the no-slip boundary conditions on the particle surfaces (8). In the force coupling method, the no-slip boundary condition on the particles is approximated by specifying a force and/or a torque in the flow at the position of the particle. This corresponds to the two-way coupling described in section 3.5, where a source term was added to the momentum equations in order to model the effect of the moving particles on the fluid motion. The first level of approximation is the monopole point particle representation, where the momentum equation becomes

$$\frac{\partial u_i}{\partial t} + u_j \frac{\partial u_i}{\partial x_j} = -\frac{\nabla p}{\rho_f} + \nu \nabla^2 u_i + \frac{1}{\rho_f} \sum_{n=1}^{N} F_i^n \delta \left(\mathbf{x} - \mathbf{Y^n} \right) \ ,$$

where F_i^n is the force exerted by particle n on the fluid, due to the no-slip particle surface. In the two-way coupling scheme in section 3.5 the force was computed using the equation of motion and in that case F_i is given by equation (24). This first order approximation only includes the force from the particle on the fluid due to translation. A higher order approximation can be obtained by adding the effect due to the torque. Using a method as the point-particle in a numerical model is subject to numerical difficulties, since a singularity like the Dirac delta function $\delta \left(\mathbf{x} - \mathbf{Y^n} \right)$ cannot be represented accurately. Furthermore, the point force apporximation may only be applied to small particles that may be apporximated with a point. Therefore a different approach is desirable and one alternative method is to replace the Dirac delta function with a Gaussian function

$$\Delta \left(\mathbf{x} - \mathbf{Y^n}, \sigma \right) = \frac{1}{\left(2\pi\sigma^2 \right)^{3/2}} \exp \left(-\frac{\left(\mathbf{x} - \mathbf{Y^n} \right)^2}{2\sigma^2} \right) \ . \tag{26}$$

The length scale σ is a parameter that may be used to ensure numerical resolution and to reflect the finite size of the particle so that it can approximate larger particles. With the localized force representation specified in this way it applies to spherical particles, while elliptical particles may be specified with two length scales σ_1 and σ_2. Even more complex particles can be specified with three different length scales.

In this chapter we consider the force coupling method for rigid spheres sedimenting in Stokes flow. A particle settling under gravity in a quiescient fluid will create a disturbance velocity, and we will describe the force coupling method for determining this disturbance velocity. Two assumptions are made regarding the fluid and particle motion:

- A low Reynolds number and a low Strouhal number are assumed, thus the fluid motion is described by the steady linear Stokes equations.
- Consistent with the neglect of fluid inertia the effect of particle inertia is neglected. Thus the fluid force on the particle balance the gravity force.

The second assumption is based on the equation of motion for the sphere

$$m_p \frac{dV_i}{dt} = F_i^{body} + F_i^{hydrodynamic} \ ,$$

where F_i^{body} are the body forces like gravity or magnetic forces, and $F_i^{hydrodynamic}$ covers the forces from the fluid on the sphere. Assuming particle inertia to be negligible, means that any changes in the particle velocity are so slow that

$$\left| \frac{dV}{dt} \right| \ll \left(1 - \frac{\rho_f}{\rho_p} \right) |g| \ .$$

The assumption that particle inertia is neglected yields a balance between the body forces and the hydrodynamic forces, i.e.

$$F_i^{body} + F_i^{hydrodynamic} = 0 \ .$$

In the following sections we will only consider the case of spherical particles dispersed in a fluid at Stokes flow conditions, for which some analytical results may be obtained. The force coupling method at finite Reynolds numbers is discussed in chapter 5. Use of the force coupling method for elliptical or more complex particles is shortly discussed in chapter 6.

4.2 The Standard Multipole Method in Stokes flow

The outset for the description of the force coupling method is a short review of the standard multipole expansion method, because this forms the basis of the force coupling method. A more detailed description, than that given below, can be found in Kim & Karrila (1991).

The Fluid Velocity Field

The standard multipole expansion method is based on the integral representation for the velocity field due to N particles dispersed in a Stokes flow with the undisturbed flow $u_i^\infty(\mathbf{x})$ (Kim & Karrila (1991))

$$u_i(\mathbf{x}) = u_i^\infty(\mathbf{x}) - \frac{1}{8\pi\mu}\sum_{n=1}^{N}\int_{S_n} O_{ij}(\mathbf{x}-\mathbf{Y^n})\left[\sigma_{jk}(\mathbf{Y^n})e_k^n(\mathbf{Y^n})\right]dS_Y \ , \tag{27}$$

where S_n is the surface of particle n, e_k^n is a surface normal vector pointing into the fluid and $O_{ij}(\mathbf{x}-\mathbf{Y^n})$ is the Oseen tensor. The Oseen tensor is determined from the Stokes flow induced by a single point force (Hasimoto & Sano (1980))

$$-\frac{\partial p}{\partial x_i} + \mu\frac{\partial^2 u_i}{\partial x_j \partial x_j} = -F_i\delta(\mathbf{x}) \ , \tag{28}$$

together with the continuity equation (6). The solution can be found in e.g. Hasimoto & Sano (1980) or Kim & Karrila (1991), and the velocity field satisfying the continuity equation (6) and the momentum equation (28) is

$$u_i(\mathbf{x}) = F_j O_{ij}(\mathbf{x}) \ , \tag{29}$$

with the Oseen tensor given as

$$O_{ij}(\mathbf{x}) = \frac{1}{8\pi\mu}\left(\frac{\delta_{ij}}{r} + \frac{x_i x_j}{r^3}\right) \ . \tag{30}$$

The multipole expansion is constructed using higher order corrections for the disturbance field. The corrections are obtained through a Taylor expansion of the Oseen tensor (30) (Kim & Karrila (1991)). When the Taylor expansion is inserted into (27) the result is

$$\begin{aligned} u_i(\mathbf{x}) &= u_i^\infty(\mathbf{x}) \\ &-\frac{1}{8\pi\mu}\sum_{n=1}^{N}\left[\left(F_j^n - F_{jk}^n\frac{\partial}{\partial x_k} + F_{jkl}^n\frac{\partial^2}{\partial x_k\partial x_l} + \ldots\right)O_{ij}\left(\mathbf{x}-\mathbf{Y^n}\right)\right] \ , \end{aligned} \tag{31}$$

where F_j^n is the monopole strength, F_{jk}^n the dipole strength, F_{jkl}^n the quadropole strength and so forth. The monopole strength corresponds to the force on the fluid from particle n, thus

$$F_j^n = \oint_{S_n}\left[\sigma_{jk}(\mathbf{Y^n})e_k^n(\mathbf{Y^n})\right]dS_Y \ .$$

The dipole strength is

$$F_{jk}^n = \oint_{S_n}\left[\sigma_{jl}(\mathbf{Y^n})e_l^n(\mathbf{Y^n})\right](x_k - Y_k)\,dS_Y \ ,$$

and this can be divided into a antisymmetric part related to the torque on the fluid from particle n and a symmetric part, known as the stresslet, related to the rate of strain field. The quadropole and higher order multipoles are induced moments which depend on the relative configuration of the particles (Durlofsky et al. (1987)), with the exceptions of a degenerate quadrupole and a degenerate octopole, which both result from the finite size of the particles. The number of moments included in the expansion determines the accuracy to which the solution is obtained. If all effects, ranging from long distance interaction down to lubrication between two particles, are to be included all the moments in the expansion (31) must be retained.

The velocity field given in (31) is in fact the solution of the continuity equation (6) and a momentum equation with a right hand side consisting of a multipole distribution of forces (Saffman (1973)), i.e.

$$\begin{aligned} -\frac{\partial p}{\partial x_i} + \mu \frac{\partial^2 u_i}{\partial x_j \partial x_j} = \\ -\sum_{n=1}^{N} \left[\left(F_i^n + F_{ij}^n \frac{\partial}{\partial x_j} + F_{ijk}^n \frac{\partial^2}{\partial x_j \partial x_k} + \dots \right) \delta \left(\mathbf{x} - \mathbf{Y^n} \right) \right] \ . \end{aligned} \tag{32}$$

Each of the terms on the right hand side of (32) correspond to the similar terms in (31). This is a result of the linearity of (32), making it possible to find the solution by solving a series of equations

$$\begin{aligned} -\frac{\partial p^1}{\partial x_i} + \mu \frac{\partial^2 u_i^1}{\partial x_j \partial x_j} &= 0 \\ -\frac{\partial p^2}{\partial x_i} + \mu \frac{\partial^2 u_i^2}{\partial x_j \partial x_j} &= -\sum_{n=1}^{N} F_i^n \delta \left(\mathbf{x} - \mathbf{Y^n} \right) \\ -\frac{\partial p^3}{\partial x_i} + \mu \frac{\partial^2 u_i^3}{\partial x_j \partial x_j} &= -\sum_{n=1}^{N} F_{ij}^n \frac{\partial \delta \left(\mathbf{x} - \mathbf{Y^n} \right)}{\partial x_j} \\ -\frac{\partial p^4}{\partial x_i} + \mu \frac{\partial^2 u_i^4}{\partial x_j \partial x_j} &= -\sum_{n=1}^{N} F_{ijk}^n \frac{\partial^2 \delta \left(\mathbf{x} - \mathbf{Y^n} \right)}{\partial x_j \partial x_k} \\ &\vdots \end{aligned}$$

The solution to (32) is constructed as the sum of the solutions to equations (4.2), i.e. $u = \sum_n u^n$. The result is the velocity field given by (31).

An example of the force multipole method is the motion induced by a single sphere with radius a translating without rotation through an infinite still fluid with velocity V_i. When the sphere centre is placed at the origin, the fluid motion is represented by a combination of a point force F_i (given by Stokes drag law) and a degenerate force quadrupole F_{ijk} (Kim & Karrila (1991) and Durlofsky et al. (1987))

$$F_i = 6\pi a \mu V_i \tag{33}$$

$$F_{ijk} = \frac{a^2}{6} F_i \delta_{jk} \left(\mathbf{x} \right) \ , \tag{34}$$

the degenerate force quadrupole accounts for the finite size of the particle and corresponds to the Faxen correction to the Stokes drag (Kim & Karrila (1991)). Due to symmetry the force dipole strength is zero ($F_{ij} = 0$). Using these Saffman (1973) solved (32) and obtained the disturbance velocity

$$u_i = \frac{1}{8\pi\mu} \left(\frac{\delta_{ij}}{r} + \frac{x_i x_j}{r^3} \right) F_j + \frac{a^2}{24\pi\mu} P \left[\frac{\delta_{ij}}{r^3} - \frac{3 x_i x_j}{r^5} \right] F_j - \frac{a^2}{9\mu} \delta \left(\mathbf{x} \right) F_i \ , \tag{35}$$

with F_i prescribed by (33). The notation $P[f]$ denotes Principal Value and means that the results are defined with a simple, small spherical region about the origin excluded (Maxey & Patel (2001)). The first part of the fluid velocity is due to the point force given by the Oseen tensor (30), while the second and third terms are from a flow induced by $\nabla^2 O_{ij}$, which is the degenerate force quadrupole. With the point force and the degenerate force quadrupole, the fluid velocity on the sphere surface equals the sphere velocity V_i exactly. This is seen by inserting $x_i = a$ and $r = a$ in (35). Using (33) and (34) Saffman (1973) obtained the pressure

$$p = \frac{1}{4\pi}\frac{x_i F_i}{r^3} + \frac{a^2}{6} F_i \frac{\partial \delta(\mathbf{x})}{\partial x_i} \ .$$

The first term in the pressure is due to the force monopole and the second is a result of the force quadrupole.

Multipole expansions have been widely used for dynamic simulations of hydrodynamic interaction among particles in Stokes flow. The investigations cover both sedimentation and shear flow examples, see e.g. Durlofsky et al. (1987), Brady & Bossis (1988), Durlofsky & Brady (1989) and Dratler & Schowalter (1996).

Particle velocity in the standard multipole representation

In the standard multipole representation the approximate particle velocity is usually found from the Stokes terminal settling velocity of the sphere corrected with the local fluid velocity induced by the motion of the other spheres, i.e.

$$V_i = u_i(\mathbf{Y}, t) + W_i \ ,$$

where W_i is the terminal (Stokes) settling velocity for the particle and $u_i(\mathbf{Y}, t)$ is the fluid velocity evaluated at the particle center Y_i. In order to avoid the infinite self-induced velocity[6] from the standard multipole expansion associated with the particle under consideration, $u_i(\mathbf{Y}, t)$ is evaluated from the disturbance flow from all particles except the particle itself. This is consistent with the linearity of the Stokes equations, where it is possible to separate the contributions from each particle. For finite (higher) Reynolds numbers this procedure cannot be used, since the nonlinearity of the Navier-Stokes equations does not allow the contributions from each particle to be separated.

4.3 The Finite Localized Force Representation in Stokes Flow

The finite localized force representation is based on the standard multipole expansion, but instead of considering the particle as a point, the particle is considered as a volume. Therefore the effect of the moving particle on the fluid flow, is spread out over a given volume related to the particle volume. This is obtained by replacing the Dirac delta function with the Gaussian envelope given by equation (26).

The description of the fluid velocity field and the determination of the particle velocity is based on the work by Maxey & Patel (2001). The descripition of the force dipole is based on work done by the author in collaboration with prof. Maxey.

The Fluid Velocity Field

The key element in the standard multipole expansion was the solution to the single point force leading to the Oseen tensor O_{ij}. When the Dirac delta function is replaced with the finite localized force envelope $\Delta(\mathbf{x} - \mathbf{Y^n}, \sigma)$, the key element

[6] due to the Dirac delta function

is the same. Therefore the solution to a single localized force must be determined. This solution is obtained by solving the continuity equation (6) in conjuction with the momentum equation for the single localized force, i.e.

$$-\frac{\partial p}{\partial x_i}+\mu\frac{\partial^2 u_i}{\partial x_j\partial x_j}=-F_i\Delta\left(\mathbf{x},\sigma\right)\ . \tag{36}$$

The solution to these equations is described in Appendix A.1. The new Oseen tensor corresponding to $\Delta\left(\mathbf{x},\sigma\right)$ becomes

$$\begin{aligned}O_{ij}\left(\mathbf{x},\sigma\right)=&\frac{1}{8\pi\mu r}\left(\delta_{ij}+\frac{x_ix_j}{r^2}\right)\mathrm{erf}\left(\frac{r}{\sqrt{2}\ \sigma}\right)\\&+\left(\delta_{ij}-\frac{3x_ix_j}{r^2}\right)\left[\frac{\sigma^2}{8\pi\mu r^3}\mathrm{erf}\left(\frac{r}{\sqrt{2}\ \sigma}\right)-\frac{\sigma^4}{2\mu r^2}\Delta\left(\mathbf{x},\sigma\right)\right]\ ,\end{aligned} \tag{37}$$

and the disturbance flow from the monopole forcing F_i is given by (29) as

$$u_i(\mathbf{x})=F_jO_{ij}(\mathbf{x},\sigma)\ , \tag{38}$$

with $O_{ij}(\mathbf{x},\sigma)$ given by (37). For large r/σ, i.e. when $\mathrm{erf}\left(r/\sqrt{2}\ \sigma\right)\approx 1$, the two first terms in the new Oseen tensor correspond to the standard Oseen tensor and the standard degenerate force quadrupole, respectively. This is seen by comparing equation (37) with (35).

As seen above the degenerate force quadrupole is significant for the motion of a single isolated particle. Therefore it is of importance to examine the flow due to a degenerated force quadrupole as represented by the localized force envelope. The force quadrupole is given as $(a^2/6)F_i\delta_{jk}$, see equation (33) and (34), and the flow is determined from

$$-\frac{\partial p}{\partial x_i}+\mu\frac{\partial^2 u_i}{\partial x_j\partial x_j}=-\frac{a^2}{6}F_i\delta_{jk}\frac{\partial^2\Delta\left(\mathbf{x},\sigma\right)}{\partial x_j\partial x_k}\ .$$

As with equation (36) this can be solved analytically and the solution is given in Appendix A.2. The fluid velocity from the degenerate force quadrupole is

$$u_i(\mathbf{x})=\frac{a^2}{6\mu}\left(F_j\frac{\partial^2 G(\mathbf{x})}{\partial x_j\partial x_i}-F_i\Delta\left(\mathbf{x},\sigma\right)\right)\ , \tag{39}$$

where the function $G(\mathbf{x})$

$$G(\mathbf{x})=-\frac{1}{4\pi\sqrt{x_ix_i}}\mathrm{erf}\left(\sqrt{\frac{x_ix_i}{2\sigma^2}}\right)\ ,$$

is given in Appendix A.1. Contrary to the new Oseen tensor, which has two types of long range[7] responses, the degenerate force quadrupole in (39) has only one and this is equivalent to a source-dipole potential flow. For more details the reader is referred to Maxey & Patel (2001). Maxey & Patel (2001) gave an example of the motion of a single isolated particle as represented by the finite localized force envelope. The flow is given as a combination of the flow from the force monopole (38) and the flow from the degenerate force quadrupole (39). They find that the accuracy improves as the ratio of the particle radius a and the length scale for the Gaussian envelope σ becomes larger. Maxey & Patel (2001) find the difference between u_i and V_i on the particle surface to be less than 1.5% for $a/\sigma\geq 2.5\sqrt{2}$ and negligible for $a/\sigma\geq 3\sqrt{2}$. Thus, their results show that the velocity is accurately represented away from the surface of the sphere, while the accuracy in the region near the surface improves as the ratio a/σ increases.

Extending the force coupling representation to include higher order approximations is done similarly to the standard multipole expansion. Hence, the equations

[7] the standard force monopole and standard degenerate force quadrupole.

determining the fluid motion for spheres dispersed in Stokes flow is

$$-\frac{\partial p}{\partial x_i}+\mu\frac{\partial^2 u_i}{\partial x_j\partial x_j}= \\ -\sum_n^N\left[\left(F_i+F_{ij}\frac{\partial}{\partial x_j}+F_{ijk}\frac{\partial^2}{\partial x_j\partial x_k}+\dots\right)\Delta\left(\mathbf{x}-\mathbf{Y^n},\sigma\right)\right]\ . \tag{40}$$

Solving these equations requires knowledge about the force multipole strengths and the parameter σ. Determination of the length scale parameter σ depends on the method for computing the particle velocity. Therefore the discussion of the determination of these parameters will be deferred until after the description of the particle tracking.

Particle velocity in the finite localized force representation

In order to find a method for determining the particle velocity consider the settling of a single isolated sphere in a still fluid with the velocity V_i equal to the Stokes settling velocity W_i. When a force monopole F_i is related to the settling velocity W_i by the Stokes drag law, the disturbance flow may be approximately represented by the single force monopole as

$$u_i=O_{ij}F_j=6\pi a\mu O_{ij}W_j\ . \tag{41}$$

Since the finite force multipole method does not have the problem with infinite self-induced velocity, because it is finite everywhere in the fluid, we may evaluate the fluid velocity at the particle centre. The new Oseen tensor O_{ij} from (37) evaluated at the particle centre Y_i is

$$O_{ij}\left(0\right)=\frac{1}{3\pi\mu\sigma}\frac{1}{\sqrt{2\pi}}\delta_{ij}\ , \tag{42}$$

and the fluid velocity at the particle centre is

$$u_i\left(\mathbf{Y},t\right)=6\pi a\mu\frac{1}{3\pi\mu\sigma}\frac{1}{\sqrt{2\pi}}\delta_{ij}W_j=\frac{a}{\sigma}\sqrt{\frac{2}{\pi}}W_i\ .$$

Thus, when the length scale σ is chosen to be equal to $\sqrt{2/\pi}\ a\approx 1.25a$, then the self-induced fluid velocity at Y_i matches the Stokes settling velocity exactly, and the particle velocity may be set to

$$V_i\left(t\right)=u_i\left(\mathbf{Y},t\right)=W_i\ . \tag{43}$$

If more spheres are considered, then the correction due to the motion of the other spheres is included in $u_i\left(\mathbf{Y},t\right)\neq W_i$ and no further correction is necessary. As already mentioned in the previous section, the results of Maxey & Patel (2001) show that the flow representation, particularly near the particle, becomes more accurate for larger values of a/σ. Maxey & Patel (2001) also computed the approximate fluid velocity for the flow represented by equation (41) with $a/\sigma=\sqrt{\pi/2}$. Their result is shown as the dotted line in figure 9 together with the Stokes result (shown as $\bullet$) for a rigid sphere. The results show that there is good agreement for distances $r/a\geq 3$, while near the sphere the discrepancy is larger.

A second method is to define a volume averaged velocity $\tilde{u}_i$ in terms of the envelope function $\Delta\left(\mathbf{x}-\mathbf{Y},\sigma\right)$, i.e.

$$\tilde{u}_i\left(t\right)=\int u_i\left(\mathbf{x},t\right)\Delta\left(\mathbf{x}-\mathbf{Y},\sigma\right)d^3\mathbf{x}\ , \tag{44}$$

where the integration is over all space. This is based on the idea that the particle has a finite size and moves due to the local average fluid velocity integrated over the particle volume. If the disturbance flow u_i is represented by the single force

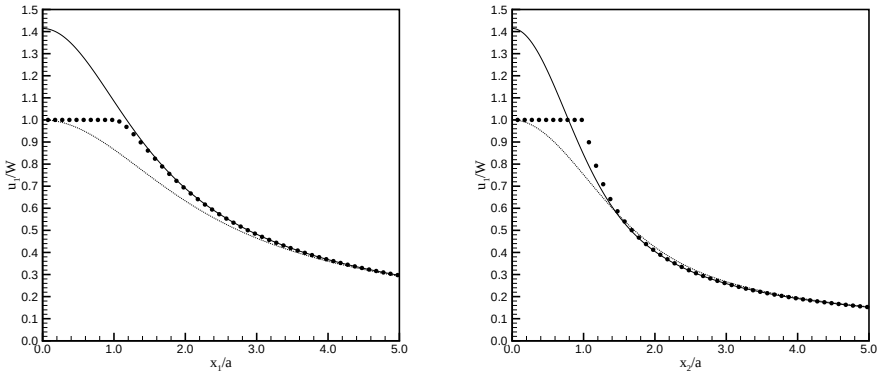

(a) u_1 velocity profile along x_1 axis for two values of a/σ

(b) u_1 velocity profile along x_2 axis for two values of a/σ

Figure 9. Comparision of u_1 velocity profiles given by the force monopole equation (41) with the Stokes solution. Stokes solution (•) *, $a/\sigma = \sqrt{\pi/2}$* $(\cdots)$ *and $a/\sigma = \sqrt{\pi}$* $(-)$

monopole given by equation (41), the ratio between the sphere radius and the length scale parameter, is determined by inserting (41) into (44) with the sphere placed at the origin and setting this equal to the Stokes settling velocity W_i, i.e.

$$\tilde{u}_i(t) = 6\pi a\mu \int O_{ij} W_j \Delta(\mathbf{x}, \sigma)\, d^3\mathbf{x} = W_i \ .$$

Performing the integral gives a match between the volume averaged velocity and the Stokes settling velocity. The integral is computed in Appendix A.3. The result of this match leads to a ratio between the sphere radius and the length scale parameter given by (Maxey & Patel (2001))

$$\frac{a}{\sigma} = \sqrt{\pi} \qquad \Rightarrow \qquad \sigma = \frac{a}{\sqrt{\pi}} \ . \tag{45}$$

With this ratio the particle velocity is simply

$$V_i(t) = \tilde{u}_i(t) \ .$$

If more spheres are considered, the correction due to the motion of the other spheres is already included in $u_i(\mathbf{x}, t)$ and therefore also in $\tilde{u}_i(t) \ = V_i(t)$. In figure 9 the disturbance velocity given by (41) with the length scale ratio given by (45) is shown as the full line. As expected the result compares better with the exact Stokes flow result, than the result for the length scale ratio $a/\sigma = \sqrt{\pi/2}$.

The volume averaged velocity (44) ensures that the mass of the particles is conserved (Dent & Maxey (2000)). Furthermore, it has the valuable property, that a consistent energy balance may be established between the potential energy released from the settling of the particle and the viscous dissipation in the fluid (Maxey & Patel (2001)). The method given by (44) can be understood as a spatial filter that approximates the presence of the particles; the filter removes the influence of small velocity scales that do not effect the particle.

Figure 10 shows the streamlines and the vorticity contours obtained with the single force monopole and $a/\sigma = \sqrt{\pi}$. The streamlines show that there exists a fictitious material boundary, larger than the actual sphere, but otherwise the streamline pattern is very similar to the exact result in figure 6(a). The vorticity contours are also very similar to those obtained from the exact solution in figure 6(b), but the vorticity at the sphere surface is $0.94W/a$ and therefore less than the

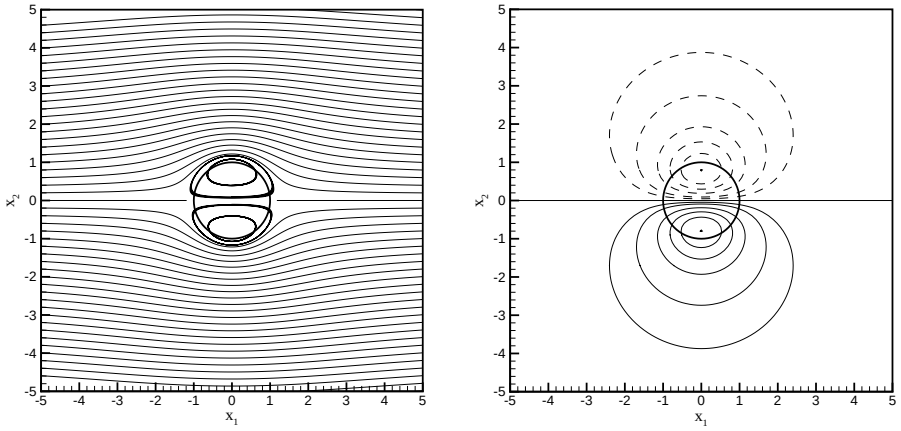

(a) Streamlines (b) Vorticity contours

Figure 10. Streamlines and vorticity contours for the steady Stokes flow past a sphere. The vorticity is made non-dimensional with W/a. The vorticity contours are ± 1 (innermost), ± 0.8, ± 0.6, ± 0.4, ± 0.2 and ± 0.1 (outermost). Negative vorticity is denoted by dashed lines.

Stokes value of $1.5W/a$. The attenuated surface vorticity and the larger material surface are effects of not fully satisfying the boundary condition at the sphere surface. Figure 9 shows that the boundary condition for u_1 is only approximated and not satisfied. Similar observations can be made for the two other velocities. Therefore the vorticity and the streamlines shown in figure 10 are approximations to the exact solution, and this causes the discrepancy between figure 6 and figure 10.

Another aspect worth noting is the Faxen correction term to the Stokes drag law. When an isolated particle is settling in a nonuniform flow, u_i, that can be approximated as

$$u_i \approx U_i^0 + x_j \frac{\partial U_i^0}{\partial x_j} + \frac{1}{2} x_j x_k \frac{\partial^2 U_i^0}{\partial x_j \partial x_k} \ ,$$

the particle velocity is modified and the corrected velocity is

$$V_i = W_i + U_i^0 + \frac{a^2}{6} \nabla^2 U_i^0 \ . \tag{46}$$

With these conditions the estimate of V_i from (44) is

$$V_i = W_i + U_i^0 + \frac{\sigma^2}{2} \nabla^2 U_i^0 \ . \tag{47}$$

The estimate (47) matches the exact expression (46) when $a/\sigma = \sqrt{3}$ and there is a small discrepancy when $a/\sigma = \sqrt{\pi}$.

The local spatially averaged velocity given by (44) has more physically valuable properties which are discussed in details in Maxey et al. (1997) and Maxey & Patel (2001).

Particle angular velocity in the finite localized force representation

If a spherical particle is free to rotate, it will rotate in correspondence with the vorticity of the surrounding fluid. The angular velocity of the sphere in the localized finite force coupling scheme is therefore found in a manner similar to the

velocity, i.e.

$$\Omega_i = \tilde{\omega}_i = \int \frac{1}{2}\omega_i\left(\mathbf{x},t\right)\Delta\left(\mathbf{x}-\mathbf{Y},\sigma_D\right)d^3\mathbf{x}\ , \tag{48}$$

where σ_D is a length scale similar to σ, but related to the force dipole. In order to determine this length scale consider a fixed sphere rotating in an infinite still fluid due to an external torque. The external torque may be defined in terms of a prescribed angular velocity of the particle

$$T_i = 8\pi\mu a^3\Omega_i^p\ , \tag{49}$$

where Ω_i^p is the prescribed angular velocity. With this torque the sphere will rotate with the angular velocity Ω_i^p (Kim & Karrila (1991)). The fluid velocity field due to the action of the torque is given by

$$-\frac{\partial p}{\partial x_i}+\mu\frac{\partial^2 u_i}{\partial x_j\partial x_j} = -T_{ij}\frac{\partial\Delta\left(\mathbf{x},\sigma_D\right)}{\partial x_j}\ , \tag{50}$$

and the continuity equation (6). In the standard multipole expansion method the force dipole strength due to the torque is given by (Kim & Karrila (1991))

$$T_{ij} = \frac{1}{2}\varepsilon_{ijk}T_k = 4\pi\mu a^3\varepsilon_{ijk}\Omega_k^p = 3\rho_f\nu\mathrm{V}_p\Omega_{ij}\ , \tag{51}$$

where $\Omega_{ij}=\varepsilon_{ijk}\Omega_k^p$. Using this definition equation (50) can be solved. The solution to equations (6) and (50) for a sphere rotating with $\Omega^p=(0,0,\Omega)$ is given in Appendix A.4. The solution is

$$\begin{aligned} u_1\left(\mathbf{x}\right) &= 4\pi a^3\Omega\frac{\partial G\left(r\right)}{\partial x_2} = 4\pi a^3\Omega\frac{x_2}{r}\frac{dG\left(r\right)}{dr} \\ u_2\left(\mathbf{x}\right) &= -4\pi a^3\Omega\frac{\partial G\left(r\right)}{\partial x_1} = -4\pi a^3\Omega\frac{x_1}{r}\frac{dG\left(r\right)}{dr} \\ u_3\left(\mathbf{x}\right) &= 0\ , \end{aligned} \tag{52}$$

where $G(r)$ is given by (A.3). The derivative of this is

$$\frac{dG\left(r\right)}{dr} = -\frac{1}{4\pi r^2}\,\mathrm{erf}\left(\frac{r}{\sqrt{2}\sigma_D}\right)+\frac{\sigma_D^2}{r}\Delta\left(\mathbf{x},\sigma_D\right)\ , \tag{53}$$

The length scale σ_D is determined by computing the volume averaged angular velocity defined in (48) using the vorticity ω_3 computed from equations (52). This is done in Appendix A.5. The resulting $\tilde{\omega}_3$ is equal to Ω, when the ratio between the sphere radius and the length scale σ_D is

$$\frac{a}{\sigma_D} = \sqrt[3]{6\sqrt{\pi}}\ \Rightarrow\ \sigma_D = \frac{a}{\sqrt[3]{6\sqrt{\pi}}}\ . \tag{54}$$

The particle angular velocity is then given by (48) and in case of more spheres the effect of the other spheres is included, as it was the case above with the particle velocity.

In figure 11(a) the streamlines for the rotating sphere computed using (52) and (54) is shown. These are very similar the streamlines for the Stokes solution and the rotational flow continues into the center of the fictitious sphere. The velocity u_1 along the axis x_2 is shown in figure 11(b) for the monopole value $a/\sigma=\sqrt{\pi}$ and the dipole value $a/\sigma_D=\sqrt[3]{6\sqrt{\pi}}$ of the scale ratio. The solution for the monopole value $a/\sigma=\sqrt{\pi}$ is accurate for distances $x_2<-1.8a$ $(r/a>1.8)$. Closer to the sphere the velocity is smaller than the analytical solution.The solution for the dipole value $a/\sigma_D=\sqrt[3]{6\sqrt{\pi}}$ gives a better approximation, where the velocity obtained with force coupling method is equal to the analytical velocity for distances $x_2<-1.3a$ $(r/a>1.3)$. Closer to sphere the velocity is small, until it overshoots $x_2\approx-0.6a$. The discrepancy between the force coupling solution and analytical solution, is again a result of the force coupling solution being an approximation to the analytical solution as observed for the velocity of the steady translating sphere in figure 9(a).

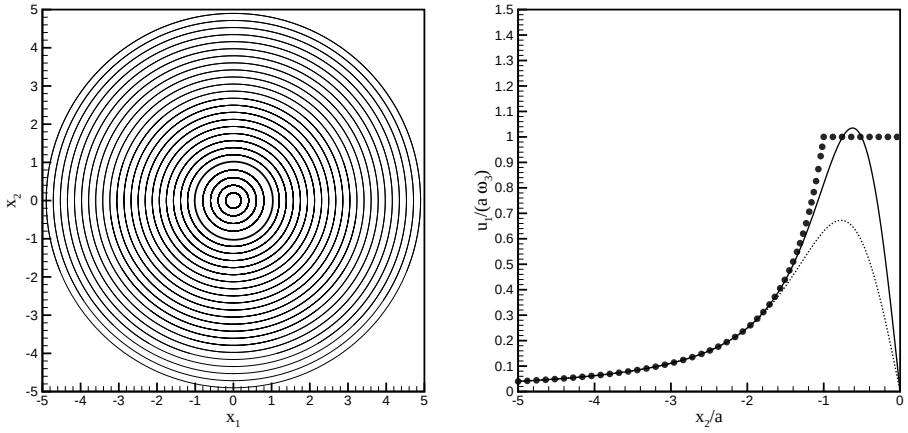

(a) Streamlines

(b) u_1 velocity along the x_2 axis for two values of a/σ_D

Figure 11. Streamlines and u_1 velocity for the fixed steady rotating sphere in Stokes flow. The Stokes solution (•), $a/\sigma_D = \sqrt{\pi}$ $(\cdots)$ and $a/\sigma_D = \sqrt[3]{6\sqrt{\pi}}$ $(-)$.

Determination of the Multipole Strengths

Solving particulate problems using the continuity equation (6) and the force coupling momentum equation given by (40) requires a determination of both the length scales involved in the Gaussian envelope and the multipole strengths. The length scales σ and σ_D were both determined above and the values are given in equations (45) and (54).

The force monopole is related to the force from the particle on the fluid. This force is the sum of the body forces acting on the particle, thus the force monopole strength is

$$F_i = F_i^{body} = (m_p - m_f) g_i \ , \tag{55}$$

where the last equality is due to the fact that particle inertia has been neglected according to the second assumption on page (42). If other body forces are considered these should be added to the right hand side of (55).

The force dipole has two components, an asymmetric part and a symmetric part. The asymmetric part is related to the torque from the particle to the fluid. This is given by the sum of the external torque acting on the particle and the inertial torque from the time derivative of the angular velocity. The inertial torque is neglected in consistency with the neglect of particle and fluid inertia. The force dipole strength due to the external torque is therefore given by (51).

The symmetric part of the force dipole strength, the stresslet, is related to the rate of strain field

$$E_{ij} = \frac{1}{2}\left(\frac{\partial u_i}{\partial x_j} + \frac{\partial u_j}{\partial x_i}\right) \ .$$

Since we consider rigid spheres that are not able to deform, the rate of strain in the volume occupied by the particle should be zero, at least in an average sense. The average rate of strain for a sphere placed at Y_i is computed similarly to the velocity and angular velocity, i.e.

$$\tilde{E}_{ij}(t) = \int E_{ij}(\mathbf{x}, t)\, \Delta(\mathbf{x} - \mathbf{Y}, \sigma_D)\, d^3\mathbf{x} \ . \tag{56}$$

In the standard multipole method the stresslet for a fixed sphere in a pure straining Stokes flow is given by (Kim & Karrila (1991))

$$F_{ij} = \frac{20}{3}\pi\mu a^3 E^{\infty}_{ij} \ , \tag{57}$$

where E^{∞}_{ij} is the undisturbed rate of strain. Therefore the force dipole strength related to the stresslet is defined as

$$F_{ij} = \frac{20}{3}\pi\mu a^3 E^{*}_{ij} \ , \tag{58}$$

where

$$E^{*}_{ij} = \tilde{E}^{\infty}_{ij} = \int E^{\infty}_{ij}\left(\mathbf{x},t\right)\Delta\left(\mathbf{x}-\mathbf{Y},\sigma_D\right)d^3\mathbf{x} \ .$$

When more than one sphere is present the elements in E^{*}_{ij} cannot be computed *a priori*, because of the influence from the other spheres. Therefore E^{*}_{ij} must be computed iteratively, see also Appendix B.2. The elements are computed in the following manner:

1. Compute the velocity with a force dipole strength $F^{[q-1]}_{ij}$. If $q = 1$ then the value from the previous time step or $F^{[0]}_{ij} = 0$ is chosen.
2. Compute the volume average rate of strain from this new velocity field, i.e. $\tilde{E}^{[q-1]}_{ij} = \int E^{[q-1]}_{ij}\left(\mathbf{x},t\right)\Delta\left(\mathbf{x}-\mathbf{Y},\sigma_D\right)d^3\mathbf{x}$.
3. If $\tilde{E}^{[q-1]}_{ij} = 0$ or $\left|\tilde{E}^{[q-1]}_{ij}\right| < \epsilon$, then the computed velocity field is correct otherwise continue.
4. Set $E^{*\,[q]}_{ij} = E^{*\,[q-1]}_{ij} + \tilde{E}^{[q-1]}_{ij}$.
5. Compute the force dipole strength $F^{[q]}_{ij}$ using (58) and add the torque dipole strength if necessary.
6. Return to 1.

The total force dipole strength is the sum of (58) and (51), i.e.

$$F_{ij} = \rho_f \nu \mathrm{V}_p \left(5E^{*}_{ij} + 3\Omega_{ij}\right) \ .$$

4.4 Stokes Flow Examples of the Force Coupling Method

In the description of the force coupling method above, we saw that it was possible to approximate the exact Stokes solution for a single sphere settling in an infinite quiescent fluid. In this section several other examples of using the force coupling method in Stokes flow will be presented. These have been computed by the author. These examples include a sphere in a straining flow, two spheres settling in an unbounded domain, and a single sphere in channel translating in a channel. Further examples with two spheres and with the single sphere in a channel is given in Lomholt & Maxey (2001a).

A Neutrally Buoyant Sphere in a Straining Flow

Consider a sphere placed at the origin in a straining flow given by

$$u^{\infty}_i = E^{\infty}_{ij} x_j \tag{59}$$

Since the force from the particle on the fluid is zero only the force dipole term is non-zero. Consequently, the flow around the neutrally buoyant sphere is given as a superposition of the straining flow and the flow due to the force dipole i.e.

$$u_i = u^{\infty}_i + T_{ijk}F_{jk} = E^{\infty}_{ij}x_j + T_{ijk}F_{jk} \tag{60}$$

The tensor T_{ijk} is determined is Appendix A.6 as the solution to

$$u_i = T_{ijk} F_{jk} \tag{61}$$

Therefore the flow is determined if the correct force dipole strengths, F_{jk}, are specified. However, these are not given and must be determined. Two conditions apply to the flow. Firstly, the divergence must be zero due to incompressibility i.e.

$$\frac{\partial u_i}{\partial x_i} = \frac{\partial E^{\infty}_{ij} x_j}{\partial x_i} + \frac{\partial T_{ijk} F_{jk}}{\partial x_i} = 0 \tag{62}$$

Since both the straining flow and the force dipole induced flow satifies the condition of incompressibility by construction, this is also satified by the combined flow. The second condition is that the volume averaged rate of strain for the particle should be zero i.e.

$$\int \frac{1}{2} \left(\frac{\partial u_i}{\partial x_j} + \frac{\partial u_j}{\partial x_i} \right) \Delta \left(\mathbf{x}, \sigma_D \right) d^3\mathbf{x} = 0 \tag{63}$$

Partial integration of this results in changing the derivative from the velocity to the Gaussian function i.e.

$$- \int \left(u_i \frac{\partial \Delta \left(\mathbf{x}, \sigma_D \right)}{\partial x_j} + u_j \frac{\partial \Delta \left(\mathbf{x}, \sigma_D \right)}{\partial x_i} \right) d^3\mathbf{x} = 0 \tag{64}$$

performing the derivative of the Gaussian function gives,

$$\int u_i \frac{x_j}{\sigma_D^2} \Delta \left(\mathbf{x}, \sigma_D \right) + u_j \frac{x_i}{\sigma_D^2} \Delta \left(\mathbf{x}, \sigma_D \right) d^3\mathbf{x} = 0 \tag{65}$$

Inserting the disturbed velocity field from (60)

$$\int \left(\left(E^{\infty}_{ik} x_k + T_{ikl} F_{kl} \right) x_j + \left(E^{\infty}_{jk} x_k + T_{jkl} F_{kl} \right) x_i \right) \frac{\Delta \left(\mathbf{x}, \sigma_D \right)}{\sigma_D^2} d^3\mathbf{x} = 0 \tag{66}$$

Rearranging this results in a condition for the force dipole strength

$$\int \left(T_{ikl} x_j + T_{jkl} x_i \right) \frac{\Delta \left(\mathbf{x}, \sigma_D \right)}{\sigma_D^2} d^3\mathbf{x} F_{kl} = - \int \left(E^{\infty}_{ik} x_k x_j + E^{\infty}_{jk} x_k x_i \right) \frac{\Delta \left(\mathbf{x}, \sigma_D \right)}{\sigma_D^2} d^3\mathbf{x} \tag{67}$$

The summations over i, j, k, and l results in a 9×9 linear system with F_{kl} as the unknowns. The coefficient matrix is created by the integral on the left hand side and the forcing vector of the system is created by the right hand side of (67).

Given a specific rate of strain field E^{∞}_{ij} this may be solved to find the force dipole strength and the fluid velocity field. This has been done for a rate of strain field

$$E^{\infty}_{ij} = \begin{bmatrix} 1 & 0 & 0 \\ 0 & -1 & 0 \\ 0 & 0 & 0 \end{bmatrix} \tag{68}$$

and the solution to this can be seen in figures 12 and 13.

The streamlines for the solution are given in figure 12(a) and this shows that the force coupling solution induces recirculating zones creating a fictitious sphere similar to the case for the single settling sphere in figure 10(a). Compared to the streamlines for the Stokes solution given in figure 12(b) we see that away from the sphere there is an excellent agreement.

Figure 13 shows a comparison between the Stokes solution and the force coupling solution in terms of the u_1 velocity along the x_1-axis (figure 13(a)) and along the line $x_1 = x_2$ (figure 13(b)) for two values of a/σ_D. Both values of a/σ_D give good results away from the sphere, but close to the sphere the value determined above for the force dipole gives the best results and moreover the force coupling solution for this value is very close to the Stokes solution for every point outside the sphere ($r > 1$).

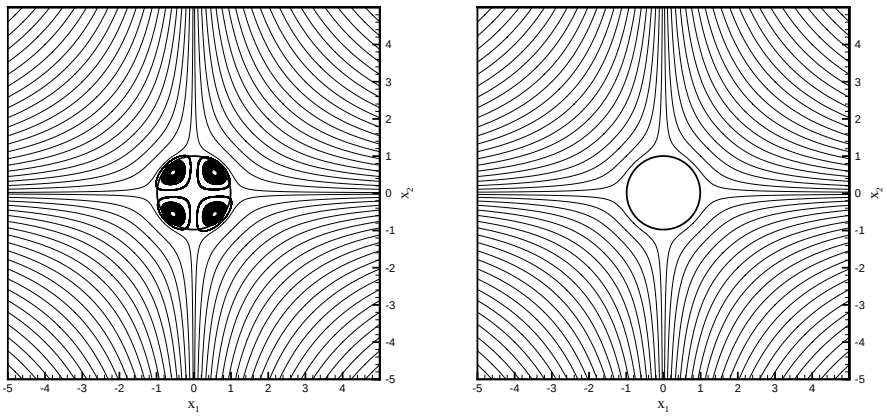

(a) Streamlines for the force coupling solution

(b) Streamlines for the Stokes solution

Figure 12. Streamlines for the Stokes and the force coupling solution to the flow field around a sphere in a pure straining flow.

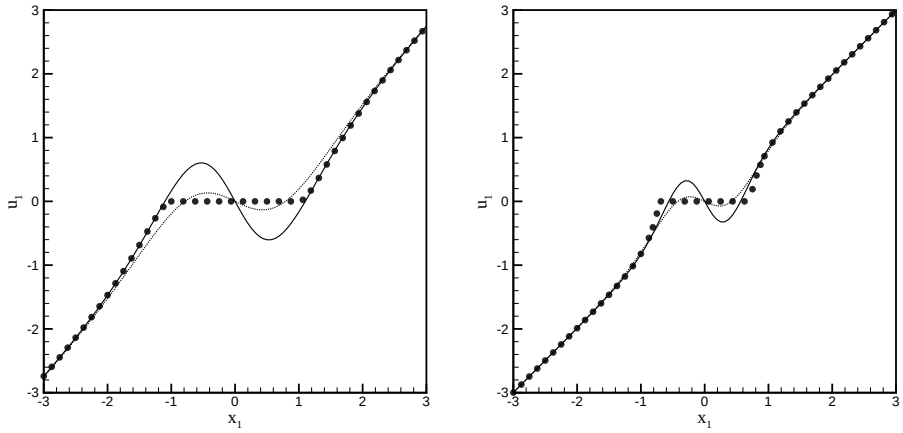

(a) u_1 velocity along the x_1 axis for two values of a/σ_D

(b) u_1 velocity along the line $x_1 = x_2$ for two values of a/σ_D

Figure 13. u_1 velocity from the force coupling method for the fixed sphere in pure straining Stokes flow and two different length scales of the Gaussian. The Stokes solution (•), $a/\sigma_D = \sqrt{\pi}$ $(\cdots)$ and $a/\sigma_D = \sqrt[3]{6\sqrt{\pi}}$ $(-)$.

Settling of two Stokes spheres

The problem of two equal spheres of radius a settling parallel or perpendicular to their line of centers in Stokes flow has previously been investigated both experimentally and analytically, see Happel and Brenner (1965). Therefore this problem poses a good test for the finite localized force coupling method. In Stokes flow two equal spheres settling either parallel or perpendicular to their line of centers will have the same drag (same velocity) and therefore the distance between them is maintained as they fall, see figure 14. More examples of two sphere configurations are given in Lomholt & Maxey (2001a).

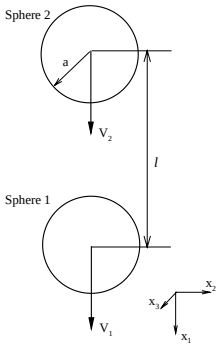

(a) Spheres settling parallel

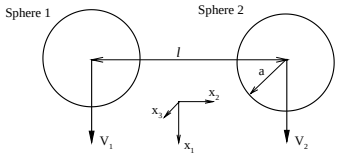

(b) Spheres settling perpendicular

Figure 14. Settling of two spheres in Stokes flow

First we consider the problem of two spheres settling parallel to their line of centers as in figure 14(a). Including only the force monopole the motion is described by

$$0 = -\nabla p + \mu \nabla^2 u_i + \sum_{n=1}^{2} F_i^n \Delta \left(\mathbf{x} - \mathbf{Y^n} \right) \ , \tag{69}$$

Since the Stokes equations are linear the disturbance velocity u_i is a sum of the disturbance velocities from each of the particles, i.e.

$$u_i = u_i^1 + u_i^2 \ , \tag{70}$$

and each of the u_i^n must satisfy the momentum equation (69), i.e.

$$0 = -\nabla p^n + \mu \nabla^2 u_i^n + F_i^n \Delta \left(\mathbf{x} - \mathbf{Y^n} \right) \ .$$

The particle velocity is found using (44), i.e. for particle $n = 1$

$$\begin{aligned} V_i^1 &= \int u_i \left(\mathbf{x} \right) \Delta \left(\mathbf{x} - \mathbf{Y^1} \right) d^3 x_i \\ &= \int \left(u_i^1 \left(\mathbf{x} \right) + u_i^2 \left(\mathbf{x} \right) \right) \Delta \left(\mathbf{x} - \mathbf{Y^1} \right) d^3 x_i \\ &= \tilde{u}_i^1 \left(\mathbf{Y^1} \right) + \tilde{u}_i^2 \left(\mathbf{Y^1} \right) = W_i + \tilde{u}_i^2 \left(\mathbf{Y^1} \right) \ , \end{aligned} \tag{71}$$

where

$$\tilde{u}_i^1 \left(\mathbf{Y^1} \right) = \int u_i^1 \left(\mathbf{x} \right) \Delta \left(\mathbf{x} - \mathbf{Y^1} \right) d^3 \mathbf{x} \ ,$$

and with the length scale ratio $a/\sigma = \sqrt{\pi}$ this is the Stokes settling velocity W_i for an isolated sphere as discussed in the previous section and indicated in (71). The particle velocity for the second particle is then similarly

$$V_i^2 = \tilde{u}_i^1 \left(\mathbf{Y^2} \right) + \tilde{u}_i^2 \left(\mathbf{Y^2} \right) = \tilde{u}_i^1 \left(\mathbf{Y^2} \right) + W_i \ .$$

Hence, we see that V_i^1 is equal to the Stokes settling velocity W_i for the isolated sphere corrected with the velocity $\tilde{u}_i^2 \left(\mathbf{Y^1} \right)$ from the disturbance flow created by the other sphere. Since $u_i^2 \left(\mathbf{Y_i^1} \right)$ is the disturbance flow from a single settling particle placed at $Y_i^2 - Y_i^1 = (d, 0, 0)$ this may be represented by the single force monopole (41), i.e.

$$u_i^2 \left(\mathbf{x} \right) = 6\pi a \mu O_{ij} W_j \ ,$$

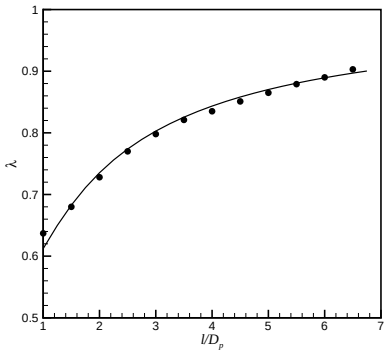

(a) Result for spheres settling parallel in an infinite fluid.

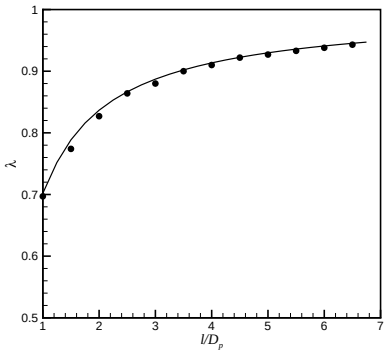

(b) Result for spheres settling perpendicular in an infinite fluid.

Figure 15. Comparision of computed $\lambda\,(-)$ with experimental $\lambda\,(\bullet)$. λ is the ratio between the Stokes settling velocity for a single sphere and the velocity obtained for both spheres. l/D_p is the ratio of the distance between the spheres and the sphere diameter.

where the force monopole strength is set to the Stokes drag, because we consider a sphere in steady Stokes flow. This gives the correction $\tilde{u}_i^2\left(\mathbf{Y^1}\right)$ to the velocity of the first particle.

The correction has been computed and the result is plotted in figure 15(a). The variable λ is the ratio between the Stokes settling velocity and the observed velocity, while l/D_p is the ratio of the distance between the spheres and the sphere diameter. Experimental results obtained from Happel & Brenner (1965) are also plotted in figure 15(a), and the result from the method shows excellent agreement with the experimental values. When the spheres are very close ($l/D_p < 1.5$) there is a slight increase in the difference between the computed and the experimental results. The reason is the lack of higher order terms in the disturbance velocity determined from (69).

For the case where the two spheres settle perpendicular to their line of centers shown in figure 14(b), the procedure is the same as above. The result is shown in figure 15(b) and again these are in fine compliance with the experiments obtained from Happel & Brenner (1965). Except when the spheres are close together, where the computed results deviate from the experimental values, due to the lack of higher order terms in the disturbance velocity determined from (69).

The results are also in agreement with the experiments by Wu & Manasseh (1998) for two spheres falling perpendicular with no separation ($l/D_p = 1.0$) and $Re_p = 0.01$, where they obtain values $\lambda = 0.67 - 0.76$.

Parallel and Perpendicular Motion of a Sphere in a Channel

Another Stokes flow example is a sphere moving parallel or perpendicular to the walls in a channel, see figure 16. Using a boundary-multipole collocation method, Ganatos et al. (1980a+b) computed the correction to Stokes drag law for a sphere moving perpendicular or parallel to the walls with constant velocity. The boundary-multipole collocation method is an exact numerical method for solution of Stokes flow problems. It uses the integral representation of the fluid velocity field given in (27). Therefore the method cannot be extended to finite Reynolds numbers. For a description of the boundary-multipole collocation

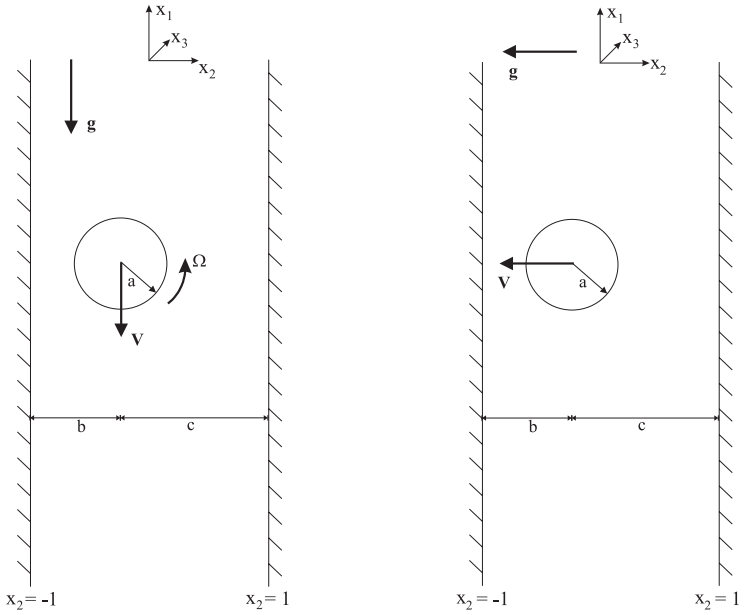

(a) Parallel Motion

(b) Perpendicular Motion

Figure 16. A sphere moving parallel or perpendicular to the walls in channel.

method, see Kim & Karrila (1991).

The drag force for the sphere may be expressed as

$$F_i = \lambda F_i^{Stokes} \ . \tag{72}$$

where λ is the correction factor. It is equal to the λ given above. Thus, λ is the ratio between the Stokes settling velocity and the velocity of the sphere in the channel. Similarly, a correction to the hydrodynamic torque acting on the sphere moving parallel to the channel walls with velocity V_i is defined as (Ganatos et al. (1980b))

$$T_i = -8\pi\mu a^2 V_i \lambda_T \ , \tag{73}$$

where λ_T is the correction to the torque.

Solving the force coupling equations in a channel the corrections λ and λ_T can be computed and compared with the exact values by Ganatos et al. (1980a+b). The solution of the force coupling equations in a three dimensional channel with periodic boundary conditions in the streamwise and spanwise directions, and no-slip boundary conditions in the normal direction is explained in Appendix B. The solution method in Appendix B is for the full Navier-Stokes equations, but the same code has been used for the Stokes flow described here. The steady Stokes flow is computed by setting the nonlinear terms equal to zero and using the time integration as an iteration scheme for obtaining the steady solution.

Ganatos et al. (1980a+b) solved the resistance problem,

$$\begin{aligned} F_i &= A_{ij} V_j + B_{ij} \Omega_j, \\ T_i &= C_{ij} V_j + D_{ij} \Omega_j, \end{aligned}$$

i.e. they specify a velocity and compute the force and torque on the sphere as it moves with this velocity. In the force coupling method the mobility problem is

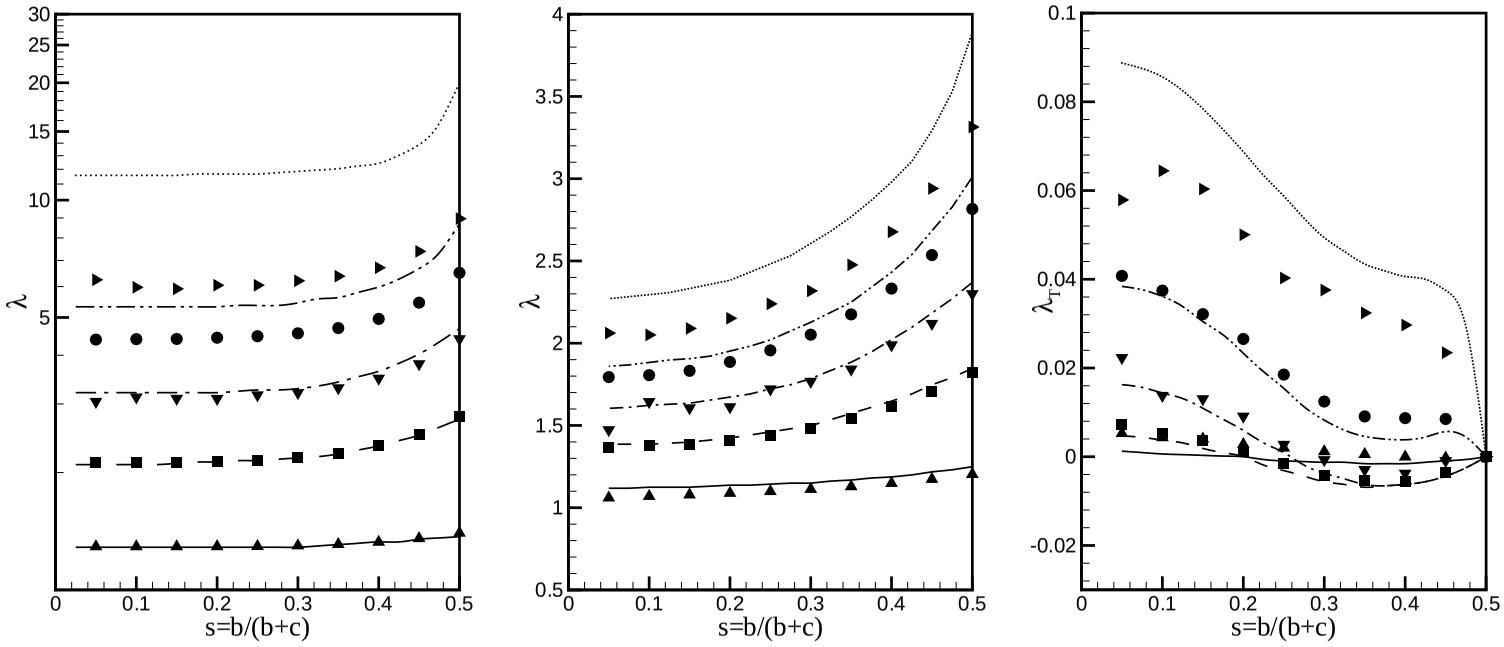

(a) λ Perpendicular Motion

(b) λ Parallel Motion

(c) λ_T Parallel Motion

Figure 17. Correction factor for a sphere moving parallel or perpendicular to the walls in channel with constant velocity. The lines denote result from Ganatos et al. and symbols denote our results. (▲) and (-) $b/a = 5.0$; (■) and (− − −) $b/a = 2.0$; (▼) and (− · −) $b/a = 1.5$; (●) and (− ·· −) $b/a = 1.25$; (▶) and (· · ·) $b/a = 1.1$.

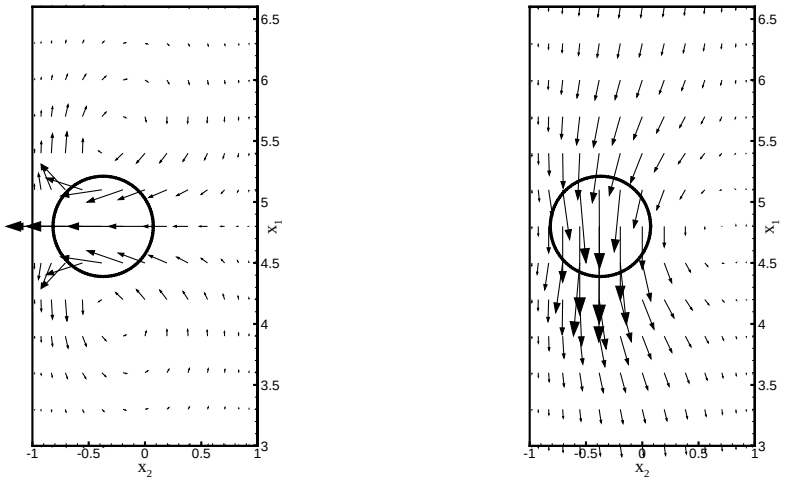

(a) Perpendicular Motion

(b) Parallel Motion

Figure 18. Vector plot of velocity fields for a sphere moving parallel or perpendicular to the walls in channel. The walls are placed at $x_2 = \pm 1$, the sphere relative radius is $b/a = 1.5$ and the position is $s = 0.3$.

solved,

$$\begin{aligned} V_i &= A'_{ij}F_j + B'_{ij}T_j, \\ \Omega_i &= C'_{ij}F_j + D'_{ij}T_j, \end{aligned}$$

i.e. the velocity and angular velocity are determined from a given force and/or torque. Since the Stokes flow is linear these problems are the inverse of each other and therefore the mobility problem may be inverted to give the restistance problem. Solving the mobility problem for a given force and no torque will give the coefficients A'_{ij} and C'_{ij} and solving the mobility problem with zero force and a given torque will give B'_{ij} and D'_{ij}. The force and torque in the case of a given velocity V_i of the sphere may then be computed from

$$V_i = A'_{ij}F_j + B'_{ij}T_j, \tag{74}$$

$$0 = C'_{ij}F_j + D'_{ij}T_j. \tag{75}$$

The correction factor λ is computed by balancing the force from (74) and (75) with the corrected Stokes drag (72). The torque coefficient λ_T is determined by matching the torque from (74) and (75) with the torque given in (73).

Values of λ and λ_T computed using both the force monopole and the force dipole for various sphere radii and positions in the channel are shown in figure 17. The results are shown as functions of the sphere position ($s = b/(b+c)$) and the relative distance to the wall (b/a). The lines denote results from Ganatos et al. (1980a+b).

The results for the perpendicular motion in figure 17(a) shows good agreement for values $b/a > 1.25$, when the sphere is not too close to the wall. Closer to the wall ($b/a < 1.25$) lubrication effects become important and higher order terms than the monopole and the dipole are needed in order to include these effects. The flow field is shown as a vector plot in figure 18(a). The moving sphere creates a ring shaped recirculating zone, where it drags fluid with it from the top and

pushes fluid away at the bottom. The vector plot is very similar to that given by Ganatos et al. (1980a).

The computed λ for the parallel motion is shown in figure 17(b). Again the computed drag coefficient is in good agreement with the exact values for distances $b/a > 1.25$. Similarly the discrepancy between the computed values and the exact values become larger closer to the wall, although the difference is much smaller than for the perpendicular motion in figure 17(a). The reason is, that to the first order the lubrication forces for a sphere moving perpendicular to the wall are $F_{lub} \sim (b/a - 1)^{-1}$, while for parallel motion they are $F_{lub} \sim \ln(b/a - 1)$ (Kim & Karrila (1991)). Therefore the lubrication forces are much weaker in the parallel motion, and the force monopole and force dipole are more able to resolve the flow. The computed values of torque coeffient λ_T are shown in figure 17(c). The comparision with the exact values by Ganatos et al. (1980b) leads to a conclusion similar to that for λ. For distances $b/a > 1.25$ the force coupling method works fine, but closer to the wall lubrication effects are important and the force coupling method predicts a lower value of the coefficient. A vector plot of the flow field is shown in figure 18(b). The moving sphere creates a recirculation zone between itself and the opposite wall, because the sphere drags fluid with it as it moves. The vector plot is similar to that given by Ganatos et al. (1980b).

The examples given in this section are described more extensively in Lomholt & Maxey (2001a), which also contains a comparision between results using only the force monopole and using both the force monopole and the force dipole. Furthermore, it contains results on a steady rotating sphere between two walls and s pshere rigidly held in a Poiseuille flow.

5 Particle Motion in a Channel at Finite Reynolds Numbers

The force coupling method described in the previous chapter was derived under Stokes flow conditions. Although some applications of Stokes flow exists, omission of the nonlinear terms is very restrictive. As we have seen in chapter 3, the inclusion of the nonlinear terms leads to effects such as lift forces due to the presence of a wall or shear in the carrying flow, and to the drafting, kissing and tumbling interaction between two particles. Even at low but finite Reynolds numbers, these effects are present and in order to compute particle motion accurately, they must be considered. Therefore it is of importance to investigate the applicability of the force coupling method at finite Reynolds numbers.

Maxey and Dent (1998) performed some investigations of particle sedimentation at finite Reynolds numbers using the force coupling method in an infinite volume of fluid. They neglected the particle inertia and considered only the gravitational force on the particles. Furthermore no force dipole was included. The results of Maxey and Dent (1998) showed qualitative agreement with the physics of particle sedimentation, but they also reveal some of the problems with the method. Firstly, there was no repulsion force to keep the particles separated and particle overlapping was observed. Secondly, the values of the scale ratios a/σ and a/σ_D may cause a problem, because at finite Reynolds numbers the Stokes values may no longer be valid. On the other hand, Dent (2000) has shown that the ratio for the force monopole is appropriate at finite Reynolds numbers up to $Re_p = 20$. This may be true for the scale ratio for the force dipole as well.

Dent (2000) and Dent & Maxey (2000) considered settling of a fixed cubic array of spheres at finite Reynolds numbers. They compared results obtained using the force coupling method with results from a direct simulation using a spectral element method. In the force coupling method they included only a force monopole. Their results show that for this problem, the force coupling model performs well for Reynolds numbers up to $Re_p = 20$.

Since the typical microflows described in chapter 2 are wall bounded shear flows, the force coupling method must be examined with respect to the effect of walls and shear flows. This is the main subject of this chapter. The force coupling method for finite Reynolds numbers and the numerical implementation are described in section 5.1. The numerical results for various cases of sedimenting particles will be compared with experimental results. The experiments were performed by B. Stenum in collaboration with the author at Optics and Fluid Dynamics Department (OFD) at Risø National Laboratory. The experimental setup is described in section 5.2. In the remaining part of the chapter various examples of particle dynamics computed using the force coupling method are described.

5.1 The Force Coupling Method for Finite Reynolds Numbers

The force coupling method for Stokes flow described in chapter 4 is easily generalized to include the fluid inertia terms. The inertia terms are simply added to the Stokes equations. Including the force monopole and the force dipole, the force coupling equations for N particles dispersed in a fluid at finite Reynolds numbers consist of the continuity equation

$$\frac{\partial u_i}{\partial x_i} = 0 \ , \tag{76}$$

and the momentum equation

$$\begin{aligned}\frac{\partial u_i}{\partial t} + u_j \frac{\partial u_i}{\partial x_j} = &- \frac{1}{\rho_f}\frac{\partial p}{\partial x_i} + \nu \frac{\partial^2 u_i}{\partial x_j \partial x_j} \\ &+ \frac{1}{\rho_f}\sum_{n=0}^{N}\left(F_i^n \Delta\left(\mathbf{x} - \mathbf{Y^n}, \sigma\right) + F_{ij}^n \frac{\partial \Delta\left(\mathbf{x} - \mathbf{Y^n}, \sigma\right)}{\partial x_j}\right) \ .\end{aligned} \tag{77}$$

Although fluid inertia is included, particle inertia is still neglected. This means that the relaxation time of the particle to changes in the body forces or the hydrodynamic force is very small. The force monopole strength is therefore given by the buoyancy force on the particle

$$F_i^n = \left(m_p^n - m_f^n\right) g_i \ .$$

The force dipole strength is given by (4.3), i.e.

$$F_{ij}^n = \rho_f \nu \mathrm{V}_p^n \left(5 E_{ij}^{*\,n} + 3\Omega_{ij}^n\right) \ .$$

The iterative computation of the force dipole strength components related to the rate of strain, E_{ij}^*, are computed using the iterative method decribed on page 52 in chapter 4 and Appendix B.2. The components related to the external torque, Ω_{ij}, are computed using $\Omega_{ij} = \varepsilon_{ijk}\Omega_k^p$, where Ω_k^p is the angular velocity due to the external torque. Based on the results by Dent (2000), we choose the length scale ratios between the particle radius a and the length scale in the envelope function (σ or σ_D), to be the Stokes values, i.e.

$$\frac{a}{\sigma} = \sqrt{\pi} \qquad \text{and} \qquad \frac{a}{\sigma_D} = \sqrt[3]{6\sqrt{\pi}} \ .$$

The particle velocity and angular velocity are determined using the volume averaged method, i.e.

$$\begin{aligned} V_i^n(t) &= \int u_i(\mathbf{x}, t)\, \Delta\left(\mathbf{x} - \mathbf{Y^n}, \sigma\right) d^3\mathbf{x} \\ \Omega_i^n(t) &= \int \frac{1}{2}\omega_i(\mathbf{x}, t)\, \Delta\left(\mathbf{x} - \mathbf{Y^n}, \sigma_D\right) d^3\mathbf{x} \ . \end{aligned}$$

The integrations are performed over the whole domain. The particle positions $Y_i^n(t)$ are determined by integration of the particle velocity.

The Numerical Method

As already mentioned in section 4.4 the force coupling equations given by (76) and (77) are solved numerically in a channel with periodic boundary conditions in the streamwise (x_1) and the spanwise (x_3) directions, and no-slip boundary conditions in the normal direction (x_2). The computational geometry is shown in figure 19.

In order to facilitate the numerical solution of equations (76) and (77), these are non-dimensionalized by a characteristic length scale L, a characteristic velocity scale U and a characteristic time scale $T = L/U$. The continuity equation is the same as (76) with the dimensional variables replaced by the non-dimensional variables. The non-dimensional momentum equations are

$$\begin{aligned}\frac{\partial \hat{u}_i}{\partial \hat{t}} + u_j \frac{\partial \hat{u}_i}{\partial \hat{x}_j} = &- \frac{\partial \hat{p}}{\partial \hat{x}_i} + \frac{1}{Re}\frac{\partial^2 \hat{u}_i}{\partial \hat{x}_j \partial \hat{x}_j} \\ &+ \sum_{n=0}^{N}\left(\hat{F}_i^n \hat{\Delta}\left(\mathbf{x} - \mathbf{Y^n}, \sigma\right) + \hat{F}_{ij}^n \frac{\partial \hat{\Delta}\left(\mathbf{x} - \mathbf{Y^n}, \sigma\right)}{\partial x_j}\right) \ ,\end{aligned} \tag{78}$$

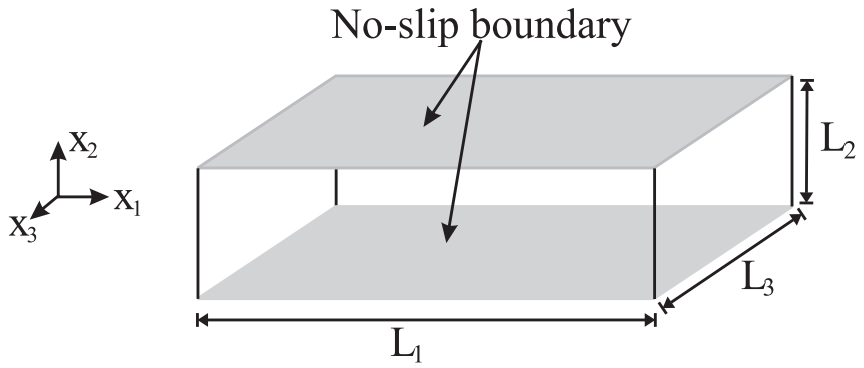

Figure 19. Computational domain and coordinate system

where $\hat{}$ denotes non-dimensional variables and $Re = LU/\nu$. The non-dimensional force monopole strength is

$$\hat{F}_i^n = \left(\frac{\rho_p^n}{\rho_f} - 1\right) \hat{\mathrm{V}}_p^n Fr_i \ ,$$

where $\hat{\mathrm{V}}_p^n$ is the non-dimensional volume of particle n and

$$Fr_i = \frac{L}{U^2} g_i \ ,$$

is a Froude number. The non-dimensional force dipole strength is

$$\hat{F}_{ij}^n = \frac{\hat{\mathrm{V}}_p^n}{Re} \left(5\hat{E^*}_{ij}^n + 3\hat{\Omega}_{ij}^n\right) \ .$$

These equations are solved using a spectral method with Fourier expansions in the spanwise and the streamwise directions, and Chebyshev polynomials in the normal direction. The original code was obtained from R. Handler (Handler et al. (1993)). The program has been modified to include the force coupling terms in equation (78) and the particle tracking. The iterative method needed for the force dipole term resulted in changing the time integration from a second order semi-implicit Adam-Bashforth/Crank-Nicholson method to a fully implicit second order Backward Difference Method (BDF). Other time integration methods were also tested. These included predictor-corrector schemes based on Adam-Bashforth/Adam-Moulton methods, implicit Stiffly-Stable schemes and a third order BDF method. The second order BDF method was chosen, because it was the most efficient and accurate of the second order methods. Compared with the third order methods it was more efficient. Descriptions of these timestepping methods can be found in Schwarz (1993).

The particle trajectories are computed using an explicit third order Adam-Bashforth method. The explicit method made it possible to compute the new particle positions, before the solution to the flow field was determined. This choice was made in order to avoid recomputing the particle positions in the iterations. Recomputing the particle positions would result in recomputing the envelope functions, which may be time consuming if many particles are present.

The iteration concerning the force dipole term was continued until the components of $\tilde{E}_{ij,n}$ from equation 56 on page 51 are below a certain accuracy ϵ, i.e. the iteration ends if

$$\left|\left|\tilde{E}_{ij,n}\right|\right|^2 = \sum_i \sum_j \tilde{E}_{ij,n}^2 < \epsilon \qquad \text{for all } n \ ,$$

or until a certain number of iterations is reached (avoid infinite looping). The limit for the iteration was set to 10^{-3} or 10^{-4}, and the maximum number of iterations

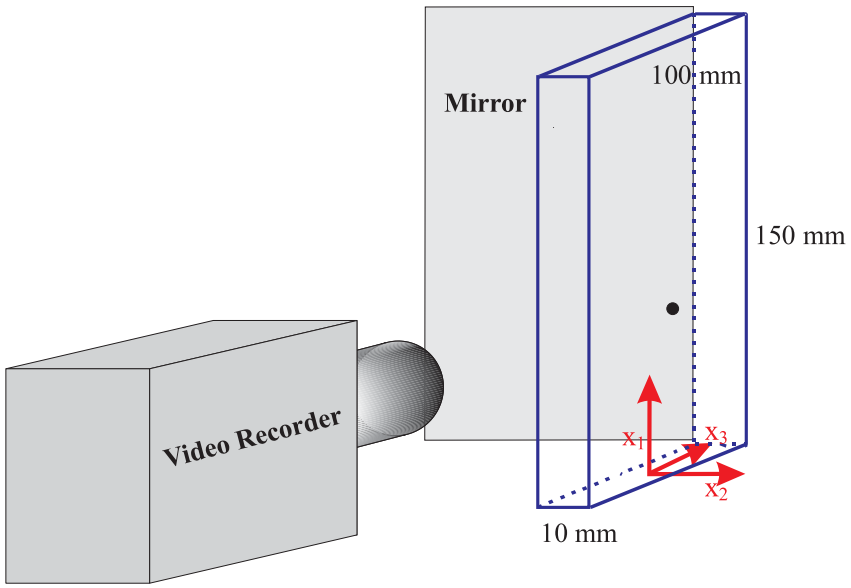

Figure 20. Experimental Setup

was set to twenty. It should be emphasized that in each iterative step the whole flow field, including the forcing from the particles, is solved. The complete solution method is described more carefully in Appendix B, which also contains a section with comments on the simulations and some advice on how to actually do the computations.

5.2 Experimental Setup

For some of the examples of particle sedimentation presented in this chapter, the numerical results will be compared with experiments. The setup for these experiments is shown in figure 20. It was designed by B. Stenum, B. Sass, and the author. The setup consists of a rectangular channel made in transparent PVC with height $L_1 = 150$mm, width $L_2 = 10$mm, and depth $L_3 = 100$mm. Thus, the aspect ratio of the channel is $L_3/L_2 = 10$. The numerical model described above is therefore a good approximation for particles moving in the center part ($40\text{mm} < x_3 < 60\text{mm}$) of the channel. The fluid was a mixture of glycerol and water in order to keep the viscosity high enough to obtain low Reynolds numbers ($Re_p < 10$). The particles were polyamid spheres with a radius of $a = 1$mm, thus the ratio of particle radius to channel width was $a/L_2 = 0.1$. The particles were introduced into the channel through five small holes in the bottom, and since the density of the polymer particles was smaller than the fluid density, the particles moved upwards toward the top of the channel.

The motion of the particles was recorded by a standard CCD camera placed in front of the channel. Therefore the motion in the x_1x_2 plane is captured immediately. The motion in the x_1x_3 plane is captured using a mirror placed on the left side of the channel at an angle of 45^0. The single video camera captures the motion in both directions with 25 whole frames pr. second. The movie is saved either on video tape or directly to a harddisk. The particle trajectories are determined afterwards using the tracking software DigImage (Dalziel (1992)). The particle positions were determined as the weighted average of the intensities from the bright particle. In this way the positions were determined with an accuracy better than 0.1mm. DigImage also computes the particle velocities from the time dependent

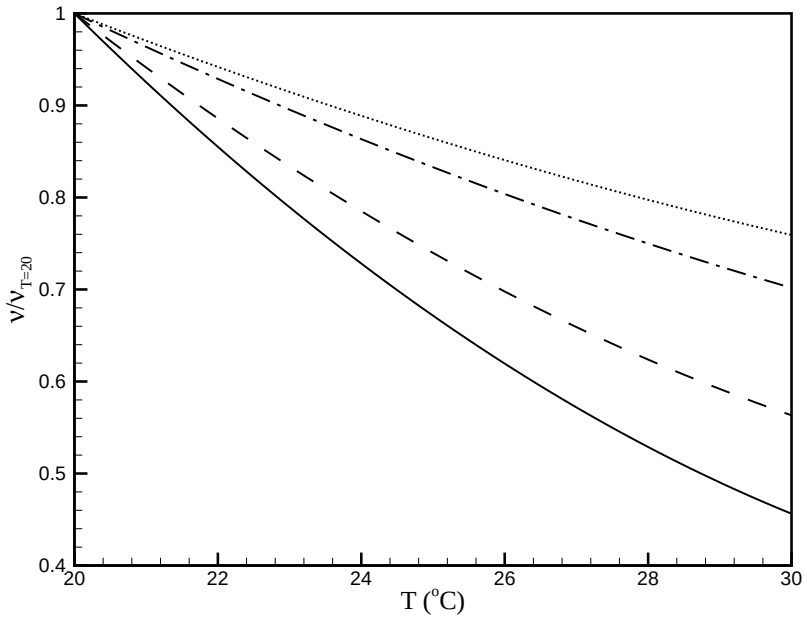

Figure 21. Temperature dependency of various aqueous glycerol solutions. The viscosity has been normalized with the value at $T = 20^oC$. The data are from Kaye & Laby. $(-)$ $\rho_f = 1.249$, $(- \ -)$ $\rho_f = 1.209$, $(- \ \cdot \ -)$ $\rho_f = 1.127$, *and* $(\cdots)$ $\rho_f = 1.061$.

trajectories. The error on the results for the particle position are ± 0.1mm and for the particle velocities it is ± 0.1mm/s.

The viscosity of glycerol solutions exhibit a strong sensitivity to temperature changes. Examples of the temperature dependence of various aqueous glycerol solutions are shown in figure 21, where the viscosity is shown as a function of the temperature. The figure shows that a temperature change of a few degrees may result in a relatively large change in the viscosity. Several techniques were tried to measure the viscosity directly, but this proved difficult due to the temperature sensitivity. Determining the viscosity prior or after the experiment typically resulted in a estimated value, that was either too large or too small due to temperature variations.

In the end the actual value of the viscosity was determined from the numerical computations by matching the computed velocities with the experimental velocities (best fit). The experiment at low Reynolds number with a single sphere satisfied the conditions for Stokes flow, and so a comparison could be made with the analytical results given by Happel & Brenner (1965) for the streamwise velocity of the sphere moving in the center plane between two infinite walls. The viscosity determined by the matching procedure and by comparison with the analytical results agreed to within 2.5 %.

Another problem is the tracking when two or more particles are present. Using the method described above, the particles are projected onto the x_1x_2 plane or the x_1x_3 plane. In these projections two particles will overlap, if the distance between their centers in one direction is smaller than the particle diameter. This overlap makes it impossible to track each particle by themselves, because they become indistinguishable from each other resulting in the missing experimental values in experiments with more than one particle.

5.3 Single Particle

The first and the simplest case of particle motion in a channel is a single sphere falling or rising due to buoyancy. In the following, three examples will be considered. The first is a sphere rising in an inclined channel, where the computed trajectories and velocities are compared with our own experimental results. The other two examples are a sphere falling either perpendicular or parallel to the walls. In these two cases some of the simulations will be compared with experiments from Gondret et al. (1999) and Feng et al. (1994a), respectively.

Experimental and Numerical Results in an Inclined Channel

The investigations presented in this section were initiated in order to see if the force coupling method was able to reproduce trajectories and velocities of a real particle. Furthermore, the inclination of the channel made it possible to study the effect of the wall, since the sphere will move across the channel toward one of the walls. The experiments were performed with the channel tilted an angle θ from vertical (the top of the channel is moved to the left). The experimental data are given in table 6.

The Reynolds number Re_p^{Stokes} based on the Stokes settling velocity W is determined as

$$Re_p^{Stokes} = \frac{2aW}{\nu} = \frac{2a}{\nu}\left|\frac{2a^2}{9\mu}\left(\rho_p - \rho_f\right)g\right| = \frac{4a^3}{9\nu^2}\left|\frac{\rho_p}{\rho_f} - 1\right| g \ ,$$

where $g = 9.82\text{m/s}^2$ is the absolute value of the gravitational acceleration. The particle Reynolds number Re_p^{max} is based on the maximum velocity of the sphere in the streamwise direction, i.e.

$$Re_p^{max} = \frac{2a\left|V_1^{max}\right|}{\nu} \ . \tag{79}$$

Values of some of the important parameters used for the simulations are given in table 7. The characteristic length was set to $L = L_2 = 10\text{mm}$ and the characteristic velocity to $U = 10\text{mm/s}$. The nondimensional radius of the particle was $a = 0.1$.

For all the results presented in this section, the figures will have the following common format. The particle trajectory is shown in subfigure (a), while the streamwise and the normal particle velocities are shown in subfigures (b) and (c), respectively. The positions and velocities are given in the frame of the experimental channel in mm and mm/s. The full drawn line shows the computational results with both the monopole and the dipole terms, while the dotted line denotes results from using the force monopole only. The experimental results are shown as (•). The straight upward line drawn at $x_2 = 4$ indicates the wall, i.e. when the center of the sphere is at $x_2 = 4$ the particle touches the wall. The straight line shown as dash-dot-dot in the figures corresponds to the direction of gravity in the frame of the channel.

Exp. no.	ρ_f (g/cm^3)	ρ_p (g/cm^3)	θ (^{0})	ν (mm^2/s)	Re_p^{Stokes}	Re_p^{max}
1	1.237	1.081	11.15	172.7	0.019	0.015
2	1.222	1.081	8.08	95.24	0.056	0.044
3	1.180	1.081	8.08	18.52	1.07	0.84
4	1.115	1.081	8.23	3.125	13.6	7.9

Table 6. Experimental values for a single particle rising in an inclined channel.

Exp. no.	$L_1 \times L_2 \times L_3$	$N_1 \times N_2 \times N_3$	δt	$Re = \frac{L_2 U}{\nu}$	$Fr = \frac{gL_2}{U^2}$
1	$10 \times 1 \times 8$	$64 \times 32 \times 48$	0.10	0.58	982.0
2	$5 \times 1 \times 4$	$64 \times 32 \times 48$	0.02	1.05	982.0
3	$5 \times 1 \times 4$	$64 \times 32 \times 48$	0.02	5.40	982.0
4	$5 \times 1 \times 4$	$64 \times 32 \times 48$	0.01	32.0	982.0

Table 7. Computational parameters for the single particle rising in an inclined channel. The characteristic length $L = L_2 = 10mm$ and the characteristic velocity $U = 10mm/s$.

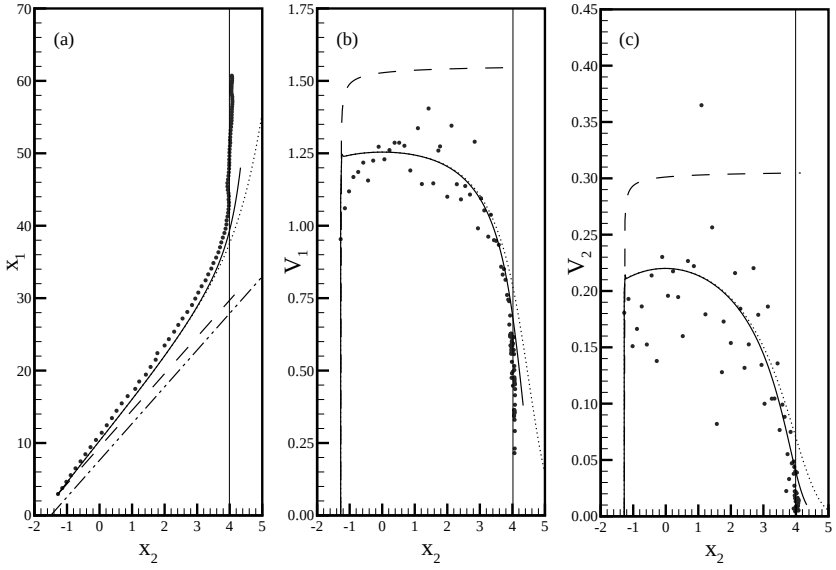

Figure 22. Comparision of experimental and computed particle trajectory (a) and velocities ((b) upward and (c) lateral) in an inclined channel for $Re_p^{max} = 0.0145$. (•) Experiment, (-) FCM with both force terms, $(\cdots)$ FCM with only the monopole, and $(- -)$ trajectory computed using equation (15). The line $(- \cdots -)$ indicate the direction of gravity in the frame of the channel. The particle positions are given in mm and the velocities are in mm/s in the frame of the experimental setup.

In figure 22 the results for $Re_p^{max} = 0.0145$ are presented. In the central part of the channel the agreement between the computed and the experimental trajectories is good, although the slope of the computed trajectory is slightly smaller than the slope of the experimental trajectory. Closer to the wall ($x_2 > 3$) the computed trajectories deviate from the experimental, and the computational spheres moves through the wall ($x_2 > 4$). The reason is the lack of a fully resolved lubrication layer in the model. When the sphere approaches the wall, a lubrication layer builds up between the sphere and the wall. During this build up the viscous friction slows down the sphere and ultimately the lateral motion of the sphere is stopped (see also the next section on page 71). In the force coupling simulation, the lubrication layer is only fully resolved if all the higher order multipoles are added to the force coupling terms. Since only the force monopole and the force dipole are included, the sphere does not "feel" the full effect of the wall and continues through it. Neglecting the force dipole leads to a coarser representation of the flow field. Therefore the trajectory computed using only the force monopole deviates more from the experimental result, than the trajectory computed using both force coupling terms. This becomes even more evident in the two figures for the particle velocities ((b) and (c) in figure 22). In these figures the difference between the

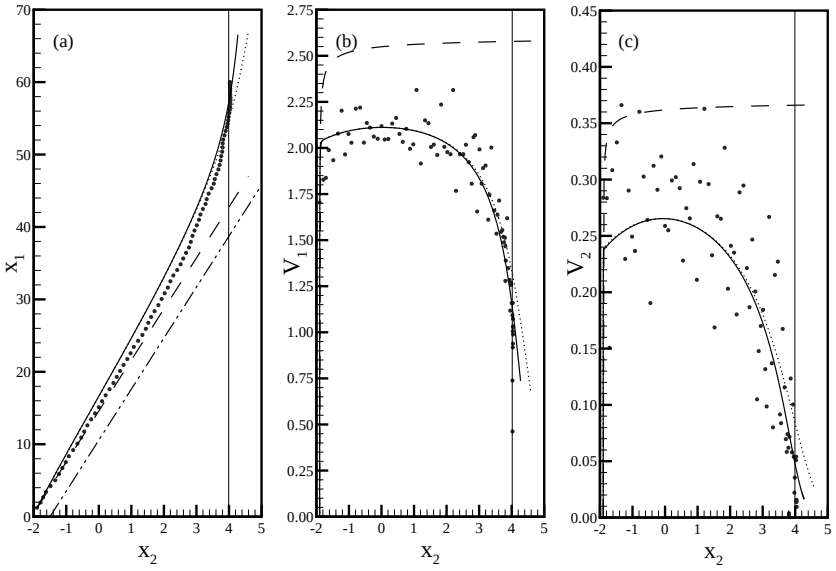

Figure 23. Comparision of experimental and computed particle trajectory (a) and velocities ((b) upward and (c) lateral) in an inclined channel for $Re_p^{max} = 0.044$. (•) Experiment, (-) FCM with both force terms, (· · ·) FCM with only the monopole, and (− −) trajectory computed using equation (15). The line (− · −) indicate the direction of gravity in the frame of the channel. The particle positions are given in mm and the velocities are in mm/s in the frame of the experimental setup.

two computed results appears, when the sphere is about one radius away from the wall ($x_2 = 3$). A comparision between the computed velocities and the experimental velocities is more difficult, because of the scatter in the experimental data. The scatter is due to experimental uncertainties, since the velocities are small and therefore relatively difficult to measure. For example the normal velocity component is of the order of the limit for the experimental accuracy of about 0.1mm/s. Nevertheless, the agreement is reasonably good. The initial steep increase in the computed velocities, is due to the initial velocities of the computational spheres being zero. Since we compute the particle velocity from the fluid velocity field, resulting from the force the particle exerts on the fluid, it is not possible to specify an initial velocity of the particle. When the computational sphere is introduced, it will almost immediately attain the velocity of a sedimenting sphere. This is a result of neglecting the particle inertia. Therefore the curves in figures 22(b) and 22(c) initially appears as a step function, but they are continuous.

Figure 23 shows a comparision at $Re_p^{max} = 0.044$ and essentially the computed trajectory and velocities agree with the experimental results. However, in contrast to the slope of the computed trajectories in figure 22, the slope of the computed trajectories in figure 23 is sligthly larger than the slope of the experimental trajectories. The reason for this difference could be an error in the measured angle from the experiment. Another more plausible explanation may be, that it is not possible to specify the initial conditions for the velocities of the sphere correctly as explained above. This is observed from the figures of the upwards velocity (figures (b) in 22 and 23), where the computed velocity overshoots that observed experimentally. A similar effect (although smaller) is seen in the figures for the lateral velocity (figures (c) in 22 and 23).

The two examples presented above were both at Reynolds number small enough to be considered as approximations to Stokes flows. The results are consistent with the Stokes flow results, given at the end of chapter 4 for a single sphere moving

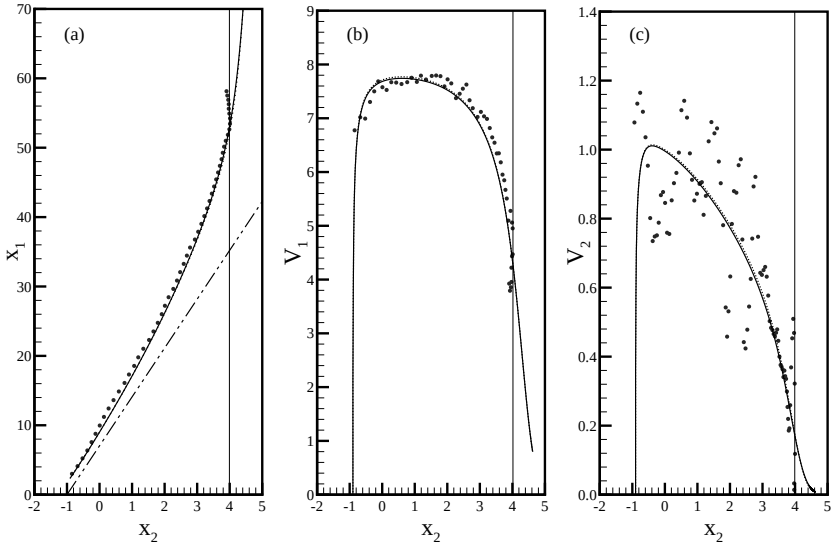

Figure 24. Comparision of experimental and computed particle trajectory (a) and velocities ((b) upward and (c) lateral) in an inclined channel for $Re_p^{max} = 0.84$. (•) Experiment, (-) FCM with both force terms, (· · ·) FCM with only the monopole. The line (— · ·—) indicate the direction of gravity in the frame of the channel. The particle positions are given in mm and the velocities are in mm/s in the frame of the experimental setup.

perpendicular or parallel to the channel walls. Namely, that for distances larger than the sphere radius the force coupling method performs very well, and it is able to reproduce the particle trajectories and velocities both qualitatively and quantitatively. For distances smaller than the sphere radius the lubrication forces are not negligible and as a result the discrepancy increases.

The dashed lines in figure 22 and figure 23 are the trajectories computed using equation (15) given by Maxey and Riley (1983). These trajectories are almost parallel to the line (dash-dot-dot) showing the direction of gravity. Consequently, the result from equation (15) is merely a balance between the Stokes drag and the buoyancy force, and the other force terms (Basset history and added mass) are negligible. Although the condition of a low particle Reynolds number is satisfied, the effect of the walls is completely lacking in the trajectories resulting from equation (15). This is clearly because equation (15) is based on the assumptions of a small particle being far from any other boundaries, and this condition is not fulfilled in this case. In the next two examples the Reynolds number is increased in order to examine the effect of the convective inertial terms.

The first higher Reynolds number example with $Re_p^{max} = 0.84$ is shown in figure 24. The first thing to notice is the very good agreement of the computed trajectory with the experimental trajectory. The trajectories are almost identical until the particle collides with the wall, where the computational particle continues its lateral motion through the wall. Comparing the normal particle velocities in figure 24(c) with those in figures 22(c) and 23(c) the profile of the velocity curve has sharpened, because of the larger maximum in the center of the channel. In figure 24, it is almost impossible to distinguish between the results for both force terms and the results for only the monopole. The effect of the force dipole for this particular example is therefore very small. Some explanation for this peculiarity can be found by comparing figures 22 through 24. In figure 22, the trajectory from the computation including only the force monopole, is placed to the left of the

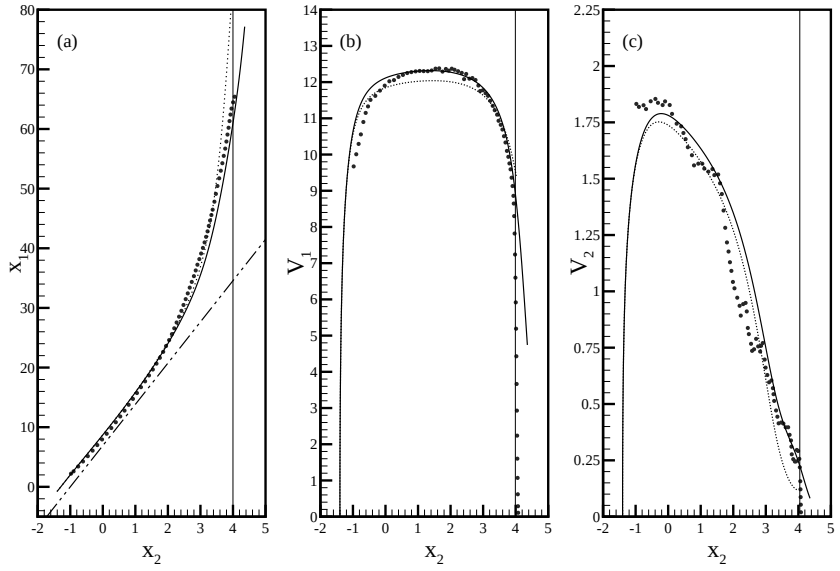

Figure 25. Comparision of experimental and computed particle trajectory (a) and velocities ((b) upward and (c) lateral) in an inclined channel for $Re_p^{max} = 7.9$. (•) Experiment, (-) FCM with both force terms, (· · ·) FCM with only the monopole. The line (— · ·—) indicate the direction of gravity in the frame of the channel. The particle positions are given in mm and the velocities are in mm/s in the frame of the experimental setup.

trajectory computed using both force terms. In the following figures 23 and 24, the monopole trajectory "moves" from the left to the right, i.e. it comes closer and closer to the trajectory obtained by including the force dipole. At an even higher Reynolds number shown in figure 25, the monopole trajectory is placed to the left of the trajectory obtained with both force terms. Therefore at some Reynolds number the two trajectories must be equal. It is interesting that this happens at a Reynolds number based on the Stokes settling velocity of about $Re_p^{Stokes} \approx 1$, since at this Reynolds number the viscous forces and the inertia forces are equal in magnitude. An explanantion of this have not been found.

The final example in this section is shown in figure 25. The particle Reynolds number for this case is $Re_p^{max} = 7.9$. Again the computed trajectories and velocities agree well with those observed experimentally. In contrast to the three previous examples the trajectory computed with both force terms is placed to the right of the result using only the force monopole. Furthermore, the difference between the two computations is larger than in the three previous examples. The velocities from the two computations differs not only near the wall, but also in the middle of the channel, where the result from the force monopole shows a lower velocity than that from both force terms. Therefore the computation with only the monopole also have a lower particle Reynolds number $Re_p^{max} = 7.7$ than the computation with both force terms and the experiment. The difference in the computed velocities is a result of the change in the rate of strain imposed by the force dipole. At small Reynolds numbers the rate of strain field was weak until the particle comes near the wall, but at larger Reynolds numbers the rate of strain field is significant also in the middle of the channel. Consequently, at this Reynolds number, the force dipole becomes important through out the channel. This leads to a different velocity field in the region of the particle and therefore to a different particle velocity. This may also explain the "movement" of the trajectory from left to right as discussed above.

Figures 24 and 25 show that near the wall, there is no large deviation of the computed trajectories from the experimental trajectories. Hence, for the higher Reynolds numbers the force coupling method performs well all the way to the wall. An explanation could be that the lubrication layer is much smaller, when the Reynolds number increases and therefore the particle must be closer to the wall before the higher order multipoles become important.

Sphere Moving Perpendicular to the Walls

In section 4.4 with Stokes flow examples, the case of a sphere moving perpendicular towards a wall was investigated. The conclusion was, that for wall to sphere distances larger than $1.25a$ the force coupling method gave good results. In this section the same case is examined, although in a slightly different manner. Referring to figure 16(b) on page 57 we will investigate a sphere falling from an initial position $b_0 = 0.75\,(c+b)$ at the top of the channel to the bottom, and compare the computed trajectories with trajectories from experiments performed by Gondret et al. (1999).

The parameters for the computations are given in tabel 8. The non-dimensional particle radius was $a = 0.1$ and the density ratio was $\rho_p/\rho_f = 2.0$. The particle Reynolds numbers are given by (79) with $|V_1^{max}|$ replaced by the maximum fall velocity $|V_2^{max}|$ the sphere obtains falling from the top to the bottom.

Trajectories computed with both force terms and with the force monopole only are shown in figure 26 at various particle Reynolds numbers. The trajectories are shown in the plane of the normalized distance to the wall, $(b-a)/a$, and the normalized time, $t\,|V_2^{max}|\,/a$. With these reduced variables, the trajectory far from the wall is a line of slope -1 also shown in figure 26. At a low particle Reynolds number the viscous forces are still able to dissipate away a considerable amount of the kinetic energy, and the sphere slows down as it approaches the wall (Gondret et al. (1999)). Therefore the trajectories deviate strongly from the line of slope -1. When the particle Reynolds number is increased, the viscous dissipation becomes weaker and the slowing down of the sphere diminishes. Hence, the trajectories for higher Re_p deviate less from the straight line. The main reason can be found in the balance between convection and diffusion. The time for convection of the sphere over the length h is $t_{con} = h/\,|V_2^{max}|$ and the time for diffusion of momentum over the same length is $t_{dif} = h^2\rho_f/\mu$. These time scales are equal at a critical distance that scales as $h/2a = 1/Re_p$ (Gondret et al. (1999)), showing that the distance where the sphere feels the wall decreases as the particle Reynolds number increases. Figure 26 compares the trajectories computed using only the force monopole (dotted lines) with trajectories computed using both force terms (full lines). When the force dipole is included, the bottom wall has a stronger effect on the sphere for wall to sphere distances smaller than the sphere radius. This is consistent with previous results for Stokes flows (Lomholt & Maxey (2000a)). In agreement with the considerations above, the distance at which the sphere feels the wall becomes smaller with increasing Reynolds number.

Re_p	$L_1 \times L_2 \times L_3$	$N_1 \times N_2 \times N_3$	δt	$Re = \frac{L_2 U}{\nu}$	$Fr = \frac{gL_2}{U^2}$
0.40	$3 \times 2 \times 3$	$64 \times 96 \times 64$	0.01	10.5	9.82
0.66	$3 \times 2 \times 3$	$64 \times 96 \times 64$	0.01	13.5	9.82
2.20	$3 \times 2 \times 3$	$64 \times 96 \times 64$	0.01	26.0	9.82
5.00	$3 \times 2 \times 3$	$64 \times 96 \times 64$	0.005	42.0	9.82

Table 8. Computational parameters for the single particle falling perpendicular towards the bottom channel. The particle radius was $a/L_2 = 0.1$ and the density ratio was $\rho_p/\rho_f = 2.0$.

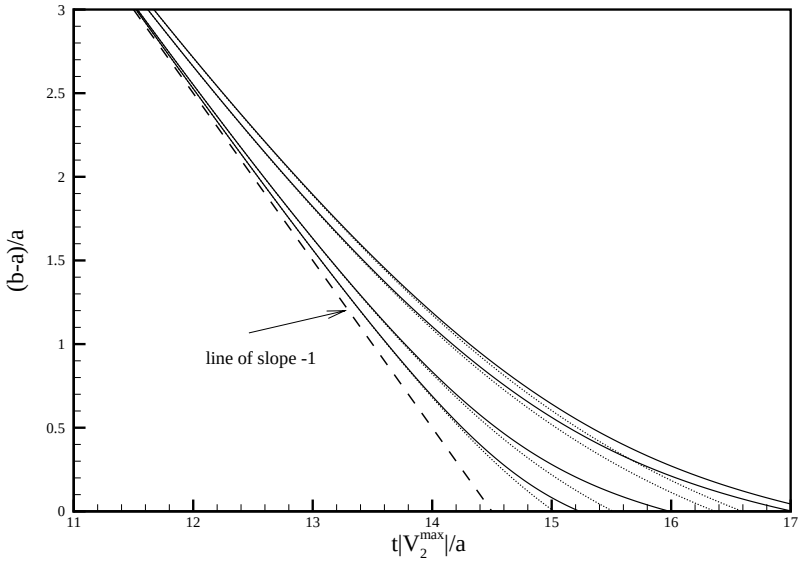

Figure 26. Comparision of trajectories for a sphere moving perpendicular towards the bottom computed with (full line) and without (dotted line) the force dipole for four Reynolds numbers. From right to left the particle Reynolds numbers are $Re_p^{max} = 0.40$*,* $Re_p^{max} = 0.66$*,* $Re_p^{max} = 2.20$*, and* $Re_p^{max} = 5.0$*.*

In figure 27 the trajectories from figure 26 are shown together with the experimental trajectories obtained by Gondret et al. (1999). The general agreement is good, but surprisingly the results with only the force monopole are better than the results with both force terms. This contradicts the comparisions between experiment and simulation for the inclined channel, and the results for the similar Stokes flow example. The origin for these unexpected results may be the difference in the setup between the experiment and the computations. Gondret et al. (1999) uses a rectangular vessel with dimensions far larger than the sphere radius, where the sphere moves from the open boundary at the top toward the wall at the bottom. Thus, in their experiments the sphere moves perpendicular to a basicly single wall. This is in contrast to the simulations, where the sphere moves perpendicular between two plane walls. This will increase the drag on the sphere and lead to a slower approach toward the wall in the computations. When only the force monopole is included, the wall effects are not as well represented as with both force terms, and the drag on the sphere will be less. This lack in the monopole results may balance the increase in the drag and result in a faster approach. Consequently, the force monopole results will agree better with the experiments than the results obtained with both force terms.

Sphere Moving Parallel to the Walls

In Stokes flow a sphere falling parallel to the walls will move along a straight line. Including the nonlinear convective terms results in a lateral lift force on the sphere, and it will move towards the center of the channel as discussed in chapter 3.4. The purpose of the examples presented in this section is to show that the wall lift is inherent in the force coupling method, because the particle velocity is computed directly from the disturbance flow created by the particle itself. The setup is similar to that shown in figure 16(a) on page 57.

The computational parameters used for these examples are shown in table 9. The particle Reynolds number is based on the final velocity of the sphere. Therefore

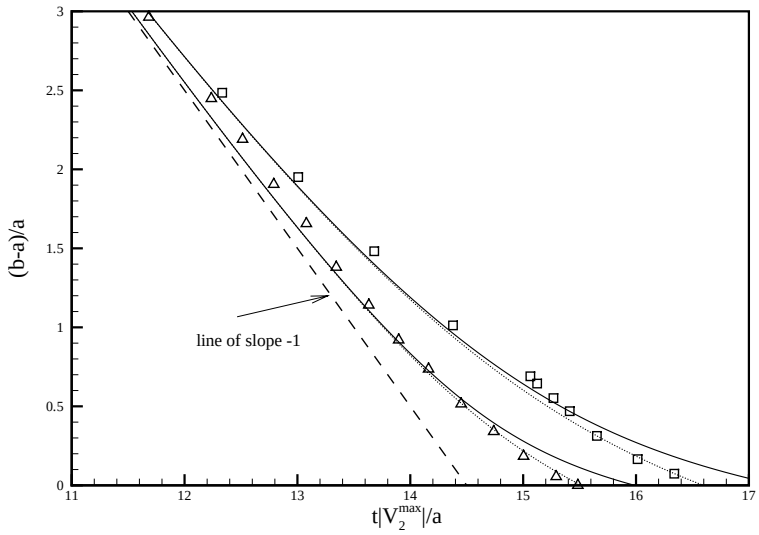

(a) $Re = 0.40$ (□) and $Re = 2.20$ (△)

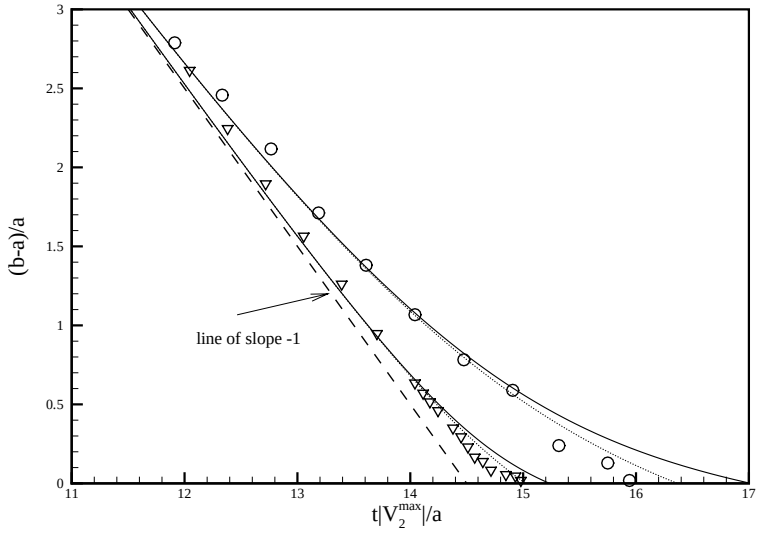

(b) $Re = 0.66$ (◯) and $Re = 5.0$ (▽)

Figure 27. Comparision of computed trajectories with experimental trajectories from Gondret et al. (1999) for Re = 0.40 (□), Re = 0.66 (◯), Re = 2.20 (△), and Re = 5.0 (▽). Full lines denote results with both force terms, while dotted lines denote results with the force monopole.

there is a difference between the particle Reynolds number found using both force terms and that found using only the monopole. This is due to the change in the rate of strain field imposed by the force dipole, as explained in the discussion of the results for the inclined channel at the high Reynolds number on page 70.

Figure 28 shows the first three cases. The channel walls are at $x_2 = \pm 1$. The sphere is initially placed at the wall with $Y_2 = -0.875$. Afterwards it falls vertically due to gravity. In all the cases the particle experiences a lateral lift force away from the wall toward the equilibrium position at the center plane between the channel

Re_p^D	Re_p^M	$L_1 \times L_2 \times L_3$	$N_1 \times N_2 \times N_3$	δt	ρ_p/ρ_f	$Fr = \frac{gL_2}{U^2}$
0.47	0.47	$6 \times 2 \times 3$	$96 \times 48 \times 48$	0.15	1.0705	9.82
0.88	0.88	$6 \times 2 \times 3$	$96 \times 48 \times 48$	0.10	1.1343	9.82
4.38	4.33	$6 \times 2 \times 3$	$96 \times 48 \times 48$	0.02	1.7745	9.82
8.10	7.94	$6 \times 2 \times 3$	$96 \times 48 \times 48$	0.02	2.6000	9.82

Table 9. Computational parameters for the single particle falling parallel to the walls. The particle radius was $a = 0.125$ and the Reynolds number was $Re = 30$.

walls. Besides the difference in the final velocity (for the high Reynolds numbers cases), including the force dipole results in a lower lift force at the beginning of the fall. Once the sphere is away from the wall, the trajectories for both force terms are very similar to those computed using the force monopole only. The difference between including the force dipole or not, diminishes as the particle Reynolds number increases. The reason for this lower lift force should probably be found in the initial vertical motion. In this part of the fall, the sphere in the force monopole results move faster than the sphere computed using both force terms. As shown in section 3.4 the lateral migration away from the wall is directly related to the velocity parallel to the wall, see equation (19). Consequently, the higher velocity of the sphere in the monopole result leads to the faster migration in the initial part of the fall.

A comparision with an experiment by Feng et al. (1994a) is shown in figure 29(a). Their experiment was performed in a channel with very high aspect ratio and the final particle Reynolds number was $Re_p = 7.85$. The two simulations both agree with the experiment. The main difference between the experiment and the simulations should probably be found in the initial motion very close to the wall. The initial conditions in the simulations are not exactly the same as in the experiment, and close to the wall the force coupling method does not resolve the flow, as explained previously. A close-up of the trajectories in the initial state of the motion is given in figure 29(b). The computed trajectories do not reproduce the fast initial motion away from the wall seen in the experiment for $x_1 < 3$. The reason is probably the lack of the lubrication forces, which assist the sphere in

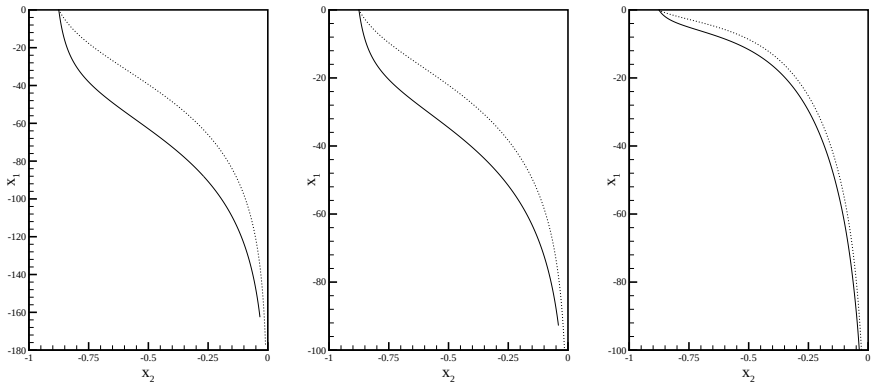

(a) $Re_p = 0.47$ (b) $Re_p = 0.88$ (c) $Re_p^M = 4.33$ and $Re_p^D = 4.38$

Figure 28. Trajectories for spheres falling parallel to the walls. Full lines denote results with both force terms, dotted lines denote results with only the force monopole. The walls are placed at $x_2 = \pm 1$, i.e. $x_2 = 0$ is the center plane of the channel.

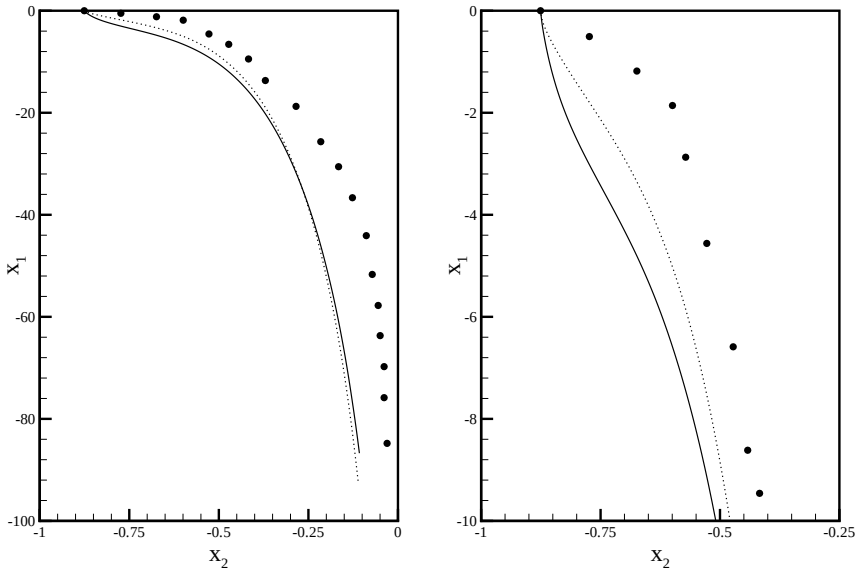

(a) Total trajectory

(b) Close up of trajectory near the wall

Figure 29. Comparision of computed trajectories with the experimental trajectory from Feng et al. (1994a). Full lines denote results with both force terms $Re_p^D = 8.10$*, dashed lines denote results with only the monopole* $Re_p^M = 7.94$*, (•) denotes the experiment by Feng et al. (1994a)* $Re_p = 7.85$*. The walls are placed at* $x_2 = \pm 1$*, i.e.* $x_2 = 0$ *is the center plane of the channel.*

moving away from the wall. The failure of reproducing the initial motion leads to the discrepancy observed for the whole trajectory. Nevertheless, the distance between the computed trajectories and the experimental trajectory is less than the radius of the sphere and qualitatively they agree well.

5.4 Dual Particle Interactions

An important feature of particulate flows is the interaction between particle pairs. Jayaweera et al. (1964) performed experiments in a rectangular tank on clusters of spheres with particle Reynolds numbers ranging from $Re_p = 10^{-4}$ up to $Re_p = 10$ and the number of particles varying from two to above seven. For particle pairs, they basically considered two initial configurations: one in which the two spheres were separated only vertically corresponding to $d_3 = d_2 = 0$ in figure 30, and one where the spheres are separated both vertically and horizontally corresponding to $d_3 = 0$ in figure 30. In the first configuration the trailing sphere accelerates into the wake of the leading sphere and tends to overtake it. Until the spheres collide no rotation is observed. After the collision the trailing sphere slides around the leading sphere. Finally, the spheres settle on the same horizontal line, rotate in opposite directions and separate laterally as they continue the fall.

Fortes et al. (1987) performed similar experiments at much higher Reynolds numbers ($Re_p \approx 700$). They observed the same process and named it drafting, kissing and tumbling (DKT). Drafting is the suction of the trailing sphere into the wake of the leading sphere, kissing is the collision, and tumbling is the sliding of the trailing sphere around the leading sphere. At the high Reynolds number that Fortes et al. (1987) performed their experiments the process could repeat

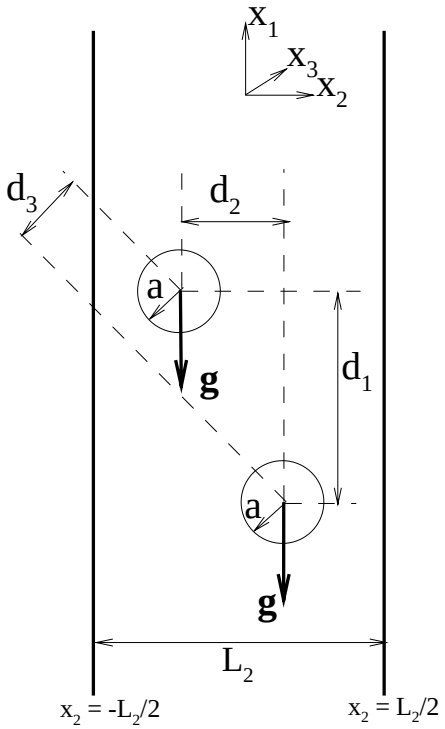

Figure 30. Settling of two particles with radius a initially separated with distance d_i in direction x_i. The walls are placed at $x_2 = \pm L_2/2$.

itself at high frequency. Johnson and Tezduyar (1996) have performed numerical experiments of multiple spheres falling in a liquid filled tube. Their results for a two sphere configuration corresponding to $d_3 = 0$ also showed the process of DKT, as already described for the experiments.

In this section experiments with two equal spheres rising in a vertical channel will be compared with numerical results from the force coupling model. The data from the experiments are given in table 10. Parameters from the simulations are given in table 11.

Exp. no.	a (mm)	ρ_f (g/cm^3)	ρ_p (g/cm^3)	ν (mm^2/s)	Re_p^{Stokes}
1	1.0	1.094	1.081	1.96	13.5
2	1.0	1.179	1.081	14.88	1.55

Table 10. Experimental values for a two particles rising in a channel.

Exp. no.	$L_1 \times L_2 \times L_3$	$N_1 \times N_2 \times N_3$	δt	$Re = \frac{L_2 U}{\nu}$	$Fr = \frac{gL_2}{U^2}$
1	$5 \times 1 \times 4$	$64 \times 32 \times 48$	0.03	51.0	982.0
2	$5 \times 1 \times 4$	$64 \times 32 \times 48$	0.01	6.72	982.0

Table 11. Computational parameters for the two particles rising in a channel. The characteristic length $L = L_2 = 10mm$ and the characteristic velocity $U = 10mm/s$.

First Experiment

The particle trajectories measured in the first experiment are shown in figure 31. The trajectories in the streamwise-normal directions are shown in figure 31(a) and the trajectories in the streamwise-spanwise directions are shown in figure 31(b). The particles are moving upwards. The symbol (▲) denotes the leading sphere and the symbol (●) denotes the trailing sphere. The first part of the figure ($x_1 < 73$) is the drafting period, where the trailing sphere moves faster than the leading sphere. As the trailing sphere approaches the leading sphere, it "pushes" the leading sphere aside. This is observed in both figure 31(a) and figure 31(b) for $60 < x_1 < 73$. Since the trailing sphere moves with a higher streamwise velocity than the leading sphere, the fluid between the two spheres will be accelerated in the direction from the trailing sphere toward the leading sphere. This acceleration causes the fluid to move faster than the leading sphere, thereby pushing it aside. The two spheres kiss at $x_1 \approx 73$. After the kiss, the trailing sphere tumbles around the leading sphere and they separate from each other. This result is consistent with the experiments of Jayaweera et al. (1964) and Fortes et al. (1987).

The trajectories from the corresponding simulation are shown as the lines in figure 31. The full drawn line is the trailing sphere and the dotted line is the leading sphere. The simulation agree qualitatively with the experiment. The discrepancy observed in figure 31(b) may result from a small error in the experimental values. In order to examine the reason for the discrepancy several experiments with a single rising sphere in the channel were performed. In these experiments the sphere was relased in the middle of the channel, and the trajectory of the single sphere was compared with a string hanging beside the channel. The sphere in these experiments tended to drift either to the left or to the right. In similar ex-

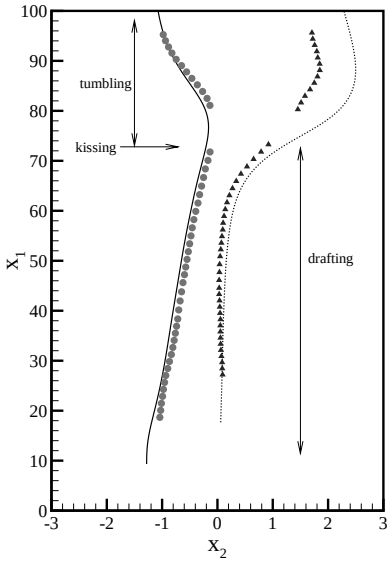

(a) Particle trajectories in the streamwise-normal directions

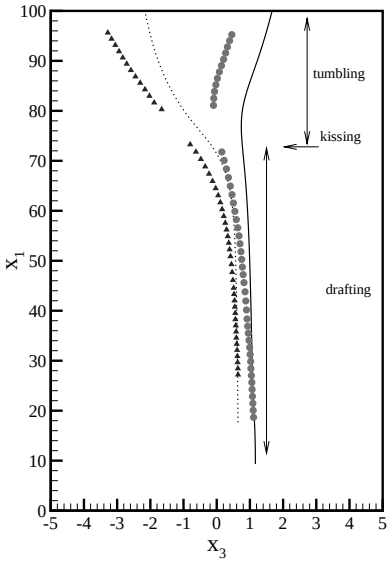

(b) Particle trajectories in the streamwise-spanwise directions

Figure 31. Comparision of computed and experimental particle trajectories for two particles rising for experiment number 1 in table 10. Symbols denote the experiment and lines denote the computation. The positions are given in mm in the frame of the experimental channel. The walls are at $x_2 = \pm 5mm$.

periments at lower Re the drift was significantly reduced. The reason for this drift is unknown, but it is probably the source for the discrepancy in figure 31(b). The difference between the simulation and the experiment seen in figure 31(a) results from the lack of lubrication forces in the simulation. When the two spheres come close together, lubrication effects become important and these are not included in the simulation.

Figure 32 shows a comparision of the particle velocities from the experiment with those from the simulation. The symbols denote the same spheres as in figure 31. The agreement is good, but two points should be noted. Firstly, the streamwise velocities in the simulation do not have the same maximum velocity as in the experiment. Further, there is a large difference in the computed streamwise velocities of the two spheres after the kiss. Therefore the trailing sphere overtakes the leading sphere. This is not the case in the experiment, where the two spheres settle on the same horizontal line and rise with equal streamwise velocity. Secondly, in the simulation the normal velocity of the leading sphere overshoots that observed experimentally. This is obviously related to the difference in the trajectories for the leading sphere seen in figure 31(a). The overshoot in the normal velocity and the difference in the streamwise velocities both results from the fact, that the interaction between the two spheres is not resolved completely.

The effect of the force dipole on the trajectories in experiment 1 is shown in figure 33. The figure compares trajectories computed using both force terms with trajectories computed using only the force monopole. Results obtained with both force terms are better than those obtained with only the force monopole. Neglecting the force dipole, results in different trajectories not only in the kissing process, but also in the drafting and tumbling processes. Therefore the force dipole is important through out the DKT-process.

In a previous investigation on two particle interaction using the force coupling method with the force monopole, Maxey & Dent (1998) found that the particles were overlapping each other before, during and after the kissing process. In order to examine overlap between the computational spheres in our example; the distance between the center of the spheres normalized with the diameter of the spheres is shown as function of time in figure 34. The horizontal line indicates where the distance between the sphere centers is equal to the diameter (the spheres touch). In the experiment the distance between the two spheres falls almost linearly with time until they kiss at $t \approx 8.5$s. The initial separation after the kiss appears to increase linearly until $t \approx 10.5$s, where the increase in the distance levels off. In the result obtained using only the force monopole, there is a considerable time of particle overlap. The two spheres overlap from $t = 7.8$s to $t = 9.1$s. On the other hand, in the result using both force terms, the two spheres do not actually kiss. Instead they begin to separate from each other, when the distance between their centers is about 1.3 times their diameter. Nevertheless, the distance from the result using both force term agrees qualitative better than the distance from the result using only the force monopole. Based on this and the results for the single sphere, we may conclude that including the force dipole term yields the best results and therefore only results with both force terms will be presented in the remaining part of the thesis.

Vector plots of the fluid velocity field at time $t = 7.88$s are shown in figure 35. The fluid velocity field is shown in the streamwise-normal plane at $x_3 = 0$ and in the streamwise-spanwise plane at $x_2 = 0$. The black circular areas are the cuts through the spheres in these planes. The difference in size is because the two spheres do not have the same x_3 and x_2 position. The pushing mechanism, described above for the experiment, is clearly seen in the vector plots. The flow around the leading sphere shows that the fluid is moving past the sphere. This faster moving fluid pushes the leading sphere aside, resulting in the increase in the

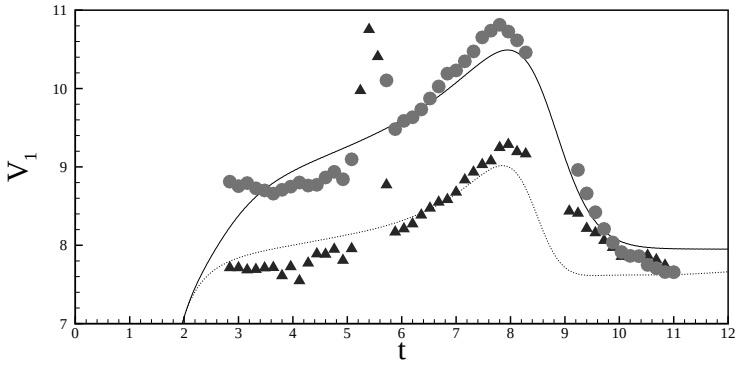

(a) Streamwise velocity

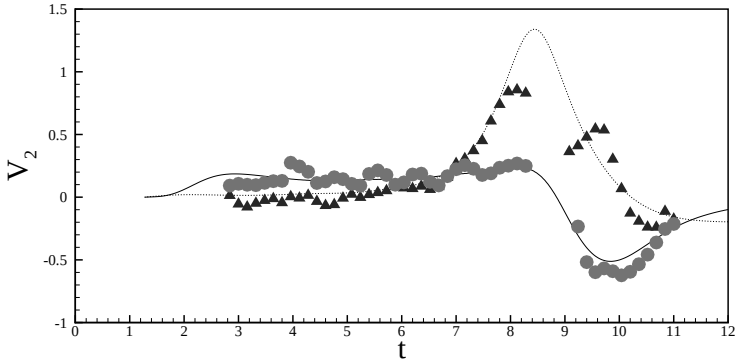

(b) Normal velocity

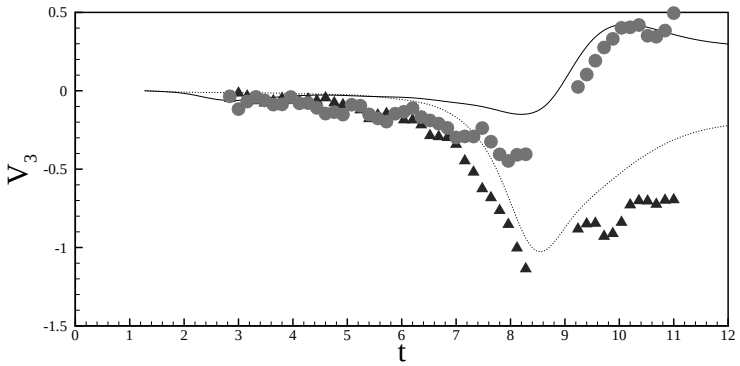

(c) Spanwise velocity

Figure 32. Comparision of computed and experimental particle velocities for two particles rising for experiment number 1 in table 10. Symbols denote the experiment and lines denote the computation. The velocities are given in mm/s in the frame of the channel and time is in seconds.

normal and the spanwise velocities of the leading sphere seen in figure 32. On the other hand, the flow around the trailing sphere shows very little influence of the leading sphere, and it is similar to that in figure 18(b) for a Stokes sphere settling vertically in a channel. Therefore the trailing sphere moves in a more straight line

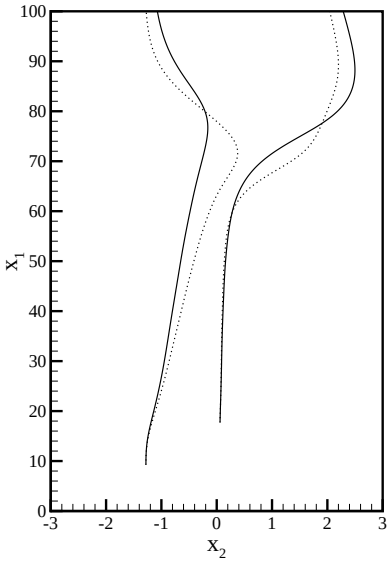

(a) Particle trajectories in the streamwise-normal directions

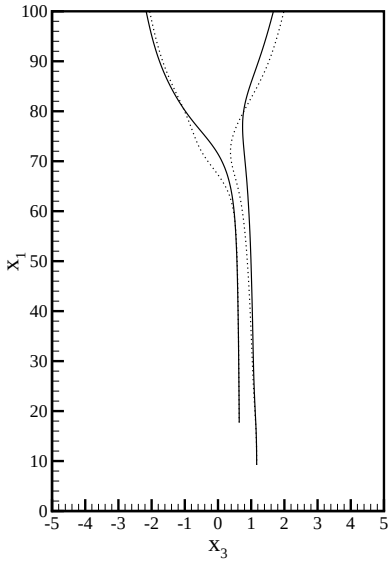

(b) Particle trajectories in the streamwise-spanwise directions

Figure 33. Comparision of particle trajectories for two particles rising computed using both force terms (full lines) and only using the force monopole (dotted lines). The example corresponds to experiment number 1 in table 10. The walls are at $x_2 = \pm 5mm$.

than the leading sphere, as observed in the trajectories in figure 31. However, due to the wake of the leading sphere, the trailing sphere moves into a fluid flow already moving in the direction of the sphere. Therefore the acceleration that the trailing must provide to the surrounding fluid is diminished. This cause the drag on the trailing sphere to be lower and consequently it moves with a higher streamwise velocity than the leading sphere, as observed in figure 32.

The velocity field for $t = 8.48$s, when the two spheres kiss, is shown in figure 36. Figure 36(a) shows the velocity field in the streamwise-normal plane at $x_3 = 0$, and figure 36(b) shows the velocity field in the streamwise-spanwise plane at $x_2 = 0.64$ (midway between the two spheres). The vector plots show the same features of the flow as in figure 35. The flow around the leading sphere is still very influenced of the flow induced by the trailing sphere. The direction of the flow around the leading sphere illustrates that, the trailing sphere is still pushing the leading sphere aside as seen in the trajectories in figure 31.

The velocity field after the kiss at time $t = 9.08$s is given in figure 37. The velocity field in the streamwise-normal plane at $x_2 = 0$ is shown in figure 37(a), and the velocity field in the streamwise-spanwise plane through the center of the trailing sphere ($x_2 = -0.183$) is shown in figure 37(b). At this time the flow around the trailing sphere has changed considerably. First consider figure 37(a). Due to the presence of the leading sphere, the flow to the right of the trailing sphere is stronger than the flow to the left. This makes the trailing sphere move to the left as observed in the trajectory in figure 31(a) and the normal velocity in figure 32(b). In figure 37(b) the flow is stronger on the left side of the sphere, forcing the sphere to the right as seen in figure 31(b). These changes in the fluid flow indicate, that the pushing mechanism changes direction when the trailing sphere has reached the leading sphere. Before the kiss, the trailing sphere was pushing

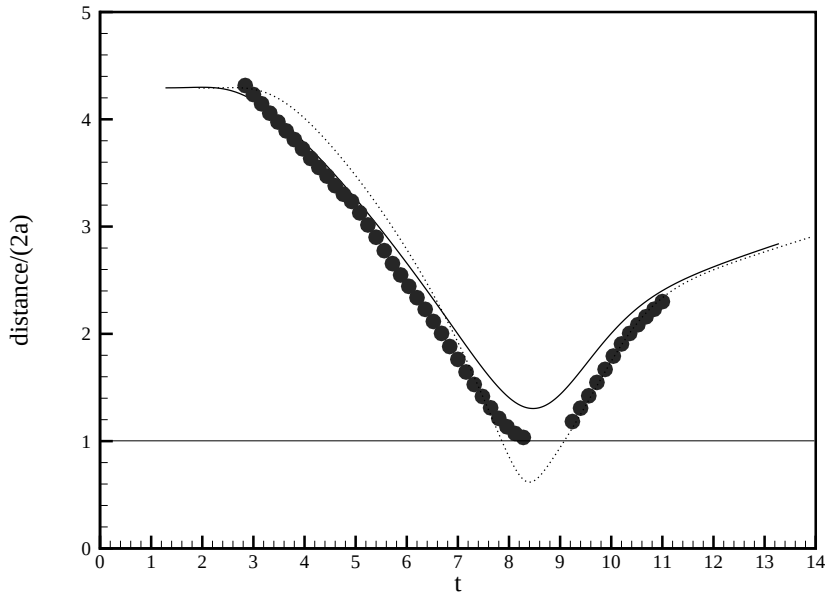

Figure 34. Distance between the particles as function of time for experiment number 1. (•) Experiment, (−) both force terms, and (· · ·) only the force monopole. Time is in seconds.

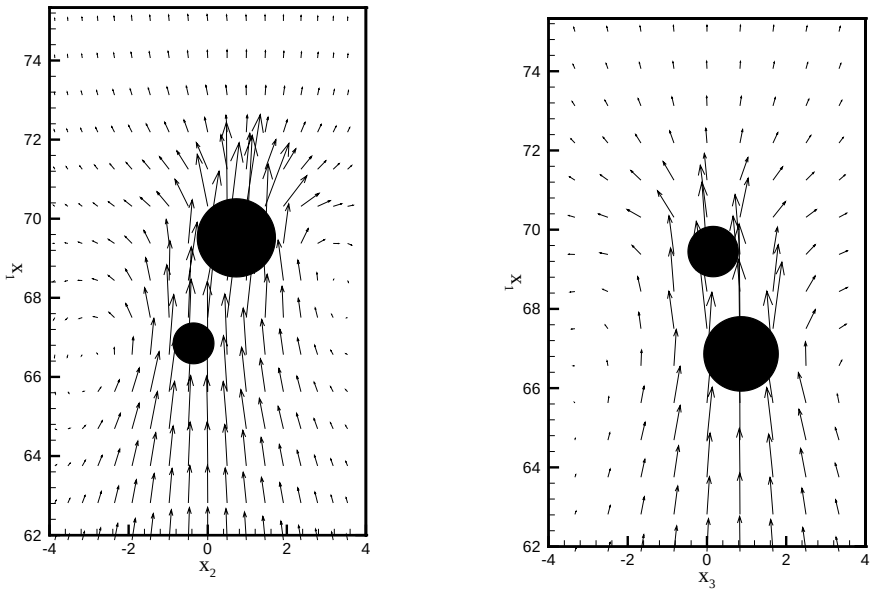

(a) Plane through $x_3 = 0$

(b) Plane through $x_2 = 0$

Figure 35. Vector plot of the fluid velocity at time $t = 7.88s$ (before the spheres kiss). The vector plots are given in a plane with $x_3 = 0$ and a plane with $x_2 = 0$.

the leading sphere, but after the kiss the leading sphere begins to push the trailing sphere. The change is probably due to several effects. Firstly, the trailing sphere moves faster than the leading sphere and therefore it will overtake the leading sphere. In order to do so, the trailing sphere must either push the leading sphere aside or go around it. The velocity fields indicate that the trailing sphere does

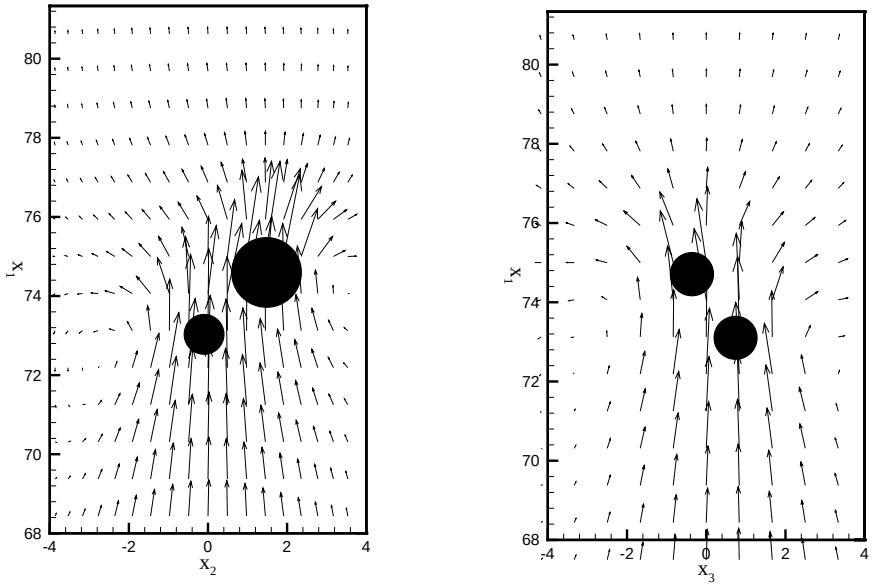

(a) Plane through $x_3 = 0$

(b) Plane through $x_2 = 0.64$ (midway between the two spheres)

Figure 36. Vector plot of the fluid velocity at time $t = 8.48s$ (the spheres kiss). The vector plots are given in a plane with $x_3 = 0$ and a plane with $x_2 = 0.64$ (midway between the two spheres).

both. Secondly, at the time of the kiss the trailing sphere is closer to the middle of the channel than the leading sphere. Therefore the lift force from the walls is smaller on the trailing sphere than on the leading sphere and it may be "easier" for the trailing sphere to go around the leading sphere instead of trying to push it aside.

In the tumbling process the two spheres rolls around each other. This is illustrated in figure 38, where the angular velocities of the two spheres from the simulation are given as function of time. Also given is the distance between the spheres. From this figure it is clear that as the trailing sphere approaches the leading sphere, the rotation of the spheres increases and in the tumbling process the trailing sphere rolls around the leading sphere. The rotation about the x_2-axis of the trailing sphere prior to the kiss, is due to the wake of the leading sphere. Similarly for the rotation about the x_3-axis, but for this direction the presence of the walls also causes the sphere to rotate. This may be the reason for the higher angular velocity about the x_3-axis than about the x_2-axis. The final rotation of the spheres agrees with the findings of Jayaweera et al. (1964). In their experiments on two sphere interaction at low Reynolds numbers, they observed that after the kiss the two spheres separate and rotate in opposite directions. However, Jayaweera et al. (1964) did not observe any rotation before the two spheres kiss. The reason could be that they performed their experiments in a tank and not a channel. Therefore there was no wall effect on the spheres. Another possibility is the low value of the Reynolds number in their experiments, which may limit the rotation of the trailing sphere due to the wake of the leading sphere.

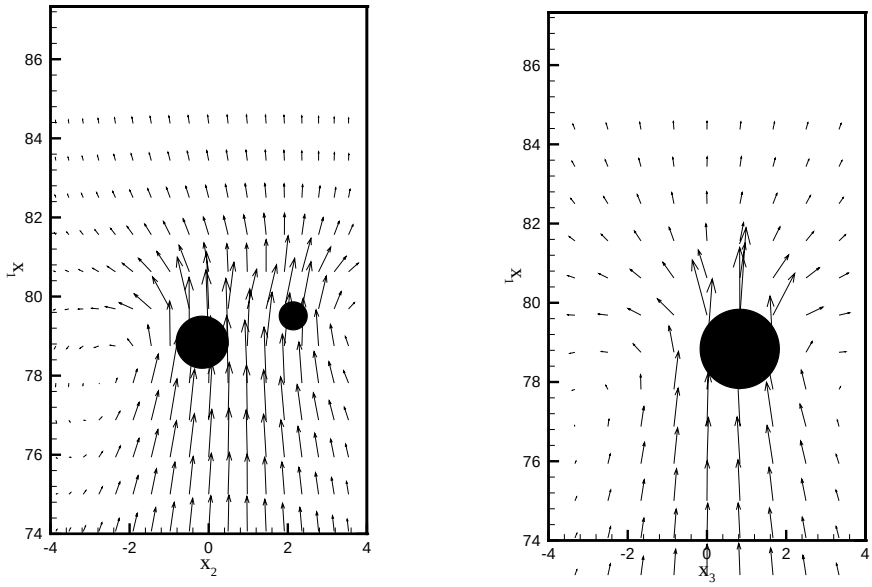

(a) Plane through $x_3 = 0$

(b) Plane through $x_2 = -0.183$ (center of trailing sphere)

Figure 37. Vector plot of the fluid velocity at time $t = 9.08s$ (after the spheres kiss). The vector plots are given in a plane with $x_3 = 0$ and a plane with $x_2 = -0.183$ (center of trailing sphere).

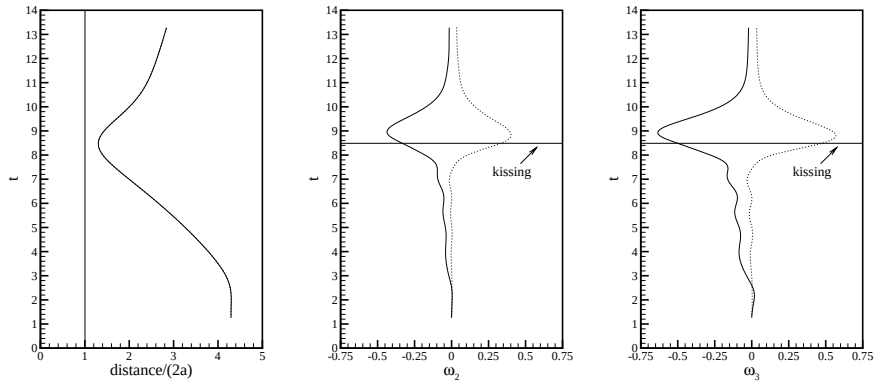

(a) Distance between spheres

(b) Rotation about x_2-axis

(c) Rotation about x_3-axis

Figure 38. Angular velocity as function of time for the particles in the simulation corresponding to experiment number 1. The angular velocities are given in s^{-1} and time is in seconds. The full line is trailing sphere and the dotted line is the leading sphere.

Second Experiment

The trajectories from the second experiment are shown in figure 39. The particles are moving upwards. The symbol (▲) denotes the leading sphere and the symbol (•) denotes the trailing sphere. The three regions of drafting, kissing and tumbling are indicated in the figure. Experiment 2 was performed with a higher viscosity than experiment 1. Therefore the nonlinear effects are weaker and the interaction between the spheres in experiment 2 is more smooth than in experiment 1.

The computed trajectories corresponding to experiment 2 are shown in figure 39 as lines, full drawn for the trailing sphere and dotted for the leading sphere. The agreement between the computed and the experimental trajectories is better for experiment 2 than for experiment 1 (compare figures 31 and 39). A probable explanantion is the neglect of particle inertia, since this will become important in the interaction process between the two spheres. In the first experiment particle inertia is more important than in the second experiment, since the first experiment was performed at a higher Reynolds number than the second experiment. Therefore the lack of particle inertia in the numerical results, leads to a worse representation of the interaction in the first experiment than in the second experiment. Another explanation could be, that the difference in the particle Reynolds number Re_p^{max} between the two spheres in experiment 1 is larger than the difference in experiment 2. In experiment 1 these particle Reynolds numbers are $Re_{p,t}^{max} = 11.03$ for the trailing sphere and $Re_{p,l}^{max} = 9.48$ for the leading sphere, while in experiment 2 these are $Re_{p,t}^{max} = 1.60$ for the trailing sphere and $Re_{p,l}^{max} = 1.71$ for the leading sphere. The smaller difference between the Reynolds numbers in experiment 2 would result in a more smooth interaction between the spheres as observed in figure 39.

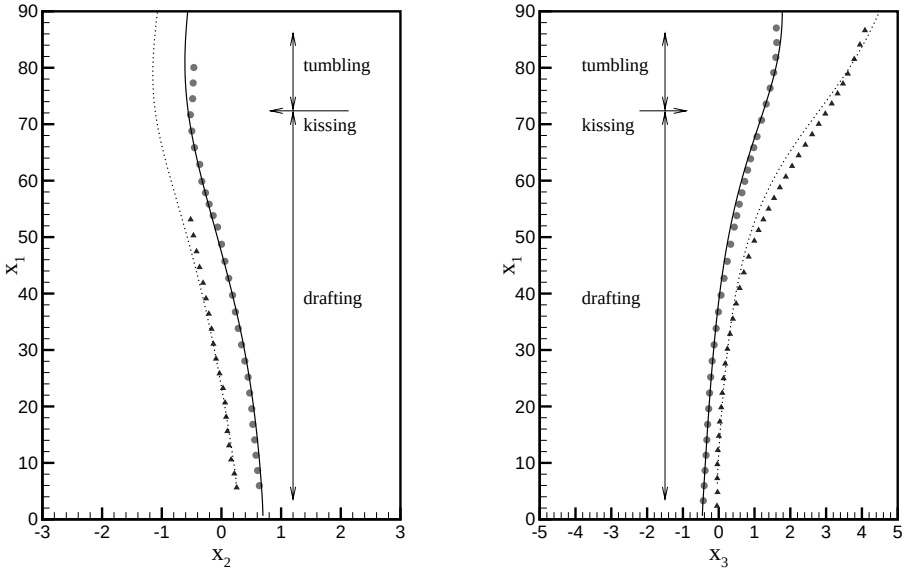

(a) Particle trajectories in the streamwise-normal directions

(b) Particle trajectories in the streamwise-spanwise directions

Figure 39. Comparision of computed and experimental particle trajectories for two particles rising for experiment number 2 in table 10. Symbols denote the experiment and lines the computation. The positions are given in mm in the frame of the experimental channel. The walls are at $x_2 = \pm 5mm$.

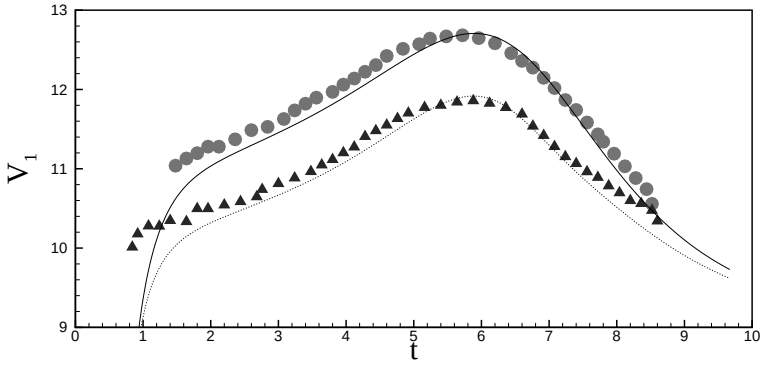

(a) Streamwise velocity

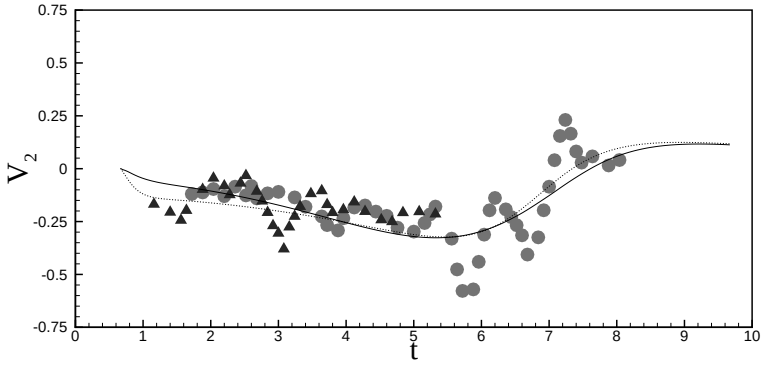

(b) Normal velocity

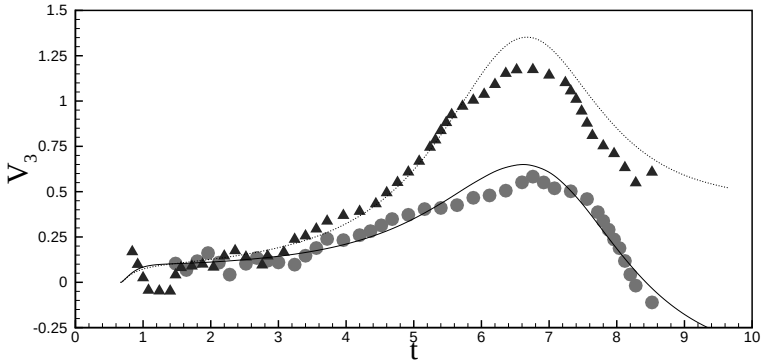

(c) Spanwise velocity

Figure 40. Comparision of computed and experimental particle velocities for two particles rising for experiment number 2 in table 10. Symbols denote the experiment and lines the computation. The velocities are given in mm/s in the frame of the experimental channel and time is in seconds.

The particle velocities from experiment 2 and the corresponding simulation are plotted in figure 40. As it was the case with the first experiment, the overall agreement is good. Since the viscosity in the second experiment is higher than in the first experiment it may surprise the reader that the streamwise velocities are

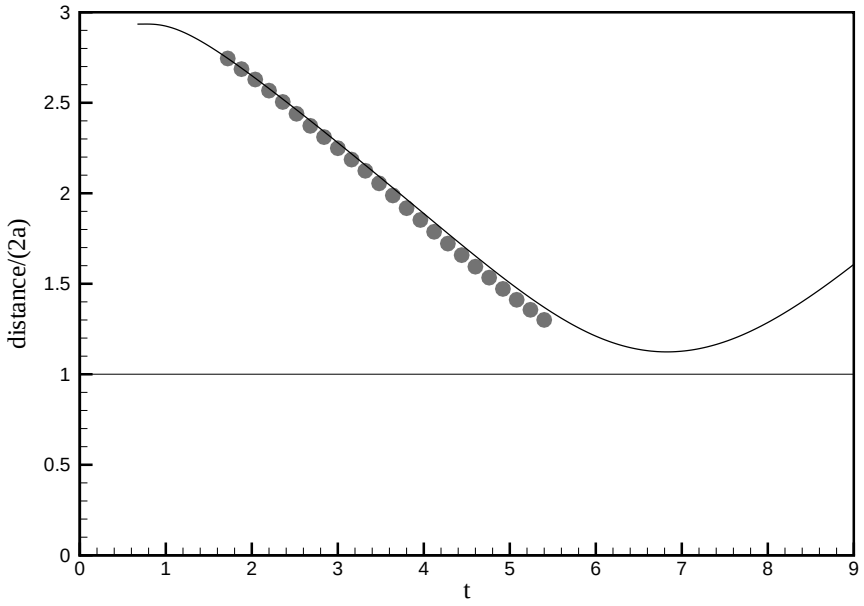

Figure 41. Distance between the particles as function of time for experiment number 2. (•) Experiment, (−) both force terms. Time is in seconds.

higher in the second experiment than in the first. The explanation is, that the two spheres in the second experiment are closer together initially and this cause the two spheres to move faster. This is a known effect previously described by Jayaweera et al. (1964) and Happel & Brenner (1965). This is also the case in the example given at end of chapter 4 of two Stokes spheres settling parallel or perpendicular to their line of centers as shown in figure 15. The higher viscosity of experiment 2 has an effect on the streamwise velocity after the kiss of the two spheres. In experiment 1, the streamwise velocities level out rather quickly after the kiss, see figure 32(a). In experiment 2, the streamwise velocities do not tend to level out, but continues to decay, see figure 40(a). The higher viscosity of experiment 2 forces the velocities after the kiss to fall more slowly and finally to a lower value (not shown) than in experiment 1.

The distance between the two spheres as function of time for both the experiment and the simulation is shown in figure 41. As in experiment 1 the distance between the spheres fall linearly with time until the spheres are very close together. In the simulation the spheres do not touch and the smallest distance between their centers is 1.12 times their diameter at time $t = 6.83$s.

The interaction process between the two spheres is similar to that described above for the first experiment. As the trailing sphere approaches the leading sphere, the trailing sphere pushes the leading sphere aside. When the spheres come close together, they rotate/roll around each other in a way similar to that given in figure 38 for the first experiment. This is shown in figure 42, where the angular velocities ω_2 and ω_3 are given as functions of time. Also seen in figure 42, is that the trailing sphere rotates in the wake of the leading sphere as in the first experiment. The magnitude of the angular velocities in experiment 2 are considerably higher for the rotation about the x_2-axis than about the x_3-axis, in contrast to the angular velocities in experiment 1. This shows that the tumbling in experiment 2 primarily appears in the streamwise-spanwise plane, where the two spheres almost roll on each other. This is also observed in the trajectories in figure 39, where the tumbling process shows a separation of the spheres in the

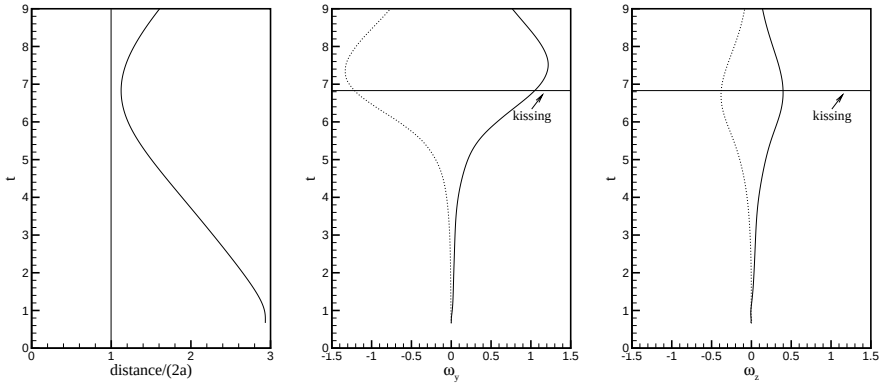

(a) Distance between spheres

(b) Rotation about x_2-axis

(c) Rotation about x_3-axis

Figure 42. Angular velocity as function of time for the particles in the simulation corresponding to experiment number 1. The angular velocities are given in s^{-1} and time is in seconds.

spanwise direction, but almost no separation in the normal direction. In contrast the tumbling in the first experiment was in both the streamwise-normal plane and the streamwise-spanwise plane. Therefore the spheres in figure 31 separate in both directions and the angular velocities in figure 38(b) and figure 38(c) are very similar in shape and magnitude.

In the previous section on conserning the first experiment it was hypothesized that the reason for the discrepancy in the rotation rate before the kiss between our results and those of Jayaweera et al. (1964) could be related to a lower Reynolds number in cases investigated by Jayaweera et al. (1964). The result on the rotation in this second experiment supports this speculation, since the angular velocity before the kiss shown in figure 42 is diminished in comparision with the those in figure 38. This indicates that decreasing the Reynolds numberresults in decreasing the angular velocity of the trailing sphere before the kiss.

5.5 Triple Particle Interactions

Experimental and Numerical Results on Three Particles

The final example of particles rising in a channel is with three spheres. For this case only one experiment has been done. The experimental data are given in tabel 12. Although is was attempted to have three equal spheres, sphere (▼) had a mass slightly lower than the other two particles. The material is the same for all three spheres. Therefore the lower mass is probably due to a slightly smaller radius resulting in a lower volume of sphere (▼). A difference in the radius of 0.17 % results in a mass difference of 0.50 %. In table 12 the mass difference is given as a lower density, because this is how it was treated in the computation.

The computational parameters are given in table 13. Compared to the two particle computations, the streamwise length has been doubled in order make sure that the periodic boundary condition does not effect the solution.

The trajectories from the experiment are drawn in figure 43. The symbols in the figure correspond to the symbols in table 12. Initially the sphere (▲) is the leading sphere, the sphere (●) is the middle sphere, and the sphere (▼) is the trailing sphere. During the experiment two kissing events appear. The first is at $t = 5.18$s between spheres (▲) and (●), this is denoted as *kissing 1-2* in figure 43.

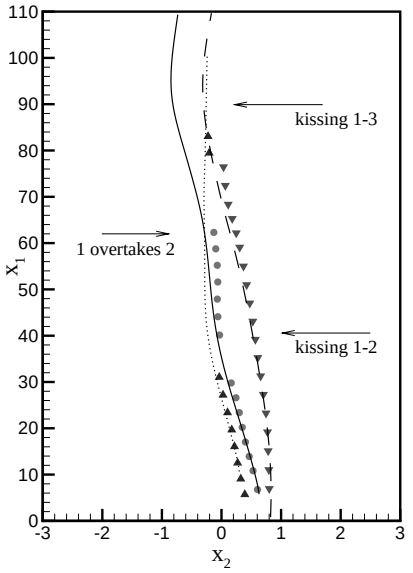

(a) Particle trajectories in the streamwise-normal directions

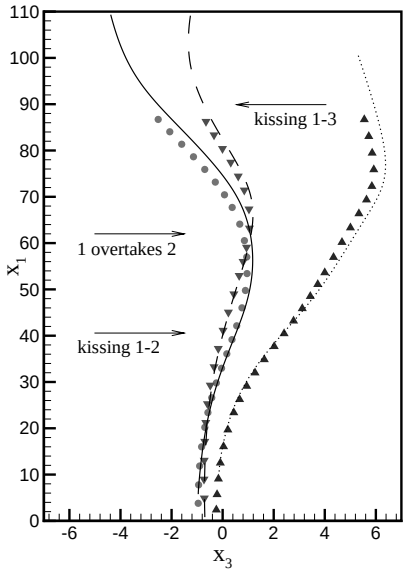

(b) Particle trajectories in the streamwise-spanwise directions

Figure 43. Comparision of computed and experimental particle trajectories for three particles rising. The experimental values are given in table 12. Symbols denote the experiment and lines denote the computation. The positions are given in mm in the frame of the experimental channel. The walls are at $x_2 = \pm 5mm$.

The second event appears at $t = 9.6$s just after the spheres leave the view of the camera. The time and place for this event is determined from the simulation. This second kissing event is between spheres (●) and (▼) and is denoted as *kissing 2-3* in figure 43. These two kissing events correspond to two drafting and tumbling processes as shown below. Furthermore, the sphere initially leading (sphere (▲)) is overtaken by the other two spheres. The position, where initially middle sphere (●) overtakes the sphere initially leading (▲) is denoted as *2 overtakes 1* in figure 43.

The trajectories from the simulation are shown as the lines in figure 43. The full drawn line corresponds to sphere (●), the dotted line corresponds to sphere (▲), and the dashed line corresponds to sphere (▼). The agreement between the experiment and the simulation is good. The computation has been continued beyond the experiment in order to capture the second kissing event, and to show that the sphere initially leading (sphere (▲)) is left behind by the other two spheres. This is best seen in figure 43(b). The final streamwise position of sphere (▲) is approximately 100mm, while the final streamwise position of spheres (●) and (▼) are approximately 110mm. The interaction between the spheres in the two DKT-processes, causes the sphere (▲) to be left behind. In the first DKT-process the

Par. no.	a (mm)	ρ_f (g/cm^3)	ρ_p (g/cm^3)	ν (mm^2/s)	Re_p^{Stokes}
(●)	1.0	1.179	1.081	15.31	1.55
(▲)	1.0	1.179	1.081	15.31	1.55
(▼)	1.0	1.179	1.075	15.31	1.64

Table 12. Experimental values for a three particles rising in a channel. The numbers

Exp. no.	$L_1 \times L_2 \times L_3$	$N_1 \times N_2 \times N_3$	δt	$Re = \frac{L_2 U}{\nu}$	$Fr = \frac{gL_2}{U^2}$
1	$10 \times 1 \times 4$	$128 \times 32 \times 48$	0.01	6.53	982.0

Table 13. Computational parameters for the three particles rising in a channel. The characteristic length $L = L_2 = 10mm$ and the characteristic velocity $U = 10mm/s$.

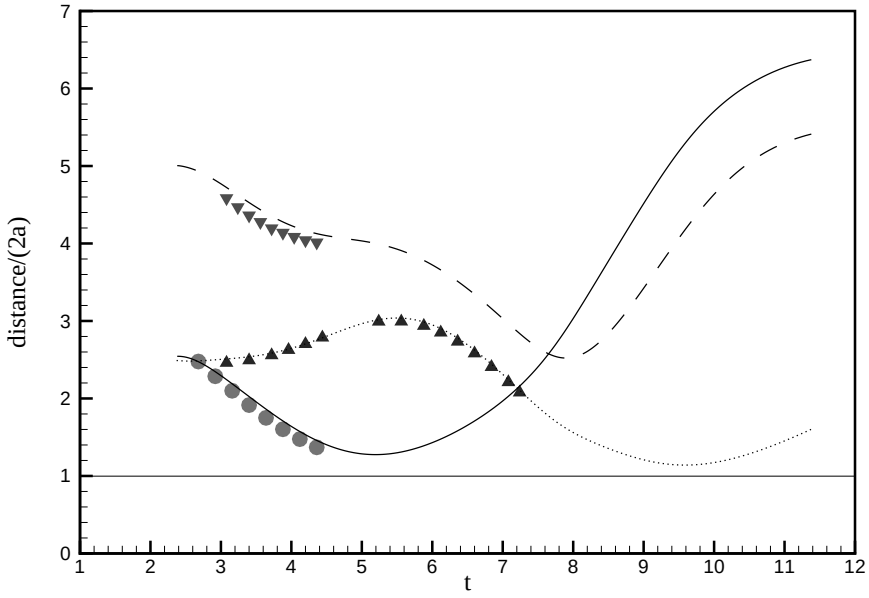

Figure 44. Distance between the particles as function of time for the three particles. (●) & (−) denotes the distance between particle (●) & (▲) in figure 43. (▲) & (· · ·) denotes the distance between particle (●) & (▼) in figure 43. (▼) & (− −) denotes the distance between particle (▲) & (▼) in figure 43. Time is in seconds.

leading sphere is pushed aside by the middle sphere, and it moves away from the two trailing spheres in the spanwise direction. Due to the DKT-process between sphere (●) and sphere (▼), these two spheres begin to move as a particle pair. This leads to a higher streamwise velocity of the two trailing spheres than of the leading sphere and therefore the two trailing spheres overtake the leading sphere leaving it behind.

Figure 44 shows the distances between the spheres as function of time. The full drawn line is the distance between sphere (▲) and sphere (●). The dotted line is the distance between sphere (●) and sphere (▼). The dashed line is the distance between sphere (▲) and sphere (▼). The kissing between sphere (▲) and sphere (●) at time $t = 5.18$s and the kissing between sphere (●) and sphere (▼) at $t = 9.6$s are clearly seen in figure 44. In the final part of figure 44 for $t > 8$s, the increase in the distance between sphere (▲) and sphere (●) and in the distance between sphere (▲) and sphere (▼) shows that sphere (▲) is left behind by the other two spheres.

The particle velocities from both experiment and simulation are shown in figure 45. The symbols and the lines denote the same particles as in figure 43. In the first part of the figure for $t = 1$s to $t = 6.5$s, the streamwise velocities for the leading sphere (▲) and the middle sphere (●) are similar to the velocities observed in figures 32(a) and 40(a) for the two particle examples. This part of the figure corresponds to the first DKT-process. The similarity of the velocities indicate that the DKT-process between the sphere (▲) and sphere (●) is independent of the trailing sphere (▼). During the DKT-process of the two leading spheres, the

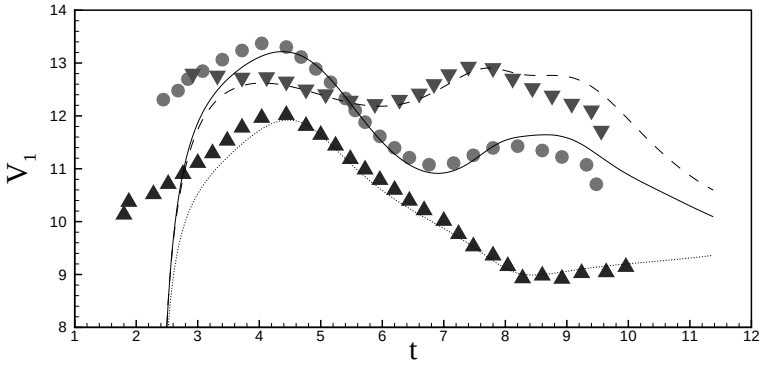

(a) Streamwise velocity

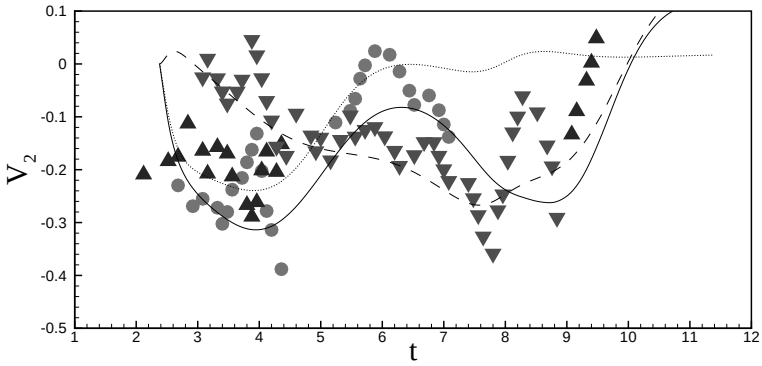

(b) Normal velocity

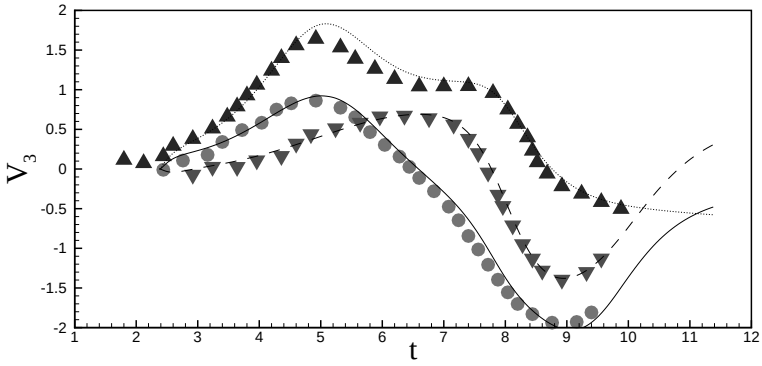

(c) Spanwise velocity

Figure 45. Comparision of computed and experimental particle velocities for three particles rising. The experimental values are given in table 10. Symbols denote the experiment and lines denote the computation. The velocities are given in mm/s in the frame of the channel and time is in seconds.

distance between sphere (•) and sphere (▼) increases (see figure 44). Therefore the drafting of sphere (▼) in the wake of sphere (•) is diminished, leading to the decrease in the streamwise velocity of sphere (▼). In the kissing and tumbling process between sphere (▲) and sphere (•) the streamwise velocity of these two

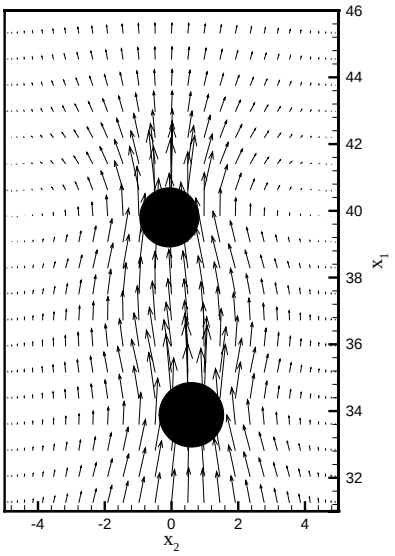

(a) Plane through $x_3 = 0$. The lower sphere correspond to (▼) and the upper sphere correspond to (●).

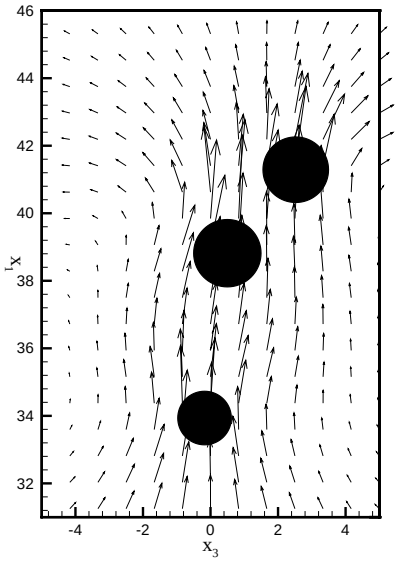

(b) Plane through $x_2 = 0$. The lower sphere correspond to (▼), the upper-left sphere correspond to (●), and the upper-right sphere correspond to (▲).

Figure 46. Vector plot of the fluid velocity at time $t = 5.18s$ (the spheres (●) & (▲) kiss). The vector plots are given in a plane with $x_3 = 0$ and a plane with $x_2 = 0$.

spheres decreases. At time $t = 5.5$s this results in the streamwise velocity of sphere (▼) being the highest. Thus, the distance between sphere (●) and sphere (▼) decreases and a drafting process between these two spheres is initiated. At time $t = 7.2$s the sphere (▼) is within one diameter of the sphere (●) (see figure 44). Due to the higher velocity of sphere (▼) it begins to push fluid around sphere (●), thereby starting a pushing of sphere (●) as described above for the two particle examples. This leads to the increase in the streamwise velocity of sphere (●) seen in figure 45(a) for $t = 7.2$s to $t = 8.2$s. The drafting of sphere (▼) initiated at $t = 5.5$s ends at $t = 9.6$s, where the kissing event between sphere (●) and sphere (▼) appears. The form of the curves for the streamwise velocity of spheres (●) and (▼) during their DKT-process from $t = 7.2$s to $t = 11.5$s, is reminiscent of the streamwise velocity observed in the DKT-processes of dual particles shown in figures 32(a) and 40(a). This indicates that sphere (▲) has little effect on the interaction between the other two spheres.

In the discussion of the distances between the spheres and of the streamwise velocity of the spheres, it was hypothesized that the two DKT-processes observed in this example of three spheres, was independent of the presence of the third sphere. This conjecture is now examined by looking at the fluid velocity field. Figure 46 shows a vector plot of the fluid velocity field at time $t = 5.18$s in two different planes. Figure 46(a) shows the streamwise-normal plane at $x_3 = 0$ and figure 46(b) shows the streamwise-spanwise plane at $x_2 = 0$. The dark circular areas are the cuts through the spheres. The flow behind sphere (●) in figure 46(a) is weaker than the flow in front of the sphere. Therefore sphere (▼) is not pushing fluid around sphere (●). The main effect of sphere (▼) on the flow around sphere (●), is a destruction of the wake created behind sphere (●). This destruction will effect the time history of the drag force (the Basset history force), and cause the

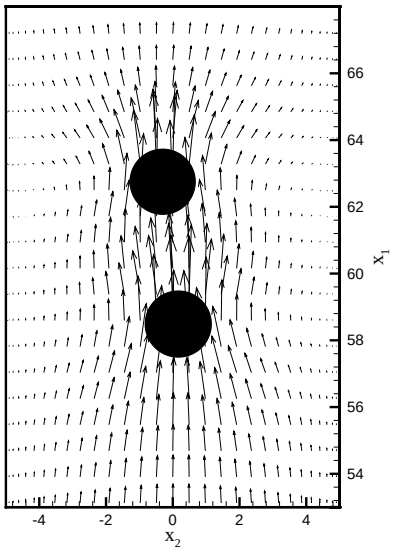

(a) Plane through $x_3 = 0.83$. The lower sphere correspond to (▼) and the upper sphere correspond to (●).

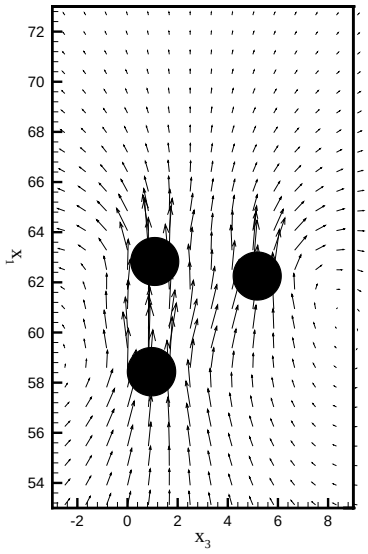

(b) Plane through $x_2 = 0$. The lower sphere correspond to (▼), the upper-left sphere correspond to (●), and the upper-right sphere correspond to (▲).

Figure 47. Vector plot of the fluid velocity at time $t = 7.18s$. The vector plots are given in a plane with $x_3 = 0.83$ and a plane with $x_2 = 0$.

drag due to viscous transport of vorticity created at the surface of sphere (●) to decrease. According to the investigations reviewed in chapter 3 the Basset history force decays as t^{-1} or t^{-2}, when convective inertia is important. Therefore the drag from the Basset history force is already relatively small, since the value of the particle Reynolds number is above one ($Re_p > 1$). Consequently, the presence of sphere (▼) has little effect on sphere (●). The same arguments, concerning the interaction between sphere (●) and sphere (▼), holds for the flow in the streamwise-spanwise plane shown in figure 46(b).

The flow around sphere (▲) and sphere (●) in figure 46(b) explains the spanwise translation of sphere (▲) observed in the trajectory in figure 43(b). Sphere (●) has a faster streamwise velocity than sphere (▲), therefore it pushes fluid past sphere (▲) on the left hand side. Consequently, the flow is stronger on the left side than on the right side of sphere (▲). This creates a flow from left to right, forcing sphere (▲) to the right. The flow from left to right is seen in the top right corner of figure 43(b). This is the same pushing mechanism as observed for the two particle example in figure 36.

The fluid velocity field in two planes at time $t = 7.18$s is shown in figure 47. The streamwise-normal plane at $x_3 = 0.83$ is shown in figure 47(a), while figure 47(b) shows the streamwise-spanwise plane at $x_2 = 0$. At this time the distance between sphere (●) and sphere (▼) is smaller than one diameter, and the streamwise velocity of sphere (▼) is higher than the streamwise velocity of sphere (●). Therefore the flow behind sphere (●) is stronger than the flow in front, and sphere (▼) is pushing fluid past sphere (●). This forces sphere (●) to accelerate, and explains the increase in the streamwise velocity of sphere (●) seen in figure 45(a). The fluid velocity field in figure 47(b) explains the spanwise drift of the trajectories for sphere (●) and sphere (▼) seen in figure 43(b) for $x_1 > 60$mm. The particle pair consisting of the

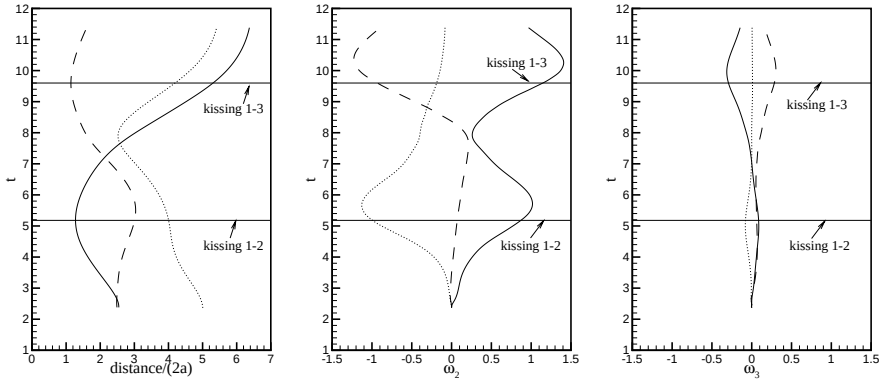

(a) Distance between spheres (same notation as in figure 44)

(b) Rotation about x_2-axis

(c) Rotation about x_3-axis

Figure 48. Angular velocity as function of time for the particles in the simulation corresponding to experiment number 1. The angular velocities are given in s^{-1} and time is in seconds.

two trailing spheres ((•) & (▼)) begins to overtake the leading sphere (▲) around $x_2 = 60$mm. Therefore the flow to the right of the particle pair is stronger than the flow to the left, as seen in figure 47(b). This generates a flow going from right to left forcing the particle pair to move in the negative spanwise direction. At the same time the sphere (▲) is forced to the right, due to the stronger flow between itself and the particle pair. Nevertheless, this appears only to have an effect on the spanwise motion of the particle pair and not on the DKT-process between them.

The main reason for the lack of influence of the third sphere on the DKT-process of the other two spheres, is that in both cases the distance from the third sphere to either of the two other spheres, was larger than one sphere diameter. In contrast, the distance between the particle pair was smaller than one diameter. Therefore the interaction between the spheres in the particle pair was more important, than the interaction with the third sphere.

The angular velocities of the spheres in the simulation are shown in figure 48. Figures 48(b) and 48(c) shows that the spheres roll around each other during the kissing event, similarly to the tumbling processes in the two particle examples. Further, figure 48 together with figure 43 shows that the spheres move around each other in the streamwise-spanwise plane. A possible explanation is the limiting effect of the walls. Due to the walls, the resistance to motion in the streamwise-normal plane is higher, than the resistance to motion in the streamwise-spanwise plane. Therefore it is easier for the spheres to go around each other in the streamwise-spanwise plane than in the streamwise-normal plane.

5.6 Poiseuille Flow

The main purpose of the previous sections on single, dual and triple particles settling in an inclined or vertical channel, was to verify the force coupling model. The examples were chosen, because they are the simplest cases of particulate flows in a channel. Additionally, it was much easier to perform experiments on settling spheres, than on spheres dispersed in a shear flow. However, the examples of particle dynamics with settling spheres have only little relevance to the particulate flows in the microdevices described in section 2.3. In these devices the particles

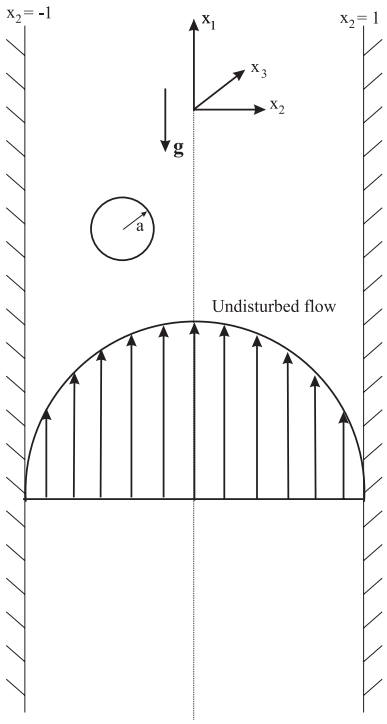

Figure 49. Particle dispersed in an upwards Poiseuille flow.

are dispersed in a carrying fluid flow typically imposed by a pressure gradient.

For the channel described in the numerical method on page 62 it is possible to examine a basic pressure driven channel flow, namely the Poiseuille flow. In the Poiseuille flow the momentum transfer is provided by a pressure gradient over the streamwise direction. This forces the fluid to move and the resulting velocity profile is shown in figure 49.

The effect of the shear flow on a dispersed sphere is an additional lift force in the direction normal to the walls. This shear induced lift force and the effects of it was discussed in section 3.4. The aim of the following section is to examine whether or not, the force coupling method reproduces the shear induced lift force. If the force coupling method is to be used for computation of the particulate microflows described in section 2.3, the shear induced lift force must be included. Three examples are considered in the following; a single neutrally buoyant sphere, a buoyant sphere (lighter or heavier than the fluid), and three neutrally buoyant spheres.

Neutrally Buoyant Sphere

The setup of a single sphere in an upwards Poiseuille flow is shown in figure 49. The sphere is initially placed somewhere between the center plane of the channel and one of the channel walls. As described in section 3.4 the flow relative to the sphere leads to a pressure distribution with a higher pressure on the side facing the center plane of the channel than on the side facing the wall. Therefore the sphere is sucked away from the center plane towards the wall. The lateral motion continues until the wall induced lift force balances the shear induced lift force, and the sphere settles on this position between the wall and the center plane.

Four simulations of a neutrally buoyant sphere in Poiseuille flow has been performed. The computational parameters are given in table 14. The sphere radius

Sim. no.	$L_1 \times L_2 \times L_3$	$N_1 \times N_2 \times N_3$	δt	$Re = \frac{L_2 U}{2\nu}$	$Y_2(t=0)$	a
1	$12 \times 2 \times 6$	$128 \times 48 \times 64$	0.02	5.0	0.05	0.250
2	$12 \times 2 \times 6$	$128 \times 48 \times 64$	0.02	40.0	0.05	0.250
3	$12 \times 2 \times 6$	$128 \times 48 \times 64$	0.02	40.0	0.70	0.250
4	$12 \times 2 \times 6$	$128 \times 48 \times 64$	0.02	56.0	0.05	0.250

Table 14. Computational parameters for the neutrally buoyant sphere in a Poiseuille flow. The characteristic length $L = L_2/2$ and the characteristic velocity $U = U_c$, where U_c is the fluid velocity in the center plane of the channel.

was $a = L_2/8 = 0.25$. The difference in the simulations is the Reynolds number for the Poiseuille flow which was varied from $Re = 5$ to $Re = 56$ in order to see the effect on the lateral motion. In simulation number 3 the initial position $Y_2(t = 0)$ was changed from close to the center plane, $Y_2(t = 0) = 0.05$, to close to the wall, $Y_2(t = 0) = 0.70$. This is included to show that close to the wall the lateral motion is governed by the wall induced lift force.

The computed trajectories in non-dimensional variabels are shown in figure 50(a). The particles, initially placed near the center plane, moves laterally toward a position approximately midway between the center plane and the wall. The final position of the sphere in the simulation with $Re = 40$ is $Y_2 = 0.516$, which is in excellent agreement with the value of $Y_2 = 0.504$ determined in the direct numerical simulation by Feng et al. (1994b). For $Re = 40$ the trajectory for a particle initially placed near the channel wall was also computed. This particle moves laterally away from the wall toward the same final position, as the particle initially placed near the center plane. Increasing the Reynolds number of the flow to $Re = 56$ leads to a final position further from the center plane. The final position of the sphere in the flow with $Re = 56$ was $Y_2 = 0.522$. Decreasing the Reynolds number to $Re = 5$ results in a much slower lateral motion. The sphere in this computation has not reached its equilibrium position. Nevertheless, the final position in figure 50(a) is $Y_2 = 0.441$, and the lateral motion is becoming weaker. Therefore it is probable, that the equilibrium position at this flow Reynolds number, will be closer to the center plane than the equilibrium position at $Re = 40$ and $Re = 56$. Consequently, decreasing the Reynolds number of the flow results in an equilibrium position closer to the center plane of the channel. This is consistent with the results of Feng et al. (1994b). Finally, no translational motion of the spheres occurs in the spanwise direction, because of the symmetry and the periodic boundary conditions.

The non-dimensional slip velocity of the spheres is shown in figure 50(b). The slip velocity is defined as the difference between the velocity of the particle, $V_1(t)$, and the velocity of the undisturbed flow at the center of the particle, $u_1(\mathbf{Y}, t) = u_1^{Poiseuille} = 1 - Y_2^2$. The results show that the neutral spheres are lagging the undisturbed fluid flow (negative slip velocity), and at higher flow Reynolds number the slip velocity becomes smaller. This does not agree with the slip velocities in the investigation of Feng et al. (1994b). Feng et al. (1994b) found that increasing the Reynolds number leads to a higher slip velocity. The reason for the discrepancy could be, that the direct simulation by Feng et al. (1994b) is two-dimensional, whereas the present simulation is three-dimensional. The decreasing slip velocity with increasing Reynolds number is consistent with the arguments in section 3.4, concerning changes in the lag velocity. In section 3.4 it was argued that an increase in the lag velocity will result in an equilibrium position closer to the center plane. This is exactly, what is observed in figures 50(a) and 50(b). In the simulation with $Re = 40$ the lag velocity is higher than the lag velocity for $Re = 56$, and the equilibrium position for $Re = 40$ is closer to the center plane than the equilibrium position for $Re = 56$. Comparing $Re = 40$ and $Re = 5$ yields the same result.

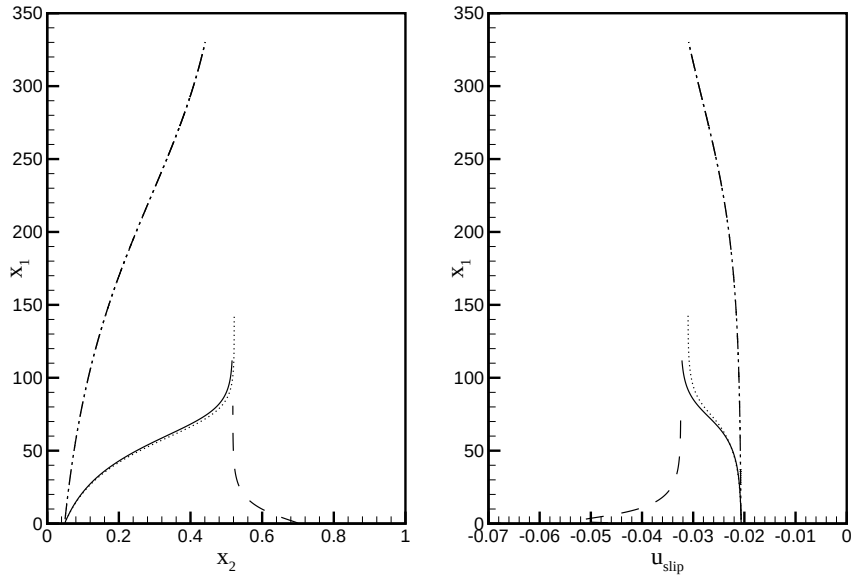

(a) Trajectories. The center plane is at $x_2 = 0$ and the wall is at $x_2 = 1$.

(b) Slip velocity $u_{slip} = V_1 - u_1^{Poiseuille}$.

Figure 50. Trajectories and lag velocity for a neutrally buoyant sphere dispersed in a Poiseuille flow. $(- \cdot\cdot -)$ $Re = 5$, $(-)$ $Re = 40$, $(\cdots)$ $Re = 56$ *for the sphere initially placed near the center plane.* $(- \ - \ -)$ $Re = 40$ *for the sphere initially placed near the wall.*

The fluid velocity field for simulation number 2 is shown in figure 51 as vector plots in the streamwise-normal plane for $x_3 = 0$. The snapshot of the flow field is taken at time $t = 10$, where the sphere position is $Y_1 = 15.75$ and $Y_2 = 0.0852$. The flow field in the frame of the channel is shown in figure 51(a). In this figure it is difficult to see any influence of the sphere on the parabolic Poiseuille flow. Subtracting the undisturbed parabolic flow field from the computed flow field, gives the disturbance flow setup by the sphere. This disturbance flow is shown in figure 51(b). The sphere creates a recirculating zone both in the front and in the back of it. These recirculating zones are related to the pressure distribution discussed in section 3.4. At the points where the flow is directed away from the sphere, the pressure is higher than in the surrounding fluid and these point corresponds to the + signs in figure 8(b). The low pressure areas in figure 8(b) (denoted −) correspond to the points in figure 51(b), where the flow is directed toward the sphere. The inward pointing flows at the upper-left and the lower-right of the sphere in figure 51(b) cancels each other. On the other hand, the outward pointing flows at the lower-left and the upper-right of the sphere do not cancel. The flow at the upper-right is larger than the flow at the lower-left. This makes the sphere move in the upward right direction, as seen in the trajectory in figure 50(a). The flow field relative to the sphere is seen in figure 51(c). This is determined by subtracting the velocity of the particle from the fluid velocity field, i.e. $u_i - V_i$. In this frame of reference, it is seen that the flow relative to the sphere is stronger on the right side of the sphere consistent with the observations by Feng et al. (1994b). As explained in section 8(b), this causes the pressure distribution sketched in figure 8(b) and leads to the disturbance flow in figure 51(b).

The flow field for simulation number 3 is shown in figure 51 as vector plots in the streamwise-normal plane for $x_3 = 0$. The snapshot of the flow field is taken at

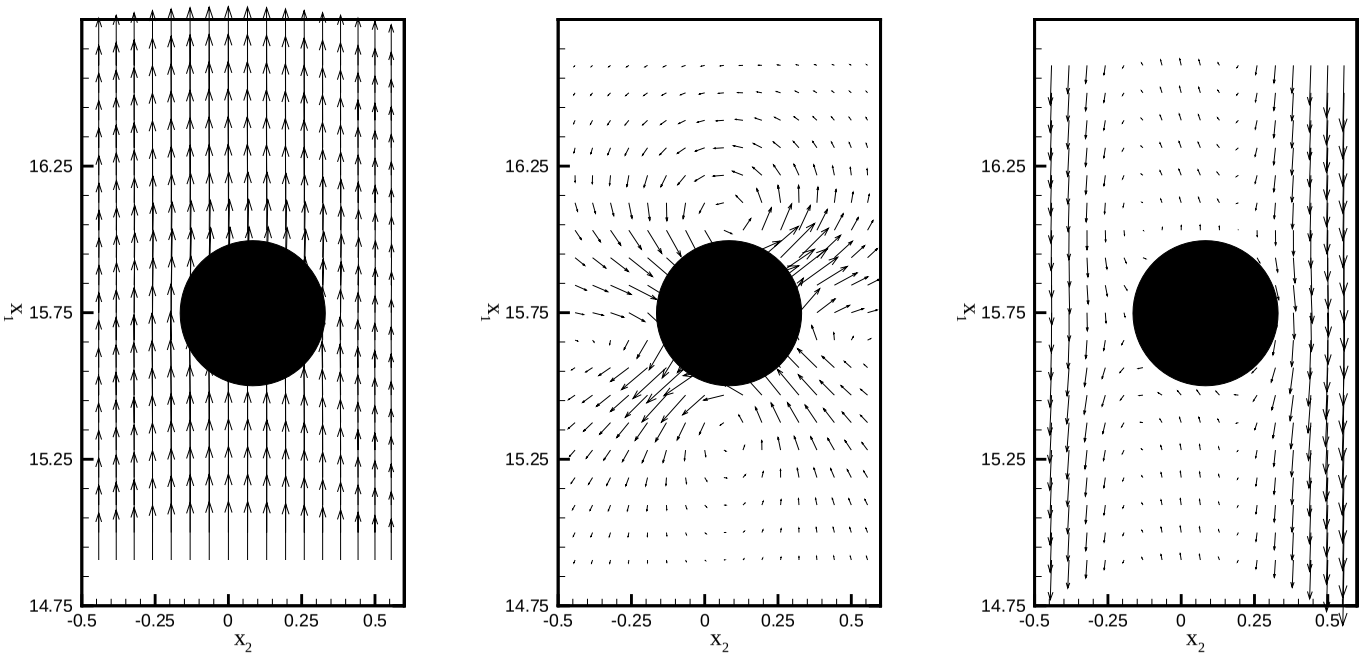

(a) Flow field in the frame of the channel.

(b) Disturbance flow in the frame of the channel.

(c) Flow field in the frame of the sphere.

Figure 51. Vector plots of the fluid velocity field for simulation number 2. The snapshots are taken at time $t = 10$ *and the sphere position is* $Y_1 = 15.75$ *and* $Y_2 = 0.0852$*. The disturbance flow is difference between the computed flow field and the undisturbed parabolic Poiseuille flow, i.e.* $u_i^{disturbance} = u_i - u_i^{Poiseuille}$*. For the flow field in the frame of the sphere, the sphere velocity has been subtracted from the computed flow field.*

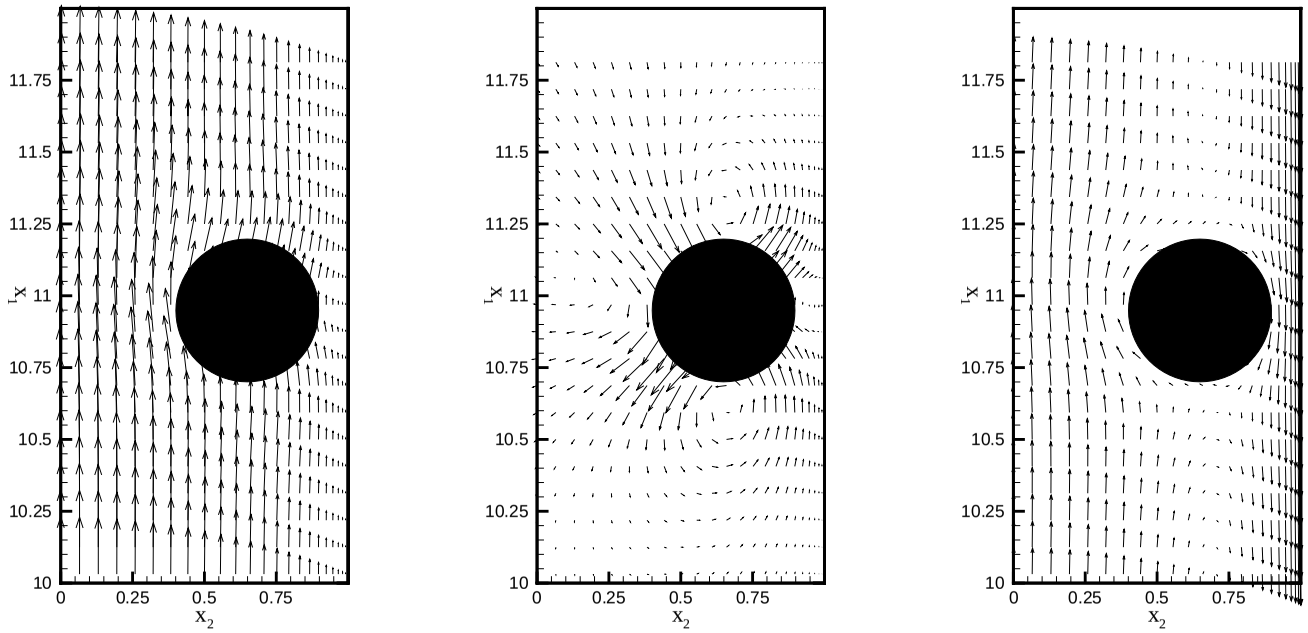

(a) Flow field in the frame of the channel.

(b) Disturbance flow in the frame of the channel.

(c) Flow field in the frame of the sphere.

Figure 52. Vector plots of the fluid velocity field for simulation number 3. The snapshots are taken at time $t = 10$ *and the sphere position is* $Y_1 = 10.95$ *and* $Y_2 = 0.6445$*. The disturbance flow is difference between the computed flow field and the undisturbed parabolic Poiseuille flow, i.e.* $u_i^{disturbance} = u_i - u_i^{Poiseuille}$*. For the flow field in the frame of the sphere, the sphere velocity has been subtracted from the computed flow field.*

time $t = 10$, where the sphere position is $Y_1 = 10.95$ and $Y_2 = 0.6445$. In figure 52(a) the velocity field in the frame of the channel is shown. In contrast to the sphere placed near the center plane (see figure 51(a)) the influence of the sphere is clearly visible in figure 52(a). On the left side of the sphere the fluid flow is slowed down and forced to go around the sphere, because the fluid moves with a higher velocity than the sphere. On the other hand, the fluid on the right side of the sphere moves with a lower velocity. Consequently, the fluid on the right side of the sphere is accelerated. The disturbance flow is shown in figure 52(b). The flow is reminiscent of the flow field in figure 51(b) for the sphere near the center plane. Again two recirculating zones are visible, but the flow on the right side of the sphere in figure 52(b) is different from the flow on the right side of the sphere in figure 51(b). This is an effect of the wall. The no-slip condition on the wall limits the fluid flow, and as a result the inward and outward flow on the left side of the sphere are stronger than the corresponding flows on the right side of the sphere. Therefore the disturbance flow forces the particle to move to the left away from the wall. The flow field relative to the sphere is shown in figure 52(c) and it shows the effect of the wall more clearly. As the sphere moves upward, the fluid on upper-right side of the sphere is squeezed in between the sphere and the wall. This causes an increase in the pressure on the right side of the sphere, forcing the sphere to move away from the wall, as seen in the trajectory in figure 50(a).

Summarizing the above results for a single neutrally buoyant sphere in a Poiseuille flow, it is clear that the shear induced lift force is small for a neutrally buoyant sphere. For $Re = 40$ and $Re = 56$ the lateral motion from start to end required a channel of length approximately 50 times the channel width ($L_1 \approx 50L_2$). The Reynolds number in the range of microflows ($Re = 5$) required a channel length of over 150 times the channel width, and for channel lengths $L_1 < 50L_2$ the lateral motion was almost negligible. These results were obtained for a relatively large particle with radius $a = L_2/8$. Since the shear induced lift force is proportional to the radius (see equation (20) and (22)), a smaller particle will result in a even weaker lateral motion. Consequently, shear induced migration of neutrally byouant particles in particulate microflows is probably negligible.

Buoyant Spheres

In an upward or downward Poiseuille flow any difference in the density of the particle compared to the carrying fluid, will cause the trajectory of the sphere to change. The cause is the buoyancy forces of the lighter or heavier particle that will lead to a change in the slip velocity and result in a change of the forces on the particle. Repetti & Leonard (1966) performed experiments with buoyant spheres in a downward Poiseuille flow. Their experimental setup consisted of a rectangular channel with aspect ratio $L_3/L_2 = 4$. In this channel Repetti & Leonard (1966) made a series of experiments with both light and heavy spheres. They recorded the trajectories on film and some of these trajectories are given in their paper. Consequently, these experiments form a good basis for comparision with the force coupling method.

Exp. No.	Q (m^3/s)	a (m)	ρ_p (kg/m^3)	ρ_f (kg/m^3)	ν (m^2/s)
RL6052	$25.1 \cdot 10^{-6}$	$4.8133 \cdot 10^{-3}$	1147.00	1148.30	$1.2096 \cdot 10^{-6}$
RL6070	$25.1 \cdot 10^{-6}$	$4.8311 \cdot 10^{-3}$	1147.65	1143.30	$1.1983 \cdot 10^{-6}$

Table 15. Experimental values for the buoyant spheres in a Poiseuille flow. The experiments were performed by Repetti & Leonard (1966) in a channel with $L_2 = 0.0254$ m and $L_3 = 4L_2$.

In this section two simulations will be presented. One with a light sphere and one with a heavy sphere. In both cases the Poiseuille flow is downward, i.e. opposite direction of that given in figure 49. In this setup the buoyancy force on the lighter sphere will create an increase in the lag velocity. As explained in section 3.4, this causes the shear induced lift force to decrease and the sphere will move toward the center plane of the channel. In the downward Poiseuille flow, the heavier sphere will have a weaker lag velocity or a lead velocity. Consequently, the mechanism forcing the sphere to move away from the center plane becomes stronger, and the particle is moved nearer to the wall, see section 3.4. Repetti & Leonard (1966) observed both these phenomena in their experiments. The case with the light sphere is denoted *RL6052* and the case with the heavy sphere is denoted *RL6070*. These numbers correspond to those given to the experiments in Repetti & Leonard (1966). The experimental values are given in table 15 and the corresponding computational values are given in table 16.

The trajectories from both the experiments and the simulations are shown in figure 53(a). The results are shown in non-dimensional variabels. For the heavy particle (RL6070), the simulation agree well with the experiment by Repetti & Leonard (1966). The heavy sphere is released near the center plane at $Y2(t = 0) = -0.145$. Due to the shear, the sphere moves laterally from the center toward the wall. The lateral migration is very similar to that observed in figure 50(a) for the neutral spheres, but the final equilibrium position is closer to the wall at $Y_2^{equi} = -0.74$ for the experiment and $Y_2^{equi} = -0.76$ for the simulation. The slip velocity for the simulation is shown in figure 53(b). Due to the buoyancy force the heavy sphere quickly attains a velocity higher than the undisturbed flow, and the result is a lead velocity. The equilibrium position closer to the wall together with the lead velocity, is consistent with the arguments given above and in section 3.4, that a lead velocity will increase the shear induced lift force and result in a stronger lateral migration. Furthermore, the migration is faster for the heavy sphere than for the neutrally buoyant spheres.

The agreement between simulation and experiment for the light sphere is not so good as for the heavy sphere, since the lateral motion from the wall to the center plane is much faster in the simulation than in the experiment. Nevertheless, the simulation does show the same trend and the trajectories agree qualitatively. Further, the final equilibrium position agrees relatively well with that of the experiment. A first thought about why the simulation goes wrong, could be the initial position close to the wall $Y_2(t = 0) = -0.794$. As the results for settling spheres showed, the force coupling method does have difficulties in resolving the fluid flow, when the particle is close to the wall. Therefore two other simulations were performed, where the initial position of the sphere was moved approximately two radii and four radii, i.e. from $Y_2(t = 0) = -0.794$ to $Y_2(t = 0) = -0.6$ and from $Y_2(t = 0) = -0.794$ to $Y_2(t = 0) = -0.4$. The result from the computation with initial position $Y_2(t = 0) = -0.6$ is shown as the dashed line in figure 53(a). Obviously, changing the initial position does not change the result. Changing the postition to $Y_2(t = 0) = -0.4$ gave the same result. Therefore the quantitative discrepancy between the simulation and the experiment for the light sphere cannot

Exp. No.	$L_1 \times L_2 \times L_3$	$N_1 \times N_2 \times N_3$	$Re = \frac{L_2 U_m}{2\nu}$	$Fr = \frac{L_2 g}{2U_m^2}$	a
RL6052	$6.75 \times 2 \times 4.5$	$96 \times 64 \times 64$	102.12	1318.33	0.1895
RL6070	$6.75 \times 2 \times 4.5$	$96 \times 64 \times 64$	103.08	1318.33	0.1902

Table 16. Computational parameters for the buoyant spheres in a Poiseuille flow. The characteristic length $L = L_2/2$ and the characteristic velocity $U = U_m$, where $U_m = Q/(L_2 L_3)$ is the mean fluid velocity through the channel. The time step was set to $\delta t = 0.01$.

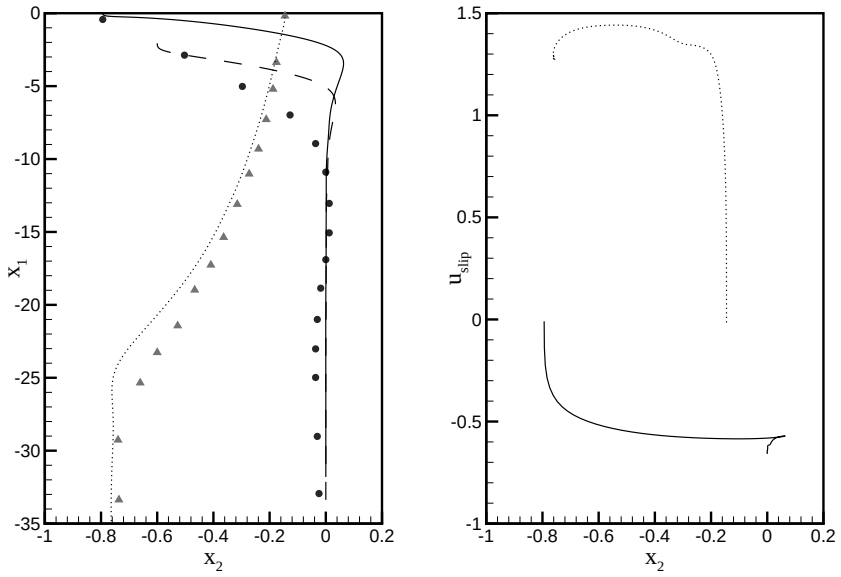

(a) Trajectories. The center plane is at $x_2 = 0$ and the wall is at $x_2 = -1$.

(b) Slip velocity $u_{slip} = V_1 - u_1^{Poiseuille}$.

Figure 53. Trajectories and slip velocity for buoyant spheres dispersed in a Poiseuille flow. Experiments: (•) *RL6052 and* (▲) *RL6070. Simulations:* (−) *RL6052 with* $Y_2(t = 0) = -0.794$, (− −) *RL6052 with* $Y_2(t = 0) = -0.6$, *and RL6070* $(\cdots)$.

be ascribed to difficulties for the force coupling method in the near wall region. An explanation for the discrepancy have not been found. The slip velocity for the light sphere is shown in figure 53(b). The buoyancy of the light sphere results in a lag velocity of the sphere being much higher than observed for a neutral sphere. In agreement with the arguments above and in section 3.4 the higher lag velocity leads to an equilibrium position closer to the center plane than for a neutral particle.

Three Neutrally Buoyant Spheres

The final example of particle dynamics at finite Reynolds numbers is three neutrally buoyant spheres dispersed in a Poiseuille flow. This example is included in order to give a first insight into the effect of interacting spheres on the lateral migration of the spheres. In the case of microflows several spheres may be present. Therefore it is of some importance to examine, whether the interaction among the spheres will increase or decrease the lateral motion. In the example presented here the Reynolds number for the flow is $Re = 100$ and the radius of the equal spheres is $a = L_2/16 = 0.125$. The computational parameters for the example in this section are given in table 17. In order to compare an additional simulation with only a single sphere was performed.

The normal positions as function of time for the three particles is shown in figure 54(a). The normal position of the corresponding single sphere is shown as the dash-dot-dot line. The sphere initially placed closest to the center plane move faster than the other two spheres, because it is placed in a stronger carrying flow. Similarly, the middle sphere move faster than the sphere closest to the wall. Due to the periodic boundary conditions, a sphere leaving the computational domain

Sim. No.	$L_1 \times L_2 \times L_3$	$N_1 \times N_2 \times N_3$	δt	$Re = \frac{L_2 U_m}{2\nu}$	a
1	$6 \times 2 \times 4$	$96 \times 64 \times 64$	0.025	100	0.125

Table 17. Computational parameters for the three neutrally buoyant spheres in a Poiseuille flow. The characteristic length $L = L_2/2$ and the characteristic velocity $U = U_c$, where U_c is the fluid velocity in the center plane of the channel.

reenters at the beginning of the domain. Therefore we are able to observe several interactions among the three spheres. The spheres were initially placed in the same streamwise-spanwise plane with $x_3 = 0$ and no movement was found in this direction. The streamwise velocities of the spheres are shown in figure 54(b). The lines correspond to the same spheres as in figure 54(a). The "bumps" on the curves in figures 54(a) and 54(b) correspond to a faster moving sphere overtaking a slower moving sphere. In the following the sphere closest to the center plane will be named *1*, the middle sphere will be called *2*, and the outermost sphere will be called *3*.

The first interaction appears at approximately $t = 28$, where sphere *1* overtakes sphere *3*. When the faster moving sphere *1* approaches sphere *3*, the disturbance flow of the slower moving sphere *3* cause sphere *1* to move in the negative normal direction. The distance between the centers of the two spheres is approximately $d \approx 3a$, and therefore the interaction is relatively weak. Two stronger interactions appears from $t = 50$ to $t = 65$. First, sphere *2* overtakes sphere *3*. Afterwards sphere *2* is overtaken by the sphere *1*. Consider the first interaction. When the faster moving sphere *2* approaches sphere *3*, the space between the sphere is too small for sphere *2* to pass. Consequently, it must go around sphere *3* as seen in the relatively large lateral motion in the negative normal direction in figure 54(a). Simultaneously sphere *2* pushes sphere *3* aside, forcing sphere *3* to move laterally toward the wall. In figure 54(b) it is seen that sphere *2* slows down as it approaches sphere *3*, simultaneously sphere *3* is accelerated. This indicates that sphere *2* pushes sphere *3* forward, before overtaking it. When sphere *2* pass sphere *3*, the imposed lateral motion of the sphere *3* results in the decrease of the streamwise velocity of the sphere, since it is pushed into a slower moving stream. Similarly, the lateral motion of sphere *2* causes its streamwise velocity to increase, because it is moving into a faster moving stream. This description of the interaction also holds for the other events observed in figures 54(a) and 54(b). In the final part of figure 54(a) for $t > 120$, sphere *3* suddenly moves toward the center plane of the channel. Before this point, the sphere reached the equilibrium position at approximately $t = 115$ and at the same time sphere *1* is catching up and pushes sphere *3* further to the wall, beyond the equilibrium position. When sphere *1* has passed, sphere *3* moves back toward the position it had, before it was overtaken by sphere *1*. During this lateral motion, the wall lift assist the sphere. This cause the sphere to overshoot the equilibrium position and move to a position closer to the center plane. Afterwards, at the very end of the figure, the sphere begins to move back towards the equilibrium position.

The line shown as $(- \cdot \cdot -)$ denotes the result for sphere *1*, when no other spheres are present. Clearly, the effect of the other two spheres is to decrease the lateral motion. The difference in the normal position at time $t = 100$ is almost a sphere radius. Consequently, the importance of the shear induced lift force will be smaller, when more spheres are present in the carrying flow. The slower lateral motion results in a higher streamwise velocity, since the sphere *1* spends more time in a faster moving stream, than the single sphere. This is shown in figure 54(b).

A series of vector plots for times from $t = 48$ to $t = 58$ are shown in figure 55 and 56. The chosen times correspond to the period of time in figure 54(a),

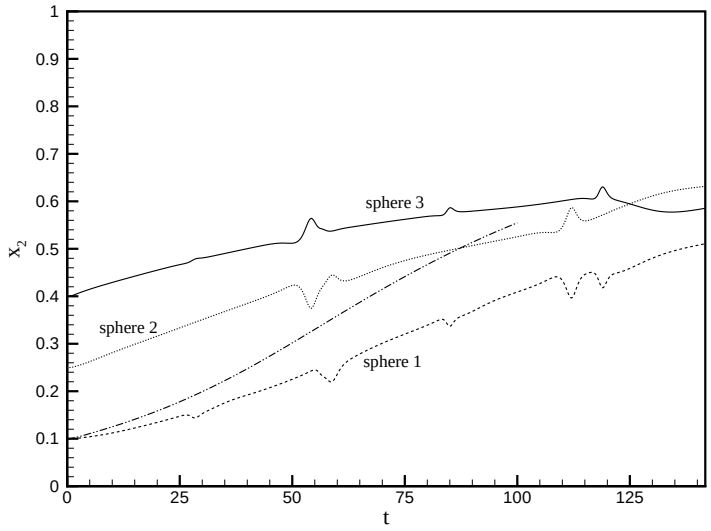

(a) Normal position. The wall is at $x_2 = 1$ and the channel center plane is at $x_2 = 0$.

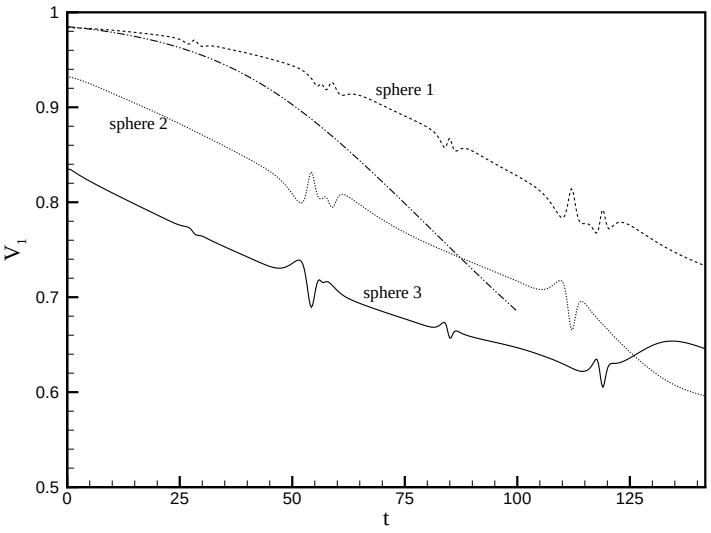

(b) Streamwise velocity

Figure 54. Normal positions and streamwise velocities of the three spehres dispersed in Poiseuille flow. The single sphere simulation is shown as the line $(- \cdot\cdot -)$.

where sphere *2* overtakes sphere *3*. The vector plots show the disturbance velocity created by the spheres, i.e. $u_i^{disturbance} = u_i - u_i^{Poiseuille}$. The figures are given in the streamwise-normal plane with $x_3 = 0$, i.e. through the centers of the spheres. Comparing the six figures, it becomes obvious that the three spheres create a wake behind them. Furthermore, the wake does not change very much as sphere *2* overtakes sphere *3*. Therefore the qualitative picture of the disturbance flow created by the three particles seems to be independent of the interaction of the spheres. In figure 55 all three spheres are placed in the wake structure. As sphere *2* begins to overtake sphere *3*, it pushes sphere *3* out of the wake structure, see

(a) $t = 48$. (b) $t = 50$. (c) $t = 52$.

Figure 55. Vector plots of the disturbance velocity field for three neutral spheres in Poiseuille flow. The snapshots are taken at times $t = 48$, $t = 50$, and $t = 52$ in the plane $x_3 = 0$. The disturbance flow is difference between the computed flow field and the undisturbed parabolic Poiseuille flow, i.e. $u_i^{disturbance} = u_i - u_i^{Poiseuille}$.

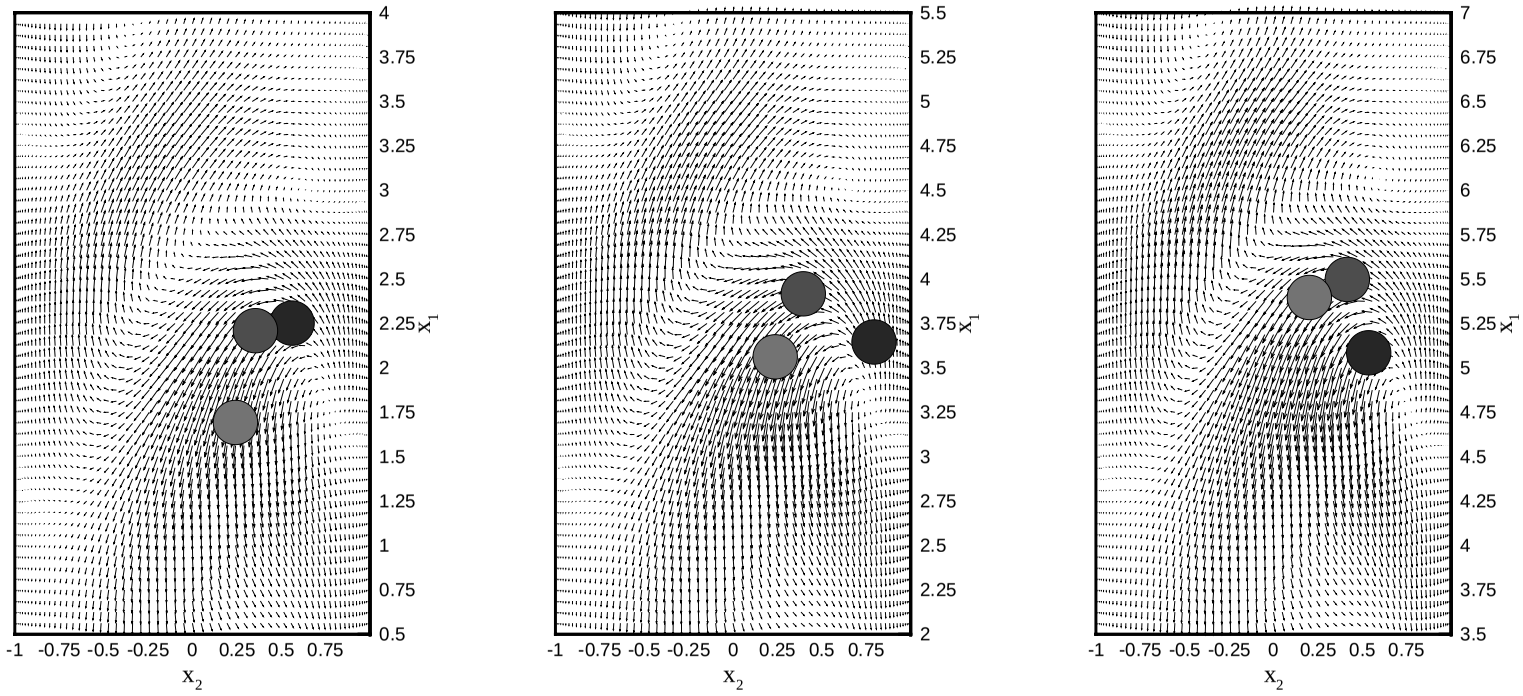

(a) $t = 54$. (b) $t = 56$. (c) $t = 58$.

Figure 56. Vector plots of the disturbance velocity field for three neutral spheres in Poiseuille flow. The snapshots are taken at times $t = 54$, $t = 56$, *and* $t = 58$ *in the plane* $x_3 = 0$. *The disturbance flow is difference between the computed flow field and the undisturbed parabolic Poiseuille flow, i.e.* $u_i^{disturbance} = u_i - u_i^{Poiseuille}$.

figure 56(a) and 56(b). After both sphere *2* and sphere *1* has passed sphere *3*, sphere *3* moves back into the wake structure, see figure 56(c).

The reason for the decrease in the streamwise velocity of sphere *2*, and the increase in the streamwise velocity of sphere *3*, can be depicted from the vector plots. As sphere *2* approaches sphere *3*, the backwards flow behind sphere *3* forces *2* to decelerate. Simultaneuosly, the movement of sphere *2* into the stream behind sphere *3*, force the flow away from sphere *3* to weaken. Therefore sphere *3* is accelerated by the carrying flow.

Finally, consider the flow around sphere *3* in figure 55(a), and compare this with the disturbance flow around the single spheres shown in figures 51(b) and 52(b). The velocity field on the bottom side of sphere *3* is very similar to the velocity field on the bottom side of the single spheres. The fluid is moving up and toward the sphere on the right side, and on the left side it moves down and away. On the top of sphere *3*, the velocity field is quite different. On the top right side it moves along the surface of the sphere, in contrast to the outwards flow observed for the single spheres. Furtermore, the fluid is flowing away toward the left near sphere *3* in figure 55(a), contrary to the inwards flow on the top left side observed in figures 51(b) and 52(b) for the single spheres. These changes in the flow on the top of the sphere obviously cause the slower lateral migration in the case of more spheres.

6 Concluding Remarks

The work presented in this thesis was initiated from the need of tools for designing microsystems, where particulate microflows are an inherent part. The discussion of particulate microflows showed, that these cover a range of different types. Some microsystems are designed to handle a few large particles, while others are designed to handle many particles in a range of sizes. Therefore a tool for simulation of particulate microflows should be able to cover the range from a few large particles to many particles of various sizes.

Although a huge amount of work has been done on the equation of motion for particles in fluid flows, the resulting equations are still limited to small particles far from any boundary and other particles. Furthermore, the effects of shear in the carrying fluid flow or the drafting, kissing and tumbling interaction between two particles is not included in the studies of the equation of motion. The lift forces due to the presence of a wall or to shear in fluid flow has been modelled by several researchers, but these models are only valid for small particles at low particle Reynolds numbers ($Re_p < 1$). Consequently, it is not possible to use any of the existing equations of motion, because the condition of small particles in general does not apply for the particulate microflows.

The lack of an equation of motion is the source for the development of an alternative method for computing particulate flows. The method is called the force coupling method. The first core part of the thesis has been on describing and developing the force coupling method. The development of the method was done in the frame of Stokes flow. The examples of two spheres settling parallel or perpendicular to their lines of center in Stokes flow showed excellent agreement with experiments. Similarly the examples of Stokes flow for a single sphere in a channel also gave good results. However, the lack of lubrication forces leads to an increasing error as the sphere comes close to a wall.

In the second core part of the thesis, the force coupling method was extended to finite Reynolds numbers, and a verification of the method was done by comparing the numerical results with experimental data. The experimental data were obtained from the experiments performed at Risø, and from experiments found in the literature. The numerical simulations of single, dual, and triple particles settling in a channel all showed good agreement with the experimental results. Furthermore, the method provided access to the disturbed fluid velocity field, and several observations regarding the interaction among two or three spheres were given. These observations gave some insight into the drafting, kissing and tumbling process between two interacting spheres. These observations are summarized as follows:

- The leading sphere drags fluid with it as it moves. Therefore the fluid in the wake of the leading sphere has a velocity in the same direction as the sphere. This causes the drag on the trailing sphere to decrease, because the acceleration that the trailing sphere has to apply to the fluid is diminished. Consequently, the trailing sphere moves faster than the leading sphere.
- Another effect of the wake, on the trailing sphere, is rotation. The wake from the leading sphere creates an asymmetric flow around the trailing sphere, thereby forcing it to rotate.
- When the trailing sphere catches up with the leading sphere, the higher velocity of the trailing sphere forces the fluid behind the leading sphere to accelerate. This causes the leading sphere to accelerate and move aside (when the line of centers of the two spheres is not parallel to the streamwise direction).

- In the tumbling process, the two spheres roll around each other.

The force coupling method also performed well for computing both neutrally buoyant and buoyant spheres in a Poiseuille flow. The numerical results of neutrally buoyant spheres were consistent with the experiments by Segre & Silberberg (1961) and the numerical simulations by Feng et al. (1994b). The simulation for $Re = 5$ showed that the shear induced lift force is very weak, and in the case of real particulate microflows, it may be neglected. This observation was further supported by the simulation with three neutrally buoyant spheres, where the interaction between the neutrally buoyant spheres led to a much slower migration of the individual spheres. Consequently, the effect of the shear induced lift force is decreased, when more spheres are present and the effect for neutrally buoyant spheres in particular microflows is negligible. The simulations with a heavy sphere showed qualitative and quantitative agreement with the experiments of Repetti & Leonard (1966), whereas the simulations with a light sphere showed only qualitative agreement. The reason for this difference between the light and the heavy sphere is unknown, and should be part of future investigations. Nevertheless, the results showed that changing the slip velocity of the sphere causes a change in the migration of the sphere. For the heavy sphere, the buoyancy force led to a positive slip velocity resulting in an increase in the shear induced lift force and thereby forcing the equilibrium position of the sphere to be closer to the wall. Moreover, the migration of the sphere is faster. For the light sphere, the buoyancy force led to an increase in the lag velocity. This causes the flow relative to the sphere to be stronger on the side of the sphere facing the center plane, than on the side facing the wall. This change in the relative flow, results in a change in the sign of the lift force, and the light sphere is moved to the center plane. Also in this case the migration is much faster than for a neutrally byouant sphere. Consequently, shear induced migration may be important if the particle is large and an external body force is acting on the particle in the streamwise direction, thereby creating a change in the slip velocity compared to the neutrally buoyant particles.

Effect of Particle Inertia

In the development of the force coupling method, particle inertia was neglected. Therefore it should be examined, whether this has any effect on the results presented in this thesis. Since fluid inertia is included, acceleration of the fluid occupying the volume of the particles is already included in the model. Therefore this must be subtracted from the particle inertia term, i.e. the particle inertia is given by

$$m_p \frac{dV_i}{dt} - m_f \frac{dV_i}{dt} \ .$$

Including this in the force monopole strength yields

$$F_i^n = \mathrm{V}_p^n \left(\rho_p - \rho_f\right) \left(g_i - \frac{dV_i^n}{dt}\right) \ .$$

Thus, particle inertia is only important, if

$$\left|\frac{dV_i^n}{dt}\right| \sim |g_i| \ .$$

A comparision of the absolute value of $\frac{dV_i^n}{dt}$ with the gravitaional acceleration is shown in table 18 for all the examples given in chapter 5. The particle acceleration has been computed from the particle velocities, and is therefore only an estimate of the actual value. However, the ratio of particle acceleration to the gravitational acceleration is small enough to ensure that the effect of particle inertia is negligible. Two exceptions exists, namely the simulation of a particle moving directly

Type of setup	Figure No.	$(\lvert\frac{dV_i}{dt}\rvert)$ (m^2/s)	$\frac{\lvert\frac{dV_i}{dt}\rvert}{\lvert g\rvert}$
Inclined Channel	22-25	$2.0 \cdot 10^{-3}$	$2.0 \cdot 10^{-4}$
Perpendicular to the walls	26	1.6	0.163
Parallel to the walls	28-29	0.049 (3.0)	$5 \cdot 10^{-3}$ (0.305)
Two particle exp. 1	31 & 32	$2.0 \cdot 10^{-3}$	$2.0 \cdot 10^{-4}$
Two particle exp. 2	39 & 40	$1.2 \cdot 10^{-3}$	$1.2 \cdot 10^{-4}$
Three particle exp.	43 & 45	$1.5 \cdot 10^{-3}$	$1.5 \cdot 10^{-4}$
Light sphere in Poiseuille flow	53	$7.44 \cdot 10^{-4}$	$7.59 \cdot 10^{-5}$
Heavy sphere in Poiseuille flow	53	$1.49 \cdot 10^{-3}$	$1.52 \cdot 10^{-4}$

Table 18. Values of the maximum particle acceleration in the results presented in chapter 5, and the ratio between the particle acceleration and the gravitional acceleration .

toward the bottom wall, and the simulation of the particle moving parallel to the walls. In the first case, the large ratio is obtained for the high Reynolds number, when the sphere is very close to the wall. Here, particle inertia will become important because the sphere decelerates very fast as the sphere approaches the wall. Therefore the lack of particle inertia may be another reason for the discrepancies observed in figure 27. In the case of the sphere moving parallel to the walls, the value in the parenthesis is taken in the initial part of the fall. Obviously, particle inertia must be important at the beginning of the fall, since the particle is accelerating. The discrepancy between the experiment by Feng et al. (1994a) and our numerical result could therefore be related to the lack of particle inertia.

In the simulation of the first experiment with two particles, it was hypothesized that particle inertia could be the reason for the difference observed in the trajectories after the kiss. The value in table 18 indicate that this is not the case. However, the gravitational acceleration only effects the streamwise component of the force monopole, while it is zero in the two other directions. In these directions the particle acceleration is not zero, and even a small contribution may lead to a different result (better result).

Conclusion

Summarizing the thesis, the following conclusions can be made:

- The existing equations of motion for a particle in a fluid flow are insufficient for computing particulate microflows.
- A force coupling method for computing particulate flows has been described and developed.
- The development and inclusion of the force dipole term, in the force coupling method, gives considerably better results.
- The force coupling method has been verified, and the results were found to be in agreement with experiments.
- The force coupling method is suitable for simulation of particulate microflows, and could therefore be used in the design phase of new microfluidic structures.

6.1 Future Directions

Although the force coupling method described and developed in this thesis performs very well, there is still a number of unsolved questions. These include:

- Lubrication forces.

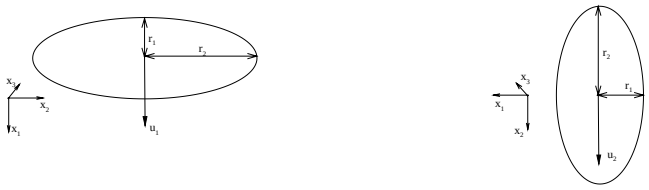

(a) Ellipsoid settling along x_1 axis with velocity u_1

(b) Ellipsoid settling along x_2 axis with velocity u_2

Figure 57. Ellipsoid settling along the axes of symmetry x_1 or x_2 (x_3)

- Including particle inertia.
- Non-spherical particles.

As shown in the Stokes flow examples, lubrication forces are not included in the force coupling model. In order to use the model for spheres close to walls, lubrication forces must be included and this work is currently undergoing at Brown University. Although the considerations above concerning particle inertia indicated that the effect of particle inertia is small, the results for the two particle interaction and the single sphere moving perpendicular or parallel to the walls suggest that particle inertia should be included. This is not a trivial task, because no explicit knowledge about the particle acceleration is avaible.

Finally, the method could be extended to include non-spherical particles. This can be done straightforward by introducing a length scale σ for each direction. A simple example is an elliptical particle, where two length scales are necessary; one for the minor axis and one for major axis. In an initial study, the author matched the settling velocity of an ellipsoid in Stokes flow computed using the force coupling method, with the analytical settling velocity from Happel & Brenner (1965). Two cases were investigated, these are shown in figure 57. The match was done similarly to the match for the sphere given in Appendix A.3. Matching the settling velocities in these cases resulted in the following ratios

$$\frac{r_1}{\sigma_1} = \sqrt{\pi} \qquad \text{and} \qquad \frac{r_2}{\sigma_2} = \sqrt{\pi} \ .$$

This is exactly the same ratio as for the sphere, and surely indicates that the method can be extended to non-spherical particles.

Since non-spherical particles do not have the complete symmetry of the sphere, knowledge about the orientation of the particles are necessary. This is obtained from the angular velocity of the particle and the external torque acting on the particle, i.e.

$$T_i = I_{ij} \frac{d\Omega_j}{dt} \ ,$$

where I_{ij} is the moment of inertia tensor.

References

Auton T.R., Hunt J.C.R. and Prud'homme M. (1988). The force exerted on a body in inviscid unsteady non-uniform rotational flow. *J. Fluid Mechanics*, **197**, 241-257.

Barton I.E. (1996). Computation of dilute particulate laminar flow over a backward-facing step. *Int. J. Numerical Meth. Fluids.*, **22**, 211-221.

Ben Salem M. and Oesterle B. (1998). A shear flow around a spinning sphere: Numerical study at moderate Reynolds numbers. *Int. J. Multiphase Flows*, **24**(4), 563-585.

Betten J. (19??). *Tensorrechnung fur Ingenieure*. B.G.-Teubner Stuttgart. 320 p.

Bird R.B., Armstrong R.C. and Hassager O. (1987). *Dynamics of Polymeric Liquids, Volume 1 Fluid Mechanics*. 2nd edition. Wiley-Interscience. 650 p.

Blankenstein G., Scampavia L., Branebjerg J., Larsen U.D. and Ruzicka J. (1996). Flow switch for analyte injection and cell/particle sorting. *Analytical Methods & Instrumentation, Special Issue μTAS'96*.

Brady J.F. and Bossis G. (1988). Stokesian Dynamics. *Ann. Rev. Fluid Mech.*, **20**, 111-157.

Canuto C., Hussaini M.Y., Quarteroni A. and Zang T.A. (1987). *Spectral Methods in Fluid Dynamics*, Springer-Verlag, Springer Series in Computational Physics, 557 p.

Chang E.J. and Maxey M.R. (1995). Unsteady flow about a sphere at low to moderate Reynolds number. Part 2. Accelerated motion. *J. Fluid Mechanics*, **303**, 133-153.

Cherukat P. and McLaughlin J.B. (1990). Wall-induced lift on a sphere. *Int. J. Multiphase Flow*, **16**(5), 899-907.

Cherukat P., McLaughlin J.B. and Graham A.L. (1994). The inertial lift on a rigid sphere translating in a linear shear flow field. *Int. J. Multiphase Flow*, **20**(2), 339-353.

Clift R., Grace J.R. and Weber M.E. (1978). *Bubbles, Drops, and Particles*. Academic Press. 380 p.

Dalziel S.B. (1992). Decay of rotating turbulence: some particle tracing experiments. *Appl. Scientific Research*, **49**, 217-244.

Dent G.L. (1999). *Aspects of particle sedimentation in dilute flows at finite Reynolds numbers*. Ph.D. thesis. Brown University, Providence, R.I. 97 p.

Dent G.L. and Maxey M.R. (2000). Flow through a periodic array of particles at finite Reynolds number. *submitted for publication in Phys. Fluids*, May 2000.

Domgin J.F., Huilier D.G.F., Karl J.J., Gardin P., and Barnage H. (1998). Experimental and numerical study of rigid particles, droplets and bubbles motion in quiescent and turbulent flows - Influence of the history force -. *Third International Conference on Multiphase Flow, ICMF98*, June 8-12, Lyon, France.

Dratler D.I. and Schowalter W.R. (1996). Dynamic simulation of suspensions of non-Brownian hard spheres. *J. Fluid Mech.*, **325**, 53-77.

Druzhinin O.A. and Ostrovsky L.A. (1994). The influence of Basset force on particle dynamics in two-dimensional flows. *Physica D*, **74**, 34-43.

Durlofsky L., Brady J.F. and Bossis G. (1987). Dynamic simulation of hydrodynamically interacting particles. *J. Fluid Mech.*, **180**, 21-49.

Durlofsky L. and Brady J.F. (1989). Dynamic simulation of bounded suspensions of hydrodynamically interacting particles. *J. Fluid Mech.*, **200**, 39-67.

Elghobashi S. and Truesdell G.C. (1993). On the two-way interaction between homogeneuos turbulence and dispersed solid particles. I: Turbulence modification. *Phys Fluids A*, **5**(7), 1790-1801.

Elghobashi S. (1994). On predicting particle-laden turbulent flows. Proc. 7th workshop on *Two-Phase Flow Predictions*.

Feng J., Hu H.H. and Joseph D.D. (1994a). Direct numerical simulation of initial value problems for the motion of solid bodies in a Newtonian fluid. Part 1. Sedimentation. *J. Fluid Mechanics*, **261**, 95-134.

Feng J., Hu H.H. and Joseph D.D. (1994b). Direct numerical simulation of initial value problems for the motion of solid bodies in a Newtonian fluid. Part 2. Couette and Poiseuille flows. *J. Fluid Mechanics*, **277**, 271-301.

Flockhart S.M. and Dhariwal R.S. (1998). Experimental and numerical investigation into the flow characteristics of channels etched in <100> silicon. *J. Fluids Engineering*, **120**, 291-295.

Fortes A.F., Joseph D.D and Lundgren T.S. (1987). Nonlinear mechanics of fluidization of beds of spherical particles. *J. Fluid Mechanics*, **177**, 467-483.

Gad-el-Hak M. (1999). The fluid mechanics of microdevices - The Freeman scholar lecture. *J. Fluids Engineering*, **121**, 5-33.

Ganatos P., Weinbaum S. and Pfeffer R. (1980a). A strong interaction theory for the creeping motion of a sphere between plane parallel boundaries. Part 1. Perpendicular motion. *J. Fluid Mech.*, **99**, 739-753.

Ganatos P., Weinbaum S. and Pfeffer R. (1980b). A strong interaction theory for the creeping motion of a sphere between plane parallel boundaries. Part 2. Parallel motion. *J. Fluid Mech.*, **99**, 755-783.

Gravesen P., Branebjerg J. and Søndergård Jensen O. (1993). Microfluidics - A Review. *J. Micromechanics and Microengineering*, **3**(4), 168-182.

Glasgow I.K., Zeringue H.C., Beebe D.J., Choi S.-J., Lyman J.T. and Wheeler M.B. (1998). Individual embryo transport and retention on a chip. *Micro Total Analysis Systems '98*, Ed. Harrison D.J. and van den Berg A., Kluwer Academic Pub., 199-202.

Gondret P., Hallouin E., Lance M. and Petit L. (1999). Experiments on the motion of a solid sphere toward a wall: From viscous dissipation to elastohydrodynamic bouncing. *Phys. Fluids*, **11**(9), 2803-2805.

Gottlieb D. and Orszag S.A. (1977). *Numerical Analysis of Spectral Methods*. SIAM Publications, SIAM Philadelphia, CBMS-NSF.

Handler R., Swean T.F. and Leighton R.I. (1993). Length scales and the energy balance for turbulence near a free surface. *AIAA J.*, **31**, 1998.

Happel J. and Brenner H. (1965). *Low Reynolds number Hydrodynamics*. Prentice-Hall. 551 p.

Harper M.J., Turner C.M. and Shaw J.E.A. (1995). *Simulation and Design of Microsystems and Microstructures*, Proc. 1st Int. Conf. MICROSIM'95, Ed. Adey R.A., 155-163.

Hasimoto H. and Sano O. (1980). Stokeslets and eddies in creeping flow. *Ann. Rev. Fluid Mech.*, **12**, 335-363.

Ho C.-M. and Tai Y.-C. (1998). Micro-electro-mechanical-systems (MEMS) and fluid flows. *Annu. Rev. Fluid Mech.*, **30**, 579-612.

Jayaweera K.O.L.F., Mason B.J. and Slack G.W. (1964). The behaviour of clusters of spheres falling in a viscous fluid. Part 1. Experiment. *J. Fluid Mechanics*, **20**(1), 121-128.

Jeffrey R.C. and Pearson J.R.A. (1965). Particle motion in laminar vertical tube flow. *J. Fluid Mechanics*, **22**(4), 721-735.

Johnson A.A. and Tezduyar T.E. (1996). Simulation of multiple spheres falling in a liquid-filled tube. *Comput. Meth. Appl. Mech. Engineering*, **134**, 351-373.

Kaye G.W.C. and Laby T.H. (1973). *Tables of physical and chemical constants*. 14th Edition. Longman.

Kim J., Moin P. and Moser R. (1987). Turbulence statistics in fully developed channel flow at low Reynolds number. *J. Fluid Mechanics*, **177**, p.138-140.

Kim I., Elghobashi S., and Sirignano W.A. (1998). On the equation for spherical-particle motion: effect of Reynolds and acceleration numbers. *J. Fluid Mechanics*, 367, 221-253.

Kim S. and Karrila S.J. (1991). *Microhydrodynamics: Principles and Selected Applications*. Butterworth-Heinemann. 507 p.

Kurose R. and Komori S. (1999). Drag and lift forces on a rotating sphere in a linear shear flow. *J. Fluid Mechanics*, **384**, 183-206.

Langlois W.E. (1964). *Slow Viscous Flow*. MacMillan. 229 p.

Lawrence C.J. and Mei R. (1995). Long-time behaviour of the drag on a body in impulsive motion. *J. Fluid Mechanics*, **283**, 307-327.

Liang L and Michaelides E.E. (1992). The magnitude of Basset forces in unsteady multiphase flow computations. *J. Fluids Engineering*, **114**, 417-419.

Lomholt S., Lynov J.-P. and Telleman P. (1998). Numerical simulation of magnetic separation of particles in a rectangular microchannel. *Micro Total Analysis Systems '98*, Ed. Harrison D.J. and van den Berg A., Kluwer Academic Pub., 419-422.

Lomholt S., Stenum B. and Maxey M.R. (2001). Force coupling method for computing particle dynamics in fluid flows. Accepted for publication in *Intl. J. Multiphase Flow*.

Lomholt S. and Maxey M.R. (2001a). Force-coupling method for particulate two-phase flow. Stokes flow. Submitted to *J. Comput. Phys.*

Lomholt S. and Maxey M.R. (2001b). Nonlinear effects in the force-coupling method for particulate two-phase flow. Submitted to *Phys Fluids*.

Lovalenti P.M. and Brady J.F. (1993a). The hydrodynamic force on a rigid particle undergoing arbitrary time-dependent motion at small Reynolds number. *J. Fluid Mechanics*, **256**, 561-605.

Lovalenti P.M. and Brady J.F. (1993b). The force on a sphere in a uniform flow with small-amplitude oscillations at finite Reynolds number. *J. Fluid Mechanics*, **256**, 607-614.

Lovalenti P.M. and Brady J.F. (1995). The temporal behaviour of the hydrodynamic force on a body in response to an abrupt change in velocity at small but finite Reynolds number. *J. Fluid Mechanics*, **293**, 35-46.

Maxey M.R. and Riley J.J. (1983). Equation of motion for a small rigid sphere in a non-uniform flow. *Phys. Fluid*, **26**(4), 883-889.

Maxey M.R. (1987). The motion of small spherical particles in a cellular flow field. *Phys. Fluids*, 30(7), 1915-1928.

Maxey M.R., Patel B.K., Chang E.J. and Wang L.-P. (1997). Simulations of dispersed turbulent mulitphase flow. *Fluid Dynamics Research*, **20**, 143-156.

Maxey M.R. and Dent G.L. (1998). Some features of particle sedimentation at finite Reynolds numbers. *Third International Conference on Multiphase Flow, ICMF98*, June 8-12, Lyon, France.

Maxey M.R. (2000a). Private communication.

Maxey M.R. (2000b). Private Communication.

Maxey M.R. and Patel B.K. 2001. Localized force representations for particles sedimenting in stokes flow. *Intl. J. Multiphase Flow* **27**, 1603-1626.

McLaughlin J.B. (1991). Inertial migration of a small sphere in linear shear flows. *J. Fluid Mechanics*, **224**, 261-274.

McLaughlin J.B. (1993). The lift on a small sphere in wall-bounded linear shear flows. *J. Fluid Mechanics*, **246**, 249-265.

Mei R., Lawrence C.J. and Adrian R.J. (1991). Unsteady drag on a sphere at finite Reynolds Number with small fluctuations in the free-stream velocity. *J. Fluid Mechanics*, **233**, 613-631.

Mei R. and Adrian R.J. (1992). Flow past a sphere with an oscillation in the free-stream velocity and unsteady drag at finite Reynolds numbers. *J. Fluid*

Mechanics, **237**, 323-341.

Mei R. (1994). Flow due to an oscillating sphere and an expression for the unsteady drag on the sphere at finite Reynolds numbers. *J. Fluid Mechanics*, 270, 133-174.

Michaelides E.E. (1997). Review - The transient equation of motion for particles, bubbles, and droplets. *J. Fluids Engineering*, **119**, 233-247.

Raju N. and Meiburg E. (1997). Dynamics of small, spherical particles in vortical and stagnation point flow fields. *Phys. Fluids*, **9**(2), 299-314.

Reeks M.W. and McKee S. (1984). The dispersive effects of the Basset history forces on particle motion in turbulent flow. *Phys. Fluid*, **27**, 1573-1582.

Repetti R.V. and Leonard E.F. (1966). Physical basis for the axial accumulation of red blood cells. *Chem. Engineering Prog. Symp. Series* **62**(66), 80-87.

Pfahler J., Harley J. and Bau H. (1991). Gas and liquid flow in small channels. *Micromechanical Sensors, Actuators and Systems*, ASME Proceedings, **32**, 49-60.

Rubinow S.I. and Keller J.B. (1961). Transverse force on a spinning sphere moving in a viscous fluid. *J. Fluid Mechanics*, **11**, 447-459.

Saffman P.G. (1965). The lift on a small sphere in a slow shear flow. *J. Fluid Mechanics*, **22**, part 2, 385-400.

Saffman P.G. (1973). On the settling speed of free and fixed suspensions. *Studies in Appl. Math.*, **LII**(2), 115-127.

Schwarz H.R. (1993). *Numerische Mathematik*. B.G. Teubner, Stuttgart. 575 p.

Segre G. and Silberberg A. 1961. Radial particle displacements in Poiseuille flow of suspensions. *Nature* **189**, 209-210.

Shaw J., Miller B., Turner C., Harper M. and Graham S. (1996). Mass transfer of species in micro-contactors: CFD modelling and experimental validation. *Analytical Methods & Instrumentation, Special Issue μTAS'96*

Shinohara M. (1998). Lateral migration of particles sedimenting in a viscous fluid inside a cylinder. *Third International Conference on Multiphase Flow, ICMF98*, June 8-12, Lyon, France.

Sommerfeld M. and Huber N. (1999). Experimental analysis and modelling of particle-wall collisions. *Int. J. Multiphase Flow*, **25**, 1457-1489.

Sommerfeld M. (2000). Overview and Fundamentals. Lecture Series 2000-06 on *Theoretical and Experimental Modeling of Particulate Flows*, April 3-7, von Karman Institute for Fluid Dynamics, Bruxelles.

Spiering V.L., van den Berg A., Lammerink T.S.J., Fluitman J.H.J. and Elwenspoek M. (1997). *Micro Devices for Fluid Handling*. 2nd edition. Swiss Foundation for Research in Microtechnology. 90 p.

Squires K.D. and Eaton J.K. (1990). Particle response and turbulence modification in isotropic turbulence. *Phys. Fluids A*, **2**(7), 1191-1203.

Telleman P., Larsen U.D., Philip J., Blankenstein G. and Wolff A. (1998). Cell sorting in microfluidic systems. *Micro Total Analysis Systems '98*, Ed. Harrison D.J. and van den Berg A., Kluwer Academic Pub., 39-44.

Thompson P.A. and Troian S.M. (1997). A general boundary condition for liquid flow at solid surfaces. *Nature*, **389**, Sep 25, 360-362.

Uijttewaal W.S. and Oliemans R.V.A. (1996). Particle dispersion and deposition in direct numerical and large eddy simulations of vertical pipe flows. *Phys. Fluids*, **8**(10), 2590-2604.

Vasseur P. and Cox R.G. (1977). The lateral migration of sphereical particles sedimentiing in a stagnant bounded fluid. *J. Fluid Mechanics*, **80**(3), 561-591.

Vojir D.J. and Michaelides E.E. (1994). Effect of the history term on the motion of rigid spheres in a viscous fluid. *Int. J. Multiphase Flow*, **20**(3), 547-556.

Wang Q. and Squires K.D. (1996). Large eddy simulation of particle-laden turbulent channel flow. *Phys. Fluids*, **8**(5), 1207-1223.

White F.M. (1991). *Viscous Fluid Flow*. 2nd edition. McGraw-Hill. 614 p.

Wolff A., Larsen U.D., Blankenstein G., Philip J. and Telleman P. (1998). Rare event cell sorting in a microfluidic system for application in prenantal diagnosis. *Micro Total Analysis Systems '98*, Ed. Harrison D.J. and van den Berg A., Kluwer Academic Pub., 77-80.

Wu J. and Manasseh R. (1998). Dynamics of dual-particles settling under gravity. *Int. J Multiphase Flow*, **24**, 1343-1358.

Yager P., Bell D., Brody J.P., Qin D., Cabrera C., Kamholz A. and Weigl B. (1998). Applying microfluidic chemical analytical systems to imperfect samples. *Micro Total Analysis Systems '98*, Ed. Harrison D.J. and van den Berg A., Kluwer Academic Pub., 207-212.

A Appendix A

In this Appendix some derivations used for the description of the loalized finite force coupling method in chapter 4 is given. Some of the derivations and integrals have been computed using MathCad. The sections A.1, A.2 and A.3 corresponds to the work described by Maxey & Patel (2000).

A.1 The Oseen Tensor for the Finite Valued Force Representation

In the derivation we will need the fundamental solution to the Poisson equation

$$\nabla^2 G = \Delta(\mathbf{x}) \tag{A.1}$$

for a sphere in an infinite volume. Since G only depends on the radial distance, $r = x_i x_i$, (A.1) becomes

$$\frac{1}{r^2}\frac{d}{dr}\left(r^2\frac{dG}{dr}\right) = \Delta(x_i) \;\Rightarrow\; G(r) = -\frac{C_1}{r} + C_2 - \frac{1}{4\pi r}\mathrm{erf}\left(\frac{r}{\sqrt{2}\sigma}\right) \tag{A.2}$$

Thus, with the assumption that $G(r)$ tend to zero at large distances and is finite at $r = 0$, the constants C_1 and C_2 are zero and the solution is

$$G(r) = -\frac{1}{4\pi r}\mathrm{erf}\left(\frac{r}{\sqrt{2}\sigma}\right) \tag{A.3}$$

The new Oseen tensor for the finite valued force representation is determined from the flow induced by a force monopole of strength F_i placed at the origin. Such a flow satisfies

$$\frac{\partial u_i}{\partial x_i} = 0 \tag{A.4}$$

$$-\frac{\partial p}{\partial x_i} + \mu\frac{\partial^2 u_i}{\partial x_j \partial x_j} = -F_i\Delta(\mathbf{x},\sigma) \tag{A.5}$$

The solution to these equations yields the Oseen tensor $O_{ij}(\mathbf{x})$ corresponding to the finite localized force envelope. In terms of a Fourier transform

$$\check{u}_i = \frac{1}{(2\pi)^3}\int u_i(\mathbf{x})\exp(-\mathrm{i}k_j x_j)\,d^3\mathbf{x} \tag{A.6}$$

equations (A.4) and (A.5) become

$$\mathrm{i}k_i\check{u}_i = 0 \tag{A.7}$$

$$-\mathrm{i}k_i\check{p} - \mu k^2\check{u}_i = -F_i\check{\Delta} \tag{A.8}$$

where $k^2 = k_j k_j$ and

$$\check{\Delta} = \frac{1}{(2\pi)^3}\exp(-k^2\sigma^2/2) \tag{A.9}$$

These four equations with four unknowns can be solved analytically and the Fourier transformed velocity is

$$\check{u}_i = \frac{F_j}{\mu k^2}\left(\delta_{ij} - \frac{k_i k_j}{k^2}\right)\check{\Delta} \tag{A.10}$$

The Fourier transform of the Oseen tensor corresponding to equations (A.4) and (A.5) is then

$$\check{O}_{ij} = \frac{1}{\mu k^2}\left(\delta_{ij} - \frac{k_i k_j}{k^2}\right)\check{\Delta} \tag{A.11}$$

The inverse of $\check{O}_{ij}$ can be found without performing the inverse transformation. From (A.11) we see that the inverse tensor O_{ij} has an isotropic dependency on x_i. Therefore it can be written as

$$O_{ij} = A(r)\,\delta_{ij} + B(r)\,x_i x_j \tag{A.12}$$

The scalar functions $A(r)$ and $B(r)$ are determined from two conditions. First the trace of O_{ij} must be equal to the inverse Fourier transformed of the trace of $\check{S}_{ij}$, i.e.

$$O_{ii} = \mathrm{FT}^{-1}\left(\check{O}_{ii}\right) = \mathrm{FT}^{-1}\left(\frac{2}{\mu k^2}\check{\Delta}(k_i)\right) \tag{A.13}$$

where FT^{-1} denotes the inverse Fourier transform. This condition yields

$$3A(r) + r^2 B(r) = -\frac{2}{\mu}G(r) \tag{A.14}$$

where

$$G(r) = -\mathrm{FT}^{-1}\left(\frac{1}{k^2}\check{\Delta}(k_i)\right) \tag{A.15}$$

is a result from Fourier transforming equation (A.3). Due to the incompressibility of the fluid, the divergence of O_{ij} must be zero, i.e.

$$\frac{\partial u_i}{\partial x_i} = \frac{\partial}{\partial x_i}\left(F_j O_{ij}\right) = F_j \frac{\partial O_{ij}}{\partial x_i} = 0 \tag{A.16}$$

this is the second condition and gives

$$\frac{dA(r)}{dr} + r^2\frac{dB(r)}{dr} + 4rB(r) = 0 \tag{A.17}$$

Inserting dA/dr from equation (A.14) into equation (A.17) results in a first order differential equation for B

$$\frac{dB}{dr} + \frac{5}{r}B = \frac{1}{\mu r}\frac{dG(r)}{dr} \;\Rightarrow\; \frac{d}{dr}\left(r^5 B(r)\right) = \frac{r^3}{\mu}\frac{dG(r)}{dr} \tag{A.18}$$

and the solution to this is

$$B(r) = \frac{1}{8\pi\mu r^3}\left(\left(1 - \frac{3\sigma^2}{r^2}\right)\mathrm{erf}\left(\frac{r}{\sqrt{2}\,\sigma}\right) + \frac{6\sigma}{\sqrt{2\pi}\,r}\exp\left(-\frac{r^2}{2\sigma^2}\right)\right) \tag{A.19}$$

and then inserting $B(r)$ into equation (A.14) gives

$$A(r) = \frac{1}{8\pi\mu r}\left(\left(1 + \frac{\sigma^2}{r^2}\right)\mathrm{erf}\left(\frac{r}{\sqrt{2}\,\sigma}\right) - \frac{2\sigma}{\sqrt{2\pi}\,r}\exp\left(-\frac{r^2}{2\sigma^2}\right)\right) \tag{A.20}$$

The Oseen tensor for the finite localized force representation becomes

$$\begin{aligned} O_{ij} = {} & \frac{1}{8\pi\mu r}\left(\delta_{ij} + \frac{x_i x_j}{r^2}\right)\mathrm{erf}\left(\frac{r}{\sqrt{2}\,\sigma}\right) \\ & + \frac{\sigma^2}{8\pi\mu r^3}\left(\delta_{ij} - \frac{3x_i x_j}{r^2}\right)\mathrm{erf}\left(\frac{r}{\sqrt{2}\,\sigma}\right) - \frac{\sigma^4}{2\mu r^2}\left(\delta_{ij} - \frac{3x_i x_j}{r^2}\right)\Delta(x_i) \end{aligned} \tag{A.21}$$

A.2 The Flow Field due to a Degenerate Force Quadrupole

The flow field due to a degenerate force quadrupole is determined from

$$\frac{\partial u_i}{\partial x_i} = 0 \tag{A.22}$$

$$-\frac{\partial p}{\partial x_i} + \mu\frac{\partial^2 u_i}{\partial x_j \partial x_j} = -\frac{a^2}{6}F_i\delta_{jk}\frac{\partial^2\Delta(x_i)}{\partial x_j \partial x_k} \tag{A.23}$$

In terms of the Fourier transformation (A.6) these equations become

$$-\mathrm{i}k_i\check{u}_i = 0 \tag{A.24}$$

$$-\mathrm{i}k_i\check{p} - \mu k^2\check{u}_i = k^2\frac{a^2}{6}F_i\check{\Delta} \tag{A.25}$$

As above in section A.1 these four equations can be solved analytically. This results in a Fourier transformed fluid velocity

$$\check{u}_i = \frac{1}{\mu}\left(\delta_{ij} - \frac{k_ik_j}{k^2}\right)\check{\Delta}\frac{a^2}{6}F_i \tag{A.26}$$

The first term in this is just the Fourier transformed of the envelope function (A.9) and the inverse of the second term is found using (A.15), hence the velocity field due to the degenerate force qaudrupole is

$$u_i(\mathbf{x}) = \frac{a^2}{6\mu}\left(F_j\frac{\partial^2 G(\mathbf{x})}{\partial x_j\partial x_i} - F_i\Delta(\mathbf{x})\right) \tag{A.27}$$

A.3 The Length Scale σ Related to the Force Monopole

The length scale related to the force monopole is determined by matching the particle velocity found from

$$\tilde{u}_i = \int u_i(\mathbf{x})\,\Delta(\mathbf{x},\sigma)\,d^3\mathbf{x} \tag{A.28}$$

with the Stokes settling velocity. In (A.28) $u_i(\mathbf{x})$ is the velocity field resulting from the single force monopole given by the Stokes drag

$$F_1 = 6\pi\mu a W_1 \tag{A.29}$$

where W_1 is the Stokes settling velocity and the sphere is moves in the x_1 direction.

Using the convolution theorem for Fourier transformations the integral in (A.28) can be computed as

$$\int u_1(\mathbf{x}')\,\Delta(\mathbf{x}'-\mathbf{x},\sigma)\,d^3\mathbf{x}' = \frac{1}{(2\pi)^3}\int \check{u}_1(\mathbf{k})\,\check{\Delta}(\mathbf{k},\sigma)\exp(-\mathrm{i}k_jx_j)\,d^3\mathbf{k} \tag{A.30}$$

with $x_i = 0$ this becomes

$$\int u_1(\mathbf{x})\,\Delta(\mathbf{x},\sigma)\,d^3\mathbf{x} = \frac{1}{(2\pi)^3}\int \check{u}_1(\mathbf{k})\,\check{\Delta}(\mathbf{k},\sigma)\,d^3\mathbf{k} \tag{A.31}$$

Inserting $\check{u}_1(\mathbf{k})$ from (A.10) and $\check{\Delta}(\mathbf{k},\sigma)$ from (A.9) the volume averaged velocity becomes

$$\begin{aligned}\tilde{u}_1 &= \frac{6\pi aW_1}{(2\pi)^3}\iiint\frac{1}{k^2}\left(1-\frac{k_1^2}{k^2}\right)\exp\left(-k^2\sigma^2\right)dk_1dk_2dk_3\\ &= \frac{6\pi aW_1}{(2\pi)^3}\int_0^\infty\int_0^\pi\int_0^{2\pi}\frac{1}{r^2}\left(1-\frac{r^2\sin^2\theta\cos^2\phi}{r^2}\right)\exp\left(-r^2\sigma^2\right)r^2\sin\theta d\phi d\theta dr\\ &= \frac{6\pi aW_1}{(2\pi)^3}\int_0^\infty\int_0^\pi\int_0^{2\pi}\left(\sin\theta-\sin^3\theta\cos^2\phi\right)\exp\left(-r^2\sigma^2\right)\sin\theta d\phi d\theta dr\end{aligned} \tag{A.32}$$

where a substitution from cartesian coordinates to spherical coordinates ($k_1 = r\sin\theta\cos\phi$, $k_2 = r\sin\theta\sin\phi$, $k_3 = r\cos\theta$, and $k^2 = r^2$) is used in the second

equality. The solution to (A.32) is easily computed with the following integrals

$$\int_0^\pi \sin\theta d\theta = 2 \tag{A.33}$$

$$\int_0^\pi \sin^3\theta d\theta = \frac{4}{3} \tag{A.34}$$

$$\int_0^{2\pi} \cos^2\phi d\phi = \pi \tag{A.35}$$

$$\int_0^\infty \exp\left(-r^2\sigma^2\right) = \frac{\sqrt{\pi}}{2\sigma} \tag{A.36}$$

Inserting these in (A.32) the result is

$$\tilde{u}_1 = \frac{6\pi a W_1}{(2\pi)^3}\frac{\sqrt{\pi}}{2\sigma}\left(2\pi 2 - \pi\frac{4}{3}\right) = \frac{6\pi a W_1}{8\pi^3}\frac{\sqrt{\pi}}{2\sigma}\frac{8\pi}{3}$$

$$= \frac{24\pi^2\sqrt{\pi}a}{24\pi^3\sigma}W_1 = \frac{a}{\sigma}\frac{1}{\sqrt{\pi}}W_1$$

If the ratio of the sphere radius to the Gaussian length scale is set to

$$\frac{a}{\sigma} = \sqrt{\pi} \tag{A.37}$$

the volume averaged velocity will match the Stokes settling. Therefore (A.37) is chosen as the value of a/σ.

A.4 The Flow Field due to a Rotating Sphere

The flow field due to a rotating sphere is given by a force dipole specified by the external torque on the sphere. The external torque is defined as (49)

$$T_i = 8\pi\mu a^3\Omega_i^p \tag{A.38}$$

where Ω_i^p is a prescribed angular velocity. The force dipole strength due to this torque is (Kim & Karrila (1991))

$$T_{ij} = \frac{1}{2}\varepsilon_{ijk}T_k = 4\pi\mu a^3\begin{bmatrix} 0 & \Omega_3 & -\Omega_2 \\ -\Omega_3 & 0 & \Omega_1 \\ \Omega_2 & -\Omega_1 & 0 \end{bmatrix} \tag{A.39}$$

Then the flow field due to the rotating sphere is given by

$$\frac{\partial u_i}{\partial x_i} = 0 \tag{A.40}$$

$$-\frac{\partial p}{\partial x_i} + \mu\frac{\partial^2 u_i}{\partial x_j \partial x_j} = -T_{ij}\frac{\partial\Delta\left(\mathbf{x},\sigma_D\right)}{\partial x_j} \tag{A.41}$$

similarly to the flow field from the force monopole the solution to these equations are found in Fourier space. Consider a sphere rotating with $\Omega_i^p = (0,0,\Omega)$, then the torque dipole strength becomes

$$T_{ij} = 4\pi\mu a^3\Omega\begin{bmatrix} 0 & 1 & 0 \\ -1 & 0 & 0 \\ 0 & 0 & 0 \end{bmatrix} \tag{A.42}$$

and the Fourier transformed of (A.40) and (A.41) beomes

$$\mathrm{i}k_i\check{u}_i = 0 \tag{A.43}$$

$$-\mathrm{i}k_1\check{p} - \mu k^2\check{u}_1 = -4\pi\mu a^3\Omega\mathrm{i}k_2\check{\Delta}\left(\mathbf{k},\sigma_D\right) \tag{A.44}$$

$$-\mathrm{i}k_2\check{p} - \mu k^2\check{u}_2 = 4\pi\mu a^3\Omega\mathrm{i}k_1\check{\Delta}\left(\mathbf{k},\sigma_D\right) \tag{A.45}$$

$$-\mathrm{i}k_3\check{p} - \mu k^2\check{u}_3 = 0 \tag{A.46}$$

The solution to these equations are

$$\check{u}_1 = 4\pi a^3\Omega\frac{\mathrm{i}k_2}{k^2}\check{\Delta}(\mathbf{k}) \tag{A.47}$$

$$\check{u}_2 = -4\pi a^3\Omega\frac{\mathrm{i}k_1}{k^2}\check{\Delta}(\mathbf{k}) \tag{A.48}$$

$$\check{u}_3 = 0 \tag{A.49}$$

Recognizing that $(1/k^2)\check{\Delta}(\mathbf{k}) = \check{G}(\mathbf{k})$ the velocity field in physical space is

$$u_1(\mathbf{x}) = 4\pi a^3\Omega\frac{\partial G(r)}{\partial x_2} = 4\pi a^3\Omega\frac{x_2}{r}\frac{\partial G(r)}{\partial r} \tag{A.50}$$

$$u_2(\mathbf{x}) = -4\pi a^3\Omega\frac{\partial G(r)}{\partial x_1} = -4\pi a^3\Omega\frac{x_1}{r}\frac{\partial G(r)}{\partial r} \tag{A.51}$$

$$u_3(\mathbf{x}) = 0 \tag{A.52}$$

where we have used

$$\frac{\partial G(r)}{\partial x_i} = \frac{\partial r}{\partial x_i}\frac{\partial G(r)}{\partial r} \tag{A.53}$$

and $A(r)$ is given by (A.20).

A.5 The Length Scale σ_D Related to the Force Dipole

Similarly to the length scale σ, the length scale σ_D is determined by matching the particle angular velocity found from

$$\tilde{\Omega}_i = \frac{1}{2}\int \omega_i(\mathbf{x})\,\Delta(\mathbf{x},\sigma_D)\,d^3\mathbf{x} \tag{A.54}$$

with the angular velocity of a fixed rotating sphere in an infinite still fluid. In (A.54) $\omega_i(\mathbf{x})$ is the vorticity field resulting from the single torque dipole given by (A.39). The vorticity resulting from this is $\omega_i = (0,0,\omega_3)$, where ω_3 is computed from (A.50) and (A.51) as

$$\omega_3(\mathbf{x}) = \frac{\partial u_2(\mathbf{x})}{\partial x_1} - \frac{\partial u_1(\mathbf{x})}{\partial x_2} \tag{A.55}$$

The integral in (A.54) is most easily computed using the convolution theorem (A.31). In Fourier space the vorticity becomes

$$\check{\omega}_3(\mathbf{k}) = \mathrm{i}k_1\check{u}_2(\mathbf{k}) - \mathrm{i}k_2\check{u}_1(\mathbf{k}) = 4\pi a^3\Omega\frac{k_1^2+k_2^2}{k^2}\check{\Delta}(\mathbf{k}) \tag{A.56}$$

Inserting this in (A.31) the volume averaged angular velocity becomes

$$\begin{aligned}\tilde{\omega}_3 =& \frac{1}{2}\frac{4\pi a^3\Omega}{(2\pi)^3}\iiint\frac{k_1^2+k_2^2}{k^2}\exp\left(-k^2\sigma_D^2\right)dk_1dk_2dk_3\\ =& \frac{2\pi a^3\Omega}{(2\pi)^3}\int_0^\infty\int_0^\pi\int_0^{2\pi}\frac{r^2\sin^2\theta\cos^2\phi + r^2\sin^2\theta\sin^2\phi}{r^2}\exp\left(-k^2\sigma_D^2\right)r^2\sin\theta d\phi d\theta dr\\ =& \frac{2\pi a^3\Omega}{(2\pi)^3}\int_0^\infty\int_0^\pi\int_0^{2\pi}\sin^3\theta r^2\exp\left(-k^2\sigma_D^2\right)d\phi d\theta dr\end{aligned} \tag{A.57}$$

where the same substitution as above in A.3 from cartesian coordinates to spherical coordinates has been used in the second equality. The solution to (A.57) is easily computed using the integral (A.34) and

$$\int_0^\infty \theta r^2\exp\left(-k^2\sigma_D^2\right)dr = \frac{\sqrt{\pi}}{4\sigma^3} \tag{A.58}$$

Inserting these in (A.57) the result is

$$\begin{aligned}\tilde{\omega}_3 =& \frac{2\pi a^3\Omega}{(2\pi)^3}(2\pi)\frac{4}{3}\frac{\sqrt{\pi}}{4\sigma^3} = \frac{\sqrt{\pi}a^3\Omega}{3\sigma^3 2\pi} \\ =& \frac{a^3}{\sigma^3}\frac{1}{6\sqrt{\pi}}\Omega\end{aligned} \tag{A.59}$$

If the ratio of the sphere radius and the length sale σ_D is set to

$$\frac{a}{\sigma} = \sqrt[3]{6\sqrt{\pi}} \tag{A.60}$$

the volume averaged angular velocity will match the prescribed angular velocity. Therefore (A.60) is chosen as the value of a/σ_D.

A.6 The Flow Field due to a Force Dipole

This section concerns the Stokes flow setup by a force dipole in the force coupling method. This can be used in conjuction with the force monopole result to create a refined solution by adding together the two solutions (since the Stokes equations are linear). The aim of the section is to determine the tensor T_{ijk} so that the fluid velocity is given by

$$u_i = T_{ijk}F_{jk} \tag{A.61}$$

where u_i is the fluid velocity and F_{jk} is the force dipole strength.

The tensor T_{ijk} is the solution to the following Stokes problem

$$\frac{\partial u_i}{\partial x_i} = 0 \tag{A.62}$$

$$-\frac{\partial p}{\partial x_i} + \mu\frac{\partial^2 u_i}{\partial x_j \partial x_j} = -F_{ij}\frac{\partial \Delta\left(\mathbf{x},\sigma_D\right)}{\partial x_j} \tag{A.63}$$

The Fourier transformed of these are

$$\mathrm{i}k_i\check{u}_i = 0 \tag{A.64}$$

$$-\mathrm{i}k_1\check{p} - \mu k^2\check{u}_1 = -\left(F_{11}\mathrm{i}k_1 + F_{12}\mathrm{i}k_2 + F_{13}\mathrm{i}k_3\right)\check{\Delta}\left(\mathbf{k},\sigma_D\right) \tag{A.65}$$

$$-\mathrm{i}k_2\check{p} - \mu k^2\check{u}_2 = -\left(F_{21}\mathrm{i}k_1 + F_{22}\mathrm{i}k_2 + F_{23}\mathrm{i}k_3\right)\check{\Delta}\left(\mathbf{k},\sigma_D\right) \tag{A.66}$$

$$-\mathrm{i}k_3\check{p} - \mu k^2\check{u}_3 = -\left(F_{31}\mathrm{i}k_1 + F_{32}\mathrm{i}k_2 + F_{33}\mathrm{i}k_3\right)\check{\Delta}\left(\mathbf{k},\sigma_D\right) \tag{A.67}$$

This system of equations with four unknowns and four equations can be solved. This is done using *Mathcad* and the result is given in the following three sections.

Fluid Velocity in the x_1-Direction

The Fourier transformed velocity in the x_1-direction, $\check{u}_1$, obtained from *Mathcad* is

$$\begin{aligned}\check{u}_1 = \frac{\mathrm{i}}{\mu k^2 k^2}\big(&k_1\left(k_2^2+k_3^2\right)F_{11} + k_2\left(k_2^2+k_3^2\right)F_{12} + k_3\left(k_2^2+k_3^2\right)F_{13} \\ &-k_1^2k_2F_{21} - k_1k_2^2F_{22} - k_1k_2k_3F_{23} \\ &-k_1^2k_3F_{31} - k_1k_2k_3F_{32} - k_1k_3^2F_{33}\big)\check{\Delta}\left(\mathbf{k},\sigma_D\right)\end{aligned} \tag{A.68}$$

The first term in (A.68) may be rewritten as

$$\begin{aligned}\frac{\mathrm{i}k_1}{\mu k^2 k^2}\left(k_2^2+k_3^2\right)F_{11}\check{\Delta}\left(\mathbf{k},\sigma_D\right) &= \mathrm{i}k_1F_{11}\left(\frac{k_2^2}{\mu k^4}+\frac{k_3^2}{\mu k^4}\right)\check{\Delta}\left(\mathbf{k},\sigma_D\right)\\ &= \mathrm{i}k_1F_{11}\left(\frac{\check{\Delta}\left(\mathbf{k},\sigma_D\right)}{\mu k^2}-\check{O}_{22}+\frac{\check{\Delta}\left(\mathbf{k},\sigma_D\right)}{\mu k^2}-\check{O}_{33}\right)\\ &= \mathrm{i}k_1F_{11}\left(2\frac{\check{\Delta}\left(\mathbf{k},\sigma_D\right)}{\mu k^2}-\check{O}_{22}-\check{O}_{33}\right)\\ &= \mathrm{i}k_1F_{11}\left(2\frac{\check{\Delta}\left(\mathbf{k},\sigma_D\right)}{\mu k^2}-2\frac{\check{\Delta}\left(\mathbf{k},\sigma_D\right)}{\mu k^2}+\check{O}_{11}\right)\\ &= \mathrm{i}k_1F_{11}\check{O}_{11}\end{aligned} \tag{A.69}$$

where we have used the element $\check{O}_{22}$ of the Oseen tensor (A.11), i.e.

$$\begin{aligned}\check{O}_{22} &= \frac{1}{\mu k^2}\left(1-\frac{k_2^2}{k^2}\right)\check{\Delta}\left(\mathbf{k},\sigma_D\right)\\ \Rightarrow \frac{k_2^2}{\mu k^4}\check{\Delta}\left(\mathbf{k},\sigma_D\right) &= \frac{\check{\Delta}\left(\mathbf{k},\sigma_D\right)}{\mu k^2}-\check{O}_{22}\end{aligned} \tag{A.70}$$

and similarly for the element $\check{O}_{33}$. Furthermore we have used that the trace of the Oseen tensor is

$$\check{O}_{ii}=\check{O}_{11}+\check{O}_{22}+\check{O}_{33}=2\frac{\check{\Delta}\left(\mathbf{k},\sigma_D\right)}{\mu k^2} \tag{A.71}$$

this is inserted in the final part of (A.69). The second term in (A.68) may be rewritten as

$$\begin{aligned}\frac{\mathrm{i}k_2}{\mu k^2 k^2}\left(k_2^2+k_3^2\right)F_{12}\check{\Delta}\left(\mathbf{k},\sigma_D\right) &= \mathrm{i}k_2F_{12}\left(\frac{k_2^2+k_3^2}{\mu k^4}\right)\check{\Delta}\left(\mathbf{k},\sigma_D\right)\\ &= \mathrm{i}k_2F_{12}\left(\frac{\check{\Delta}\left(\mathbf{k},\sigma_D\right)}{\mu k^2}-\check{O}_{22}+\frac{\check{\Delta}\left(\mathbf{k},\sigma_D\right)}{\mu k^2}-\check{O}_{33}\right)\\ &= \mathrm{i}k_2F_{12}\left(2\frac{\check{\Delta}\left(\mathbf{k},\sigma_D\right)}{\mu k^2}-\check{O}_{22}-\check{O}_{33}\right)\\ &= \mathrm{i}k_2F_{12}\check{O}_{11}\end{aligned} \tag{A.72}$$

where the elements $\check{O}_{11}$, $\check{O}_{22}$ and $\check{O}_{33}$ have been used according to (A.70), and (A.71) have been used in the final part. Third term in (A.68) can be rewritten similarly to the second term, i.e.

$$\begin{aligned}\frac{\mathrm{i}k_3}{\mu k^2 k^2}\left(k_2^2+k_3^2\right)F_{13}\check{\Delta}\left(\mathbf{k},\sigma_D\right) &= \mathrm{i}k_3F_{13}\left(\frac{k_2^2+k_3^2}{\mu k^4}\right)\check{\Delta}\left(\mathbf{k},\sigma_D\right)\\ &= \mathrm{i}k_3F_{13}\check{O}_{11}\end{aligned} \tag{A.73}$$

The fourth, the fifth, the seventh, and the ninth terms are also rewritten using (A.70), and the results are

$$-\frac{\mathrm{i}k_2}{\mu k^2 k^2}k_1^2F_{21}\check{\Delta}\left(\mathbf{k},\sigma_D\right) = -\mathrm{i}k_2F_{21}\left(\frac{\check{\Delta}\left(\mathbf{k},\sigma_D\right)}{\mu k^2}-\check{O}_{11}\right) \tag{A.74}$$

$$-\frac{\mathrm{i}k_1}{\mu k^2 k^2}k_2^2F_{22}\check{\Delta}\left(\mathbf{k},\sigma_D\right) = -\mathrm{i}k_1F_{22}\left(\frac{\check{\Delta}\left(\mathbf{k},\sigma_D\right)}{\mu k^2}-\check{O}_{22}\right) \tag{A.75}$$

$$-\frac{\mathrm{i}k_3}{\mu k^2 k^2}k_1^2F_{31}\check{\Delta}\left(\mathbf{k},\sigma_D\right) = -\mathrm{i}k_3F_{31}\left(\frac{\check{\Delta}\left(\mathbf{k},\sigma_D\right)}{\mu k^2}-\check{O}_{11}\right) \tag{A.76}$$

$$-\frac{\mathrm{i}k_1}{\mu k^2 k^2}k_3^2F_{33}\check{\Delta}\left(\mathbf{k},\sigma_D\right) = -\mathrm{i}k_1F_{33}\left(\frac{\check{\Delta}\left(\mathbf{k},\sigma_D\right)}{\mu k^2}-\check{O}_{33}\right) \tag{A.77}$$

Finally, the sixth and the eighth term are rewritten using

$$\check{O}_{23} = -\frac{k_2 k_3}{\mu k^4}\check{\Delta}\left(\mathbf{k}, \sigma_D\right) \tag{A.78}$$

the results are

$$-\frac{\mathrm{i}}{\mu k^2 k^2} 2k_1 k_2 k_3 F_{23}\check{\Delta}\left(\mathbf{k}, \sigma_D\right) = \mathrm{i}k_1 F_{23}\check{O}_{23} \tag{A.79}$$

$$-\frac{\mathrm{i}}{\mu k^2 k^2} 2k_1 k_2 k_3 F_{32}\check{\Delta}\left(\mathbf{k}, \sigma_D\right) = \mathrm{i}k_1 F_{32}\check{O}_{32} \tag{A.80}$$

Using the Oseen tensor, O_{ij} from equaiton (A.21), and the fundamental solution to the Poisson equation, $G(r)$ from equation (A.3), these terms can now be transformed in to physical space resulting in the velocity u_1. The fundamental solution to the Poisson equation is used for transforming $\frac{\check{\Delta}(\mathbf{k},\sigma_D)}{\mu k^2}$, since

$$\nabla^2 G(r) = \Delta\left(\mathbf{r}, \sigma_D\right) \qquad \Rightarrow \qquad \check{\Delta}\left(\mathbf{k}, \sigma_D\right) = -k^2 G(\mathbf{k}) \tag{A.81}$$

Hence the fundamental solution is the Fourier transformed of $\frac{\check{\Delta}(\mathbf{k},\sigma_D)}{\mu k^2}$, i.e.

$$\frac{\check{\Delta}\left(\mathbf{k}, \sigma_D\right)}{\mu k^2} = -\frac{1}{\mu} G(\mathbf{k}) \tag{A.82}$$

The nine terms in physical space then becomes

$$\mathrm{i}k_1 F_{11}\check{O}_{11} \;\Rightarrow\; u_1^1 = F_{11}\frac{\partial O_{11}}{\partial x_1} \tag{A.83}$$

$$\mathrm{i}k_2 F_{12}\check{O}_{11} \;\Rightarrow\; u_1^2 = F_{12}\frac{\partial O_{11}}{\partial x_2} \tag{A.84}$$

$$\mathrm{i}k_3 F_{13}\check{O}_{11} \;\Rightarrow\; u_1^3 = F_{13}\frac{\partial O_{11}}{\partial x_3} \tag{A.85}$$

$$-\mathrm{i}k_2 F_{21}\left(\frac{\check{\Delta}\left(\mathbf{k}, \sigma_D\right)}{\mu k^2} - \check{O}_{11}\right) \;\Rightarrow\; u_1^4 = F_{21}\frac{\partial}{\partial x_2}\left(O_{11} + \frac{1}{\mu}G(r)\right) \tag{A.86}$$

$$-\mathrm{i}k_1 F_{22}\left(\frac{\check{\Delta}\left(\mathbf{k}, \sigma_D\right)}{\mu k^2} - \check{O}_{22}\right) \;\Rightarrow\; u_1^5 = F_{22}\frac{\partial}{\partial x_1}\left(O_{22} + \frac{1}{\mu}G(r)\right) \tag{A.87}$$

$$\mathrm{i}k_1 F_{23}\check{O}_{23} \;\Rightarrow\; u_1^6 = F_{23}\frac{\partial O_{23}}{\partial x_1} \tag{A.88}$$

$$-\mathrm{i}k_3 F_{31}\left(\frac{\check{\Delta}\left(\mathbf{k}, \sigma_D\right)}{\mu k^2} - \check{O}_{11}\right) \;\Rightarrow\; u_1^7 = F_{31}\frac{\partial}{\partial x_3}\left(O_{11} + \frac{1}{\mu}G(r)\right) \tag{A.89}$$

$$\mathrm{i}k_1 F_{32}\check{O}_{32} \;\Rightarrow\; u_1^8 = F_{32}\frac{\partial O_{32}}{\partial x_1} \tag{A.90}$$

$$-\mathrm{i}k_1 F_{33}\left(\frac{\check{\Delta}\left(\mathbf{k}, \sigma_D\right)}{\mu k^2} - \check{O}_{33}\right) \;\Rightarrow\; u_1^9 = F_{33}\frac{\partial}{\partial x_1}\left(O_{33} + \frac{1}{\mu}G(r)\right) \tag{A.91}$$

These can now be expressed in terms of the functions $A(r)$ and $B(r)$ from the relation $O_{ij} = A(r)\delta_{ij} + B(r)x_i x_j$, and the function $G(r)$. The first term becomes

$$\begin{aligned} u_1^1 &= F_{11}\frac{\partial}{\partial x_1}\left(A(r) + B(r)x_1 x_1\right) \\ &= F_{11}\frac{x_1}{r}\left(\frac{dA(r)}{dr} + x_1 x_1 \frac{dB(r)}{dr}\right) + 2F_{11}x_1 B(r) \\ &= \left(\frac{x_1}{r}\left(\frac{dA(r)}{dr} + x_1 x_1 \frac{dB(r)}{dr}\right) + 2x_1 B(r)\right) F_{11} \end{aligned} \tag{A.92}$$

where we have used $\partial r/\partial x_1\ \partial/\partial r$ and $\partial r/\partial x_1 = x_1/r$. The results for the second and third terms are

$$\begin{aligned} u_1^2 &= F_{12}\frac{\partial}{\partial x_2}\left(A(r) + B(r)x_1x_1\right) \\ &= \frac{x_2}{r}\left(\frac{dA(r)}{dr} + x_1x_1\frac{dB(r)}{dr}\right)F_{12} \end{aligned} \tag{A.93}$$

$$\begin{aligned} u_1^3 &= F_{13}\frac{\partial}{\partial x_3}\left(A(r) + B(r)x_1x_1\right) \\ &= \frac{x_3}{r}\left(\frac{dA(r)}{dr} + x_1x_1\frac{dB(r)}{dr}\right)F_{13} \end{aligned} \tag{A.94}$$

The fourth term becomes

$$\begin{aligned} u_1^4 &= F_{21}\frac{\partial}{\partial x_2}\left(A(r) + B(r)x_1x_1 + \frac{1}{\mu}G(r)\right) \\ &= \frac{x_2}{r}\left(\frac{dA(r)}{dr} + x_1x_1\frac{dB(r)}{dr} + \frac{1}{\mu}\frac{G(r)}{dr}\right)F_{21} \\ &= \frac{x_2}{r}\left(\frac{dA(r)}{dr} + x_1x_1\frac{dB(r)}{dr} - \frac{dA(r)}{dr} + rB(r)\right)F_{21} \\ &= \frac{x_2}{r}\left(rB(r) + x_1x_1\frac{dB(r)}{dr}\right)F_{21} \end{aligned} \tag{A.95}$$

where we have used

$$\frac{1}{\mu}\frac{dG(r)}{dr} = r^2\frac{dB(r)}{dr} + 5rB \tag{A.96}$$

and

$$\frac{dA(r)}{dr} = -r^2\frac{dB(r)}{dr} - 4rB(r)\ \Rightarrow\ \frac{1}{\mu}\frac{dG(r)}{dr} = -\frac{dA(r)}{dr} + rB(r) \tag{A.97}$$

The fifth, seventh, and ninth terms are similar and become

$$\begin{aligned} u_1^5 &= F_{22}\frac{\partial}{\partial x_1}\left(A(r) + B(r)x_2x_2 + \frac{1}{\mu}G(r)\right) \\ &= \frac{x_1}{r}\left(\frac{dA(r)}{dr} + x_2x_2\frac{dB(r)}{dr} + \frac{1}{\mu}\frac{G(r)}{dr}\right)F_{22} \\ &= \frac{x_1}{r}\left(\frac{dA(r)}{dr} + x_2x_2\frac{dB(r)}{dr} - \frac{dA(r)}{dr} + rB(r)\right)F_{22} \\ &= \frac{x_1}{r}\left(rB(r) + x_2x_2\frac{dB(r)}{dr}\right)F_{22} \end{aligned} \tag{A.98}$$

$$\begin{aligned} u_1^7 &= F_{31}\frac{\partial}{\partial x_3}\left(A(r) + B(r)x_1x_1 + \frac{1}{\mu}G(r)\right) \\ &= \frac{x_3}{r}\left(\frac{dA(r)}{dr} + x_1x_1\frac{dB(r)}{dr} + \frac{1}{\mu}\frac{G(r)}{dr}\right)F_{31} \\ &= \frac{x_3}{r}\left(\frac{dA(r)}{dr} + x_1x_1\frac{dB(r)}{dr} - \frac{dA(r)}{dr} + rB(r)\right)F_{31} \\ &= \frac{x_3}{r}\left(rB(r) + x_1x_1\frac{dB(r)}{dr}\right)F_{31} \end{aligned} \tag{A.99}$$

$$
\begin{aligned}
u_1^9 &= F_{33}\frac{\partial}{\partial x_1}\left(A(r) + B(r)x_3x_3 + \frac{1}{\mu}G(r)\right) \\
&= \frac{x_1}{r}\left(\frac{dA(r)}{dr} + x_3x_3\frac{dB(r)}{dr} + \frac{1}{\mu}\frac{G(r)}{dr}\right)F_{33} \\
&= \frac{x_1}{r}\left(\frac{dA(r)}{dr} + x_3x_3\frac{dB(r)}{dr} - \frac{dA(r)}{dr} + rB(r)\right)F_{33} \\
&= \frac{x_1}{r}\left(rB(r) + x_3x_3\frac{dB(r)}{dr}\right)F_{33}
\end{aligned}
\tag{A.100}
$$

The sixth and the eighth terms are similar to the first and become

$$
\begin{aligned}
u_1^6 &= F_{23}\frac{\partial}{\partial x_1}\left(B(r)x_2x_3\right) \\
&= \frac{x_1}{r}\left(x_2x_3\frac{dB(r)}{dr}\right)F_{23}
\end{aligned}
\tag{A.101}
$$

$$
\begin{aligned}
u_1^8 &= F_{32}\frac{\partial}{\partial x_1}\left(B(r)x_3x_2\right) \\
&= \frac{x_1}{r}\left(x_3x_2\frac{dB(r)}{dr}\right)F_{32}
\end{aligned}
\tag{A.102}
$$

These solutions then give the elements for the part T_{1jk} of the tensor T_{ijk}, since the velocity $u_1 = \sum_{n=1}^{9} u_1^n$ and

$$
\begin{aligned}
u_1 &= T_{1jk}F_{jk} \\
&= T_{111}F_{11} + T_{112}F_{12} + T_{113}F_{13} \\
&+ T_{121}F_{21} + T_{122}F_{22} + T_{123}F_{23} \\
&+ T_{131}F_{31} + T_{132}F_{32} + T_{133}F_{33}
\end{aligned}
\tag{A.103}
$$

Comparing with the equations for the different terms u_1^n we are able to specify the coefficients in the above equation, i.e.

$$T_{111} = \frac{x_1x_1x_1}{r}\frac{dB(r)}{dr} + \frac{x_1}{r}\frac{dA(r)}{dr} + 2x_1B(r) \tag{A.104}$$

$$T_{112} = \frac{x_2x_1x_1}{r}\frac{dB(r)}{dr} + \frac{x_2}{r}\frac{dA(r)}{dr} \tag{A.105}$$

$$T_{113} = \frac{x_3x_1x_1}{r}\frac{dB(r)}{dr} + \frac{x_3}{r}\frac{dA(r)}{dr} \tag{A.106}$$

$$T_{121} = \frac{x_2x_1x_1}{r}\frac{dB(r)}{dr} + x_2B(r) \tag{A.107}$$

$$T_{122} = \frac{x_1x_2x_2}{r}\frac{dB(r)}{dr} + x_1B(r) \tag{A.108}$$

$$T_{123} = \frac{x_1x_2x_3}{r}\frac{dB(r)}{dr} \tag{A.109}$$

$$T_{131} = \frac{x_3x_1x_1}{r}\frac{dB(r)}{dr} + x_3B(r) \tag{A.110}$$

$$T_{132} = \frac{x_1x_3x_2}{r}\frac{dB(r)}{dr} \tag{A.111}$$

$$T_{133} = \frac{x_1x_3x_3}{r}\frac{dB(r)}{dr} + x_1B(r) \tag{A.112}$$

Fluid Velocity in the x_2-Direction

The Fourier transformed of the fluid velocity in the x_2-direction, $\check{u}_2$, obtained from *Mathcad* is

$$\begin{aligned}\check{u}_2 = \frac{\mathrm{i}}{\mu k^2 k^2}\big(&-k_1^2 k_2 F_{11} - k_1 k_2^2 F_{12} - k_1 k_2 k_3 F_{13} \\ &k_1\left(k_1^2+k_3^2\right)F_{21} + k_2\left(k_1^2+k_3^2\right)F_{22} + k_3\left(k_1^2+k_3^2\right)F_{23} \\ &-k_1 k_2 k_3 F_{32} - k_2^2 k_3 F_{32} - k_2 k_3^2 F_{33}\big)\end{aligned} \tag{A.113}$$

Comparing (A.113) with (A.68) it is obvious that the solutions are similar, i.e. the indices have been "switched" around. Therefore we may directly write down the nine terms making up the solution $\check{u}_2$, i.e.

$$-\mathrm{i}k_2 F_{11}\left(\frac{\check{\Delta}\left(\mathbf{k},\sigma_D\right)}{\mu k^2} - \check{O}_{11}\right) \Rightarrow u_2^1 = F_{11}\frac{\partial}{\partial x_2}\left(O_{11} + \frac{1}{\mu}G(r)\right) \tag{A.114}$$

$$-\mathrm{i}k_1 F_{12}\left(\frac{\check{\Delta}\left(\mathbf{k},\sigma_D\right)}{\mu k^2} - \check{O}_{22}\right) \Rightarrow u_2^2 = F_{12}\frac{\partial}{\partial x_1}\left(O_{22} + \frac{1}{\mu}G(r)\right) \tag{A.115}$$

$$\mathrm{i}k_1 F_{13}\check{O}_{13} \Rightarrow u_2^3 = F_{13}\frac{\partial O_{13}}{\partial x_2} \tag{A.116}$$

$$\mathrm{i}k_1 F_{21}\check{O}_{22} \Rightarrow u_2^4 = F_{21}\frac{\partial O_{22}}{\partial x_1} \tag{A.117}$$

$$\mathrm{i}k_2 F_{22}\check{O}_{22} \Rightarrow u_2^5 = F_{22}\frac{\partial O_{22}}{\partial x_2} \tag{A.118}$$

$$\mathrm{i}k_3 F_{23}\check{O}_{22} \Rightarrow u_2^6 = F_{23}\frac{\partial O_{22}}{\partial x_3} \tag{A.119}$$

$$\mathrm{i}k_1 F_{31}\check{O}_{31} \Rightarrow u_2^7 = F_{31}\frac{\partial O_{31}}{\partial x_2} \tag{A.120}$$

$$-\mathrm{i}k_3 F_{32}\left(\frac{\check{\Delta}\left(\mathbf{k},\sigma_D\right)}{\mu k^2} - \check{O}_{22}\right) \Rightarrow u_1^8 = F_{32}\frac{\partial}{\partial x_3}\left(O_{22} + \frac{1}{\mu}G(r)\right) \tag{A.121}$$

$$-\mathrm{i}k_2 F_{33}\left(\frac{\check{\Delta}\left(\mathbf{k},\sigma_D\right)}{\mu k^2} - \check{O}_{33}\right) \Rightarrow u_1^9 = F_{33}\frac{\partial}{\partial x_2}\left(O_{33} + \frac{1}{\mu}G(r)\right) \tag{A.122}$$

These solutions then give the elements for the part T_{2jk} of the tensor T_{ijk}, since the velocity $u_2 = \sum_{n=1}^{9} u_2^n$ and

$$\begin{aligned}u_2 &= T_{2jk}F_{jk} \\ &= T_{211}F_{11} + T_{212}F_{12} + T_{213}F_{13} \\ &+ T_{221}F_{21} + T_{222}F_{22} + T_{223}F_{23} \\ &+ T_{231}F_{31} + T_{232}F_{23} + T_{233}F_{33}\end{aligned} \tag{A.123}$$

Comparing with the equations for the different terms u_2^n we are able to specify the coefficients in the above equation, i.e.

$$T_{211} = \frac{x_2 x_1 x_1}{r}\frac{dB(r)}{dr} + x_2 B(r) \tag{A.124}$$

$$T_{212} = \frac{x_1 x_2 x_2}{r}\frac{dB(r)}{dr} + x_1 B(r) \tag{A.125}$$

$$T_{213} = \frac{x_2 x_1 x_3}{r}\frac{dB(r)}{dr} \tag{A.126}$$

$$T_{221} = \frac{x_1 x_2 x_2}{r}\frac{dB(r)}{dr} + \frac{x_1}{r}\frac{dA(r)}{dr} \tag{A.127}$$

$$T_{222} = \frac{x_2 x_2 x_2}{r}\frac{dB(r)}{dr} + \frac{x_2}{r}\frac{dA(r)}{dr} + 2x_2 B(r) \tag{A.128}$$

$$T_{223} = \frac{x_3 x_2 x_2}{r}\frac{dB(r)}{dr} + \frac{x_3}{r}\frac{dA(r)}{dr} \tag{A.129}$$

$$T_{231} = \frac{x_2 x_3 x_1}{r}\frac{dB(r)}{dr} \tag{A.130}$$

$$T_{232} = \frac{x_3 x_2 x_2}{r}\frac{dB(r)}{dr} + x_3 B(r) \tag{A.131}$$

$$T_{233} = \frac{x_2 x_3 x_3}{r}\frac{dB(r)}{dr} + x_2 B(r) \tag{A.132}$$

Fluid Velocity in the x_3-Direction

The Fourier transformed of the fluid velocity in the x_3-direction, $\breve{u}_3$, obtained from *Mathcad* is

$$\begin{aligned}\breve{u}_3 = \frac{\mathrm{i}}{\mu k^2 k^2}\big(&-k_1^2 k_3 F_{11} - k_1 k_2 k_3 F_{12} - k_1 k_3^2 F_{13} \\ &-k_1 k_2 k_3 F_{21} - k_2^2 k_3 F_{22} - k_2 k_3^2 F_{23} \\ &k_1\left(k_1^2 + k_2^2\right) F_{31} + k_2\left(k_1^2 + k_2^2\right) F_{32} + k_3\left(k_1^2 + k_2^2\right) F_{33}\big)\end{aligned} \tag{A.133}$$

Comparing (A.133) with (A.68) it is obvious that the solutions are similar, i.e. the indices have been "switched" around. Therefore we may again directly write

down the nine terms making up the solution $\check{u}_3$, i.e.

$$-\mathrm{i}k_3F_{11}\left(\frac{\check{\Delta}\left(\mathbf{k},\sigma_D\right)}{\mu k^2}-\check{O}_{11}\right) \Rightarrow u_3^1 = F_{11}\frac{\partial}{\partial x_3}\left(O_{11}+\frac{1}{\mu}G(r)\right) \quad \text{(A.134)}$$

$$\mathrm{i}k_3F_{12}\check{O}_{12} \Rightarrow u_3^2 = F_{12}\frac{\partial O_{12}}{\partial x_3} \quad \text{(A.135)}$$

$$-\mathrm{i}k_1F_{13}\left(\frac{\check{\Delta}\left(\mathbf{k},\sigma_D\right)}{\mu k^2}-\check{O}_{33}\right) \Rightarrow u_3^3 = F_{13}\frac{\partial}{\partial x_1}\left(O_{33}+\frac{1}{\mu}G(r)\right) \quad \text{(A.136)}$$

$$\mathrm{i}k_3F_{21}\check{O}_{21} \Rightarrow u_3^4 = F_{21}\frac{\partial O_{21}}{\partial x_3} \quad \text{(A.137)}$$

$$-\mathrm{i}k_3F_{22}\left(\frac{\check{\Delta}\left(\mathbf{k},\sigma_D\right)}{\mu k^2}-\check{O}_{22}\right) \Rightarrow u_3^5 = F_{22}\frac{\partial}{\partial x_3}\left(O_{22}+\frac{1}{\mu}G(r)\right) \quad \text{(A.138)}$$

$$-\mathrm{i}k_2F_{21}\left(\frac{\check{\Delta}\left(\mathbf{k},\sigma_D\right)}{\mu k^2}-\check{O}_{11}\right) \Rightarrow u_3^6 = F_{21}\frac{\partial}{\partial x_2}\left(O_{33}+\frac{1}{\mu}G(r)\right) \quad \text{(A.139)}$$

$$\mathrm{i}k_1F_{31}\check{O}_{33} \Rightarrow u_3^7 = F_{31}\frac{\partial O_{33}}{\partial x_1} \quad \text{(A.140)}$$

$$\mathrm{i}k_2F_{32}\check{O}_{33} \Rightarrow u_3^8 = F_{32}\frac{\partial O_{33}}{\partial x_2} \quad \text{(A.141)}$$

$$\mathrm{i}k_3F_{33}\check{O}_{33} \Rightarrow u_3^9 = F_{33}\frac{\partial O_{33}}{\partial x_3} \quad \text{(A.142)}$$

These solutions then give the elements for the part T_{3jk} of the tensor T_{ijk}, since the velocity $u_3 = \sum_{n=1}^{9} u_3^n$ and

$$\begin{aligned} u_3 &= T_{3jk}F_{jk} \\ &= T_{311}F_{11}+T_{312}F_{12}+T_{313}F_{13} \\ &+ T_{321}F_{21}+T_{322}F_{22}+T_{323}F_{23} \\ &+ T_{331}F_{31}+T_{332}F_{23}+T_{333}F_{33} \end{aligned} \quad \text{(A.143)}$$

Comparing with the equations for the different terms u_3^n we are able to specify the coefficients in the above equation, i.e.

$$T_{311} = \frac{x_3x_1x_1}{r}\frac{dB(r)}{dr}+x_3B(r) \quad \text{(A.144)}$$

$$T_{312} = \frac{x_3x_1x_2}{r}\frac{dB(r)}{dr} \quad \text{(A.145)}$$

$$T_{313} = \frac{x_1x_3x_3}{r}\frac{dB(r)}{dr}+x_1B(r) \quad \text{(A.146)}$$

$$T_{321} = \frac{x_3x_2x_1}{r}\frac{dB(r)}{dr} \quad \text{(A.147)}$$

$$T_{322} = \frac{x_3x_2x_2}{r}\frac{dB(r)}{dr}+x_3B(r) \quad \text{(A.148)}$$

$$T_{323} = \frac{x_2x_3x_3}{r}\frac{dB(r)}{dr}+x_2B(r) \quad \text{(A.149)}$$

$$T_{331} = \frac{x_1x_3x_3}{r}\frac{dB(r)}{dr}+\frac{x_1}{r}\frac{dA(r)}{dr} \quad \text{(A.150)}$$

$$T_{332} = \frac{x_2x_3x_3}{r}\frac{dB(r)}{dr}+\frac{x_2}{r}\frac{dA(r)}{dr} \quad \text{(A.151)}$$

$$T_{333} = \frac{x_3x_3x_3}{r}\frac{dB(r)}{dr}+\frac{x_3}{r}\frac{dA(r)}{dr}+2x_3B(r) \quad \text{(A.152)}$$

$$\quad \text{(A.153)}$$

Final Tensor T_{ijk}

Combining the above tensor elements the final tensor, T_{ijk}, for the flow induced by a force dipole is

$$T_{ijk} = \frac{x_i x_j x_k}{r}\frac{dB(r)}{dr} + \delta_{ij}\frac{x_k}{r}\frac{dA(r)}{dr} + \delta_{ik}x_j B(r) + \delta_{jk}x_i B(r) \tag{A.154}$$

Note that in this derivation it has not been assumed that F_{ij} is symmetric and the length scale σ determined for the rotating sphere should be used here as well. The velocity field due to this force dipole is then given as

$$u_i = T_{ijk}F_{jk} \tag{A.155}$$

It should be noted that the solution (A.154) could be found by

$$T_{ijk} = \frac{\partial O_{ij}}{\partial x_k} \tag{A.156}$$

which may be an easier approach (Maxey (2000b)).

B Appendix B

This appendix concerns the methods implemented in the program *channel3d*. The program solves the Navier-Stokes equations in a three dimensional channel with periodic boundary conditions in the streamwise and spanwise directions, while no-slip or no-stress boundary conditions are employed in the normal direction. The method is based on a rewriting of the momentum equations into a fourth order equation for the normal velocity and a second order equation for the normal vorticity. The solution method is given by Kim, Moin and Moser (1987). The original code was obtained from R. Handler and is described in Handler et al. (1993).

B.1 Rewriting the Navier-Stokes Equations

The fluid flow is governed by the continuity equation (incompressible flow)

$$\frac{\partial u_1}{\partial x_1} + \frac{\partial u_2}{\partial x_2} + \frac{\partial u_3}{\partial x_3} = 0 \tag{B.1}$$

and Navier-Stokes equations with the force coulping terms for the three velocity components

$$\frac{\partial u_1}{\partial t} + u_j \frac{\partial u_1}{\partial x_j} = -\frac{\partial p}{\partial x_1} + \frac{1}{Re}\nabla^2 u_1 + G_1 \tag{B.2}$$

$$\frac{\partial u_2}{\partial t} + u_j \frac{\partial u_2}{\partial x_j} = -\frac{\partial p}{\partial x_2} + \frac{1}{Re}\nabla^2 u_2 + G_2 \tag{B.3}$$

$$\frac{\partial u_3}{\partial t} + u_j \frac{\partial u_3}{\partial x_j} = -\frac{\partial p}{\partial x_3} + \frac{1}{Re}\nabla^2 u_3 + G_3 \tag{B.4}$$

where u_i is the velocity in the x_i direction and

$$G_i = \sum_{n=0}^{N} F_i^n \Delta\left(\mathbf{x} - \mathbf{Y^n}, \sigma\right) + F_{ij}^n \frac{\partial \Delta\left(\mathbf{x} - \mathbf{Y^n}, \sigma_D\right)}{\partial x_j} \tag{B.5}$$

with the multipole strengths given by

$$F_i^n = \frac{\mathrm{V}_p\left(\delta - 1\right) g_i L}{U} = \frac{\mathrm{V}_p}{Fr_i} \tag{B.6}$$

$$F_{ij}^n = \frac{\mathrm{V}_p}{Re}\left(5\tilde{E^*_{ij}}^n + 3\tilde{\Omega}_{ij}^n\right) \tag{B.7}$$

where Fr_i is the Froude number, Re is the Reynolds number, and $\tilde{E^*_{ij}}^n$ and $\tilde{\Omega}_{ij}^n$ are the non-dimensional force dipole strength related to the rate of strain and the external torque, respectively. All variables have been made non-dimensional with a characteristic velocity U, a characteristic length L and a characteristic time $T = L/U$.

Taking the derivative with respect to x_1 of equation (B.2) gives

$$\frac{\partial}{\partial t}\left(\frac{\partial u_1}{\partial x_1}\right) = -\frac{\partial^2 p}{\partial x_1^2} + \frac{\partial\left(H_1 + G_1\right)}{\partial x_1} + \frac{1}{Re}\nabla^2 \frac{\partial u_1}{\partial x_1} \tag{B.8}$$

where $H_1 = -u_j \frac{\partial u_1}{\partial x_j}$. The derivative of equation (B.4) with respect to x_3 gives

$$\frac{\partial}{\partial t}\left(\frac{\partial u_3}{\partial x_3}\right) = -\frac{\partial^2 p}{\partial x_3^2} + \frac{\partial\left(H_3 + G_3\right)}{\partial x_3} + \frac{1}{Re}\nabla^2 \frac{\partial u_3}{\partial x_3} \tag{B.9}$$

where $H_3 = -u_j \frac{\partial u_3}{\partial x_j}$. Combining equations (B.8) and (B.9) by adding the left hand sides together and the right hand sides together yields

$$\begin{aligned}\frac{\partial}{\partial t}\left(\frac{\partial u_1}{\partial x_1}+\frac{\partial u_3}{\partial x_3}\right) &= -\left(\frac{\partial^2 p}{\partial x_1^2}+\frac{\partial^2 p}{\partial x_3^2}\right) \\ &\frac{\partial\left(H_1+G_1\right)}{\partial x_1}+\frac{\partial\left(H_3+G_3\right)}{\partial x_3}+\frac{1}{Re}\nabla^2\left(\frac{\partial u_1}{\partial x_1}+\frac{\partial u_3}{\partial x_3}\right)\end{aligned} \tag{B.10}$$

From the continuity equation (B.1) we have

$$\frac{\partial u_1}{\partial x_1}+\frac{\partial u_3}{\partial x_3} = -\frac{\partial u_2}{\partial x_2} \tag{B.11}$$

Inserting this into (B.10) and taking the derivative with respect to x_2 gives

$$\begin{aligned}-\frac{\partial}{\partial t}\left(\frac{\partial^2 u_2}{\partial x_2^2}\right) &= -\frac{\partial}{\partial x_2}\left(\frac{\partial^2 p}{\partial x_1^2}+\frac{\partial^2 p}{\partial x_3^2}\right) \\ &+\frac{\partial}{\partial x_2}\left(\frac{\partial\left(H_1+G_1\right)}{\partial x_1}+\frac{\partial\left(H_3+G_3\right)}{\partial x_3}\right)-\frac{1}{Re}\nabla^2\frac{\partial^2 u_2}{\partial x_2^2}\end{aligned} \tag{B.12}$$

In order to eliminate the pressure we take the second derivative of (B.3) with respect to x_1

$$\frac{\partial}{\partial t}\left(\frac{\partial^2 u_2}{\partial x_1^2}\right) = -\frac{\partial}{\partial x_2}\frac{\partial^2 p}{\partial x_1^2}+\frac{\partial^2\left(H_2+G_2\right)}{\partial x_1^2}+\frac{1}{Re}\nabla^2\frac{\partial^2 u_2}{\partial x_1^2} \tag{B.13}$$

where $H_2 = -u_j \frac{\partial u_2}{\partial x_j}$ and the second derivative of (B.3) with respect to x_3

$$\frac{\partial}{\partial t}\left(\frac{\partial^2 u_2}{\partial x_3^2}\right) = -\frac{\partial}{\partial x_2}\frac{\partial^2 p}{\partial x_3^2}+\frac{\partial^2\left(H_2+G_2\right)}{\partial x_3^2}+\frac{1}{Re}\nabla^2\frac{\partial^2 u_2}{\partial x_3^2} \tag{B.14}$$

The pressure can now be eliminated by adding together equations (B.13) and (B.14) and then subtracting equation (B.12). This gives

$$\begin{aligned}&\frac{\partial}{\partial t}\left(\frac{\partial^2 u_2}{\partial x_1^2}+\frac{\partial^2 u_2}{\partial x_3^2}+\frac{\partial^2 u_2}{\partial x_2^2}\right) = \\ &\left(\frac{\partial^2}{\partial x_1^2}+\frac{\partial^2}{\partial x_3^2}\right)\left(H_2+G_2\right)-\frac{\partial}{\partial x_2}\left(\frac{\partial\left(H_1+G_1\right)}{\partial x_1}+\frac{\partial\left(H_3+G_3\right)}{\partial x_3}\right) \\ &+\frac{1}{Re}\nabla^2\left(\frac{\partial^2 u_2}{\partial x_1^2}+\frac{\partial^2 u_2}{\partial x_3^2}+\frac{\partial^2 u_2}{\partial x_2^2}\right)-\frac{\partial}{\partial x_2}\left(\frac{\partial^2 p}{\partial x_1^2}+\frac{\partial^2 p}{\partial x_3^2}-\left(\frac{\partial^2 p}{\partial x_1^2}+\frac{\partial^2 p}{\partial x_3^2}\right)\right)\end{aligned} \tag{B.15}$$

The pressure terms drop out and the following fourth order equation for the normal velocity u_2 is obtained

$$\begin{aligned}\frac{\partial}{\partial t}\left(\nabla^2 u_2\right) &= \left(\frac{\partial^2}{\partial x_1^2}+\frac{\partial^2}{\partial x_3^2}\right)\left(H_2+G_2\right) \\ &-\frac{\partial}{\partial x_2}\left(\frac{\partial\left(H_1+G_1\right)}{\partial x_1}+\frac{\partial\left(H_3+G_3\right)}{\partial x_3}\right)+\frac{1}{Re}\nabla^4 u_2\end{aligned} \tag{B.16}$$

In order to reconstruct the other two velocities two more equations are necessary. One is the continuity equation already given in (B.1). The other is the tranport equation of normal vorticity. This is determined by the derivative of equation (B.2) with respect to x_3

$$\frac{\partial}{\partial t}\left(\frac{\partial u_1}{\partial x_3}\right) = -\frac{\partial^2 p}{\partial x_1 \partial x_3}+\frac{\partial\left(H_1+G_1\right)}{\partial x_3}+\frac{1}{Re}\nabla^2\frac{\partial u_1}{\partial x_3} \tag{B.17}$$

and the derivative of equation (B.4) with respect to x_1

$$\frac{\partial}{\partial t}\left(\frac{\partial u_3}{\partial x_1}\right) = -\frac{\partial^2 p}{\partial x_3 \partial x_1}+\frac{\partial\left(H_3+G_3\right)}{\partial x_1}+\frac{1}{Re}\nabla^2\frac{\partial u_3}{\partial x_1} \tag{B.18}$$

The transport equation for the normal vorticity, $\omega_2 = \frac{\partial u_1}{\partial x_3} - \frac{\partial u_3}{\partial x_1}$, is the given by subtracting equation (B.18) from equation (B.17)

$$\frac{\partial \omega_2}{\partial t} = \frac{\partial \left(H_1 + G_1\right)}{\partial x_3} - \frac{\partial \left(H_3 + G_3\right)}{\partial x_1} + \frac{1}{Re}\nabla^2 \omega_2 \tag{B.19}$$

When u_2 and ω_2 are found the other velocities are determined from

$$\frac{\partial u_1}{\partial x_1} + \frac{\partial u_3}{\partial x_3} = -\frac{\partial u_2}{\partial x_2} \qquad \omega_2 = \frac{\partial u_1}{\partial x_3} - \frac{\partial u_3}{\partial x_1} \tag{B.20}$$

and the other vorticity elements are found from

$$\omega_1 = \frac{\partial u_2}{\partial x_3} - \frac{\partial u_3}{\partial x_2} \qquad \omega_3 = \frac{\partial u_2}{\partial x_1} - \frac{\partial u_1}{\partial x_2} \tag{B.21}$$

B.2 Numerical Implementation

The implementation of these equations in *channel3d* follows the method described by Kim, Moin and Moser (1987). The solution is found using a spectral method. The variables are Fourier transformed in the streamwise and spanwise directions and in the normal direction Chebyshev polynomials are used. The sections below will not contain any information on spectral methods. For a description of spectral methods the reader is referred to Canuto et al. (1986) or Gottlieb & Orszag (1977).

Solution of the fluid velocity field

The fourth order equation (B.16) is solved by splitting it into two second order equations

$$\begin{aligned} \frac{\partial \phi}{\partial t} &= h_u + f_u + \frac{1}{Re}\nabla^2 \phi \\ \nabla^2 u_2 &= \phi \\ u_2\left(\pm 1\right) &= \frac{\partial u_2}{\partial x_2}|_{x_2=\pm 1} = 0 \end{aligned} \tag{B.22}$$

where h_u is the nonlinear terms in equation (B.16),

$$h_u = \left(\frac{\partial^2}{\partial x_1^2} + \frac{\partial^2}{\partial x_3^2}\right) H_2 - \frac{\partial}{\partial x_2}\left(\frac{\partial H_1}{\partial x_1} + \frac{\partial H_3}{\partial x_3}\right) \tag{B.23}$$

and f_u is the force coupling terms in equation (B.16),

$$f_u = \left(\frac{\partial^2}{\partial x_1^2} + \frac{\partial^2}{\partial x_3^2}\right) G_2 - \frac{\partial}{\partial x_2}\left(\frac{\partial G_1}{\partial x_1} + \frac{\partial G_3}{\partial x_3}\right) \tag{B.24}$$

The time advancement is performed using a second order implicit Backward Difference Method (BDF), i.e.

$$\begin{aligned} &\frac{3}{2}\phi^{k+1} = 2\phi^k - \frac{1}{2}\phi^{k-1} + \delta t\left(h_u^{k+1} + f_u^{k+1} + \frac{1}{Re}\nabla^2 \phi^{k+1}\right) \\ &\Rightarrow \left(\nabla^2 - \frac{3Re}{2\delta t}\right)\phi^{k+1} = -\frac{Re}{\delta t}\left(2\phi^k - \frac{1}{2}\phi^{k-1}\right) - Re\left(h_u^{k+1} + f_u^{k+1}\right) \end{aligned} \tag{B.25}$$

where k denote the number of the time step, δt is the size of the time step.

The system is solved by the Chebyshev-tau method, in which the four boundary conditions

$$u_2\left(x_2 = \pm 1\right) = 0 \qquad \frac{\partial u_2^{k+1}}{\partial x_2}|_{x_2=\pm 1} = 0 \tag{B.26}$$

are satified as follows. The velocity u_2 is split into a particular and two homogeneous solutions

$$u_2 = u_{2,p} + c_1 u_{2,1} + c_2 u_{2,2} \tag{B.27}$$

where the particular solution satisfies

$$\begin{aligned}\left(\nabla^2 - \frac{3Re}{2\delta t}\right)\phi^{k+1} &= -\frac{Re}{\delta t}\left(2\phi^k - \frac{1}{2}\phi^{k-1}\right) - Re\left(h_u^{k+1} + f_u^{k+1}\right)\\ \phi_p^{k+1}(\pm 1) &= 0\end{aligned} \tag{B.28}$$

$$\begin{aligned}\nabla^2 u_{2,p}^{k+1} &= \phi_p^{k+1}\\ u_{2,p}^{k+1}(\pm 1) &= 0\end{aligned}$$

and the two homogeneous solutions satisfy

$$\begin{aligned}\left(\nabla^2 - \frac{3Re}{2\delta t}\right)\phi_1 &= 0\\ \phi_1(x_2 = 1) = 0,\ \phi_1(x_2 = -1) &= 1\end{aligned} \tag{B.29}$$

$$\begin{aligned}\nabla^2 u_{2,1} &= \phi_1\\ u_{2,1}(x_2 = \pm 1) &= 0\end{aligned}$$

$$\begin{aligned}\left(\nabla^2 - \frac{3Re}{2\delta t}\right)\phi_2 &= 0\\ \phi_2(x_2 = 1) = 1,\ \phi_2(x_2 = -1) &= 0\end{aligned} \tag{B.30}$$

$$\begin{aligned}\nabla^2 u_{2,2} &= \phi_2\\ u_{2,2}(x_2 = \pm 1) &= 0\end{aligned}$$

Equations (B.29) and (B.30) are solved only once since these are independent of time. They only depend on the geometry, the time step and the Reynolds number. Equations (B.28) to (B.30) ensure that the zero velocity ($u_2(x_2 = \pm 1) = 0$) is satified. The condition that the normal derivative of u_2 is zero at the top and bottom wall determines the coefficients c_1 and c_2 in (B.27). The condition

$$\frac{\partial u_2^{k+1}}{\partial x_2}|_{x_2=\pm 1} = 0 \tag{B.31}$$

yields a linear system of equations that is easily inverted to give c_1 and c_2 and the composite solution is then constructed from (B.27). Thus for each time step equation (B.28) for the particular solution and (B.31) for the coefficients are solved to give u_2 from (B.27).

In the BDF time advancement scheme the equation for the normal vorticity (B.19) becomes

$$\left(\nabla^2 - \frac{3Re}{2\delta t}\right)\omega_2^{k+1} = -\frac{Re}{\delta t}\left(2\omega_2^k - \frac{1}{2}\omega_2^{k+1}\right) - Re\left(h_\omega^{k+1} + f_\omega^{k+1}\right) \tag{B.32}$$

where h_ω is the nonlinear terms

$$h_\omega = \frac{\partial H_1}{\partial x_3} - \frac{\partial H_3}{\partial x_1} \tag{B.33}$$

and f_ω is the force coupling terms

$$h_\omega = \frac{\partial G_1}{\partial x_3} - \frac{\partial G_3}{\partial x_1} \tag{B.34}$$

in (B.19). The boundary conditions for (B.32) is

$$\omega_2^{k+1}(\pm 1) = 0$$

when u_2 and ω_2 have been found the other velocity and vorticity components are determined from (B.20) and (B.21) respectively.

Since the BDF method is implicit, each time step requires iteration until some given accuracy. The iteration is also needed for determining the six elements[8] in ${E_{ij}^*}^n$ and therefore the elements in ${E_{ij}^*}^n$ determine the number of iteration steps. An essential part of the method is the update of the six elements in ${E_{ij}^*}^n$ during the iteration and this is done with the value of $\tilde{E}_{ij}^n$ in the following manner

$$\left({E_{ij}^*}^n\right)^{[q]} = \left({E_{ij}^*}^n\right)^{[q-1]} + \left(\tilde{E}_{ij}^n\right)^{[q]} \tag{B.35}$$

where q is the iteration number. Therefore if the average rate of strain is not zero (or below some small number ϵ) then dipole strength is corrected with the value of the average rate of strain. This is consistent with the dipole strength that was needed for the neutral sphere in pure straining Stokes flow, where the dipole strength was set equal to the value of the average strain rate for the undisturbed flow (the flow without the dipole).

The iteration is then to be continued until a certain accuracy ϵ is obtained, i.e. the iteration ends when

$$\left|\left|\tilde{E}_{ij}^n\right|\right|^2 = \sum_i \sum_j \left(\tilde{E}_{ij}^n\right)^2 < \epsilon \qquad \text{for all } n \tag{B.36}$$

or until a certain number of iterations is reached (avoid infinite looping).

Using this iteration scheme the time discretized equations (B.25) and (B.32) become

$$\left(\nabla^2 - \frac{3Re}{2\delta t}\right)\phi^{q+1} = -\frac{Re}{\delta t}\left(2\phi^k - \frac{1}{2}\phi^{k-1}\right) - Re\left(h_u^q + f_u^q\right) \tag{B.37}$$

$$\left(\nabla^2 - \frac{3Re}{2\delta t}\right)\omega_2^{q+1} = -\frac{Re}{\delta}\left(2\omega_2^k - \frac{1}{2}\omega_2^{k+1}\right) - Re\left(h_\omega^q + f_\omega^q\right) \tag{B.38}$$

The initial guesses h_ω^1 and f_ω^1 are the values obtained at the previous time step. The iteration requires updating of both the non-linear terms and the force coupling terms.

Particle time stepping

The particles are time stepped using a explicit third order Adams-Bashforth method

$$Y_i^{k+1} = Y_i^k + \frac{\delta t}{12}\left(23V_i^k - 16V_i^{k-1} + 5V_i^{k-2}\right) \tag{B.39}$$

Therefore the particles are moved before the iteration process for the velocity field is performed. Thereby the particles are placed at their "correct" positions for the iteration procedure.

B.3 Parameters for the simulations presented in chapter 5

In this section we present two tables 20 and 22 containing relevant parameters for the simulations presented in chapter 5. The table gives the dimension of the

[8] these depend on the non-linear velocity field, where the effect of the other particles must be included

computational domain (L_1, L_2, and L_3) and the number of points used in each direction (N_1, N_2, and N_3). Three other characteristic parameters for the computations are the time step (δt), the Reynolds number ($Re = L_2 U/\nu$), and the Froude number ($Fr = gL_2/U^2$). Finally, the table also shows three runtime parameters namely the maximum number of iterations, the maximum CFL number and the CPU time spent on the computations. The CPU time is given as the number of seconds to perform 100 time steps.

Conserning the CPU time the reason for the variations result from the fact that a different number of iterations were needed for the different cases. Furthermore various types of CPU's have been used and probably these CPU's are already outdated at the time of writing.

In the cases were the maximum number of iterations was reached the condition of on the rate of strain did not satisfy the specified criteria, but the average rate of strain was below 10^{-3} (denoted †) or 10^{-2} (denoted $\spadesuit$). Some of these runs were checked by increasing the number of iterations, however this had only neglegible effect on the results and it proved very difficult to obtain the lower value of the average rate of strain. Generally, the simulations showed that a very low value of the average rate of strain is not necessary and a limit of about 10^{-2} is probably accurate enough at least for the cases considered here. This means that an exact value of the force dipole term is not important, but it is important to have a value that is within a certain range of the exact value. The computation of the force dipole terms proved to be must difficult when two or more particles were interacting. The reason is probably that the spheres will move in a direction which is not parallel to the monopole forcing and thereby create of diagonal elements in the force dipole tensor. Furthermore, the effect of the other spheres will other contribute to the off diagonal elements and this may cause a slower convergence in the iterations. Thus as an advice to others who may want to use this method: Keep the limit on the average rate of strain relatively high (10^{-2} or even 10^{-1}), since this will limit the number of iterations. Another approach would be to find a different method for computing the force dipole terms as mentioned in the text.

Exp. no.	$L_1 \times L_2 \times L_3$	$N_1 \times N_2 \times N_3$	δt	$Re = \frac{L_2 U}{\nu}$	$Fr = \frac{g L_2}{U^2}$	ϵ	IT_{max}	CFL_{max}	CPU_{time}
1st inclined	$10 \times 1 \times 4$	$64 \times 32 \times 48$	0.10	0.58	982.0	10^{-4}	5-9	0.235	18355
2nd inclined	$5 \times 1 \times 4$	$64 \times 32 \times 48$	0.02	1.05	982.0	10^{-4}	5	0.081	618
3rd inclined†	$5 \times 1 \times 4$	$64 \times 32 \times 48$	0.02	5.40	982.0	10^{-4}	10-20	0.298	1979
4th inclined†	$5 \times 1 \times 4$	$64 \times 32 \times 48$	0.01	32.0	982.0	10^{-4}	20	0.264	3713
1st perpendicular‡†	$3 \times 2 \times 3$	$64 \times 96 \times 64$	0.01	10.5	9.82	10^{-5}	1-9	0.012	2861
2nd perpendicular‡†	$3 \times 2 \times 3$	$64 \times 96 \times 64$	0.01	13.5	9.82	10^{-5}	4-6	0.015	2650
3rd perpendicular‡†	$3 \times 2 \times 3$	$64 \times 96 \times 64$	0.01	26.0	9.82	10^{-5}	5-8	0.034	3672
4th perpendicular‡†	$3 \times 2 \times 3$	$64 \times 96 \times 64$	0.005	42.0	9.82	10^{-5}	10	0.130	5428
1st parallel	$6 \times 2 \times 3$	$96 \times 48 \times 48$	0.15	30.0	9.82	10^{-5}	11	0.222	3034
2nd parallel	$6 \times 2 \times 3$	$96 \times 48 \times 48$	0.10	30.0	9.82	10^{-5}	14-16	0.280	4107
3rd parallel†	$6 \times 2 \times 3$	$96 \times 48 \times 48$	1.7745	30.0	9.82	10^{-5}	20	0.294	5599
4th parallel†	$6 \times 2 \times 3$	$96 \times 48 \times 48$	2.6000	30.0	9.82	10^{-4}	20	0.565	7577
1st two spheres♠	$5 \times 1 \times 4$	$64 \times 32 \times 48$	0.03	51.0	982.0	10^{-3}	20	0.484	1095
2nd two spheres	$5 \times 1 \times 4$	$64 \times 32 \times 48$	0.01	6.72	982.0	10^{-3}	10-13	0.219	534
Three spheres	$10 \times 1 \times 4$	$128 \times 32 \times 48$	0.01	6.53	982.0	10^{-3}	11	0.231	1980

Table 20. Computational parameters for the settling simulations presented in chapter 5. † *Although* IT_{max} *reached the limit, the volume averaged rate of strain satisfied* $\epsilon < 10^{-3}$. ‡ *The total number of iterations was limited to* 10 *instead of* 20. ♠ *Although* IT_{max} *reached the limit, the volume averaged rate of strain satisfied* $\epsilon < 10^{-2}$.

Exp. no.	$L_1 \times L_2 \times L_3$	$N_1 \times N_2 \times N_3$	δt	$Re = \frac{L_2 U}{\nu}$	$Fr = \frac{g L_2}{U^2}$	ϵ	IT_{max}	CFL_{max}	CPU_{time}
1st neutral Poiseuille†‡	$12 \times 2 \times 6$	$128 \times 48 \times 64$	0.02	5.0	49.0	10^{-5}	10	0.214	439
2nd neutral Poiseuille	$12 \times 2 \times 6$	$128 \times 48 \times 64$	0.02	40.0	49.0	10^{-5}	20	0.214	9101
3rd neutral Poiseuille	$12 \times 2 \times 6$	$128 \times 48 \times 64$	0.02	40.0	49.0	10^{-5}	20	0.214	9879
4th neutral Poiseuille	$12 \times 2 \times 6$	$128 \times 48 \times 64$	0.02	56.0	49.0	10^{-4}	14	0.214	5494
Light Poiseuille†	$6.75 \times 2 \times 4.5$	$96 \times 64 \times 64$	0.03	102.12	1318.33	10^{-4}	20	0.444	7610
Heavy Poiseuille†	$6.75 \times 2 \times 4.5$	$96 \times 64 \times 64$	0.01	103.08	1318.33	10^{-4}	20	0.515	7650
Three Poiseuille†	$6 \times 2 \times 4$	$96 \times 64 \times 64$	0.02	100	49.0	10^{-4}	20	0.320	7663

Table 22. Computational parameters for the Poiseuille flow simulations presented in chapter 5. † *Although* IT_{max} *reached the limit, the volume averaged rate of strain satisfied* $\epsilon < 10^{-3}$. ‡ *The total number of iterations was limited to* 10 *instead of* 20. $^{\spadesuit}$ *Although* IT_{max} *reached the limit, the volume averaged rate of strain satisfied* $\epsilon < 10^{-2}$.

Bibliographic Data Sheet **Risø–R–1215(EN)**

Title and author(s)

Numerical Investigations of Macroscopic Particle Dynamics in Microflows

Sune Lomholt

ISBN	ISSN
87–550–2584–6(Internet)	0106–2840

Dept. or group	Date
Optics and Fluid Dynamics	Oktober 2001

Groups own reg. number(s)	Project/contract No.

Pages	Tables	Illustrations	References
139	22	57	94

Abstract (Max. 2000 char.)

Particle dynamics in microflows is investigated using a force coupling method that incoporates two-way coupling between the continuous phase and the particulate phase. The force coupling method is explained and several examples of particle dynamics are given. Furthermore, the model is compared with experimental results with good agreement.

Descriptors

Microflow; Particulate flow; Two-phase flow; Navier-Stokes equations; Force Coupling; Numerical Studies; Shear flow; Dual particle interaction; Triple particle interaction